



HAL
open science

Structure de surface d'alliages et de composés intermétalliques in-Pd

Garry Mcguirk

► **To cite this version:**

Garry Mcguirk. Structure de surface d'alliages et de composés intermétalliques in-Pd. Other. Université de Lorraine, 2014. English. NNT : 2014LORR0196 . tel-01751161

HAL Id: tel-01751161

<https://hal.univ-lorraine.fr/tel-01751161>

Submitted on 29 Mar 2018

HAL is a multi-disciplinary open access archive for the deposit and dissemination of scientific research documents, whether they are published or not. The documents may come from teaching and research institutions in France or abroad, or from public or private research centers.

L'archive ouverte pluridisciplinaire **HAL**, est destinée au dépôt et à la diffusion de documents scientifiques de niveau recherche, publiés ou non, émanant des établissements d'enseignement et de recherche français ou étrangers, des laboratoires publics ou privés.



AVERTISSEMENT

Ce document est le fruit d'un long travail approuvé par le jury de soutenance et mis à disposition de l'ensemble de la communauté universitaire élargie.

Il est soumis à la propriété intellectuelle de l'auteur. Ceci implique une obligation de citation et de référencement lors de l'utilisation de ce document.

D'autre part, toute contrefaçon, plagiat, reproduction illicite encourt une poursuite pénale.

Contact : ddoc-theses-contact@univ-lorraine.fr

LIENS

Code de la Propriété Intellectuelle. articles L 122. 4

Code de la Propriété Intellectuelle. articles L 335.2- L 335.10

http://www.cfcopies.com/V2/leg/leg_droi.php

<http://www.culture.gouv.fr/culture/infos-pratiques/droits/protection.htm>

UNIVERSITÉ DE LORRAINE
Institut Jean Lamour UMR 7198
Centre National de la Recherche Scientifique
Parc de Saurupt, 54011 Nancy Cedex, France

DOCTORAT

Spécialité: Science des Matériaux
Présentée et soutenue publiquement par

Garry M^cGUIRK

Le 15 Décembre 2014

Surface structures of In-Pd alloys and intermetallic compounds

JURY

Mme. M.G. BARTHÉS-LABROUSSE, Directrice de Recherche. Rapporteur.
Mr. R. McGRATH, Professeur. Rapporteur.
Mr. M. ARMBRÜSTER, Professeur. Examineur.
Mr. G. HENRION, Directeur de Recherche. Examineur.
Mr. J. LEDIEU, Chargé de Recherche, HDR. Co-directeur de thèse.
Mr. V. FOURNÉE, Directeur de Recherche. Directeur de thèse.

“I have had my results for a long time: but I do not yet know how I am to arrive at them.”

Carl Friedrich Gauss

Acknowledgements

First and foremost, I would like to express my sincere gratitude to my advisor and co-advisor Dr. Vincent Fournée and Dr. Julian Ledieu for their continuous support during my Ph.D study and research. I certainly appreciate the mentorship and time they both gave me over the past three years. I could not have imagined a better advisor with more patience, knowledge and experience than Dr. Fournée. And Dr. Ledieu's motivation, enthusiasm, and willingness to guide me was unmatched. Together, they helped me develop an intuition to be a successful experimentalist.

In addition to my advisors, I would like to thank the rest of my thesis committee: Mme. M. G. Barthés-Labrousse, Mr. R. McGrath, Mr. M. Armbrüster, and Mr. G. Henrion for their guidance, insightful comments, and thought-provoking questions.

My sincere thanks also goes to all the scientists I've worked with in collaboration. Firstly, I thank Prof. Renee Diehl for giving me the opportunity to perform LEED I(E) experimental work at her lab. I also thank John Stevens for the technical insight during all my work at Penn State. Additionally, my appreciation goes out to Katariina Pussi for the theoretical LEED I(E) structural analysis of InPd(111). I also extend my thanks to the staff at beamline I06 at the Diamond Light Source in Reading, UK, and those who assisted me with the analysis of the beamline data: Francesco Maccherozzi, Georg Held, Marc Armbrüster, and Jacopo Ardini. Additionally, the single crystal samples provided by Peter Gille and Michael Hahne, and the EBSD analysis of our polycrystal sample by Matthieu Salib, is certainly appreciated.

I thank my fellow research group team members (past and present): Jean-Marie Dubois, Emilie Gaudry, Marie-Cécile de Weerd, Dmytro Kandaskalov, Matthias Meier, Adnene Sakly, Laura Serkovick, and Joris Kadok for all the insightful conversations and helpful tips about living in France! A very special thanks to Emilie Gaudry for the theoretical DFT contribution to my thesis, and to Marie-Cécile de Weerd for growing our InPd polycrystal sample (and giving me a good introduction to XRD and crystal growth!).

I would also like to recognize the sources of funding that made this project possible: The European COST Action CM0904 "Network for intermetallic compounds as catalysts for steam reforming of methanol (IMC-SRM)" and C-MAC consortium, and the ANR CAPRICE project 2011-INTB 1001-01. My appreciation goes out to all the hard-working people who ensured we were provided the resources for our work.

Last but not the least, I would like to thank my family. The support of my loving wife Jolene, parents Robert and Arlene, brother Darren, sister Leah, best pal Evan, and all my closest friends was of the utmost importance.

Contents

Quotation	i
Acknowledgements	ii
Contents	iii
List of Figures	v
List of Tables	x
Résumé	xi
Abstract	xvi
1 Introduction	1
1.1 Overview	1
1.2 Intermetallic compounds in heterogeneous catalysis	1
1.3 Methanol steam reforming (MSR)	3
1.3.1 The reaction and its importance	3
1.3.2 Recent interest in M-Pd (M=Zn, Ga, In)	4
1.4 Other interest in In-Pd intermetallics	8
1.5 Surface alloys	9
1.5.1 Intermixing and segregation	9
1.5.2 In-Pd and similar systems: top-layer substitutional alloys	11
1.5.3 In-Pd and relevant systems: multilayer alloys and IMCs	12
1.6 Bulk In-Pd phases	14
1.6.1 Elemental palladium and indium	14
1.6.2 Discovery of the phases	15
1.6.3 In-rich Phases	16
1.6.4 Pd-rich Phases	17
1.6.5 InPd	18
1.7 Bulk IMC and alloy surfaces	19
1.8 Summary	20
2 Experimental Methods	22
2.1 Experimental Background	22
2.1.1 Experimental set-up	22
2.1.2 STM	22

2.1.3	LEED	24
2.1.4	XPS	26
2.1.5	Diamond Beamline I06	27
2.2	XPS data analysis	29
2.2.1	μ XPS	29
2.2.2	Inelastic mean free path (IMFP) calculations	30
2.2.3	Quantifying in-house XPS data	31
2.2.4	Polycrystalline and bulk InPd surfaces	32
2.2.5	In/Pd(111) surface IMCs and alloys	35
3	Surface structures of In-Pd intermetallic compounds	39
3.1	Overview	39
3.2	Part I: Experimental study of In thin films on Pd(111) and alloy formation (Article)	42
3.3	Part II: Theoretical study of surface energies, alloying and segregation effects (Article)	53
4	Bulk InPd IMC surfaces	63
4.1	Introduction	63
4.2	Growth of bulk InPd	63
4.2.1	InPd single crystals	63
4.2.2	Polycrystalline InPd	65
4.3	Single crystal InPd surfaces	66
4.3.1	Overview	66
4.3.2	InPd(100)	67
4.3.3	InPd(110)	70
4.3.4	InPd(111)	75
4.4	The polycrystalline surface	78
4.5	Discussion and Conclusion	85
5	Conclusion	88
A	Pendry R-Factor	91
B	LEED	92
	Bibliography	94
	Publications	110

List of Figures

1	Diagramme de phase schématique indiquant les différentes structures de surface observées dans le système In/Pd (111) en fonction de l'épaisseur du film d'In déposé et de la température de recuit.	xiii
2	Résumé graphique illustrant la thématique de la thèse.	xv
1.1	The above XPS data compare VB spectra of Cu, Pd, and 'copper-like' ZnPd (PdZn). This figure is taken directly from the work by Tsai <i>et al.</i> [118].	8
1.2	The above surface alloy examples, taken directly from ref. [168], are a modification of the work from Christensen <i>et al.</i> [27]. The plots represent each of the four combinations of positive (negative) slope/curvature. A negative slope (negative curvature) indicates the deposited element will stay on the top (separate into A and B elements), whereas a positive slope (positive curvature) suggests intermixing (surface alloying) will occur.	11
1.3	The phase diagram of the In-Pd system [112].	16
1.4	The above images show the In-rich In-Pd phases from a 3-d perspective. The unit cell dimensions (not to scale between a, b, and c) correspond to values in Table 1.1. a) InPd and c) In ₇ Pd ₃ are cubic, and b) In ₃ Pd ₂ is a trigonal system where the angle between <i>a</i> and <i>b</i> is 120°. In all phases above, the <i>c</i> vector is perpendicular to both <i>a</i> and <i>b</i> . The silver (light grey)/red (dark grey) atoms are In/Pd [127].	17
1.5	The Pd-rich In-Pd phases are shown from a 3-D perspective. The images are orientated such that <i>a</i> points upwards and unit cell dimensions (not to scale relative to each other) are proportional to values in Table 1.2. The angle between all unit cell vectors is 90° for all three phases. The silver (light grey) and red (dark grey) atoms represent In and Pd respectively for b) InPd ₂ and c) In ₃ Pd ₅ . For a) InPd ₃ , the silver (light grey) atoms are occupied by In or Pd 50 % of the time, whereas the red (dark grey) atom is Pd. This is represented by the crystal chemical formula (In _{0.5} Pd _{0.5})Pd = InPd ₃ [76, 127].	18
2.1	A top view schematic of the vacuum chambers used for 'in-house' experiments is shown above. UHV pressures are maintained by turbo-pumps (green/dark gray circles), rotary vane pumps (green/dark gray rectangles), and ion pumps (not shown) located underneath each chamber.	23
2.2	The above illustration shows the very basic LEEM design concept [35].	27
2.3	Pd 3d _{5/2} spectra were fitted with a Voigt function after a removal of a localized linear background.	29

2.4	The Pd 3d region of polycrystalline InPd is fitted with four Gaussian - Lorentzian peaks following the removal of a Shirley background in the selected (blue/gray) region. The large left/right peaks are Pd 3d _{3/2} /Pd 3d _{5/2} and the small left/right peaks are K _{α3} /K _{α4} of Pd 3d _{3/2}	33
2.5	The selected (blue/gray) region within the In 3d spectrum above, defines the endpoints for removal of a Shirley background. Within this region are two Doniach-Sunjic (In 3d _{3/2} /In 3d _{5/2} , large left/right peaks) and two Gaussian (In 3d _{3/2} K _{α3} /K _{α4} , small left/right peaks) peaks.	34
2.6	The Pd 3d _{5/2} region is defined above (shaded blue/gray) with a Shirley background subtracted. The peak information is displayed in the second row of Table 2.2.	35
2.7	Peak information (shown in the second row Table 2.2) from the shaded region (blue/gray) of In 3d _{5/2} was taken in the same manner as for Fig. 2.6.	36
2.8	Peak fitting of Pd 3d _{5/2} spectra indicate 1:1 InPd and formation of additional surface alloy(s). The positions and FWHM were fixed ($\leq \pm 0.02$ eV) for Pd bulk and surface components with respect to clean Pd(111) fits, and likewise the InPd 1:1 component to the InPd polycrystal. The unknown alloy component varied in FWHM and position, suggesting formation of other phases.	37
2.9	In 3d _{5/2} XPS components show relatively small shifts in comparison to Pd 3d _{5/2} shifts of Fig. 2.8.	37
3.1	The STM image on the left (50×50 nm ² , $U = 1.2$ V; $I = 0.08$ nA) is dominated by three rotational domains (a,b,c) of InPd(110)-c(4×2) or In ₇ Pd ₃ (110); they have equivalent 2D unit cells. Small patches of corresponding InPd(110) coexist as shown in the zoomed-in rectangular section. The calculated FFT of the whole image is equivalent to the sum of individual reciprocal lattice images shown on the far right. The real space models, having white backgrounds, show the structures are incommensurate to the underlying Pd(111) substrate. This is also true for smaller rectangular InPd(110) domains (not modeled here).	40
4.1	Images (a) and (b) are the single crystals grown at the Ludwig-Maximilians-Universität in München. The regions where single crystal samples were taken are labeled appropriately (a) - InPd(110) and (b) - InPd(100) and InPd(111). A chemical analysis taken from a different portion of crystal (a) showed 52.1:47.9 In:Pd. Towards the bottom of the samples, EPMA axial measurements indicated our samples were slightly more Indium rich ($\lesssim 54$ at. % In) [50, 64].	64
4.2	The images above show a) InPd(110) and b) InPd(100) and InPd(111) samples mounted on a Ta back plate. For LEED I(E), the InPd(100) and InPd(111) samples (b) were additionally mounted to a Mo sample holder. This sample holder was attached to a manipulator having an extra degree of freedom so that normal incident LEED I(E) data could be acquired.	65
4.3	Optical micrography using polarized light (left) and normal photographed images (right) were taken of the InPd polycrystalline surface.	65

4.4	The three crystal surfaces examined under UHV conditions are shown above (theoretical). The unit cells of all surface reconstructions observed during surface preparation are drawn and labeled accordingly. A InPd(100)-(1x1) is shown for reference (not observed), represented by the small black square. The corresponding unit cell dimensions and interlayer spacings are found in Table 4.1	66
4.5	Concentration measurements after Ar+ sputtering (2 keV for 30 minutes) and annealing the InPd(100) surface are deduced from XPS data for two different take-off angles (θ is the angle between the surface normal and analyzer). The solid line in this figure is a guide for the eye only.	67
4.6	For InPd(100), the above p(4x4) (left) and $c(3\sqrt{2} \times \sqrt{2})R45^\circ$ (right) LEED images (48 eV) were obtained before and after the transition depicted in Fig. 4.5. The thickest lines, shown in the simulated LEED patterns, represent primitive reciprocal space unit cells for p(4x4) (black) and $c(3\sqrt{2} \times \sqrt{2})R45^\circ$ domains (dark red/blue). The InPd(100)-(1x1) reciprocal space unit cell corresponds to the dashed line.	68
4.7	STM images of the InPd(100)- $c(3\sqrt{2} \times \sqrt{2})R45^\circ$ superstructure are shown above. The FFT-filtered top image (a) (15 nm x 11 nm, +1.4 V, 0.25 nA) shows two domains of atomically resolved InPd(100)- $c(3\sqrt{2} \times \sqrt{2})R45^\circ$. At the bottom (b), both rectangular (solid line) and primitive (dashed line) unit cells are superimposed over a zoomed-in portion of (a) (5 nm x 5 nm). The calculated FFT (c), taken over the original image (a), shows the primitive reciprocal space unit cells from both domains. Note that the images are rotated by 45° with respect to all other InPd(100) STM images.	68
4.8	STM images and corresponding LEED pattern of the InPd(100)-p(4x4) structure are shown above. The quasi-ordered square structures (b - 15 nm x 15 nm/+1.8 V; 0.09 nA) form on top of the terraces (a - 80 nm x 80 nm/+1.8 V; 0.09 nA). The calculated FFT (c) taken over a larger, well-resolved image (not shown - 50 nm x 50 nm/-0.7 V; 0.07 nA) corresponds to a p(4x4). This is in agreement with the LEED pattern (50 eV) presented in (d).	69
4.9	Concentration measurements after Ar+ sputtering (2 keV for 30 minutes) and annealing the InPd(110) surface are deduced from XPS data for two different take-off angles (θ is the angle between the surface normal and analyzer). The solid line in this figure is a guide for the eye only.	70
4.10	This LEED pattern (a) and STM image (b) were acquired immediately following the transition to near stoichiometric InPd(110) (after annealing to 640 K as seen in Fig. 4.9). The LEED pattern, taken at 140 eV, is clearly InPd(110)-(1x1). The corresponding STM (8 nm x 4.7 nm/-1.5 V; 0.08 nA) shows atomically resolved rows of either In or Pd atoms (one element slightly protrudes from the surface plane).	71
4.11	The diffuse LEED images from the first set of experiments on InPd(110) show additional (h,k) beams from a faceted surface seen in scanning electron micrography (c). These beams are barely visible in both (2x1) (a) and (1x1) LEED patterns taken at 70 and 80 eV respectively. They are located at the bottom of the arrow or enclosed in circles. The arrows show the directions of the beams with increasing beam energy. The double arrow represents streaking observed for the (2x1) (a) reconstruction.	72

4.12	The above $c(4\times 2)$ (a), (2×1) (b), and (1×1) (c) LEED patterns are the three reconstructions of the InPd(110) surface. The primitive reciprocal space unit cells for each image, taken at the same beam energy of 63 eV, are shown.	72
4.13	These STM images, show both small rounded terraces (a) and large flat terraces (b) formed on InPd(110). The formations of (a) occurred in conjunction with the (2×1) LEED pattern in Fig. 4.12 (b), whereas InPd(110)- (1×1) formed on the flat terraces of (b) (corresponding LEED image: Fig. 4.12 (c)). A histogram (c) taken over four terraces was used to approximate step height measurements for InPd(110)- (1×1) . The STM image size/tunneling conditions for (a) and (b), are $(50\text{ nm} \times 50\text{ nm})/(+1.4\text{ V}; 0.07\text{ nA})$ and $(40\text{ nm} \times 40\text{ nm})/(-0.5\text{ V}; 0.09\text{ nA})$ respectively.	73
4.14	Surface compositions and LEED observations from the second set of InPd(110) experiments are displayed above. Each measurement/observation was performed after sputtering and annealing the surface. The windows labeled ‘Facets’ and ‘Dull Luster’ represent the respective annealing temperature range where initial faceting and surface appearance change can be expected. However once observed, it seems faceting can occur at all temperatures. The ‘Dull Luster’ is irreversible until the sample is re-polished.	74
4.15	Concentration measurements after Ar+ sputtering (2 keV for 30 minutes) and annealing the InPd(111) surface are deduced from XPS data for two different take-off angles (θ is the angle between the surface normal and analyzer). The solid line in this figure is a guide for the eye only.	75
4.16	These LEED images, both taken at 50 eV, show the two superstructures for InPd(111). The unit cells of the $(\sqrt{3} \times \sqrt{3})R30^\circ$ (a) and (1×1) (b) LEED patterns are marked accordingly.	76
4.17	The above STM images correspond to InPd(111)- $(\sqrt{3} \times \sqrt{3})R30^\circ$ (a) and InPd(111)- (1×1) phases (b). The $(\sqrt{3} \times \sqrt{3})R30^\circ$ phase includes a 1D plot to show the difference between the two main types of contrast. An FFT of the $30\text{ nm} \times 30\text{ nm}$ image $(+1.8\text{ V}; 0.09\text{ nA})$ confirms the hexagonal superstructure defined as a $(\sqrt{3} \times \sqrt{3})R30^\circ$ surface reconstruction. Image (b) $(62\text{ nm} \times 62\text{ nm}/+0.5\text{ V}; 0.07\text{ nA})$ shows the step edge between two large terraces.	76
4.18	The experimental vs. theoretical $I(E)$ curves for 12 separate beams of the Pd-rich InPd(111)- (1×1) structure are shown. The theoretical data are from the best-fitted model of Fig. 4.19 and Table 4.2. Individual R factors for each (h,k) beam are indicated next to respective plots. A total R factor of .26 was calculated from the entire data set (total range of 2700 eV).	77
4.19	The above profile of the Pd-rich InPd(111)- (1×1) surface, viewed along the $[\bar{1} 0 1]$ axis, illustrates interlayer spacings in accordance with values of Table 4.2. The expansions/contractions of planes are slightly exaggerated for clarity.	78

4.20	These LEEM images (a - 80 μm field of view (FOV) and b - 30 μm FOV) show InPd polycrystalline grain boundaries that are surrounded by features ~ 4 to 14 μm (a-SG1) and ~ 3 μm wide (b-SG2). Note that the ‘rough grains’ surrounding both ‘smooth grains’ are similar to, but not the same as RG1 and RG2.	79
4.21	Contrast from flat features on SG1 (InPd polycrystal) are shown in two different imaging modes. Both images were taken at a 50 μm FOV.	80
4.22	a) The 29 eV micro-spot LEED Image of SG1 (InPd polycrystal) shows a square unit cell having interior beams from an unknown surface reconstruction. b) This image of SG2, taken at 30 eV, shows a well-ordered InPd phase.	80
4.23	The LEED (left: 38 eV) and LEEM image (right: 50 μm FOV) of SG2 (InPd polycrystal) were acquired after 20L exposure to H_2 . The electron beam caused damage to the surface in LEED mode; this shows the micro-spot sampling area (~ 6 μm diameter).	81
4.24	The spectra show VB data of SG2 and RG2 (InPd polycrystal). The calculated IMFPs were based on stop voltages of 445.5 eV (top) and 545.1 eV (middle). Another smooth grain (SG3) shows similar features to SG2 despite a small but measurable amount of surface oxygen. At the bottom of the figure, overlapped intensities shows substantial difference in the DOS between SG1 and SG2.	82
4.25	The VB data from SG1 and RG1 (InPd polycrystal) are displayed such that the top spectra is more surface sensitive whereas the bottom spectra is more bulk-like. The IMFPs displayed next to the graph were approximated using the kinetic energy within the dispersion plane corresponding to the stop voltages, from top to bottom: 245.5 eV, 445.5 eV, 543.5 eV, and 643.5 eV.	82
4.26	The STM images above show formations of quasi-ordered rectangular centered structures on terraces of the polycrystalline sample. The upper-left image (100 nm^2 ; $V=+1.1$ V; $I=0.08$ nA) and lower-left image (50 nm^2 ; $V=+1.1$ V; $I=0.08$ nA) show respective terraces and atomically resolved quasi-ordered structures. Measurements of the average terrace height and FFT of the primitive unit cell are indicated appropriately.	83
4.27	The following EBSD data of the polycrystalline sample shows a variety of grain orientations (color coded). The EBSD data is acquired from probing depth on the order of 1 μm . The grain orientations are deduced from an average surface normal (of the area sampled, shown by the dotted rectangle).	84
4.28	The XPS VB data of Cu, ZnPd and GaPd are retraces from the work by Tsai <i>et al.</i> [118]* and Kovnir <i>et al.</i> [79]. [‡] These data, and our VB data from the InPd polycrystal, exhibit a ‘Cu-like’ DOS.	85

List of Tables

1.1	The space group (Hermann-Mauguin international symbol and number), structure type, and lattice constants of In-rich InPd phases [39] and the InPd phase [49] are shown above.	16
1.2	The Pd-rich In-Pd phases shown above include space group (Hermann-Mauguin international symbol and number), structure type, and lattice constant information [76].	17
2.1	Functional forms of fitted Pd and In 3d regions, as shown in Figs. 2.4 and 2.5, are indicated above. The peaks are fitted with either Gaussian - Lorentzian product (GL) or sum (SGL) functions, or Doniach - Sunjic (DS) functions.	33
2.2	Shown above are specified values of fitted Pd 3d _{5/2} and In 3d _{5/2} regions, as discussed in the text and shown in Figs. 2.4 and 2.5, compared to ‘raw’ data measurements from Figs. 2.6 and 2.7. The first two rows are from the same data set obtained after sputtering the sample for 30 min. at 2 keV and annealing to 1073 K for 1.5 hrs. The last row (*) is from another experiment where the sample was annealed to 933 K for 1.5 hrs following the same sputtering condition; this is the preparation referred to in upcoming chapters, i.e. the In ₅₃ Pd ₄₇ polycrystal surface composition.	34
4.1	The theoretical unit cell dimensions of 2D surface meshes of all InPd(110), InPd(111), and InPd(100) surface reconstructions shown in Fig. 4.4 are displayed above. <i>Bulk-truncated InPd(100) is the only phase listed above not observed.</i> The primitive unit cell dimension of ‘c’ (centered) lattices are: $a=b=7.959 \text{ \AA}$, $\psi=70.5^\circ$ *; and $a=b=7.265 \text{ \AA}$, $\psi=36.9^\circ$ ‡. The angle ψ between a and b is 90° for InPd(110)/InPd(100), and 120° for the hexagonal InPd(111) reconstructions.	66
4.2	The above values are the relaxed interlayer spacings for the best fit geometry of InPd(111)-(1x1) LEED I(E) analysis; they correspond to an overall R factor of 0.26.	78

Résumé

Ce travail de thèse s'inscrit dans un programme de recherche européen qui vise à développer de façon rationnelle de nouveaux catalyseurs possédant une activité et une sélectivité élevées. La réaction chimique ciblée est le vaporeformage du méthanol dont l'impact socio-économique est considéré comme très important. En effet, le méthanol est facile à transporter et à stocker et il est un vecteur important d'hydrogène pour la production d'énergie dans les piles à combustible via la réaction $\text{CH}_3\text{OH} + \text{H}_2\text{O} \rightarrow \text{CO}_2 + 3\text{H}_2$. Les catalyseurs actuellement utilisés sont des particules de cuivre supportées sur des oxydes de zinc (Cu/ZnO) qui présentent une activité et une sélectivité élevées mais dont l'inconvénient est le manque de stabilité au cours de la réaction dû au phénomène de coalescence des grains. Depuis quelques années, la communauté scientifique s'intéresse à une nouvelle génération de matériaux catalytiques de type Pd/ZnO, Pd/Ga₂O₃ ou encore Pd/In₂O₃. En effet, les travaux pionniers de Iwasa et al. ont montré une plus grande stabilité thermique de ces matériaux tout en préservant des propriétés catalytiques équivalentes à celles de Cu/ZnO. L'origine des propriétés catalytiques est généralement attribuée à la formation de composés intermétalliques de type M-Pd (M=Zn, Ga ou In) au cours de la réaction après réduction de l'oxyde. De manière générale, les composés intermétalliques présentent une immense variété de structure électronique et géométrique et possèdent à ce titre un potentiel important en catalyse. Le développement rationnel de nouveaux catalyseurs nécessite de bien comprendre les mécanismes de la réaction chimique à l'échelle atomique sur des systèmes modèles. Il est donc essentiel de déterminer les structures électroniques et géométriques des surfaces de ces intermétalliques pour pouvoir ensuite appréhender leur réactivité chimique.

C'est dans ce cadre que s'inscrivent les travaux de thèse résumés ci-dessous. En particulier, nous nous sommes intéressés au système In-Pd pour lequel très peu d'informations étaient disponibles dans la littérature comparativement aux systèmes Zn-Pd et Ga-Pd.

Nous avons donc étudié la structure de surfaces de composés intermétalliques In-Pd modèles en utilisant essentiellement des méthodes expérimentales de science des surfaces. Nous avons en particulier utilisé les techniques de spectroscopie de photoémission X et UV (XPS, UPS), la microscopie à effet tunnel (STM) et la diffraction d'électrons lents (LEED) sous ultravide (UHV) rassemblées sur une même plate-forme instrumentale disponible au sein de l'équipe. Cette plate-forme possède également des outils de préparation de surface (bombardement ionique et recuit en température) et des sources de dépôt pour élaborer des films minces in situ. Nous avons également utilisé de grands instruments comme les sources de rayonnement synchrotron ESRF et DIAMOND. Certaines expériences complémentaires de LEED dynamique (LEED-IV) ont été réalisées au département de physique de l'université de Penn State aux Etats-Unis en collaboration avec le groupe du Prof. Renee Diehl au cours de plusieurs séjours. Par ailleurs, ces résultats expérimentaux ont été confrontés à des calculs théoriques utilisant la théorie de la fonctionnelle de la densité (DFT) réalisés au sein de l'équipe.

Dans un premier temps, nous avons étudié la formation d'alliages de surface In-Pd obtenus par dépôt de films d'In sur une surface monocristalline de Pd (111) sous UHV. Il a été montré que différentes phases se forment en fonction de l'épaisseur du film d'In (de 0 à 35 monocouches (MC)) et de la température de recuit. Pour des films très minces (1 à 2 MC), les clichés de diffraction LEED montrent que l'In déposé s'allie avec le Pd à température ambiante et on observe la formation de trois domaines rotationnels de faible épaisseur d'une phase InPd (110) de faible qualité structurale dans une zone proche de la surface. Par recuit à 690 K, on obtient une nouvelle phase de structure $(\sqrt{3} \times \sqrt{3})R30^\circ$ localisée dans le plan d'extrême surface. Pour des films d'épaisseur comprise entre 4 et 35 MC, on observe la formation de trois domaines rotationnels du composé bcc-In₇Pd₃ (110). Cette phase riche en In croît vraisemblablement au-dessus d'une couche d'interface de type InPd (110). La phase In₇Pd₃ est métastable et se transforme en une phase InPd (110) homogène dans une zone proche de la surface. Ces conditions expérimentales permettent donc de former le composé souhaité en catalyse sous forme d'alliage de surface. Les déplacements chimiques et la structure de la bande de valence sont à ce stade identiques à ce qui est observé pour le composé stœchiométrique In-Pd 1:1. La bande de valence présente en particulier des caractéristiques proches de celle du cuivre pur auxquelles sont attribuées (pour partie) les propriétés catalytiques. On montre également que ces alliages de surface ne sont pas stables pour des températures de

recuit supérieures à 600 K. Dans ces conditions, la concentration d'In dans la zone proche de la surface diminue autour de 20 % at. et on retrouve une structure de type (1x1). Ce dernier résultat est en accord avec l'étude théorique qui montre que des couches de Pd dopées In dans Pd (111) ne sont énergétiquement stables que pour des concentrations inférieures à 50 % at. Une couche dopée contenant plus de 50 % d'In aura tendance à se transformer en un multicouche de couches dopées, chacune possédant une concentration d'In inférieure à 50 %. Les énergies de cohésion du composé InPd (-3.57 eV/atome) sont également cohérentes avec l'interdiffusion et la formation spontanée d'un alliage à la température ambiante.

> 690 K	(1x1)					
690 K	$(\sqrt{3} \times \sqrt{3})R30^\circ$	(1x1)				
550-600 K	undefined	3xInPd-(110)				
500 K		3xIn ₃ Pd ₇ -(110)				
300 K	3xInPd(110)					
T / θ	1 MLE	2 MLE	4 MLE	8 MLE	16 MLE	35 MLE

FIGURE 1: Diagramme de phase schématisé indiquant les différentes structures de surface observées dans le système In/Pd (111) en fonction de l'épaisseur du film d'In déposé et de la température de recuit.

Dans une deuxième partie de la thèse, nous nous sommes intéressés aux surfaces de bas indices d'un monocristal de la phase cubique InPd, c'est-à-dire aux trois surfaces (100), (110) et (111). Le monocristal a été élaboré par la méthode Czochralski par nos collègues de l'Université de Munich en Allemagne. On montre par XPS que ces trois surfaces présentent un appauvrissement en In (40 % at.) sous l'effet du bombardement ionique nécessaire à la préparation d'une surface propre, sans contaminant, sous UHV. A l'inverse, on observe un enrichissement en In (60 % at.) de la zone proche de la surface au cours du recuit. La transition entre ces deux régimes a lieu approximativement entre 550 et 650 K. Pour chacune des surfaces, on observe que ces variations de composition chimique sont corrélées à des transitions structurales. Ainsi pour la surface (100), on passe d'une reconstruction de type (4x4) assez diffuse à basse température à une structure en $(3\sqrt{2} \times \sqrt{2})R45^\circ$ au-dessus de la transition. Pour la surface (110), le LEED indique une structure diffuse (1x1) avant la transition puis une reconstruction de type c(4x2) et p(2x1) autour de la transition puis de nouveau une structure (1x1) au-delà de la transition. Dans le cas de la surface (111), on passe d'une structure (1x1) riche

en Pd à une structure (1x1) riche en In avec une transition présentant une structure en $(\sqrt{3} \times \sqrt{3})R30^\circ$. Les structures atomiques de ces différentes phases sont rapportées en se basant sur les données de diffraction (LEED et LEED-IV) et de STM. Les résultats sont interprétés en utilisant des calculs théoriques d'énergie de surface et de ségrégation. Sont également présentés des résultats expérimentaux de microscopie d'électrons lents (LEEM) et de micro-diffraction d'électrons lents (μ -LEED) réalisées sur synchrotron sur un polycristal de la phase InPd élaboré au sein de l'équipe.

Le manuscrit est organisé de la façon suivante. Un premier chapitre présente une introduction générale sur l'intérêt des composés intermétalliques en catalyse hétérogène avec un accent particulier sur le vaporeformage du méthanol. On trouvera également quelques généralités sur les alliages de surface ainsi qu'une revue bibliographique présentant l'état de l'art des connaissances sur les systèmes M-Pd (M=Zn, Ga et In). Les différentes phases connues du diagramme In-Pd sont décrites dans ce chapitre également. Le deuxième chapitre concerne les méthodes expérimentales. Un bref exposé des différentes techniques expérimentales utilisées est présenté. Les détails concernant l'analyse des niveaux de cœur en XPS sont exposés dans ce chapitre. Tous les résultats sont rassemblés dans les chapitres III et IV. Ils constituent une description assez exhaustive de la variété des phases de surface rencontrées dans ce système In-Pd. L'étude portant sur la formation et la structure d'alliages de surface dans le système In/Pd (111) est présentée dans le chapitre III et consiste en une brève introduction suivie des deux articles publiés dans *The Journal of Chemical Physics*, à savoir 'Surface structures of In-Pd intermetallic compounds. I. Experimental study of In thin films on Pd(111) and alloy formation' et 'Surface structures of In-Pd intermetallic compounds. II. A theoretical study'. L'étude portant sur les surfaces de monocristaux ainsi que sur le polycristal InPd est présentée dans le chapitre IV. Finalement, les conclusions et perspectives de ce travail sont exposées dans le chapitre V.

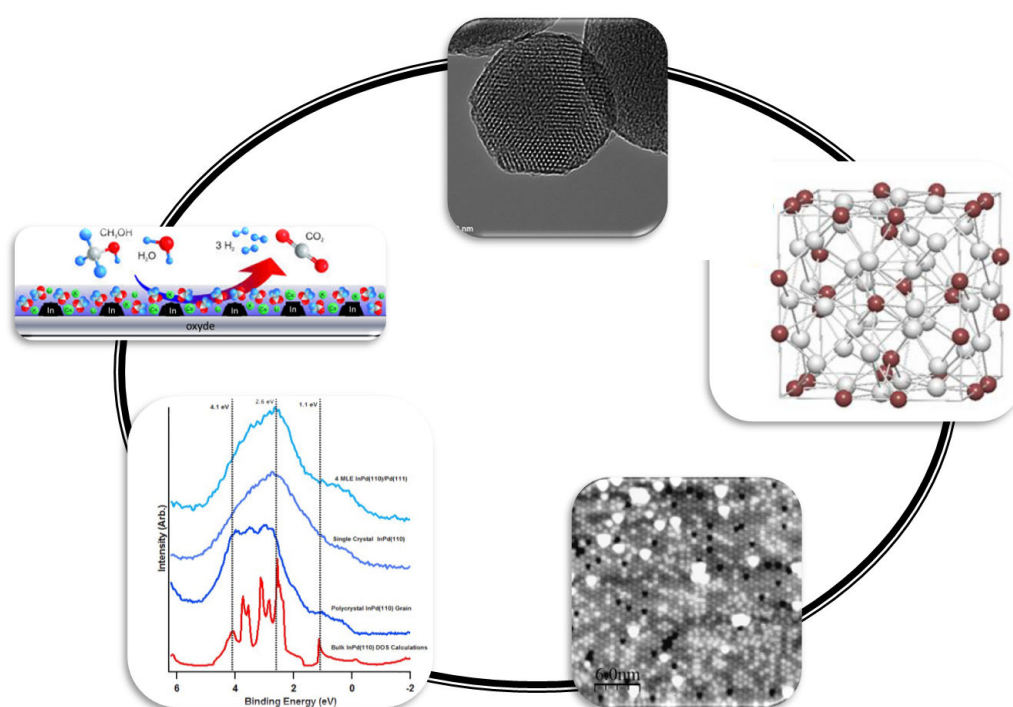
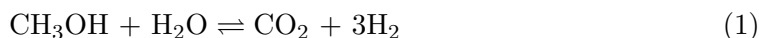


FIGURE 2: Résumé graphique illustrant la thématique de la thèse.

Abstract

The frontier of modern day research in methanol steam reforming (MSR) catalysis lies in intermetallic compound (IMC) surfaces. MSR involves a reaction of water and methanol occurring at a solid surface, i.e., it is a form of heterogeneous catalysis. The overall MSR reaction



relies on an intricate pathway involving intermediates and water \rightleftharpoons gas shifts. During the process, CO₂ and CO are the predominately detected gases. The former is associated with desirable H₂ production, whereas the latter degrades performance in Pt-based polymer electrolyte membrane (PEM) fuel cells [2, 134, 151]. Hydrogen-based PEM fuel cells are a primary industrial application for MSR. In part, methanol is a safe and affordable source of hydrogen. The desired production of hydrogen is realized near the surface - gas interface of MSR catalysts. More specifically, this is attributed to atomic and electronic structures of bi-metallic constituents within the top few layers of the surface. In this respect, Pd-based MSR catalysts have been widely studied in modern times since the momentous performance of Pd/ZnO catalysts was uncovered by Iwasa and co-workers around two decades ago [65, 66]. Recently, a paradigm shift focusing on Pd-based IMCs has been underway. This is largely due to the strong bonding nature of IMCs being correlated to surface stability during reaction conditions [1]. Stable IMCs would be ideal over weaker bonded surface alloys found in catalysts currently used by industry, which exhibit unwanted effects such as metal sintering, surface segregation and catalyst deactivation.

The most recent focus is on M-Pd (M=Zn, Ga, In) IMCs in MSR catalysis. In a broad sense, the surface science literature can be classified into four primary categories a) oxide-supported catalysis b) thin films and near surface intermetallic phases (NSIPs) c) ultra-thin film surface alloys and d) bulk alloy and IMC surfaces.

- a) Findings of bi-metallic formations of oxide-supported Pd often promotes work in categories b, c, and d. Under various reaction conditions, different bi-metallic formations have been correlated to the overall performance of a catalyst. However,

contributions of the support and metal-support interface also have a role. In the sequential step towards understanding IMCs in MSR catalysis, pure oxide supports and bimetallic NSIPs are tested separately under the same reaction conditions.

b) NSIPs have been studied in M/x systems, where x is a Pd polycrystalline foil, or Pd(111) or Pd(110) single crystals. Typically, around 4 ML of M are deposited on a Pd substrate.

c) Ultra-thin film studies consist of depositing sublayer to a few layers of M on Pd(111) or Pd(110). At coverages up to a single layer, M is interchanged with Pd surface atoms forming substitutional surface alloys. Beyond 1 ML, surface alloying can persist, bulk M can grow, or multi-layer NSIPs can form. In a few studies, molecular adsorption has been performed over NSIPs and (ultra-)thin films.

d) Studies of molecular adsorption on bulk alloy and IMC surfaces have also been performed. However, the successful growth of these crystals is often a timely and difficult prerequisite to surface characterization. Thus, experimental studies on $M_xPd_{1-x}(h, k, l)$ single crystal and M_xPd_{1-x} polycrystal surfaces are far and few.

The work herein provides a comprehensive collection of In-Pd studies, contributing to the above categories (b),(c), and (d). This includes the initial reports of InPd/Pd(111) NSIPs (b), and InPd(110) and InPd(100) IMC single crystal surfaces (d). A low-energy electron diffraction (LEED) I(E) structural analysis of InPd(111) (1x1) is also included. Furthermore, the first characterizations of electronic and atomic surface structures on grains of bulk polycrystalline InPd (d), and on In/Pd(111) ultra-thin film growth (c) are reported.

In-Pd NSIPs and the InPd polycrystal were examined experimentally with low energy electron diffraction (LEED), X-ray photoemission spectroscopy (XPS), and scanning tunneling microscopy (STM). Individual grains and grain boundaries of the polycrystal sample were further characterized by micro-spot XPS (μ XPS) and LEED, and low-energy microscopy (LEEM) at beamline I06 of the Diamond Light Source X-ray synchrotron facility in the UK. The single crystals were studied by LEED, XPS, STM, and density functional theory (DFT). Theoretical DFT calculations, LEED, XPS, and STM were also performed on In/Pd(111) ultra-thin film surface alloys.

DFT calculations, LEED I(E) structural analysis, EBSD, and all the crystal growth were performed by the respective individuals mentioned in the Acknowledgments. So, an in-depth background to these techniques is excluded in the following chapters. Chapter 1 is a summary of relevant literature. Chapter II consists of a discussion of the experimental techniques performed under ultra-high vacuum conditions and data extrapolation methods. The major results of In/Pd(111) ultra-thin films and NSIPs are

briefly summarized at the beginning of Chapter 3. This is followed by a two-part publication on experimental (Part I) and DFT theoretical (Part II) findings. The second paper (Part II) also includes DFT work for the single crystal surfaces, which carries over to discussions in Chapter 4. This chapter is based on InPd polycrystalline and single crystalline experimental findings, but incorporates some relations to DFT calculations. Our conclusions and perspectives are discussed in Chapter 5. This includes comparisons between our work and the pertinent findings of previous research.

Chapter 1

Introduction

1.1 Overview

This chapter is intended to describe the motivations, challenges, and past and present works for In-Pd bimetallic compound surface research. First, the importance of understanding atomic-level electronic and geometric properties of surface structures in heterogeneous catalysis is discussed; this being the fundamental goal of our research. Specifically, the correlation of surface structures and reaction mechanisms of Pd-based intermetallic compounds (IMCs) for methanol steam reforming (MSR) is highlighted. MSR is the primary industry-driven motivation for our studies and is discussed in some detail. Other applications of In-Pd systems are briefly mentioned as well. Next, a basic introduction to the fundamental concepts of surface alloys is presented. This is followed by examples of top-layer and multilayer surface alloys for In-Pd and similar systems. A description of multilayer In-Pd phases ties into a discussion on In-Pd bulk phases. Then, the challenges associated with preparing surfaces of bulk alloys and IMCs are presented. In particular, preferential sputtering and surface segregation are addressed. Finally, a brief summary is given of the most relevant literature pertaining to our work, which will be presented in the upcoming chapters.

1.2 Intermetallic compounds in heterogeneous catalysis

IMCs have been the frontier of heterogeneous catalysis research over the past few years. This is primarily because the unique combination of ionic and covalent interactions found in IMCs [1] can lead to stable structures, which isolate active sites. These sites can be tailored to the desired surface reaction(s) by selecting an IMC having a well-suited crystal structure [78]. For IMCs, stronger A-B atomic interactions result in a lattice different

than each metal constituent. For the predominantly studied bimetallic alloys, the lattice structure of one element is retained with atoms of the other species occupying sites either orderly or randomly. But what exactly defines the unique catalytic properties of IMCs? Unfortunately, the answer is not crystal clear since only scarce investigations exist on this topic. What is apparent though, is that the covalent bonding can stabilize the intermetallic compound of the catalyst against segregation during reactions [1]. This is exemplified by recent investigations of IMCs in acetylene semi-hydrogenation reactions, especially in GaPd [1, 133].

Surface segregation in bimetallic alloys can lead to undesirable effects in catalysis. This is realized in Pd-based alloys, such as Ag-Pd and Au-Pd substitutional alloys used in industry for the semi-hydrogenation of acetylene [1]; this is a process that alleviates acetylene, which is a poison for ethylene polymerization catalysts [1, 14, 15]. Under nominal circumstances, Pd, the active hydrogenation sites, rely on a Pd-Pd separation imparted by the inactive element (Au or Ag) for the desired adsorption configuration of acetylene. The carbon atoms of acetylene (C_2H_2) form weak bonds at the surface; this is a prerequisite for the transformation to ethylene. However, the segregation of Pd to the surface yields adsorption sites that allow strong C bonds of the acetylene molecules. This leads to deactivation of the catalyst by carbonaceous deposits [1]. IMCs can remedy these negative effects, while upholding the fundamental ideals of the active site isolation concept, and ensemble and ligand effects learned over decades of surface alloy investigations in catalysis.

In heterogeneous catalysis, i.e. adsorption and reaction occurring at the boundary between a reactant and catalyst of differing phases, the formation of ordered structures such as bimetallic alloys and IMCs can exemplify the active site isolation concept. This concept was developed by Sinfelt, Sachtler and Ponc in the 1970s [135] following several investigations of the hydrogenation of ethylene and acetylene [1, 135]. In a general sense, it refers to the catalytically active element being surrounded by the inactive one. The isolation of surface sites allows for improved selectivity (partial conversion towards a certain product) because of less possible adsorption configurations available for reactants [165]. These properties are generally related to the 1) ensemble effect and 2) the ligand effect [168].

- 1) The ensemble effect pertains to the local geometry of an adsorption site. This requires specific sites adjacent to the adsorbing molecule to be unoccupied and is altered by the composition, crystallographic orientation, and terminating surface plane.
- 2) The ligand effect refers to modifications of electronic properties at a given adsorption site from neighboring atoms. This effect is frequently studied via examinations of changes to occupied electronic density of states (DOS) near the Fermi energy (E_F).

For many transition metal (TM)-based alloys and compounds, positioning and occupancy of 4d states near E_F (valence band (VB) states) are associated with surface reactivity. This reactivity is correlated to positioning of d-band centers with respect to Fermi levels [13, 51, 110]. Generally, d-band centers shifted towards E_F imply gas adsorbates will form stronger bonds to the surface and dissociation barriers are lowered. Shifts in TM d-bands can occur from mixing with other metals or from changes in surface plane density. A closed pack surface of a given TM usually exhibits a shift away from E_F as opposed to more open surfaces shifting towards E_F [13].

Ensemble and ligand effects are rarely disentangled during investigations of heterogeneous catalysts. This is largely from difficulties in deciphering metallic surface compositions in the presence of a gas phase [168]; i.e., it is difficult to correctly correlate the exact stoichiometry of some $A_{1-x}B_x$ phase to its pure metallic DOS (ligand) and surface absorption sites (ensemble). Moreover, compositional information usually encompasses multi-phase and/or multi-faceted nano-particle surfaces, the scenario for real catalysts, so identifying/isolating reactive sites can be somewhat overzealous. Contrarily, single crystal facets examined individually under ultra-high vacuum conditions (UHV), as in most of our work, bring about atomic-level understanding but surface composition characteristics will likely differ from those of real catalysts [168]. To help bridge the gap, it is advantageous to study surface compositions of multi-grained polycrystalline intermetallic samples under UHV and during reaction conditions near ambient pressures.

Most of the work described herein is geared towards the understanding of how, why, and what pure intermetallic and alloy In-Pd atomic surface structures form. This is a first step for developing realistic models and experiments to explain surface-gas reactions in heterogeneous catalysis from a point of view of the site isolation concept, and ensemble and ligand effects. So far, the overwhelming majority of interest in this information stems from the MSR industry.

1.3 Methanol steam reforming (MSR)

1.3.1 The reaction and its importance

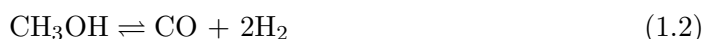
The world's energy supply still has a high reliance on fossil fuels. But the diminishing fossil fuel reserve coupled with current environmental problems call for a change towards a CO₂ neutral and sustainable energy supply and infrastructure [2]. Part of this transformation encompasses hydrogen for the generation of electricity via proton exchange membranes (PEM) fuel cells.

MSR is of high interest to the hydrogen-based alternative energy community. This is because methanol can act as an intermediate carrier of hydrogen, potentially lessening current hydrogen storage problems [46, 89, 90, 151]. The storage of elemental hydrogen, being in liquid form or under high pressure, lacks public acceptance because of cost, safety, and sustainability concerns [2]. Methanol however, offers a viable solution to these problems.

With only one C atom, methanol is the simplest of all alcohols and can be reformed at low temperatures between 200-300 °C since there are no strong C-C bonds [134]. Near these temperatures, when mixed with water over an appropriate catalyst, the overall steam reaction can occur:



The reaction mechanism towards hydrogen production was originally thought to involve methanol decomposition (Eq. (1.2)) and the water-gas shift reaction (Eq. (1.3)).



It was later shown that methanol decomposition produced intermediates that led to $\text{H}_2 + \text{CO}_2$ rather than $\text{H}_2 + \text{CO}$ [134, 152, 153], and that the presence of CO resulted from the reverse water-gas shift reaction [122, 134]. Some of the intermediates proposed were methyl formate (HCOOCH_3), formic acid (HCOOH) and formaldehyde (HCHO). However, a general consensus regarding the overall MSR reaction kinetics seems non-existent, except that two distinctive sites are required; one site adsorbs intermediates and the other, hydrogen [134].

1.3.2 Recent interest in M-Pd (M=Zn, Ga, In)

It is well known that the generation of CO during the reforming process poisons the PEM fuel cell anode [151]. The CO levels around 1500 ppm produced by Cu-catalysts are too high (>20 ppm) for long-term performance without a cleaning step [2]. However, Pd-based IMCs as catalysts offer ideal selectivity over Cu/ZnO catalysts currently used by industry. In turn, CO levels can be substantially reduced.

Supported IMCs as catalysts in MSR were introduced by Iwasa and co-workers in the 1990s [1, 65, 66]. In particular, the authors reported on the remarkably high performance of Pd/ZnO [65, 134]. Consequently, the vast majority of recent literature pertains to the Zn-Pd system, although the Ga-Pd and In-Pd systems have proven just as portentous.

To understand the reaction mechanism involving intermediates over Pd-based bimetallic surfaces, knowledge of crystallite surfaces is crucial. This is because Pd reacts with both carbon and oxygen atoms, whereas bimetallic M-Pd formations can reduce C - Pd interactions. These interactions are especially important for converting formaldehyde to CO₂ [69, 128].

Formaldehyde was recognized as an important intermediate in the most recent In-Pd studies [128, 176]. Calculations by Ye *et al.*, indicated that the most stable HCHO adsorption configuration on stoichiometric InPd (i.e., a InPd(110) surface) had the O atom binded between two In atoms, with the C atom bound to a neighboring Pd atom [176]. However, HCHO was predicted to interact weakly with the surface [176], as expected since it was readily detected with, but to a lesser degree than, CO₂ over an InPd near-surface intermetallic phase (NSIP) [128]. Additionally, the energetically unfavorable dehydrogenation of methanol on InPd(110), predicted by DFT calculations [176], was realized in recent experiments by low levels of CO detection and high CO₂ selectivity [93, 128].

Rameshan *et al.* found, through room temperature deposition of 4 MLE (equivalent monolayers) of In on a Pd polycrystalline foil followed by annealing to 453 K, that a stoichiometric InPd multilayer NSIP was formed; this phase almost eliminated CO formation during MSR up to a reaction temperature of 623 K. At this temperature CO₂ and HCHO formation were at maximum levels. These authors also explored an In₂O₃ layer covering a Pd substrate under MSR conditions. While annealing up to ~523 K, In was not reduced and CO formation dominated due to the presence of monometallic Pd. When annealing beyond ~523 K, a ‘diluted’ bi-metal surface state was evidenced in VB and In 3d photoemission spectra [128]. Moreover, examinations of Pd particles supported on In₂O₃ have shown both the In-Pd interaction and the support itself are CO₂-selective catalysts in MSR [93, 128]. However, In₂O₃ by itself is not very active [92, 128] (overall H₂ yield). It loses lattice oxygen when subjected to CO and hydrogen at elevated temperatures, in-turn eliminating inverse water-gas shift reactions [12, 128] and spoiling MSR CO₂ selectivity [128].

A couple of years earlier, Men *et al.* found indium in contact with Pd (forming InPd) in In-Pd/Al₂O₃ was essential for high CO₂ selectivity; its initial start-up properties were an improvement from Pd/ZnO catalysts [100]. The authors also found In:Pd compositional

changes from 10:5 to 10:10 to substantially affect total conversion and CO production rates. At 350 K, CO [Vol. %]/methanol conversion [%] levels were roughly 0/40 % for 10:5 In:Pd and 2.3/95 % for 10:10 In:Pd [100].

In another study that year, Lorenz *et al.* reported bimetallic InPd formed during reduction from room temperature to around 573 K on a Pd/In₂O₃ thin film model catalyst. This was compared to reduction of a Pd/In₂O₃ powder catalyst. For the powder catalyst, mostly bcc In₂O₃ and metallic Pd was observed at temperatures below 473 K. From 473 K to 573 K, CO₂-selective MSR was observed. At 573 K, only bimetallic InPd was detected. Upon reduction to \gtrsim 673 K, In₃Pd₂ and bimetallic particles encapsulated by In₂O₃ shells was observed. These formations clearly observed at 673 K, likely accounted for the loss of CO₂ selectivity, which left the system to behave as In₂O₃. Because of the encapsulation of these bimetallic particles, which occurred from strong metal-supported interaction effects, only the high CO₂ selectivity of the InPd phase in contact with the oxide could be verified. As a result, the system proves more complex to study at considerably lower temperature than Pd supported Ga₂O₃ and ZnO powder systems [93].

Pd/ZnO catalysts have shown high selectivity towards the production of H₂ and CO₂ (>95 %) [66–68, 71] compared to bulk Pd as favoring almost 100 % selectivity to formation of H₂ and CO under typical MSR conditions [71, 153]. This is because CO interacts weakly with Zn atoms above 100 K on ZnPd alloys and does not adsorb on sites containing Zn [71]. Several studies have investigated the structure and composition of ZnPd surface alloys. The consensus reached was that CO₂ selectivity depends on ZnPd corrugation changes resulting from bulk diffusion processes [46, 130, 131, 151]. Catalytic changes occurring between 570 K and 630 K [130, 151], could be explained by a Pd-out/Zn-in [75, 164] or a relatively flat surface corrugation [2, 151]. This followed diffusion of sublayer Zn at 550 K and disassembly of Zn-out/Pd-in ZnPd bilayer surface alloys attributed to the high CO₂ selectivity (these structures will be further discussed shortly under the section ‘surface alloys’). In another paper, it was determined that a Zn overlayer diffused above 650 K, following multilayer Zn desorption from Pd(111) between 400 to 600 K; this diffusion was evident by increased CO adsorption [46]. Furthermore, Rameshan *et al.* claimed ZnPd films annealed above 573 K resulted in Zn diffusion causing a transition away from a CO₂ selective state. The CO₂ selective multilayer corresponded to a ZnPd alloy with Zn-out/Pd-in corrugation and a lowered DOS at the Fermi edge [131].

Interestingly, the same authors found GaPd films to be non-selective towards CO₂ during MSR conditions. This was likely caused by an inefficiency to activate water, being in contrast to GaPd₂/Ga₂O₃ and GaPd/Ga₂O₃, which showed increased CO₂ selectivity

at $T \leq 550$ K [129]. However, these non-supported compounds exhibited a ‘copper-like’ DOS similar to pure ZnPd and InPd films. This emphasizes the requirement for knowledge of ensemble effects, where quantitative information on atomic structures is lacking. Moreover, the generic ‘copper-like’ DOS observations often exclude subtleties in electronic structures at given compositions and crystallographic orientations.

The high selectivity of InPd, GaPd and ZnPd during MSR is attributed, in part, to Pd valence d-band filling, altering the DOS at the Fermi edge. It is known that compositional changes, particularly within the InPd stoichiometry window (45 to 61.5 % at. Pd), influence valence electron distribution and density. The Fermi level tends to shift towards higher energy with increasing In concentration, while Pd antisite atoms tend to broaden the d-bands [175]. Note that the abundant constitutional point defects on the Pd-rich side are antisite defects. The d-band broadening, being a consequence of fewer In-Pd pairs, is analogous for the ZnPd compound (47 to 62.5 % at. Pd) [2]; its band width shrinks as a function of increasing Zn [2, 109]. For GaPd intermetallic compounds, Kovnir *et al.* note the negative polarity of Pd atoms in GaPd were responsible for 4d band filling, core hole screening effects, and shifting of 3d XPS spectra towards higher binding energy as compared to pure Pd [78, 79, 136]. The 3d binding energy shift (335.0 eV in pure Pd to 336.0 eV in GaPd), was also observed in ZnPd (Pd: 335.04 eV to ZnPd: 335.92 eV) [10] and InPd (Pd: 335.0 eV to InPd: 335.8 eV) [128].

In InPd however, the subtleties between 3d binding energy shifts, VB states, 3d peak asymmetry and shake-up satellites remain unclear. Although, there is agreement that Pd has partially filled d-bands, which gain electrons upon alloying, further experiments and simulations are needed for a less elusive description of the concurring Pd 3d spectra region. Carazzolle *et al.* found, after dosing ~ 3.6 ML of In on Pd(111) and annealing to ~ 530 K for 30 minutes, negligible Pd 3d peak shifting accompanied by loss of peak asymmetry and suppression of satellite shake-up peaks. The authors suggest that this behavior is consistent with a Fuggle model [19, 45, 56], having initially unoccupied 4d states pushed above E_F and initially filled states pulled below. This coincides with final states of the Pd main line ($4d^{10}s^1$ configuration) and satellite peak ($4d^9s^2$ configuration) resulting from s- and d- electron screening respectively. Upon alloying, 4d electron band-filling reduces the DOS at E_F . This consequently reduces the probability of a transition to a $4d^9$ configuration responsible for the satellite peak. The d-band electron density also pertains to asymmetry of core levels. In Cu, core levels are symmetric and have full d-bands [19, 117], so the loss of asymmetry in Pd 3d levels with increasing In-concentration would be expected.

The DOS of Cu was compared to pure Pd and ZnPd by Tsai *et al.*, as shown in Fig. 1.1 [118]. In ZnPd compounds, the outer shells of Pd and Zn ($4d^{10}$ and $3d^{10}4s^2$ respectively)

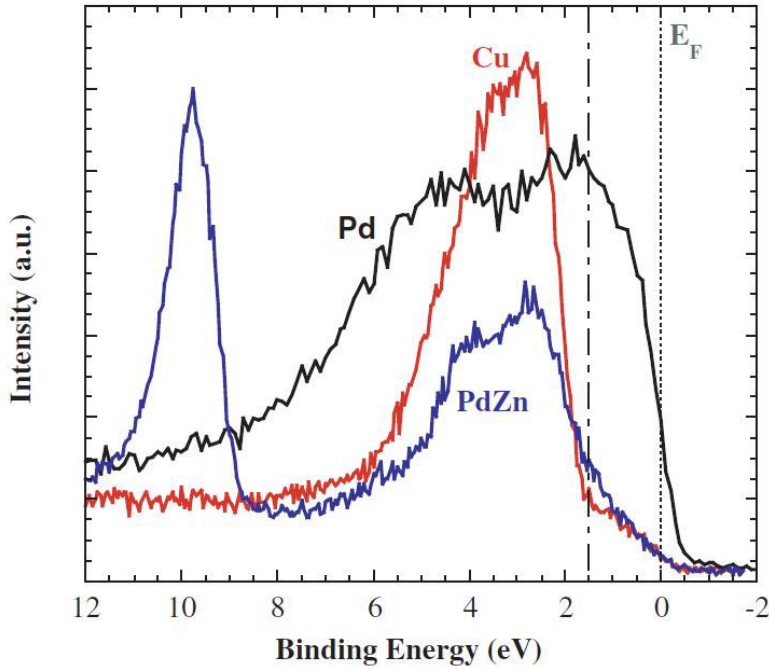


FIGURE 1.1: The above XPS data compare VB spectra of Cu, Pd, and ‘copper-like’ ZnPd (PdZn). This figure is taken directly from the work by Tsai *et al.* [118].

can be thought to have an average $d^{10}s^1$ configuration as copper [10, 25]. The bulk Pd shell, considered not completely full, was represented with a $4d^{9.5}5s^{0.5}$ electronic structure [10, 47, 97]. Unlike previous works on In/Pd(111), stoichiometric ZnPd surface alloys have been formed after deposition of 3 ML of Zn on Pd(111) at 105 K, followed by subsequent annealing to 600 K, and via 3 or 5 ML deposited at 550 K [10]. The corresponding UPS spectra revealed Pd 4d bands with maxima at ~ 2.4 eV and 3.9 eV, closely resembling that of Cu(111). These findings were in agreement with local DOS calculations [10, 25]. DFT calculations also indicate ZnPd 1:1 as having the most stable configuration from substitution of 50 % of Pd atoms in the Pd(111) surface [26, 46]. The bulk ZnPd tetragonal CuAu-L1₀ structure, being the most thermally stable one [52, 164], has a bulk lattice constant of 4.10 Å, in between that of GaPd (FeSi structure with $a = 4.89$ Å) and InPd (CsCl structure with $a = 3.26$ Å).

1.4 Other interest in In-Pd intermetallics

Although the vast majority of recent In-Pd research is motivated by catalysis, other studies have explored electronic and structural/mechanical properties for applications related to semiconductor devices. For example, selectivity and sensitivity of semiconductor metal oxide gas sensors are influenced by the bonding of Pd (or transition metals such as Pt or Ag) atoms at bulk or surface sites [146]. Additionally, semiconductor/metal and metal/metal interfaces influence the construction of electronic devices [38], so multilayer In films on Pd(100) [37, 38], and In/Pd films over fused silica [172, 173] and

GaAs (ohmic contacts) [44] have been studied. The authors often identify structural properties of compounds formed at interfaces, which influence both electrical and mechanical properties of the systems (i.e. the integrity of semiconductor chips bound to substrates with In solder) [172]. For a detailed description of these applications, please see references [37, 38, 44, 146, 172, 173].

Furthermore, variations in optical properties of In-Pd films were primarily influenced by DOS changes from point defects [174]. The color variations of In-Pd, resulting from these changes, ranges from a copper-color (near stoichiometric composition) to a gold-color (Pd-rich); this being useful for other applications in jewelery and dental prosthetics [106]. Additionally, surface segregation was studied to better understand mechanical stability in thin Pd-based membranes for hydrogen separation [95]. Although this study did not directly apply to In-Pd, it provided insight for segregation trends in 12 different Pd substitutional surface alloys.

1.5 Surface alloys

We provide below a short introduction on surface alloys pertaining to our work on the In-Pd system.

1.5.1 Intermixing and segregation

The ordering tendency of alloys and IMCs can be represented by the effective interaction energy. When the effective interaction between two elements (A and B) of a binary alloy

$$V \equiv V^{A-B} = \frac{1}{2}(\mu^{A-A} + \mu^{B-B} - 2\mu^{A-B}) \quad (1.4)$$

is > 0 (μ^{A-A} , μ^{B-B} , μ^{A-B} are the interaction energies between respective X-X atoms), formation of ordered IMCs having a fixed composition, or ordered alloys over a given compositional range are likely to form. Negative values of V favor a separation of elements into A and B near homoatomic clusters of short range order. These ordering tendencies however, are generally incompatible with top-layer phase separation or surface segregation of ordered alloys [168].

Surface segregation energy and mixing energy are fundamental concepts frequently used to describe behavior of surface alloys. When a metal (A) is deposited over a bulk metallic surface (B), forces drive inter-diffusion between the two elements. At $T=0$ K, this can be understood by an exchange of B and A atoms, such that the energy cost of removing

a B-atom is the negative B-component chemical potential μ_B [168]. By also considering the chemical potential of A (μ_A), the effective chemical potential of the bulk, $\mu = \mu_B - \mu_A$ is as follows,

$$\mu \equiv \frac{1}{N} \frac{\partial E_{B-tot}}{\partial c} \quad (1.5)$$

where E_{B-tot} and N represent the total energy of the bulk and total number of A and B atoms ($N=N_A + N_B$) exchanged between the bulk and surface regions respectively. The concentration of surface B atoms is c , and Δc is the difference between the surface region and bulk region concentrations. Now the total surface energy of the surface alloy γ is:

$$\gamma = \frac{1}{n_s} (E_{S-tot} - E_{B-tot}) - n_l \mu \Delta c \quad (1.6)$$

with n_s being the total number of atoms at the surface, n_l the number of surface region layers, and E_{S-tot} the total energy of the surface region of given configuration and composition [168]. By plotting γ as a function of c , information regarding segregation and mixing can be obtained. The slope of this curve is the segregation energy,

$$E_{seg} = \frac{\partial \gamma}{\partial c} = \mu_s - \mu \quad (1.7)$$

and is also equivalent to the effective chemical potential differences of bulk and surface layer components, where

$$\mu_s = \frac{\partial E_{S-tot}}{\partial c} \quad (1.8)$$

Generally, negative E_{seg} values indicate the A element stays at the top (segregation) while positive values suggest intermixing. Furthermore, the curvature of $\gamma(c)$ indicates whether or not elements will separate into pure A and B islands (negative) or surface alloying will occur (positive). This is clarified along with the segregation energy by the examples shown in Fig. 1.2. The mixing energy is opposite in sign to the curvature and can be expressed in terms of interaction potentials of coordination shells. By assuming small multi-site and dominant nearest-neighbor interactions, the effective interaction of the first coordination shell is approximately proportional to minus the mixing energy [168]. This establishes a link between ordering tendency and surface alloying.

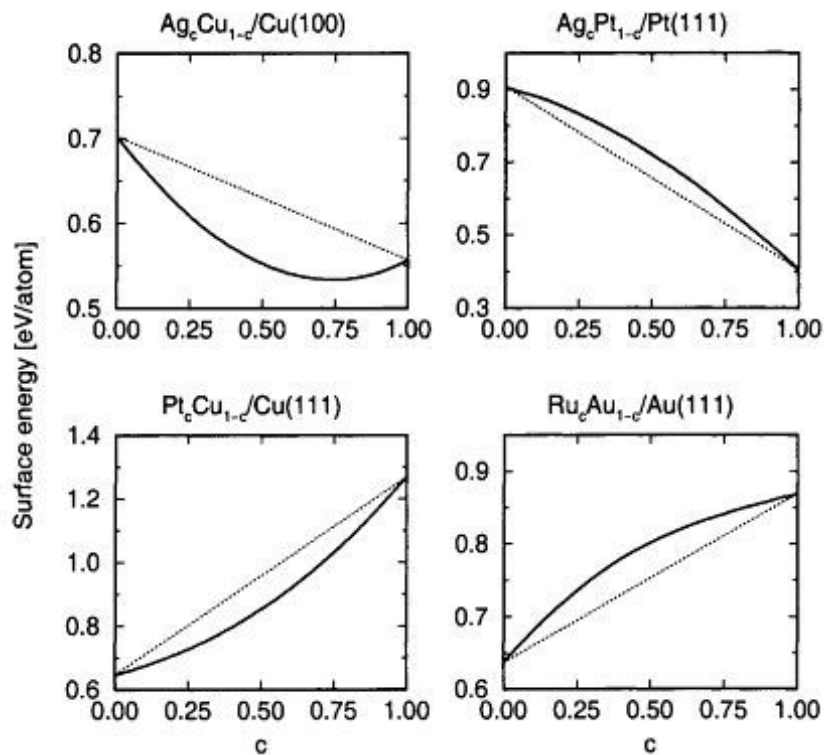


FIGURE 1.2: The above surface alloy examples, taken directly from ref. [168], are a modification of the work from Christensen *et al.* [27]. The plots represent each of the four combinations of positive (negative) slope/curvature. A negative slope (negative curvature) indicates the deposited element will stay on the top (separate into A and B elements), whereas a positive slope (positive curvature) suggests intermixing (surface alloying) will occur.

1.5.2 In-Pd and similar systems: top-layer substitutional alloys

Top-layer substitution alloying has been observed for In/Pd(111) at very low coverage. Using perturbed γ - γ -angular correlation (PAC) spectroscopy, Hunger *et al.* found 10^{-4} ML of ^{111}In probe atoms deposited on Pd(111) at 80 K occupied mostly substitutional step sites upon annealing to 350 K and mostly substitutional terrace sites at 380 K. The authors claim at 380 K, the axial symmetry from substitutional terrace site occupancy is consistent with In atoms replacing Pd atoms in the top layer. The axial symmetry was extrapolated from the electric field gradient signal so a z -axis tilt could be assigned to a likely adsorption configuration at each given site. This site occupancy was deduced from a simple model inclusive of above terrace, step edge, step edge kink, substitutional step edge, and substitutional terrace In atom positionings. After annealing slightly past 500 K, only signals corresponding to In in substitutional terrace sites were detected [62].

To our knowledge, the above study of In/Pd(111) is the only one performed at coverages ≤ 1 ML but no substitutional ordered structures, such as Pd(111) $(\sqrt{3} \times \sqrt{3})\text{R}30^\circ$ -In

have been reported. The existence of a Pd(111) $(\sqrt{3} \times \sqrt{3})R30^\circ$ -In substitutional 2D surface alloy seems plausible considering the substitutional behavior already observed at very low coverages [62] coupled with surface energies of other systems that exhibit this superstructure. For example, the surface energies of Cu/Sn, Cu/Sb, Pt/Sn, Ni/Sn, Pd/Sb are 1.85/.71, 1.85/.68, 2.55/.71, 2.45/.71, 2.1/.68 compared to 2.1/.69 [J/m^2] for Pd/In [101]. This phase can be formed after annealing from over 0.33 ML (\lesssim 1ML) of tin deposited on Cu(111), Ni(111), and Pt(111) [6, 116]. Also, annealing a higher coverage of \sim 3.6 ML for Sb/Pd(111), resulted in a $(\sqrt{3} \times \sqrt{3})R30^\circ$ LEED pattern. Structural analysis of the closest candidate, Sb/Pd(111), revealed that substitutional Sb in the first layer formed the structure [19]. These authors also observed a $(\sqrt{3} \times \sqrt{3})R30^\circ$ phase after depositing \sim 3.6 ML of In on Pd(111) and annealing to around 530 K, but difficulties induced by indium diffusion seemed to have prevented any publications of quantitative findings [19, 117].

Unlike their In-Pd counterpart, Zn-Pd and Ga-Pd thin films on Pd single crystals have been studied from a perspective of IMCs in catalysis. However, structural information on top-layer substitutional alloys is vague in comparison to the more chemically interesting alloys and IMC formations of several layers. Annealing Zn films on Pd(111) or Pd(110) over 600 K results in a Pd-Zn monolayer. The former has been described as a Pd adlayer being substitutional in nature and having a (1x1) LEED pattern [164]. The monolayer for Zn/Pd(110) was identified as a Zn:Pd 1:1 NSIP having a p(2x1) LEED pattern [2, 150]. In both cases, the surfaces showed a low corrugation with a slight Pd-up/Zn-down buckling. Stadlmayr *et al.* suggested this was from increasing Pd in surface and second layers pulling Zn atoms inward (for Zn/Pd(111)) [151]. More recently, the authors observed similar buckling on Ga/Pd(111) and Ga/Pd(110) films. For Ga/Pd(110), as for Zn/Pd(110), only Pd-up/Zn-down buckling was observed. Annealing both Zn (Ga) films on Pd(111) to around 600 K showed a Zn(Ga)-up/Pd-down to Pd-up/Zn(Ga)-down corrugation change. The Pd-up/Ga-down buckling found on Ga/Pd(111) was not directly associated with a top layer alloy as opposed to Zn/Pd(111) findings. Instead, the authors describe this as a GaPd₂ film [149].

1.5.3 In-Pd and relevant systems: multilayer alloys and IMCs

After depositing 4 ML of Ga on Pd(111) and annealing between \sim 500 to 800 K, a bulk-truncated GaPd₂ structure was observed by LEED. Moreover, the authors found annealing 1 ML to similar temperatures resulted in a weak c(4x2) pattern and alluded the structure could also be construed as GaPd₂ [149]. These findings suggest that, unlike Zn/Pd(111) films of various thicknesses annealed to similar temperatures, a multilayer surface IMC (GaPd₂) existed. This is not surprising since the cohesive energy of Ga in

Ga-Pd is more than double that of Zn in Zn-Pd [149]; so much higher annealing temperatures would be required to drive sub-surface Ga to the top layer prior to desorption.

A two-layer thick ZnPd film on Pd(111) was stable at lower annealing temperatures ($\lesssim 550$ K) in comparison to GaPd₂/Pd(111) and revealed a (2x2) LEED pattern. The (2x2) LEED pattern resulted from 3-rotational domains of p(2x1) ZnPd. This was clearly observed and further understood by STM. Weirum *et al.* found growth of p(2x1) ZnPd bi-layer islands after dosing submonolayer to ~ 2 ML of Zn on Pd(111) at room temperature. Above 2 ML, the LEED pattern transformed to a (1x1) phase indicative of the onset of bulk Zn growth over the ZnPd bilayer. The same authors also note that thermal stability of ZnPd/Pd(111) decreased with decreasing film thickness [164].

The results from the most recent In-Pd surface study suggest perpendicular inhomogeneity in multilayer intermetallic compounds/alloys formed after depositing 4 MLE of In on a polycrystalline Pd film and annealing. After annealing to 363 K, In_xPd_{1-x}, with $x = 0.63$ in top layers and $x = 0.51$ in sub-surface layers formed, whereas In depletion upon annealing above 623 K leveled-out the concentration gradient ($x = 0.19$) [128]. The latter potentially compares well with multi-layer InPd₃ films found in another In-Pd study [59].

A disordered fcc crystal structure with a lattice constant of 4.0028 Å is known to form on sputtered InPd₃ thin films [59]. Such a configuration, with theoretical (111) atomic spacings of 2.8304 Å is close to Pd(111) bulk registry (2.75 Å). A multilayer of similar composition was found after annealing 4-5 ML of Sn layers on Pt(111). It was described as a stacking of fcc Pt₃Sn(111) having a (2 × 2) periodicity with the bulk [48]. Bulk Pt₃Sn(111) also shows a (2 × 2) phase, but can be reconstructed with a top-layer having ($\sqrt{3} \times \sqrt{3}$)R30° ordering resulting from a slight depletion of tin in sublayers. This had the same composition as the Pt(111) ($\sqrt{3} \times \sqrt{3}$)R30°-Sn bidimensional surface alloy [3, 6].

Likewise, the possibility of surface reconstructions on multilayer In-Pd alloys cannot be overlooked. This may explain the formation of the In/Pd(111) ($\sqrt{3} \times \sqrt{3}$)R30° phase reported by Carazzolle and Pancotti *et al.* [19, 117]. It is possible that In/Pd(111) could form both multilayer and top layer ($\sqrt{3} \times \sqrt{3}$)R30° structures, analogous to (2x2) phases of Pt(111)-Sn [48].

Room temperature inter-diffusion of Pd and In has been studied in several amorphous/polycrystalline multi-layer films, showing some consistency with Pd(100)-In alloys formed upon annealing In/Pd(100) surface films at low temperature ($\lesssim 400$ K). For example, (a) 5 nm and (b) 10 nm of Pd were deposited on an In/Pd covered SiO₂ substrate in two separate experiments. The fixed In/Pd layers were respectively 50/100 nm thick.

AES depth profiling data showed 1:1 InPd at ~ 35 to 45 nm (a) and within the top 5 nm (b). Before Pd deposition however, nearly symmetric gradients of Pd diffusion into the In layers and In diffusion into the Pd layers was observed at the In/Pd interface region of 50 nm [172]. The authors indicate that the alloy formed in the region above 50 nm was probably In₃Pd [172, 173]. In₃Pd (tetragonal lattice with $a = 3.25$ Å, $c = 4.94$ Å) [93, 132] was also observed using PAC spectroscopy by placing local ¹¹¹In probes on a Pd(100) surface preceding 100 ML In deposition at liquid N₂ temperature and annealing to 350 K; this was explained as an amorphous In₃Pd interface layer [37]. A separate study using the same experimental conditions and method, showed no In-Pd inter-diffusion when annealing to 340 K, however inter-diffusion and formation of several Pd/In compounds occurred when annealing to 360 K. After annealing to 390 K, only In₃Pd was detected, whereas further annealing to 450 K, for an extended period, showed a mixture of InPd₂ and In₃Pd₂ [38]. More recently, for a Pd/In₂O₃ catalyst, In₃Pd₂ was formed during reduction at 673 K, and overlapped with In₃Pd at $T > 673$ K [93] forming a bcc lattice with $a = 9.433$ Å [53, 93].

This bcc phase had the same lattice constant as In₇Pd₃; the most recently added inter-metallic compound to the In-Pd phase diagram (Ref. 1.3). In fact, it has been deemed as the corrected interpretation of In₃Pd. This probably better explains some mixed or overlapped structures previously observed, as discussed in the last paragraph.

1.6 Bulk In-Pd phases

1.6.1 Elemental palladium and indium

Palladium is a silvery-white metal with a melting point of 1828.05 K (1554.9 °C). It can reversibly adsorb hydrogen, as much as 935 times its own volume, at atmospheric pressure and room temperature [119]. At elevated temperature hydrogen readily diffuses in Pd, so it is used in gas purification and catalytic hydrogenation/dehydrogenation applications [94]. Palladium is part of the group 10 transition metals, having a stable fcc crystal structure up to its melting point [74]. The majority of recent Pd crystal structure entries in Pearson's Crystal Database, identify it as Fm $\bar{3}$ m (No. 225) with a lattice constant of 3.895 Å [127].

Indium can also be described as a face-centered structure, however it is tetragonal (fct, $a = b \neq c$ and $\alpha = \beta = \gamma = 90^\circ$) rather than cubic. Alternatively, a 45° rotation of coordinate systems about the c - axis transforms an fct to a bct (body-centered tetragonal), where a_1 and $b_1 \Rightarrow a_1/\sqrt{2}$ and $b_1/\sqrt{2}$; it is apparent that when c is near a factor of $\sqrt{2}$ difference from a and b , it would be difficult to distinguish a bct from

an fcc. The most recent crystallographic data describes In as body-centered (I4/mmm (No. 139), ditetragonal - dipyramidal crystal symmetry) with unit cell measurements of $a = b = 3.256(2)$ Å and $c = 4.94(1)$ Å [39, 127]. Indium has a similar color as palladium, but its melting temperature of 429.75 K (156.6 °C) is substantially lower. It is a soft metal with a brilliant luster. A high-pitched ‘cry’ is given when the pure metal is bent. In 1924 the world’s supply of isolated indium surpassed a gram or so [94]. Shortly thereafter, the exploration of In - based alloy phases had begun.

1.6.2 Discovery of the phases

The existence of In-Pd phases was reported by Hellner and Laves in 1947 [55, 74], but a thorough exploration over the whole composition range using X-ray, metallographic, and thermal analysis techniques was not accomplished until 1959 by Knight and Rhys [72, 74]. These initial findings consisted of the following five phases: InPd₃, InPd₂, InPd, In₃Pd₂, and In₃Pd. During the same year, the phase In₃Pd₅ was reported by Schubert *et al.* [18, 138] but not detected by other workers. Consequently, it was omitted from the phase diagram published in 1965 [18, 34]. In 1972, calorimetric studies indicated its presence in a mixed state with InPd₂ and InPd, on the Pd-rich side of the composition window [18]. The following year, the phase was seen at grain boundaries of InPd at 41 % In [40]. In 1991, it was finally added to the phase diagram, along with the high-temperature InPd₃ phase, following the work of Schmid *et al.* in the late eighties [72, 137, 166].

The current phase diagram [112] (shown in Fig. 1.3) however, appeared after a re-examination of the In-rich part of the phase diagram. Findings in the In-rich part of the In-Pd-Sb and In-P-Pd ternary systems led authors to believe a phase isotopic to Ir₃Sn₇, namely In₇Pd₃, was the richest In compound [33, 39, 102]. These findings, in part, brought forth an investigation by Flandorfer regarding In-rich In-Pd binary phase relationships [39]. Through a comprehensive literature review, the author found a In₇₅Pd₂₅ (for In₃Pd) composition, in the original work by Hellner *et al.* [55], to be only an estimate. Also, X-ray powder data was only qualitatively compared such that In₃Pd, a “partially filled γ -brass-type structure,” was presumed [39, 55]. In work succeeding that of Hellner *et al.*, In₃Pd remained the candidate for the In-richest phase mostly due to lack of quantitative X-ray findings. Surprisingly, it took 55 years for In₇Pd₃ to officially replaced In₃Pd as the elusive In-rich equilibrium phase [39].

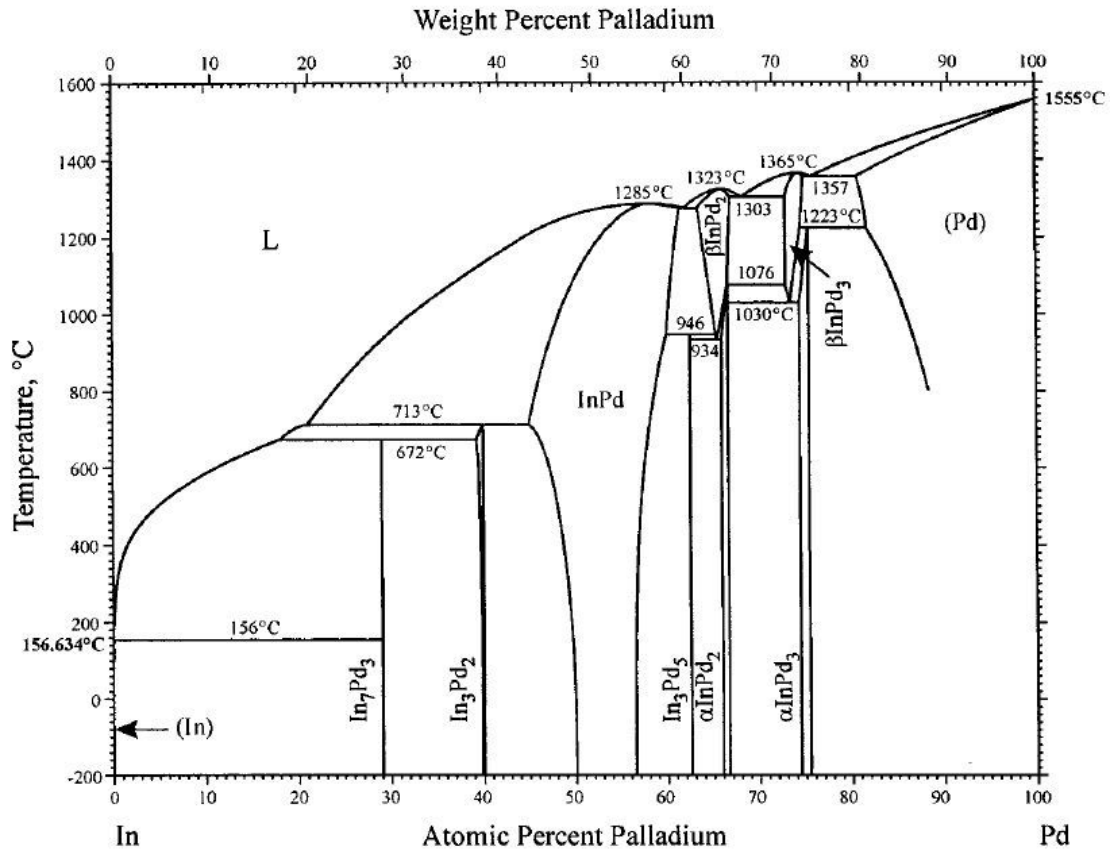


FIGURE 1.3: The phase diagram of the In-Pd system [112].

Name	Type	$H - M$	No.	a [Å]	b [Å]	c [Å]
InPd	CsCl	Pm$\bar{3}$m	221	3.249(2)	3.249(2)	3.249(2)
In ₃ Pd ₂	Ni ₂ Al ₃	P $\bar{3}$ m1	164	4.5371(3)	4.5371(3)	5.508(1)
In ₇ Pd ₃	Ir ₃ Sn ₇	Im $\bar{3}$ m	229	9.4359(4)	9.4359(4)	9.4359(4)

TABLE 1.1: The space group (Hermann-Mauguin international symbol and number), structure type, and lattice constants of In-rich InPd phases [39] and the **InPd** phase [49] are shown above.

1.6.3 In-rich Phases

In₇Pd₃ is defined as a body-centered cubic structure (Im $\bar{3}$ m). This is the largest In-Pd structure with 42 atoms per unit cell (parameters/dimensions shown in Fig. 1.4 and Table 1.1). It has a very narrow homogeneity range (< 0.5 at. %), as suggested due to Flandorfer's composition measurements of In₇₁Pd₂₉ (± 0.5 at. %) [39]. In₇Pd₃ has a peritectic temperature of 672.0(5) °C; this is the transformation point to liquid + In₃Pd₂ [39].

The peritectic temperature of In₃Pd₂ is 713.0(5) °C ($L + \text{InPd} \rightleftharpoons \text{In}_3\text{Pd}_2$) [39]. In₃Pd₂ also has a narrow composition window (39-40 at. % Pd) [112] and is the only In-Pd

Name	Type	$H - M$	No.	a [Å]	b [Å]	c [Å]
InPd ₃	AuCu	P4/mmm	123	2.87244(4)	2.87244(4)	3.80079(7)
InPd ₂	Co ₂ Si	Pnma	62	5.61676(6)	4.21710(4)	8.2278(8)
In ₃ Pd ₅	Rh ₅ Ge ₃	Pbam	55	11.0420(2)	5.61346(8)	4.24263(6)

TABLE 1.2: The Pd-rich In-Pd phases shown above include space group (Hermann-Mauguin international symbol and number), structure type, and lattice constant information [76].

phase where all unit cell vectors are $\neq 90^\circ$ with respect to each other as shown in Fig. 1.4. It is a trigonal structure ($P\bar{3}m1$) with 5 atoms per unit cell.

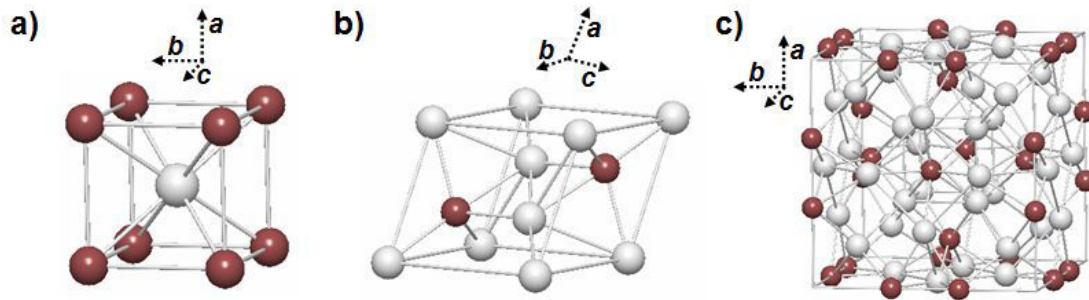


FIGURE 1.4: The above images show the In-rich In-Pd phases from a 3-d perspective. The unit cell dimensions (not to scale between a, b, and c) correspond to values in Table 1.1. a) InPd and c) In₇Pd₃ are cubic, and b) In₃Pd₂ is a trigonal system where the angle between a and b is 120° . In all phases above, the c vector is perpendicular to both a and b . The silver (light grey)/red (dark grey) atoms are In/Pd [127].

For In-rich solutions, the left side of the phase diagram (Fig. 1.3) shows no solubility of Pd in In. However, on the Pd-rich side, solid solutions exist [112].

1.6.4 Pd-rich Phases

Upon dilute mixing of In in Pd, solid solutions were formed while a hypothetical fcc lattice constant (based on Pd) increased with increasing amounts of In [53]. The solid solubility has been reported between 17-18 % In at 600 °C [74] and 17.6 % In at 900 °C [53]. Harris *et al.* identified InPd₃ in a mixed state at 19 % In, which existed solely at 25 % In [53]. Although it was originally reported as an f.c.t. structure, when transformed to a b.c.t. (as previously discussed), its unit cell dimensions agree within 0.01 Å to current data reported in Table 1.2 [53, 55, 76, 127].

InPd₃ is a tetragonal system (P4/mmm). The unit cell (primitive ‘P’) has 2 atoms per unit cell and is described as a partially disordered AuCu-type structure [76] (see caption of Fig. 1.5). This phase lies within a composition window between 74.5 - 75.5 at. % Pd [112]. More specifically, this refers to the low-temperature InPd₃ phase as shown in Fig.

1.3. The phase diagram also shows a high-temperature phases. This phase exists as a tetragonal $ZrAl_3$ -type structure ($I4/mmm$ (No. 139), $a = 4.06196(5)$ Å $c = 15.2031(2)$ [77]. A high-temperature $InPd_2$ phase also exists, but to our knowledge, no detailed structural information is found in literature.

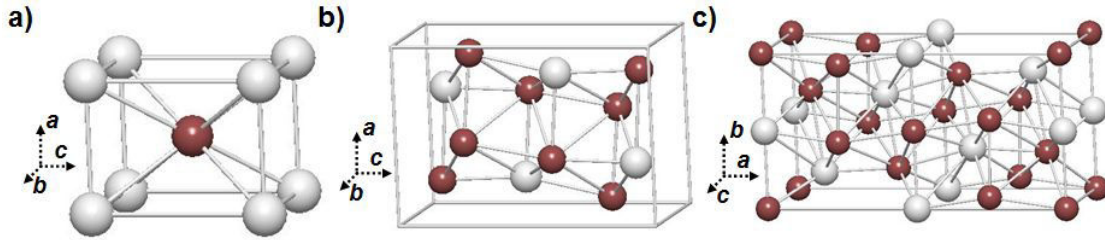


FIGURE 1.5: The Pd-rich In-Pd phases are shown from a 3-D perspective. The images are orientated such that a points upwards and unit cell dimensions (not to scale relative to each other) are proportional to values in Table 1.2. The angle between all unit cell vectors is 90° for all three phases. The silver (light grey) and red (dark grey) atoms represent In and Pd respectively for b) $InPd_2$ and c) In_3Pd_5 . For a) $InPd_3$, the silver (light grey) atoms are occupied by In or Pd 50 % of the time, whereas the red (dark grey) atom is Pd. This is represented by the crystal chemical formula $(In_{0.5}Pd_{0.5})Pd = InPd_3$ [76, 127].

The composition of low-temperature $InPd_2$ is slightly less In-rich at 66.0-66.7 at. % Pd [112]. $InPd_2$ is an orthorhombic structure ($Pnma$) with 12 atoms per unit cell ($a \neq b \neq c$). The In_3Pd_5 phase is also orthorhombic ($Pbam$) with 16 atoms per unit cell. This phase forms with a composition of 62.5 at. % Pd, bordering the Pd-rich side of the $InPd$ compound (45 - 61.5 at. % Pd) [112].

1.6.5 InPd

Although 8 (6 low temperature and 2 high temperature) In-Pd compounds have been identified (shown in Fig. 1.3), stoichiometric $InPd$ is currently of the highest interest in MSR because of a valence band structure being presumably the closest to that of copper. $InPd$ is a CsCl type structure with two atoms per unit cell and a lattice of constant of $3.249(2)$ Å [49] as shown in Fig. 1.4 (a) and Table 1.1. This lattice dimension corresponds to the maximum size of $InPd$ and occurs at stoichiometric compositions (50 % at. In). It decreases to ~ 3.22 Å [53] somewhat linearly, at both extremities of the composition window. On the In-rich side, this is attributed to the formation of constitutional vacancies in order to maintain an electron per atom ratio (e/a) of $3/2$ similar to $NiAl$ [16, 53]. These are Pd site vacancies, whereas Pd antisite atoms shrink the unit cell size towards Pd-rich compositions [40]. Both vacancy and electronic structures will be discussed further in the ‘results’ sections.

The ideal CsCl structure ($Pm\bar{3}m$) has all the same symmetry properties as In_7Pd_3 ($Im\bar{3}m$), except for the unit cell (2 atoms) which is primitive (P). Its structure is the simplest of all known In-Pd phases, but growing a well-ordered single phase and preparing its surface are not so trivial.

1.7 Bulk IMC and alloy surfaces

Bulk alloy and IMC surface preparation under UHV often involves sputtering - annealing cycles to remove contaminants and obtain flat, reconstructed surfaces suitable for characterization by various experimental methods. During ion bombardment at the surface (sputtering), one of the elements can be removed from the surface at a faster rate than the other (preferential sputtering). Often, the element having less mass is ejected. According to Bardi, the light element irreversibly depleted after extended ion bombardment for $Pt_{80}Co_{20}(100)$ [6, 7], $Pt_{80}Fe_{20}(111)$ [6, 11], and $NiAl(100)$ [6, 105]. In $NiAl(111)$, Al re-segregated to the surface above ~ 400 °C after being depleted from sputtering. Further annealing between 900 °C and 1000 °C resulted in a faint $(\sqrt{3} \times \sqrt{3})R30^\circ$ LEED pattern [108]. A $(\sqrt{3} \times \sqrt{3})R30^\circ$ phase was also observed for Pt_3Sn , but only after ion bombardment depleted subsurface tin [3, 6]. Furthermore, it was suggested that sputtering-induced loss of titanium of the selvedge region for $Pt_3Ti(100)$ was responsible for a pure, rather than a mixed surface termination [6]; the bulk terminated planes of $Pt_3Ti(100)$, an $AuCu_3$ - type ordered alloy, alternate between 1:1 Pt:Ti (mixed termination) and 100 % Pt (pure termination) [4]. Excess Pt in Pt_3Ti was expected to lead to Pt segregation [6, 148] and indeed was the case for Pt-enriched $Pt_3Ti(111)$ [6, 24, 120]. The preferentially sputtered species can be the heavier element when its bonding is weaker in the solid. Recently, Zn depletion was noted after sputtering an $Al_{57}Pd_{30}Zn_{13}$ complex metallic alloy [177]. This being different than findings in Al-rich ternary quasicrystals where Al, the lightest element, was often preferentially sputtered [87, 177].

The notion of altered layer(s) from ion bombardment/segregation is a known phenomenon and can be attributed to athermal and thermal processes. At or below RT, the athermal processes of displacement mixing and radiation-induced segregation cause the preferentially sputtered species to reach the surface. On the other hand, radiation-enhanced segregation and Gibbsian segregation are thermal processes. Gibbsian segregation increases the likelihood of the ejected element also being the segregated species [168]. Although not stated by the authors, this may explain the re-segregation of Al while annealing $NiAl(111)$ [108]. It seems that annealing a preferentially sputtered surface first establishes a local equilibrium between the altered surface and bulk regions. After annealing to $\sim 60 - 70$ % of the melting temperature, bulk diffusion occurs and

equilibrium with the bulk is established [168]. Here, equilibrium segregation can be observed and interface defects vanish. For example, Pt₂₅Ni₇₅(111) STM showed a network of dark lines appeared from misfit dislocations between altered and bulk regions. They disappeared when reaching the annealing temperature of bulk-surface thermodynamic equilibrium [163, 168].

Relevant findings of preferential sputtering and/or surface segregation have not been reported for the M-Pd (M=Ga,Zn,In) IMC/alloy surfaces of recent interest. Sputtering bulk GaPd(111) and GaPd($\bar{1}\bar{1}\bar{1}$) single crystal surfaces did not result in ejection of a particular element [124–126]. For Zn-Pd and In-Pd bulk surfaces, to our knowledge, UHV surface preparation details regarding these phenomena are non-existent.

In regards to bulk InPd surfaces in general, there has been only a few studies performed using single crystalline and polycrystalline samples. For an InPd polycrystal, surface microstructures were examined to understand deformations during tensile testing [106]. As for single crystal surface, one study correlated optical reflectivity minimum decreases with increasing In concentration for InPd single crystals grown over indium concentrations between 42 to 52 %; this explained a yellowish \rightarrow yellow-gold \rightarrow pinkish luster observed from lower to higher In concentration [107]. Another study examined an InPd(111) single crystal surface exposed to oxygen under UHV conditions [42]. The surface was first prepared by consecutive cycles of Ar⁺ ion sputtering - annealing to 1070 K. This preparation produced a (1x1) LEED pattern of poor quality and broadened reflexes, manifested by triangulated distortions of (h,k) beams. The energy dependence of Bragg reflexes was characteristic of faceting. The authors identify a ($2\sqrt{3} \times 2\sqrt{3}$)R30° oxygen superlattice forms, via LEED and STM upon O₂ dosing at 750 K. This structure had a unit cell lattice constant of 15.97 Å, which was $\sim 2\sqrt{3}$ the size of top layer InPd(111) horizontal nearest neighbor distance of 4.61 Å. The terrace heights were measured at ~ 1 Å [42]; this would be consistent with alternating Pd and In InPd(111) surface terminations. No further details were given in this short publication, in particularly regarding single crystal growth.

1.8 Summary

The material presented above focuses on relevant literature to serve as a basis for expectations and anomalies when discussing our results in upcoming chapters. Previously observed In-Pd intermetallic compounds and alloys are reasonably documented in both bulk phases and thin-film interfaces. However, very few studies with information pertaining to In-Pd surface structures exist. For In/Pd(111), only ($\sqrt{3} \times \sqrt{3}$)R30° and

$p(2 \times 2)$ superstructures have been reported (qualitatively) [117]. For InPd single crystal and polycrystal surfaces, to our knowledge, there has been one theoretical InPd(110) study [176], one experimental study of InPd(111) [42], no studies for InPd(100), and just one polycrystal study pertaining to its mechanical properties [106]. In cases where no In-Pd literature exists, we have discussed relevant phenomena in other intermetallic compounds and alloy systems.

Chapter 2

Experimental Methods

2.1 Experimental Background

2.1.1 Experimental set-up

The examination of In-Pd surface alloys and InPd IMC surfaces was performed under ultra-high vacuum conditions (UHV). These experiments were performed in three separate chambers, as shown in Fig. 2.1. The samples were transferred *in-situ* between vessels for characterization by LEED, XPS, and STM. A 4-grid LEED was used to image the surface diffraction from prepared samples. XPS was from an unmonochromatized Al/Mg source (anode). These XPS data were generated by photoelectrons dispersed across the exit plane of a hemispherical analyzer. The detector had seven channel (Channeltron) electron multipliers that amplified the signal by a factor of $\sim 10^8$. The STM data was collected by constant current imaging with a VT-STM.

Samples were prepared by consecutive Ar⁺ sputter - annealing cycles in either the preparation chamber or the analysis chamber (Fig. 2.1). The Pd(111) surface included an extra-step involving O₂ (discussed in Chapter 3). Furthermore, In films on Pd(111) were deposited by heating an In evaporant in an e-beam cell. This *in-situ* In deposition was followed by examination using STM.

2.1.2 STM

STM has been a premier surface characterization technique since 1982 when it was discovered at IBM in Switzerland by Gert Binnig and Heinrich Rohrer [5]. The technique is based on quantum mechanical tunneling of electrons, i.e. there is a probability that

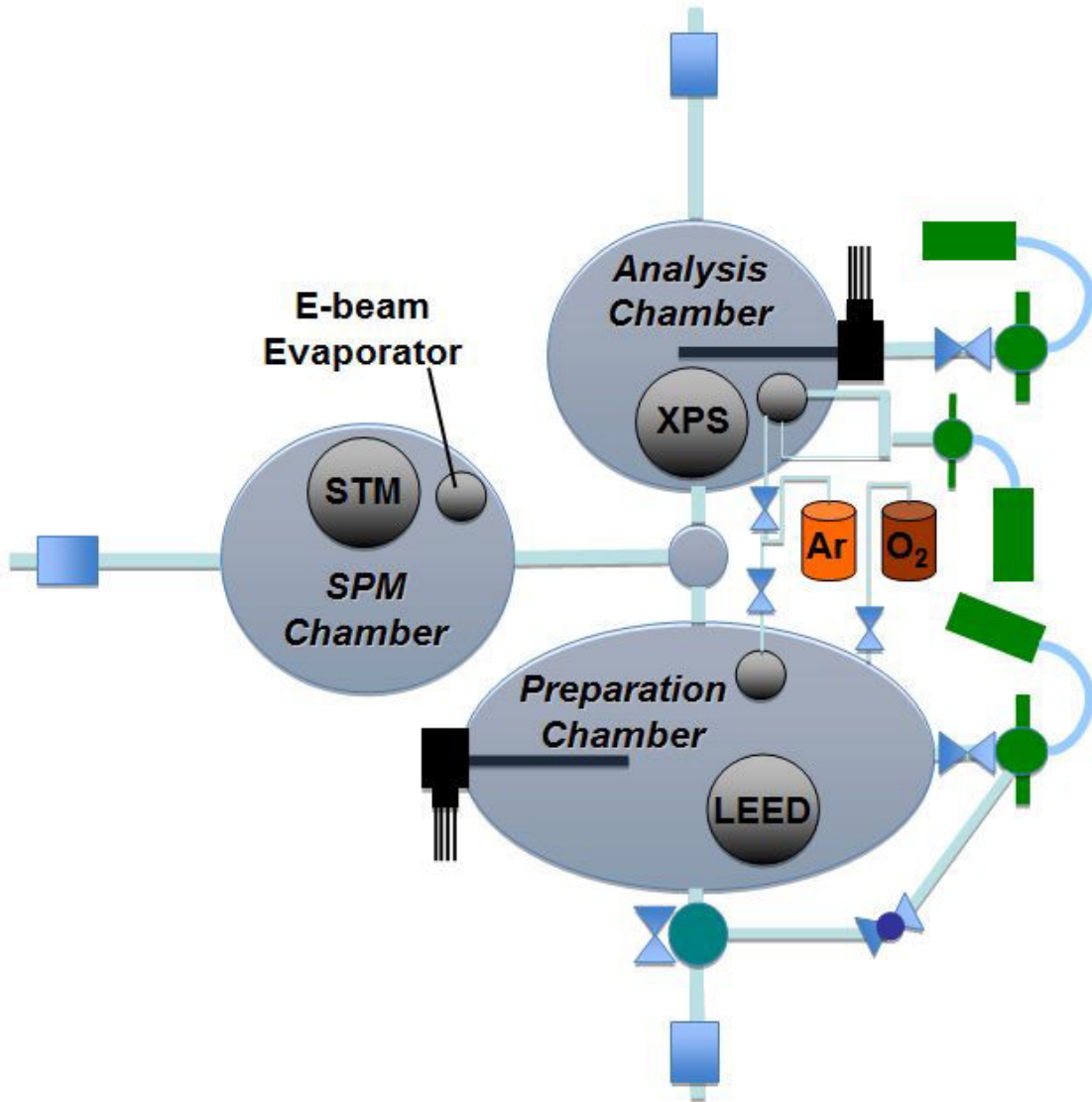


FIGURE 2.1: A top view schematic of the vacuum chambers used for ‘in-house’ experiments is shown above. UHV pressures are maintained by turbo-pumps (green/dark gray circles), rotary vane pumps (green/dark gray rectangles), and ion pumps (not shown) located underneath each chamber.

electrons will penetrate an energetic barrier between the tip and sample that would otherwise be impossible classically. This is realized by bringing a conducting tip (tungsten in our case) near the sample surface to form barrier width of a few angstroms. The tunneling current I exponentially decays with the barrier width w :

$$I \propto V \exp(-2\chi w) \quad (2.1)$$

where V is a low tip-sample bias and χ depends on an effective local potential barrier height ϕ [167].

$$\chi = \frac{\sqrt{2m\phi}}{\hbar} \quad (2.2)$$

An appropriate method to gain insight into the physics of Eq. (2.1) comes from a time-dependent perturbative approach to Schrödinger's equation in three dimensions. This is the Bardeen's transfer Hamiltonian formalism, which was first applied to STM by Tersoff and Hamann [160, 161, 167]. The authors used a s-type wave function for the tip to evaluate the tunneling matrix element having overlapping tip - surface wave functions. Although later it was shown that tip states with angular dependence ($l \neq 0$) and dangling bonds of W clusters affect tunneling current, Tersoff and Hamann's approach can be taken as a first approximation [167].

Furthermore, this approach reveals the tunneling current I is proportional to the local density of states (LDOS) at the Fermi energy (E_F) and delineated by the STM image [170]. The image is generally obtained using constant current or constant height mode. As the tip is scanned across the surface, V or I is measured at a stationary z-position (constant height) [170] or the z-position is adjusted to keep I fixed (constant current). This is possible because of a feedback system where I or V tip changes are compensated by necessary height adjustments with piezo-electric elements; they also control lateral tip displacements. During scanning, it is also possible to constrain the height, ramp the bias, and measure I to obtain LDOS information at selected areas (STS - scanning tunneling spectroscopy). Topographical imaging was used during acquisition of our data. In particular, all topographical images were obtained using constant current mode with Omicron's Matrix SPM control system (V 3.0) [115].

The contrast in topographical imaging of bimetallic alloys can be interpreted in three primary ways. First, a geometric effect can be (rarely) observed when large enough atomic heights or radii differences exist between the two elements [168]. However, measured heights are often not as expected of those predicted by hard shell atomic radii models. It seems this can be explained by effective radii of surface atoms, contributions from tip-sample interaction, or electronic density of states [168, 171]. A pure electronic effect from different LDOS and tip - sample interaction are the second and third contributions to chemical contrast [168]; these are likely the two reasons for atomically resolved In-Pd contrast given the small (~ 15 pm) [147] atomic radii difference.

2.1.3 LEED

LEED images portrait periodic patterns in reciprocal space over a sampling area proportional to the e-beam diameter ($\sim 5.0 \times 10^{+2}$ μm). The reciprocal lattice (h,k) beams

generally account for 2-D lattice structures. These beams are imaged when low energy electrons ($\sim 20\text{-}1000$ eV) strike a phosphor screen after being diffracted at the sample. Discrete diffraction beams will appear at different angles from the surface normal θ (one-dimensionally) as follows [5]:

$$n\lambda = a \sin \theta \quad (2.3)$$

where n are integers, a is the real-space lattice constant, and λ is a fixed de Broglie wavelength:

$$\lambda = \frac{h}{p} \quad (2.4)$$

Here, p is the electron momentum and h is planck's constant. The wave-particle duality of an electron allows for the constructive interference condition of Eq. (2.3).

The average real-space unit cell dimension of superstructures were measured by LEED images, but only if a reference dimension was assumed. For example, measurements of In/Pd(111) reconstructions assumed Pd(111) (1x1) hexagonal unit cell with $|\vec{a}_s| = |\vec{b}_s| = 2.75 \text{ \AA}$ with an angle of $\psi = 120^\circ$ between vectors. From this, a transformation to reciprocal lattice vectors $|\vec{a}_s^*|$ and $|\vec{b}_s^*|$ was easily accomplished by the following relation:

$$\vec{a}_{s,r}^* = 2\pi \frac{\vec{b}_{s,r} \times \hat{n}}{|\vec{a}_{s,r} \times \vec{b}_{s,r}|} \quad \text{and} \quad \vec{b}_{s,r}^* = 2\pi \frac{\hat{n} \times \vec{a}_{s,r}}{|\vec{a}_{s,r} \times \vec{b}_{s,r}|} \quad (2.5)$$

where \hat{n} is the surface normal unit vector. Now $|\vec{a}_s^*|$ of the clean InPd(111)-(1x1) surface was proportional to measured pixel spacing A and the overlayer $|\vec{a}_r^*|$ proportional to B , so the following fraction relationship was set-up:

$$\frac{|\vec{a}_s^*|}{|\vec{a}_r^*|} = \frac{|\vec{a}_r|}{|\vec{a}_s|} = \frac{A}{B} \quad (2.6)$$

and by presuming $|\vec{a}_s| = 2.75 \text{ \AA}$, the reconstructed lattice constant for $|\vec{a}_r|$ in [\AA] was easily solved. Measurements could only be performed using the same e-beam energy and sample position because (h,k) beam positions changed as a function of energy.

Beam intensities also changed with e-beam energy. Information buried within these intensity curves is the basis for LEED I(E) calculations and quantitative structural information regarding the top few layers. The first step was to record a sequence of LEED images of increments of 1 eV using a CCD camera. Then, the image stack was loaded

into a Python-based program called EasyLEED [98]. An integration window was chosen around each clearly identifiable (h,k) beam. The total pixel intensity within the window was taken above an average background determined at the integration window boundary. This gave a data point at each incremental energy step as the window continually tracked (h,k) beams. Plotted spectra of these $I(E)$ data points were compared to those from a theoretical model using the SATLEED code [58]. The reliability of experimental vs. theoretical $I(E)$ data was calculated using the Pendry R-factor [121], which is described in Appendix A.

LEED data for measurements were taken by an Omicron NG SpectraLEED [113], whereas LEED data for LEED $I(E)$ analysis were taken by OCT's BLD800 [111] in collaboration with the group of Professor Renee Diehl at the Pennsylvania State University. Additional details regarding LEED theory are found in the excerpt in Appendix B. Information on the theoretical portion of the LEED $I(E)$ analysis of InPd(111)-(1x1), from K. Pussi at LUT Lappeenranta University of Technology, Finland, is found in Chapter 4.

2.1.4 XPS

Based on Einstein's photoelectron effect, XPS probes atoms by absorption of 'energy packets' (photons, $E/\text{photon} = h\nu$) followed by photoelectron ejections. By energy conservation,

$$h\nu = E_k + E_B + \phi \quad (2.7)$$

where E_K is the kinetic energy and E_B is the binding energy (atomic) of ejected photoelectrons. The photoelectron also has to overcome a potential barrier at the surface, ϕ (this is the work function). Photons were generated by a Mg K_α X-ray source (Omicron DAR 400) and photoelectrons detected by an analyzer (Omicron Sphera).

The generation of X-rays occurred when high energy electrons (15 to 20 keV), from a thoria coated iridium filament [114], struck a Mg anode. This caused (in part) 1s Mg electron holes, which were filled by $2p_{3/2} \rightarrow 1s$ and $2p_{1/2} \rightarrow 1s$ radiative transitions (respective $K_{\alpha 1}$ - $K_{\alpha 2}$ lines) [17]. The average photon energy/FWHM from the transition was 1253.6/0.65 eV. These two transitions were not monochromatized, so the FWHM was the broadening uncertainty. Although much better resolution of ~ 0.01 eV to 0.02 eV was attainable with the analyzer, the resolution of the source was the limiting factor.

The analyzer entrance was positioned at an angle of 53° with respect to the X-ray source. The sample was rotated such that the surface normal - analyzer entrance angle

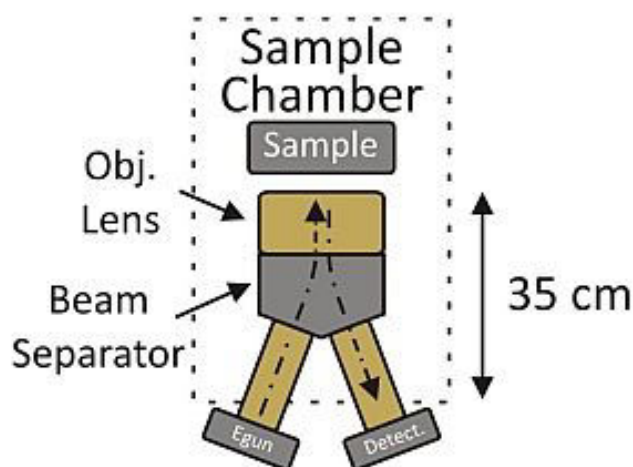


FIGURE 2.2: The above illustration shows the very basic LEEM design concept [35].

was θ . Most measurements were made with $\theta=70^\circ$, 45° , and/or 20° where a larger angle corresponded to a higher surface sensitivity.

2.1.5 Diamond Beamline I06

The polycrystalline sample not only was investigated ‘in-house’ using STM and XPS as described above, but also studied at beamline I06 of the Diamond Light Source (UK) using micro - XPS (μ XPS) and low energy electron microscopy (LEEM) techniques [29]. Measurements were carried out using an Elmitec LEEM III and PEEM (Photoemission electron microscope) III [35]. The sample was probed with a linear polarized beam of monochromatic soft X-rays (μ XPS) from the beamline (at a specified energy, between 80-2100 eV) [28], or a 15-20 keV electron beam (LEEM/LEED) [63].

LEEM is a surface sensitive technique that samples an object with an electron beam between 1-100 eV [8]. Aside from using very low energy electrons, LEEM differs from other electron microscopic techniques because the objective lens is placed between the sample and electron source. The objective lens is a ‘cathode,’ which de-accelerates the incoming high-energy beam of electrons towards the desired low-energy [9]. The sample is biased close to the energy of the source and the low-energy is chosen based on a required probing depth and imaging mode. The sampling depth is proportional to the inelastic mean free path (IMFP) of electrons within the material. Backscattered electrons from (or near) the surface pass back through the objective lens, then various other lenses (depending on instrument design) direct the beam towards a magnetic beam splitter. The beam splitter sends the backscattered electrons in the opposite direction of the incoming source electrons. Finally, a set of condenser optics produces an image on a phosphorescent screen or CCD camera (Fig.2.2 by Elmitec shows the elementary operating principle). The image results in contrast produced from the interaction of

electrons with differing geometrical and chemical surface features. Please see Refs. [8, 9] for further information on LEEM imaging theory and instrument design.

Moreover, the diffraction on the back focal plane of the objective lens can produce a LEED pattern in dark field imaging mode. These μ -spot LEED patterns are similar to those of conventional LEED except (h, k) beam positions, which remain constant as a function of energy. This can be explained by combining the LEED diffraction condition (Eq. (2.8)), with Snellius' law (Eq. (2.9)), leading to Eq. (2.10) which show beam positions $|\mathbf{h}| = (h, k)$ are independent of λ_0 and henceforth E_0 [9].

$$\sin \beta_0 = \lambda_0 |\mathbf{h}| \quad (2.8)$$

$$\frac{\sin \beta}{\lambda} = \frac{\sin \beta_0}{\lambda_0} \quad (2.9)$$

$$\sin \beta = \lambda |\mathbf{h}| \quad (2.10)$$

In turn, when certain instrument parameters are known, beam position can be correlated to crystal facet/2-D surface structures.

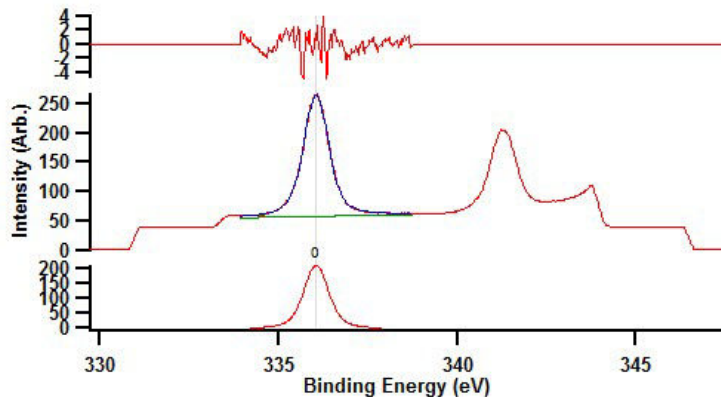
Diffraction is a limiting factor in the instrument resolution when the contrast aperture minimizes spherical and chromatic aberrations; they are proportional to the starting angle β_0 . The total resolution δ is related to spherical, chromatic and diffraction (at the contrast aperture) aberration disks as follows [8, 9]:

$$\delta^2 = \delta_s^2 + \delta_c^2 + \delta_d^2 \quad (2.11)$$

LEEM resolution at beamline I06 is ~ 15 nm for good samples [29]. The spatial resolution from a photon source, however is somewhat larger. Particularly, our measurements with μ XPS were taken with a lateral resolution of ~ 2 μ m and an energy resolution of ~ 220 meV.

In μ XPS, a beam of polarized soft X-rays impinge the sample at a specified grazing angle (17° angle from the surface at beamline I06) [63]. The kinetic energy of normal emission (within a $\sim 3^\circ$ acceptance angle [96]) photoelectrons generated by the X-rays, are dispersed in the analyzer near a selected stop voltage (STV) (by applying a bias to the sample). The dispersive plane of analyzer is projected onto a spatially resolved

FIGURE 2.3: Pd $3d_{5/2}$ spectra were fitted with a Voigt function after a removal of a localized linear background.



detector; a line having a profile indicative of the photoemission spectrum intensity is displayed [91, 96].

2.2 XPS data analysis

2.2.1 μ XPS

We have extracted the intensity profiles (imaged by a CCD camera) using a PEEM macro for image analysis with Igor software. An integration width was chosen at the boundary of illuminated pixels. This method optimized the signal to noise ratio and was easily applied to each data set. For consistency, an integration window of the same width was used to extract all intensities within a complete μ XPS data set. A data set, taken at a specific point, consisted of spectra from Pd 3d, In 3d, C 1s, O1s, and Fermi levels.

The intensities of Pd 3d, In 3d, C 1s, and O 1s spectra were normalized to respective integration times. Then, a Voigt function above a linear subtracted background was fitted (Fig. 2.3). Slightly different quantification methods have been used for μ XPS data taken at I06 [96, 103], however our parameters were most appropriate for the very low asymmetry and absence of shake-up peaks in Pd and In core level spectra. Finally, composition was measured by re-normalizing intensities I with respect to σ and the appropriate IMFP $\lambda(E_k)$, such concentration i was as follows:

$$\frac{\frac{I_i}{\lambda_i(E_k)\sigma_i}}{\frac{I_i}{\lambda_i(E_k)\sigma_i} + \sum_{j \neq i} \frac{I_j}{\lambda_j(E_k)\sigma_j}} \quad (2.12)$$

Note that photon beam intensity was near constant (\pm a few percent) during measurements. Decay of current in the storage ring was negligible before reaching a total

acquisition time of ~ 10 min.[63]. So decay terms were excluded from the normalization factors; this was not the case during μ XPS data collection at some other synchrotrons [103].

b) The contribution to a total intensity I is the summation of originating electron currents dI from a dz - thick layer at depth z [61]

$$dI \propto \exp\left(\frac{-z}{\lambda(E_k) \cos \phi}\right) dz \quad (2.13)$$

where $\cos \phi$ is the angle of the analyzer from the surface normal. At normal incidence when $z = \lambda(E_k)$, intensity (probability) drops to $1/e$ of its original value. This is the IMFP, i.e. the estimated path an electron can travel, on average, without losing significant energy [5, 61]. At I06, the analyzer was fixed in very close alignment to the surface normal, so the $\cos \phi$ factor could be ignored in IMPFs ($\lambda(E_k)$) calculations of detected photoelectrons.

2.2.2 Inelastic mean free path (IMFP) calculations

Our estimations of the IMFP were calculated based on an empirical relationship of data fitting found by Seah and Dench as follows [144]:

$$\lambda(E_k)[nm] = \frac{538a}{E_k^2} + 0.41a^{\frac{3}{2}} E_k^{\frac{1}{2}} \quad (2.14)$$

where a is a monolayer thickness derived from the elemental/compound value as such:

$$a[nm] = \left(\frac{A \cdot 10^{24}}{\rho \cdot n \cdot N_A} \right)^{1/3} \quad (2.15)$$

Here, A is the atomic (molecular) weight, n is number of atoms per molecule, N_A is Avogadro's number, and ρ is the density of the bulk [144]. We used a value for ρ (10640 kg/m^3) that was measured by Haung *et al.* for InPd [60], and A was the average atomic weight of Pd and In. We did not use suggested fits for inorganic compounds by Tanuma [154, 156–158] and Seah,[142–144] since an accurate universal curve is not agreed upon and only a few studies of IMFP measurement on comparative alloys (Pd or In) exist (Pd-Au, Pd-Ag, Pd-Ni [81], CoPd [83], InAs, InP and InSb [157]). Being said, the error still present in IMFP calculations for inorganic compounds, coupled with complicated surface phenomena in In-Pd, meant there was no reason to go beyond an original formula for a first order approximation of $\lambda(E_k)$.

2.2.3 Quantifying in-house XPS data

Quantification of XPS data is usually not a trivial process. Many authors have devoted much of their careers developing better methods, to include refinements in predicting IMFPs, and determination/eradication of instrumental and analytic error [70, 81–85, 104, 141, 142, 154, 155, 159], to improve the reliability of concentration measurements. As shown later, in Eq. 2.20, the normalization to account for 100 % of the surface area sampled depends on the photoionization cross section σ and the IMPF $\lambda(E_k)$. However, a dependence on an analyzer transmission function should also be considered (this was negligible for the synchrotron data). The transmission function is defined as follows:

$$ATF = \left(\frac{a^2}{a^2 + R^2} \right)^b \quad (2.16)$$

where $R = (E_k/E_p)$ and a, b are parameters relevant to the analyzer. For the Sphera analyzer used in our experiments, $a = 21.0025$ and $b = 0.2015$ (provided by the manufacturer). E_k and E_p are electron kinetic energy and analyzer pass energy respectively; normally, E_p was set at 10 eV.

Other factors (OF) such as photon flux, angular efficiency based on the angle between detected electrons and X-rays impinging the surface, detection area, and photoelectron detection efficiency [61, 162] also contribute to the total intensity (I_i). I_i is defined as:

$$I_i = n_i \cdot \sigma_i \cdot \lambda_i \cdot ATF_i \cdot OF \quad (2.17)$$

Now n_i is the number of atoms per cm^3 of element i , so

$$\frac{n_i}{n_i + \sum_{j \neq i} n_j} \Rightarrow \frac{\frac{I_i}{N_i}}{\frac{I_i}{N_i} + \sum_{j \neq i} \frac{I_j}{N_j}} \quad (2.18)$$

where $N_{i,j} = \sigma_{i,j} \cdot \lambda_{i,j} \cdot ATF_{i,j}$ is the normalization factor (OF can be considered independent of E_k and factors out when determining concentrations).

However, before applying the equation above, data acquisition settings and sample positioning had to be fixed between consequent Pd 3d and In 3d scans. Then, the spectra could be fitted/adjusted to obtain area measurements as a quantifiable representation of intensity.

2.2.4 Polycrystalline and bulk InPd surfaces

To develop a procedure for extracting peak areas, we fit Pd $3d_{3/2,5/2}$ and In $3d_{3/2,5/2}$ peaks from scans of the polycrystal sample following a 2 keV/30 min. - 800 °C/90 min. sputter - anneal cycle. First, a Shirley background [145] was taken over both In and Pd 3d regions as shown in Figs. 2.4 and 2.5. Steps in metallic data are generally fitted with a Shirley background (poorly defined backgrounds in XPS measurements are the largest source for precision errors) [36]. A Shirley background (SB) is constructed based on the area above it as follows:

$$SB(E) = I_2 + \xi \frac{A_2(E)}{A_2(E) + A_1(E)} \quad (2.19)$$

It is an iterative algorithm that guesses $SB(E)$ to find and refine peak areas A_1 and A_2 . I_1 and I_2 are intensity of the spectrum at respective left and right endpoints of the defined region and ξ is proportional to $I_1 - I_2$ [21]. Second, we determined Gaussian - Lorentzian product formula ($GL(p)$) and convoluted Doniach - Sunjic [31] ($DS(\alpha, n)SGL(p)$) fits yielded the best replication of respective Pd and In $3d_{3/2,5/2}$ spectra after comparisons of multiple fitting functions of several different parameters. The $GL(p)$ fit is a Gaussian \times Lorentzian curve with a mixing parameter $m = p/100$ such that when $p = 0$, the curve is pure Gaussian, and when $p = 100$, it is pure Lorentzian. This is also true for the $SGL(p)$, except it is the sum of Gaussian + Lorentzian functions [21, 23, 36]. The Doniach - Sunjic fit for In $3d_{3/2,5/2}$ was chosen since a slight asymmetry was observed towards the bottom ends of the two peaks. The fit had a small asymmetry parameter of $\alpha = 0.01$ and a small Gaussian width convolution integer $n = 0.10$ when optimized/blended with an $SGL(p)$ function ($p = 40$). Adjustments to α change the slope of the fit at the high-BE side along with the asymptotic tail height (increasing $\alpha \leftrightarrow$ increasing tail height and decreasing slope). A DS profile is Lorentzian in nature, but experimental parameters cause Gaussian broadening. So the DS profile is convoluted by a Gaussian width (with a characteristic integer $0 \leq n \leq 499$). Furthermore, the low-BE side can be matched to G-L type profiles by attaching $GL(p)$ or $SGL(p)$ functions as was necessary for In $3d_{3/2,5/2}$ fits. For further information regarding pure DS parameters and Casa fitting functions discussed above, see Refs. [41, 57] and see Refs. [20, 21, 23, 36] respectively.

The values used for fits shown in Figs. 2.4 and 2.5 are found in Table 2.1. In addition to $3d_{3/2,5/2}$, $3d_{3/2}$ $K_{\alpha 3, \alpha 4}$ data were fitted with $GL(p)$ functions ($GL(0)$ is a pure Gaussian, as used in the In 3d region). $K_{\alpha 3, \alpha 4}$ peaks arise from $2p \rightarrow 1s$ transitions of doubly-ionized Mg X-ray source atoms [17]. They have intensities roughly 8-9 % ($K_{\alpha 3}$) and 4-5 % ($K_{\alpha 4}$) of $K_{\alpha 1, 2}$ peaks composing intensities of primary $3d_{3/2}$ peaks [17, 80, 162]. The $K_{\alpha 3}$ and $K_{\alpha 4}$ peaks are positioned at respective values of 8.4 and 10.2 eV from

<i>Region</i>	$3d_{3/2}$	$3d_{5/2}$	$3d_{3/2}\kappa_{\alpha 3}$	$3d_{3/2}\kappa_{\alpha 4}$
Pd 3d	GL(91)	GL(91)	GL(50)	GL(50)
In 3d	DS(0.01,10)SGL(40)	DS(0.01,10)SGL(40)	GL(0)	GL(0)

TABLE 2.1: Functional forms of fitted Pd and In 3d regions, as shown in Figs. 2.4 and 2.5, are indicated above. The peaks are fitted with either Gaussian - Lorentzian product (GL) or sum (SGL) functions, or Doniach - Sunjic (DS) functions.

$K_{\alpha 1,2}$ towards higher KE (lower BE) [162]. This was the first constraint used while fitting the 3d regions as seen in Figs.2.4 and 2.5. Another constraint was to fix area ratios of $3d_{3/2}:3d_{5/2}$ intensities as 2:3. This is from the multiplicity of the state, namely $2j+1$, which is proportional to intensity where $j=l\pm 1/2$ and l is the angular momentum ($s,p,d,f,\dots = 0,1,2,3,\dots$) [21]. The intensity ratio of double pairs for d states is then, $2j+1:2j+1 \rightarrow 2(2-1/2)+1:2(2+1/2)+1 = 4:6$ (2:3).

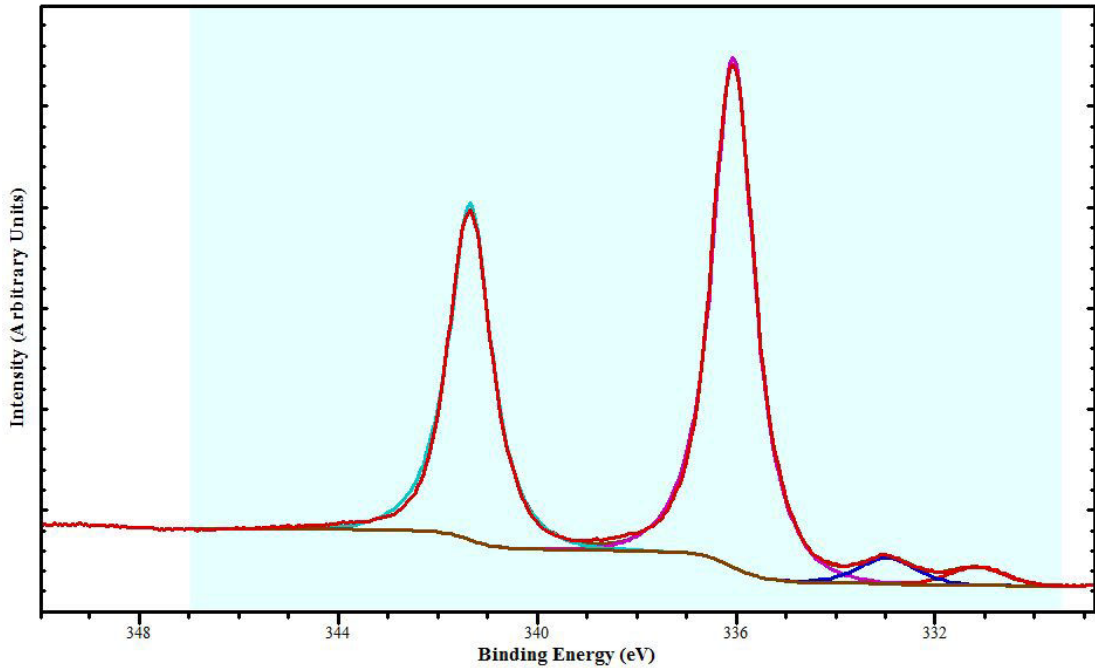


FIGURE 2.4: The Pd 3d region of polycrystalline InPd is fitted with four Gaussian - Lorentzian peaks following the removal of a Shirley background in the selected (blue/gray) region. The large left/right peaks are Pd $3d_{3/2}$ /Pd $3d_{5/2}$ and the small left/right peaks are $K_{\alpha 3}$ / $K_{\alpha 4}$ of Pd $3d_{3/2}$.

To perform the fits, we used CasaXPS (version 2.3.15). First, all components described above were manually adjusted as an initial guess. Next, a combination of both Marquardt and Simplex-type fitting was accomplished until negligible differences in residual standard deviation resulted (the difference between the total synthetic envelope and raw data) [22]. Finally, the peak areas, positions and FWHM values for the $3d_{3/2,5/2}$ were

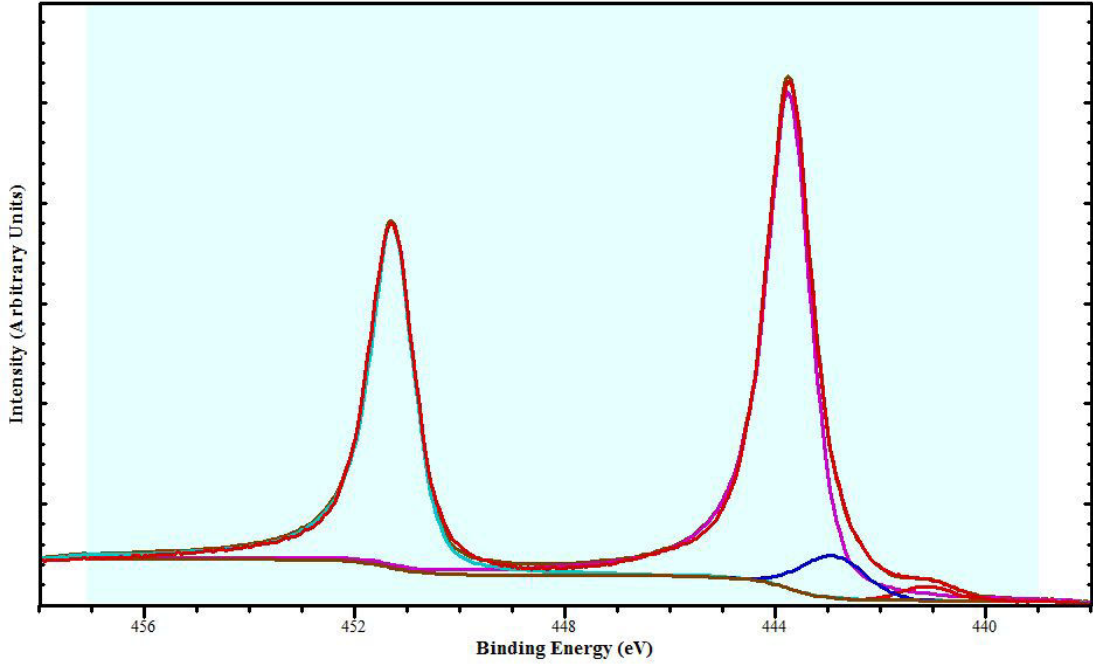


FIGURE 2.5: The selected (blue/gray) region within the In 3d spectrum above, defines the endpoints for removal of a Shirley background. Within this region are two Doniach-Sunjic (In $3d_{3/2}$ /In $3d_{5/2}$, large left/right peaks) and two Gaussian (In $3d_{3/2}$ $K_{\alpha 3}$ / $K_{\alpha 4}$, small left/right peaks) peaks.

<i>Spectra</i>	<i>Pd</i> $3d_{5/2}$ <i>Pos./FWHM</i>	<i>In</i> $3d_{5/2}$ <i>Pos./FWHM</i>	<i>Comp.In : Pd</i>
Fitted	336.06/1.00	443.77/1.02	54.3:45.7
Non-Fitted	336.05/1.02	443.75/1.07	53.9:46.1
Non-Fitted*	336.05/1.00	443.75/1.06	52.8:47.2

TABLE 2.2: Shown above are specified values of fitted Pd $3d_{5/2}$ and In $3d_{5/2}$ regions, as discussed in the text and shown in Figs. 2.4 and 2.5, compared to ‘raw’ data measurements from Figs. 2.6 and 2.7. The first two rows are from the same data set obtained after sputtering the sample for 30 min. at 2 keV and annealing to 1073 K for 1.5 hrs. The last row (*) is from another experiment where the sample was annealed to 933 K for 1.5 hrs following the same sputtering condition; this is the preparation referred to in upcoming chapters, i.e. the $\text{In}_{53}\text{Pd}_{47}$ polycrystal surface composition.

extracted. Surface composition information was derived from the peak areas as shown on the top row of Table 2.2.

We also compared concentration measurements from these ‘fitted areas’ to the raw (non-fitted) areas, using different background subtraction ranges, until very similar concentrations were obtained. So, why was this necessary? It was mainly to have consistency amongst measurements, while eliminating the time-consuming unnecessary tampering with fitting parameters for each polycrystal/bulk InPd data set. Moreover, there is only one reasonable fitting parameter (for each $3d_{3/2,5/2}$ component), so if the background is chosen correctly ‘raw area’ measurements would be most accurate.

This was accomplished by first defining the entire 3d region (as in Figs. 2.4 and 2.5) and then satellite peaks were subtracted using CasaXPS software. Next, the region was redefined to solely encompass $3d_{5/2}$ regions as shown in Figs. 2.6 and 2.7. The left boundary was centered in-between peaks. The right boundary was equidistant from the peak center as the left boundary. Peak data was then taken and compared to the fitted data as shown in Table 2.2. We found surface composition measurements compared well, so this extrapolation method was used to obtain reported results in following chapters.

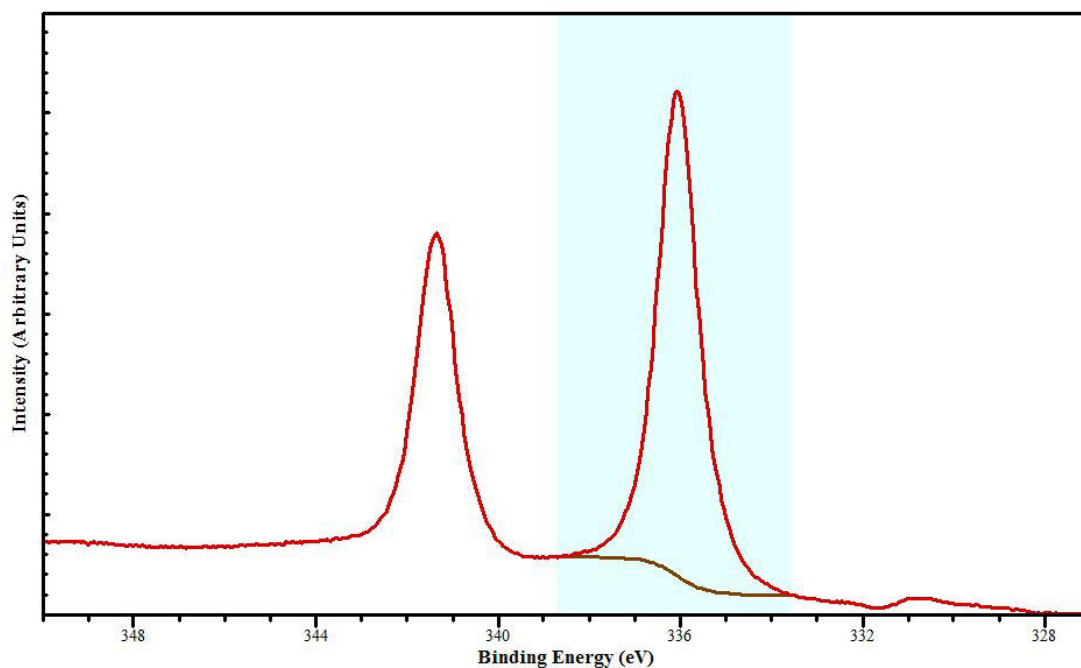


FIGURE 2.6: The Pd $3d_{5/2}$ region is defined above (shaded blue/gray) with a Shirley background subtracted. The peak information is displayed in the second row of Table 2.2.

Note that because areas under split 3d peaks are proportional to one another, their sums yield a factor that cancels-out in concentration measurements. So only area measurement of $3d_{5/2}$ peaks were performed and will be discussed from this point forward. This is the case herein for all reported concentration measurements and kinetic energies/corresponding IMFP calculations; photoionization cross-sections used were also from $3d_{5/2}$ tables [139, 140].

2.2.5 In/Pd(111) surface IMCs and alloys

The fitting of Pd 3d components from In/Pd(111) ultra-thin film experiments was less trivial than for the bulk IMC surfaces discussed in the last section. First, we had to determine how many components likely accounted for shifts and changes to positions and FWHMs. The spectra after dosing both 1 and 2 MLE clearly showed peak shifts towards

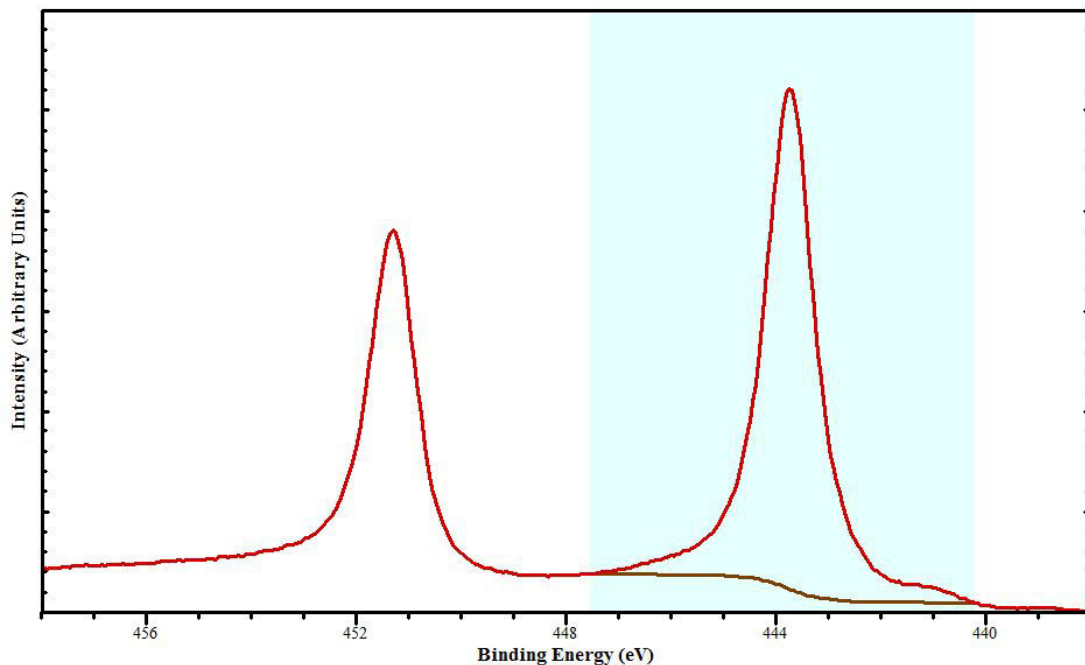


FIGURE 2.7: Peak information (shown in the second row Table 2.2) from the shaded region (blue/gray) of In $3d_{5/2}$ was taken in the same manner as for Fig. 2.6.

higher BE and much broader FWHMs (Fig. 2.8). The double hump in 2 MLE spectra clearly indicated that a minimum of 2 peaks would be required to obtain a fit. At 2 MLE, corresponding LEED and STM data revealed that one of the components must be from the InPd IMC. Therefore we first attempted to fit data with just a single clean Pd(111) and an InPd component. However, this was not possible and we eventually determined two other components were required for satisfactory replication of experimental data.

The four curves used to fit the overall Pd 3d spectra will be referred to as (a) (b) (c) and (d) as follows: a) Pd - surface, b) Pd - bulk, c) InPd, and d) unknown $\text{In}_x\text{Pd}_{1-x}$. Clean Pd(111) can be fitted using two peaks indicative of bulk and surface components (respective 335.04 eV and 334.79 eV peaks were used by other authors [10]). For our Pd(111) crystal, the best peak fits were 334.69 eV (a) and 335.06 eV (b) fitted with respective GL(5) and A(0.14,0.3,95)GL(96) profiles. This was confirmed in a separate clean Pd(111) fit (not shown) by a significant increase in surface component intensity at grazing angle measurements having the same Pd $3d_{5/2}$ FWHM (Bulk = 1.17 eV; Surface = 0.63 eV) and peak positions mentioned above. A(a,b,n)GL(p) is a Gelius profile convoluted with a Gaussian width ($0 \leq n \leq 499$), similar to the Doniach - Sunjic fits discussed in the last section. Also similar, there is an alteration to the low-BE side by a GL(p) function. The difference from DS(α,n) profiles, is the high-BE asymptotic tail truncation of A(a,b,n). However, it does retain asymptotic form, which is adjusted, along with asymmetry by parameters, a and b [23]. The InPd (c) peak information was taken

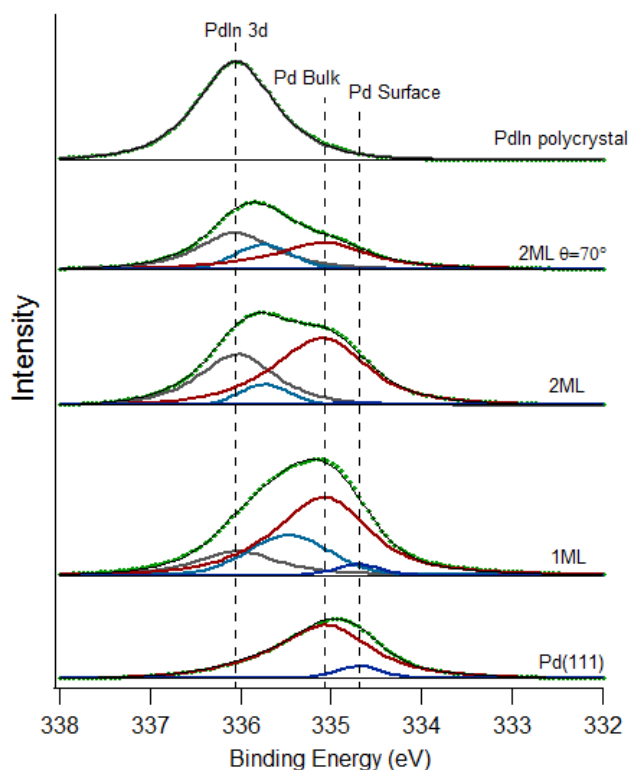


FIGURE 2.8: Peak fitting of Pd $3d_{5/2}$ spectra indicate 1:1 InPd and formation of additional surface alloy(s). The positions and FWHM were fixed ($\leq \pm 0.02$ eV) for Pd bulk and surface components with respect to clean Pd(111) fits, and likewise the InPd 1:1 component to the InPd polycrystal. The unknown alloy component varied in FWHM and position, suggesting formation of other phases.

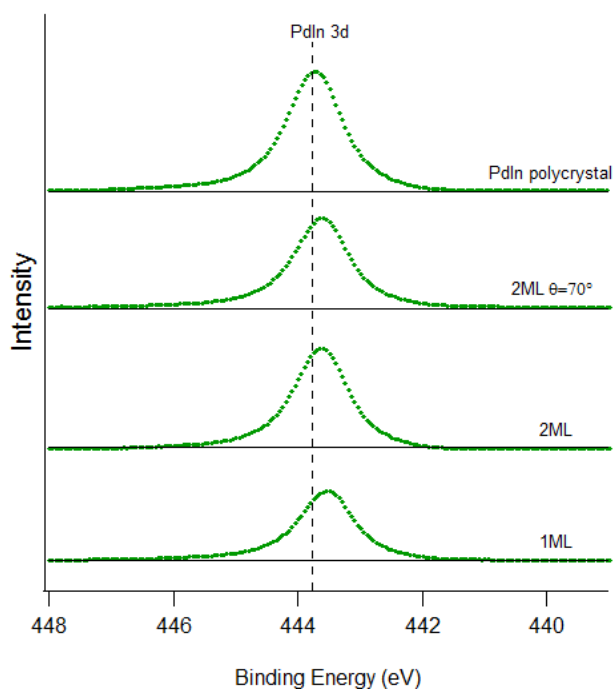


FIGURE 2.9: In $3d_{5/2}$ XPS components show relatively small shifts in comparison to Pd $3d_{5/2}$ shifts of Fig. 2.8.

from a single fit of the $3d_{5/2}$ (Polycrystal) with a Shirley background as described in the previous section. The final peak (d) within the Pd 3d region, was a non-constrained SGL(5) representative of a Pd-rich surface alloy and/or possible interface layer (noted in similar fits for Zn/Pd(111) [10]).

On the other hand, In 3d peaks were analyzed without component fits. Only relative

FWHM and position shifts were examined, since In $3d_{5/2}$ peak data was extrapolated using the method discussed in the previous section for the primary purpose of surface composition measurements. The peaks could not be reasonably fitted with additional components because relative position/FWHM values were too similar to the polycrystal In $3d_{5/2}$ values (within 0.2 eV/0.05 eV respectively).

Lastly, surface composition measurements were carried out by comparing areas under raw In $3d_{5/2}$ peaks to those of Pd $3d_{5/2}$ alloy components as follows:

$$\text{For In}_A\text{Pd}_B; B = \frac{\frac{I_{alloy}}{N_{Pd3d5/2}}}{\frac{I_{alloy}}{N_{Pd3d5/2}} + \frac{I_{In3d5/2}}{N_{In3d5/2}}} \quad (2.20)$$

where *alloy* is the total Pd $3d_{5/2}$ alloy contribution at the surface, based on the assumption of homogeneous globally distributed surface alloy/IMC phases (as suggested by LEED and STM). To obtain the area of *alloy* (I_{alloy}), the Pd bulk and surface components were subtracted from the total Pd $3d_{5/2}$ region's raw area. Pd(111) was presumed to be covered and can simply be excluded when considering top-layer concentrations. This was the most precise method because too much uncertainty exists in peak-fitting to break down *alloy* into separate $\text{In}_x\text{Pd}_{1-x}$ (d) and InPd (c) coverages, while perhaps accounting for an implicit interfacial component.

Although the two-component alloy/IMC fit was first justified based on LEED and STM findings at 2 MLE, the same fitting method was used to obtain compositional information higher coverage films ($\gtrsim 4$ MLE) of succeeding experiments. At higher coverage, the $\text{In}_x\text{Pd}_{1-x}$ (d) and Pd $3d_{5/2}$ surface (a) components vanished when annealing above ~ 550 K in accordance with LEED and STM findings showing only InPd(110)/Pd(111) domains.

Chapter 3

Surface structures of In-Pd intermetallic compounds

3.1 Overview

We provide the first comprehensive experimental study of the In/Pd(111) system by STM, XPS and LEED. This is complemented by DFT calculations performed within our group. The determination of a surface phase diagram, depending on initial In coverage ($0 < \theta < 35$ MLE) and annealing temperature is presented. This work precedes our studies on both polycrystal and single crystal InPd surfaces (discussed in the next chapter). The next few paragraphs are intended to briefly summarize our major findings for In/Pd(111), which are described with greater detail in the attached articles.

For ultra-thin films, we found that both (2×2) - like and $(\sqrt{3} \times \sqrt{3})R30^\circ$ structures can be formed as observed by LEED and STM. The MLE, monolayer equivalent condition was established once STM images revealed a complete In-Pd film covered large terraces. The film growth was monitored by STM following successive intervals of low-flux In dosing at room temperature. Film growth was approximately linear up to 2 MLE. At ≈ 1 MLE and ≈ 2 MLE, a (2×2) - like LEED pattern was observed and stable upon annealing to ~ 625 K. However, for the 1 MLE film, a $(\sqrt{3} \times \sqrt{3})R30^\circ$ pattern was found in coincidence. Further annealing the first layer to ~ 690 K resulted in a well-ordered $(\sqrt{3} \times \sqrt{3})R30^\circ$ phase with a surface lattice constant of 4.75 \AA , as measured with LEED and STM. This phase shows a slightly ruffled top-layer, characteristic of a $(\sqrt{3} \times \sqrt{3})R30^\circ$ surface alloy. Annealing the 2-layer thick film to the same temperature (± 10 K) led to a diffuse (1×1) LEED pattern. Furthermore, a (1×1) structure was observed after annealing both films beyond ~ 750 K.

Corresponding DFT calculations indicated segregation energies of In-doped Pd layer(s) of Pd(111) decreased towards the surface. This suggested the reconstructed surface structures mentioned above, were no more than a few layers thick. In particular, a single top layer with 33 % ($(\sqrt{3} \times \sqrt{3})R30^\circ$) of Pd atoms substituted by In had a negative segregation energy, meaning that In should remain in the top layer. However, when top-layer In concentrations (c) exceeded ~ 50 %, intermixing with sub-layers ($n = 1, 2, 3$, and 4) was more favorable (with each layer containing c/n % In).

From experimental XPS data, we determined the top couple of layers had about 50:50/60:40 In:Pd composition after dosing 1 MLE/2 MLE. The distribution of In in lower layers was unknown. When considering the DFT calculations however, we can presume 1 MLE/2 MLE were at least 2-layer thick/4-layer thick surface alloys or IMCs. Moreover, the formation of the $(\sqrt{3} \times \sqrt{3})R30^\circ$ superstructure had ~ 10 % less In than the originally prepared 1 MLE film, but we cannot attribute it as being top-layer substitutional or multilayer in nature.

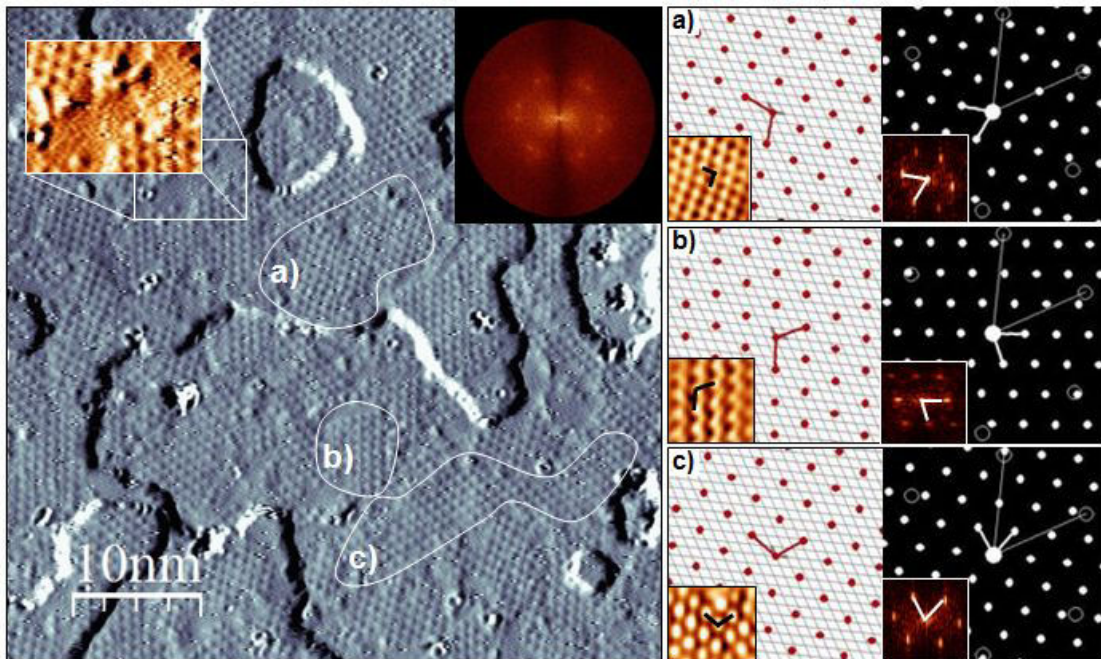


FIGURE 3.1: The STM image on the left ($50 \times 50 \text{ nm}^2$, $U = 1.2 \text{ V}$; $I = 0.08 \text{ nA}$) is dominated by three rotational domains (a,b,c) of $\text{InPd}(110)\text{-c}(4 \times 2)$ or $\text{In}_7\text{Pd}_3(110)$; they have equivalent 2D unit cells. Small patches of corresponding $\text{InPd}(110)$ coexist as shown in the zoomed-in rectangular section. The calculated FFT of the whole image is equivalent to the sum of individual reciprocal lattice images shown on the far right. The real space models, having white backgrounds, show the structures are incommensurate to the underlying $\text{Pd}(111)$ substrate. This is also true for smaller rectangular $\text{InPd}(110)$ domains (not modeled here).

The (2×2) - like LEED pattern first appeared with broad and diffuse diffraction spots (1 MLE). At 2 MLE, however, a splitting of (2×2) $(1,1)$ diffraction beams first appeared.

This was clear evidence formations of InPd and In₇Pd₃ IMCs were underway, but not realized until after obtaining results on 4 MLE films. Here a similar splitting of LEED beams was found upon dosing. The beams sharpened upon annealing to 500 K and well-ordered structures were imaged by STM, as shown and described in 3.1. Annealing to 550 K revealed a surface covered mostly by smaller rectangular structures along 3-fold symmetric directions of Pd(111). Precise STM and LEED measurements eluded to InPd(110)/Pd(111), which were indeed confirmed by XPS concentration measurement of near perfect stoichiometry. Thicker films (\gtrsim 4 MLE) formed In₇Pd₃(110) upon dosing and InPd(110) phases after heating between 500 and 600 K. Furthermore, VB XPS data of all InPd(110) data \geq 4 MLE compared well to those of bulk polycrystalline InPd.

Before the polycrystalline sample was studied in detail (next chapter), we obtained XPS data for comparative electronic information. This was important because existing literature on InPd IMCs in catalysis, pertain to MSR reactions over ‘real’ catalysts or InPd polycrystalline foils. Because the polycrystal data represented an ‘average’ taken over several InPd grains of different orientations, we can better understand how the electronic structures of InPd(110)/Pd(111) fit into the larger picture. We found the VB data agreed well in position, shape and width and concluded a ‘Cu-like’ VB exists for not only bulk polycrystalline InPd, but InPd(110)/Pd(111) IMC surfaces. Furthermore, bulk-truncated InPd(110) is the only stoichiometric InPd surface. Each In(Pd) atom is surrounded by four nearest neighbor Pd(In) atoms. So InPd(110) is an ideal surface for active-site isolation concept studies. Our work provides the experimental recipe for InPd(110)/Pd(111), which we find exhibits the nominal ‘Cu-like’ DOS and domains of bulk-truncated InPd(110). This is a first step towards decoupling electronic and geometric properties for future gas adsorption studies and ultimately gaining a complete atomic-level understanding of InPd in the MSR reaction mechanism.

**3.2 Part I: Experimental study of In thin films on Pd(111)
and alloy formation (Article)**



Surface structures of In-Pd intermetallic compounds. I. Experimental study of In thin films on Pd(111) and alloy formation

G. M. McGuirk, J. Ledieu, É. Gaudry, M.-C. de Weerd, and V. Fournée
*Institut Jean Lamour (UMR7198 CNRS-Nancy-Université de Lorraine), Parc de Saurupt,
54011 Nancy Cedex, France*

(Received 29 April 2014; accepted 5 June 2014; published online 25 August 2014)

A combination of experimental methods was used to study the structure of In thin films deposited on the Pd(111) surface and the alloying behavior. X-ray photoelectron spectroscopy (XPS), low-energy electron diffraction (LEED), and scanning tunneling microscopy results indicate that surface alloying takes place at room temperature. Below 2 monolayer equivalents (MLEs), the LEED patterns show the formation of three rotational domains of InPd(110) of poor structural quality on top of the Pd(111) substrate. Both core-levels and valence band XPS spectra show that the surface alloy does not yet exhibit the electronic structure characteristic of the 1:1 intermetallic compound under these conditions. Annealing the 1 MLE thin film up to 690 K yields to a transition from a multilayer InPd near-surface intermetallic phase to a monolayer-like surface alloy exhibiting a well ordered ($\sqrt{3} \times \sqrt{3}$) R30° superstructure and an estimated composition close to In₂Pd₃. Annealing above 690 K leads to further In depletion and a (1 × 1) pattern is recovered. The ($\sqrt{3} \times \sqrt{3}$) R30° superstructure is not observed for thicker films. Successive annealing of the 2 MLE thin film leads the progressive disappearance of the InPd diffraction spots till a sharp (1 × 1) pattern is recovered above 690 K. In the high coverage regime (from 4 to 35 MLE), the formation of three rotational domains of a *bcc*-In₇Pd₃ compound with (110) orientation is observed. This In-rich phase probably grows on top of interfacial InPd(110) domains and is metastable. It transforms into a pure InPd(110) near-surface intermetallic phase in a temperature range between 500 and 600 K depending on the initial coverage. At this stage, the surface alloy exhibits core-level chemical shifts and valence band (VB) spectra identical to those of the 1:1 InPd intermetallic compound and resembling Cu-like density of states. Annealing at higher temperatures yields to a decrease of the In concentration in the near-surface region to about 20 at.% and a (1 × 1) LEED pattern is recovered. © 2014 AIP Publishing LLC. [<http://dx.doi.org/10.1063/1.4892408>]

I. INTRODUCTION

The catalytic properties of Pd nanoparticles on oxide supports have recently received much attention for hydrogen production in the methanol stream reforming (MSR) process ($\text{CH}_3\text{OH} + \text{H}_2\text{O} \rightarrow \text{CO}_2 + 3\text{H}_2$).¹⁻⁶ They are considered as potential alternatives to Cu/ZnO catalysts used today by industry, offering an improved thermal stability as well as an enhanced activity and selectivity for MSR.^{3,7,8} The high selectivity and activity towards MSR of Pd/ZnO, Pd/Ga₂O₃, and Pd/In₂O₃ was attributed to the formation of intermetallic compounds by reduction of the powder catalyst under H₂ at high temperature,^{9,10} linked to a shift towards higher binding energies of the Pd d-band upon alloying, making the density of states (DOS) of the alloy resembling that of Cu metal.¹¹ However recent studies have shown that the formation of intermetallic compounds is a necessary but not sufficient condition to gain high selectivity.^{12,13}

Many studies have been devoted to the electronic and crystallographic structure of Pd-M (M = Zn, Ga, or In) intermetallic phases, which is a prerequisite to understand the chemical reactivity of these prospective catalysts at a microscopic level. Most of them deal with ZnPd intermetallics and a recent review can be found in Ref. 14. The catalytic prop-

erties of Pd nanoparticles supported on ZnO are ascribed to the formation of a stable ZnPd intermetallic phase with a 1:1 concentration ratio and a tetragonal structure.^{15,16} Experimental studies of the Zn/Pd(111) system reported the formation of different surface alloys as a function of temperature and coverages, including a near stoichiometric ZnPd phase. The latter one is characterized by an apparent p(2 × 2) low-energy electron diffraction (LEED) pattern corresponding in fact to 3 rotational domains of a p(2 × 1) structure resembling a tetragonal ZnPd(111) surface with alternating rows of Pd and Zn atoms. This near-surface intermetallic phase (NSIP) exhibits the expected Cu-like DOS as well as a rumpling of the outermost surface layer induced by an outward shift of the Zn atoms and an inward shift of the Pd atoms (into the bulk),^{16,17} associated with a high CO₂ selectivity. Upon annealing the film above 550 K, the Zn concentration in the near-surface region decreases rapidly although an almost stoichiometric monolayer surface alloy remains in the topmost layer. This change in sub-surface chemistry is associated with an inversion of the surface buckling (*i.e.*, Pd-up/Zn-down) and an increased DOS at the Fermi level together with a loss of CO₂ selectivity.¹⁸ Similar trends have also been reported for the Ga/Pd(111) system.¹⁹ These results show that rather subtle modifications of the

surface alloys can have dramatic effects on their catalytic properties.

In contrast to the Zn-Pd and Ga-Pd systems, surface alloys in the In-Pd system have received much less attention although $\text{In}_y\text{Pd}_x/\text{In}_2\text{O}_3$ are also highly active and selective supported catalysts.²⁰ Earlier work by Fink *et al.*^{21–23} reported compound formation upon In deposition on Pd(100) surface using perturbed $\gamma\gamma$ -angular correlation spectroscopy. A more recent report by Rameshan *et al.*²⁴ found that room temperature deposition of a 4 monolayer equivalents (MLEs) of In on Pd foil followed by subsequent annealing to 453 K yields an almost stoichiometric InPd NSIP exhibiting a Cu-like DOS similar to the ZnPd counterparts. *In situ* X-ray photoelectron spectroscopy (XPS) under near-ambient pressure demonstrated an almost 100% CO_2 selectivity in a temperature range between 493 and 550 K. A change towards CO selectivity upon annealing above 600 K is explained by a decrease in the In sub-surface content. This behavior presents some similarities with the ZnPd system. However little is known about the structure of such near-surface intermetallic InPd phases.

In this work, we investigate the alloying tendency and the structure of In thin films grown on the Pd(111) surface using a combination of experimental methods (XPS, LEED, and STM). We show that different phases form depending on the initial In coverage and annealing temperatures, each possessing different chemical compositions and structural/electronic signatures.

The paper is organized as follows. We first provide experimental details in Sec. II. The results are presented in Sec. III, first for the low coverage regime, then for higher coverages. The main findings are summarized in Sec. IV and compared with the existing literature on related Pd-M ($M = \text{Zn}, \text{Ga}, \text{or In}$) systems. We also discuss our experimental results in the light of a joint theoretical study of InPd surface alloys using first-principle calculations.²⁵

II. EXPERIMENT

A well-polished Pd(111) sample was placed under ultra-high vacuum (UHV) conditions with base pressures below 1×10^{-10} mbar. An atomically smooth surface free of sub-surface carbon contamination was achieved by cycles of Ar^+ sputtering at 1 keV, followed by annealing to 1173 K, then O_2 exposure ($P_{\text{O}_2} = 10^{-6}$ mbar, 15 mn, 873 K) and a final flash annealing to 1173 K. After multiple cycles, a sharp (1×1) LEED pattern was obtained and the absence of surface contamination was verified by XPS analysis. Indium was deposited *in situ* using an e-beam evaporator (EFM3, flux monitored) with the sample held at room temperature in the scanning tunneling microscopy (STM) stage. Thin film growth was investigated from submonolayer coverage up to 35 monolayer equivalent (MLE). Here an MLE is defined as the exposure required to complete one monolayer as observed by STM. The coverage as determined from STM images is found to increase linearly with exposure in the submonolayer regime. The films were annealed at different temperatures measured using a pyrometer with the emissivity set to 0.1. The temperature was also measured with a K-type thermocouple attached on the manipulator at some distance from the sam-

ple. There is a linear relationship between both measurements with an offset of approximately 150° (thermocouple reading is lower than pyrometer reading).

A polycrystalline InPd sample was also used in the study. An ingot was prepared by induction melting with a nominal composition of $\text{In}_{47}\text{Pd}_{53}$. Then the ingot was annealed in an evacuated quartz glass tube sealed under Ar atmosphere up to 1248 K, maintained at this temperature for 36 h and then cooled down to room temperature at a rate of 10 K/min. The crystallographic structure was checked by powder x-ray diffraction (XRD) (space group $Pm\bar{3}m$, CsCl type, $a = 3.23 \text{ \AA}$). The final composition as determined by energy dispersive x-ray analysis was $\text{In}_{47}\text{Pd}_{53}$, consistent with the existence domain of the InPd.²⁶ The surface of the polycrystalline sample was prepared under UHV conditions by sputtering and annealing cycles (Ar^+ , 1 keV, 973 K). The surface composition measured by XPS was $\text{In}_{53}\text{Pd}_{47}$, *i.e.*, within the compositional range of the InPd compound.

III. RESULTS

A. Low coverage regime ($\theta \leq 2$ MLE)

1. Room temperature deposition

Figure 1 shows a sequence of STM images of the In film on Pd(111) with increasing coverage up to $\theta \sim 2$ MLE. Small islands of irregular shape are observed on terraces in the early stage of the growth with no preferential nucleation at step edges. With increasing coverage, the number of islands increases, with no obvious coalescence, until completion of the first layer. Then the second layer grows with a similar behavior. The islands exhibit a dendritic shape indicative of a diffusion limited growth process. A similar behavior has been

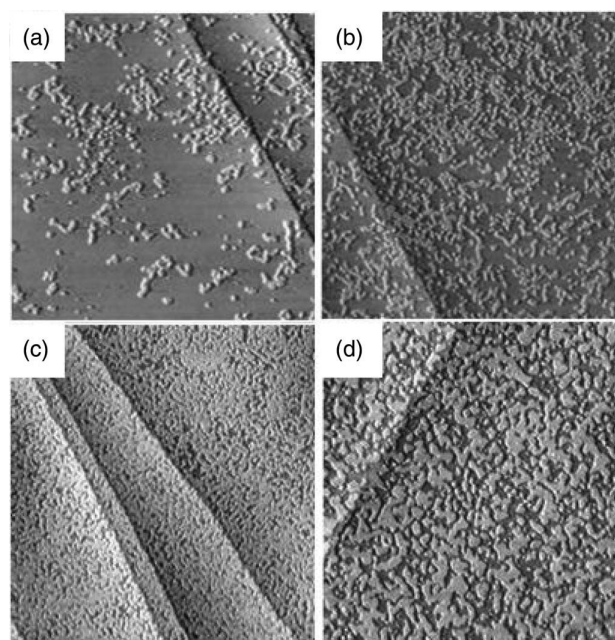


FIG. 1. STM images ($200 \times 200 \text{ nm}^2$) of the In thin film on Pd(111) surface for increasing coverage. (a) 0.2 MLE and (b) 0.4 MLE, $V = -2.0 \text{ V}$, $I = 0.06 \text{ nA}$; (c) 0.8 MLE, $V = +2.0 \text{ V}$, $I = 0.06 \text{ nA}$; (d) 1.7 MLE, $V = -1.4 \text{ V}$, $I = 0.10 \text{ nA}$.

084702-3 McGuirk *et al.*

J. Chem. Phys. 141, 084702 (2014)

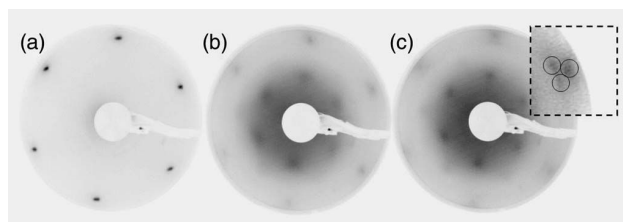


FIG. 2. LEED patterns of (a) the clean Pd(111) surface and after dosing (b) 1 MLE and (c) 2 MLE of In at room temperature. All patterns were recorded at an incident beam energy of 55 eV. The dotted rectangle in (c) is a blow-up of one of the outermost diffraction spots showing that they are actually poorly defined triplets.

observed in a study of Zn thin films on Pd(111).²⁷ The Pd step height is measured at 2.25 ± 0.05 Å corresponding to the theoretical Pd(111) interplanar spacing. The height of the islands is measured at 2.15 ± 0.05 Å.

Figure 2 shows the LEED patterns of the clean Pd(111) surface (Fig. 2(a)) and after dosing 1 MLE (Fig. 2(b)) and 2 MLE of In (Fig. 2(c)) at room temperature. Already at 1 MLE, a new pattern starts to appear which is slightly improved at 2 MLE coverage. The LEED patterns are quite diffuse in both cases and could be interpreted as either a (2×2) reconstruction or three rotational domains of a (2×1) reconstruction or three rotational domains of another structure resembling a (2×1) reconstruction. However, at 2 MLE, the outer spots appear to be poorly defined triplets (see blow-up in Fig. 2(c)), which rules out the first two hypothesis.

At this stage, the film is not sufficiently ordered to obtain atomically resolved STM images. However, domains can be identified exhibiting atomic rows, rotated by 120° from each other. The formation of these domains suggests that intermixing already occurs at room temperature. Further evidence for intermixing is provided by the core-level XPS data shown in Fig. 3. The Pd 3d core-level lines of the clean Pd(111) substrate can be fitted with a bulk and a surface contribution as described in Ref. 10. With increasing coverage, an additional peak grows on the high binding energy side, which is further enhanced at high take-off angle of the photoelectrons to increase the surface sensitivity. This peak corresponds to the surface alloy contribution. The position of this additional peak is shifted from the bulk Pd peak by +0.65 eV at 1 MLE and by +0.9 eV at 2 MLE. The shift is however smaller than the binding energy shift (+1.0 eV) observed for the InPd polycrystalline reference sample, suggesting that the surface alloy formed at room temperature is different from the stoichiometric compound in this coverage regime. Core-level peak fitting of the Pd 3d line indicates that the alloy contribution is more symmetric than the Pd bulk peak. The asymmetry of metal core-level line shapes results from intrinsic energy losses through electron-hole pairs excitations across the Fermi level and thus depends on the local density of states (DOS) at the Fermi level ($N(E_F)$).^{28,29} Therefore the more symmetric line shape of the alloy component indicates a reduced $N(E_F)$ in the surface alloy compared to the substrate DOS. Another observation is the disappearance of the shake-up satellite at +5.9 eV from the Pd $3d_{3/2}$ upon alloying. The intensity of the shake-up satellite depends on the weight of unoccupied Pd 4d character and its position above E_F .³⁰ The disappearance

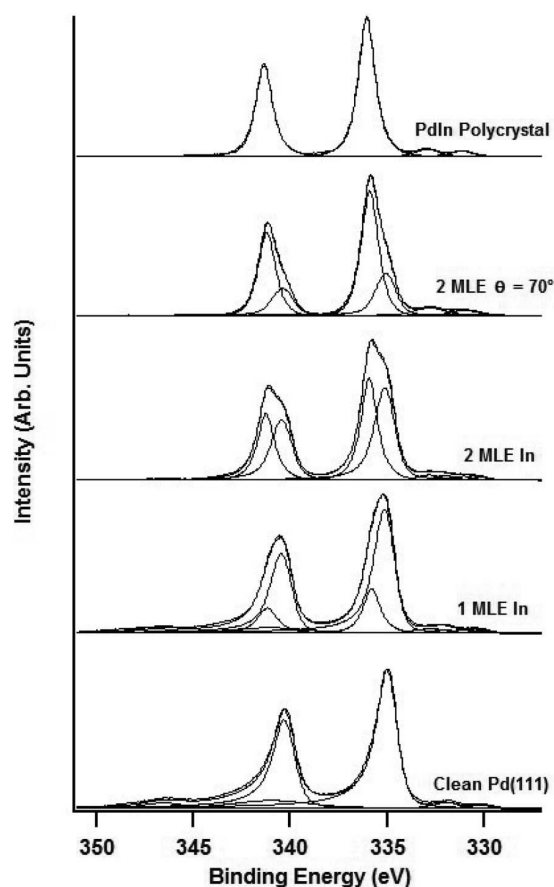


FIG. 3. XPS Pd 3d spectra of the clean Pd(111) surface, after dosing 1 and 2 MLE of In and of the clean polycrystalline InPd sample. All spectra were recorded at 45° take-off angle except for the second from the top spectrum which was collected at 70° to enhance surface sensitivity. A clear alloy component can be seen upon In dosing the Pd surface as well as the loss of the asymmetric tail and the disappearance of the shake-up satellites at 346.3 eV binding energy.

of the satellite upon alloying suggests that the Pd d band is being filled and shifted below the Fermi level upon alloying, a feature commonly observed upon intermetallic compound formation.³¹ This is confirmed by XPS valence band measurements shown in Fig. 4. The main peak corresponds to the Pd d band which is shifted towards higher binding energies with increasing film thickness to resemble that of the polycrystalline reference sample. However at 2 MLE, the spectral weight within 2 eV below E_F is larger than for the polycrystalline sample. This is probably due to a Pd bulk contribution to the XPS signal in this low coverage regime. The chemical composition of the surface alloy formed at room temperature can be roughly estimated by considering the area of the In 3d peak and that of the alloy component of the Pd 3d peak, assuming that the In concentration is homogeneous across the alloy thickness. This gives a composition of $\text{In}_{47}\text{Pd}_{53}$ at 1 MLE and $\text{In}_{57}\text{Pd}_{43}$ at 2 MLE.

2. Annealing 1 MLE thin films

Upon successive annealing of the 1 MLE thin film up to 690 K, the broad diffraction spots observed at 300 K

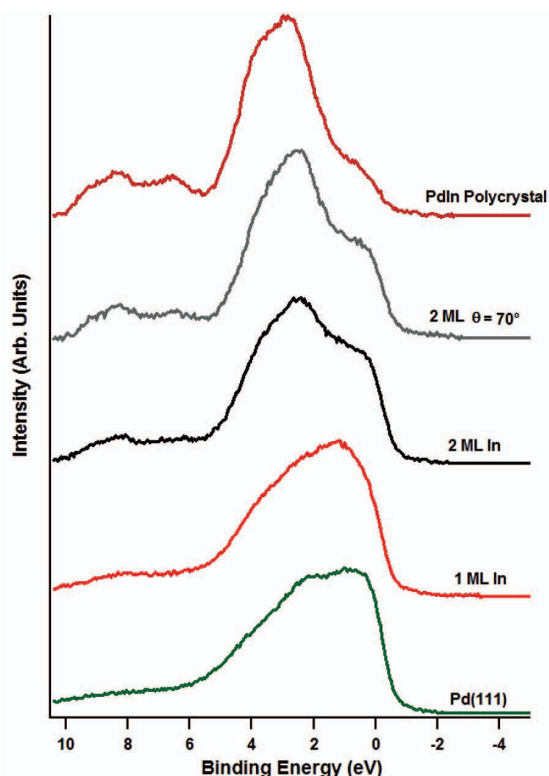
084702-4 McGuirk *et al.*J. Chem. Phys. **141**, 084702 (2014)

FIG. 4. Experimental XPS VB spectra of the clean Pd(111) surface, after dosing 1 and 2 MLE of In and of the clean polycrystalline InPd sample. All spectra were recorded at 45° take-off angle except for the second from the top spectrum which was collected at 70° to enhance surface sensitivity.

vanish and are replaced by a new well ordered ($\sqrt{3} \times \sqrt{3}$) $R30^\circ$ superstructure (Fig. 5(a)). The corresponding STM image is shown in Fig. 5(b). On large scale images, one observes a two phase mixture, one phase being disordered and covering less than 30% of the surface area, and an ordered phase with an hexagonal unit cell of dimension 4.75 \AA consistent with the ($\sqrt{3} \times \sqrt{3}$) $R30^\circ$ superstructure observed by LEED. The STM contrast is not uniform, suggesting either chemical inhomogeneity and/or rumpling and/or structural imperfections. After annealing at 690 K, XPS core-level measurements show a decrease in the In content in the near-surface region. The estimated composition of the surface alloy is equal to $\text{In}_{41}\text{Pd}_{59}$. The uncertainty in this case is rather large because of the difficulty in extracting the Pd 3d alloy component out of the total Pd 3d line. The surface alloy is most likely confined in the top-most surface layers. Above 690 K, the LEED pattern evolves towards a (1×1) pattern. By XPS, the alloy component of the Pd 3d line has almost disappeared while the intensity of the In 3d line strongly decreases, indicating that the In atoms have either desorbed or diffused into the bulk.

3. Annealing 2 MLE thin films

Upon successive annealing of the 2 MLE thin film, the broad diffraction spots of the reconstruction observed at 300 K progressively vanish with no evidence of ($\sqrt{3} \times \sqrt{3}$) $R30^\circ$ ordering in this case. At $690 \pm 10 \text{ K}$, the LEED pattern

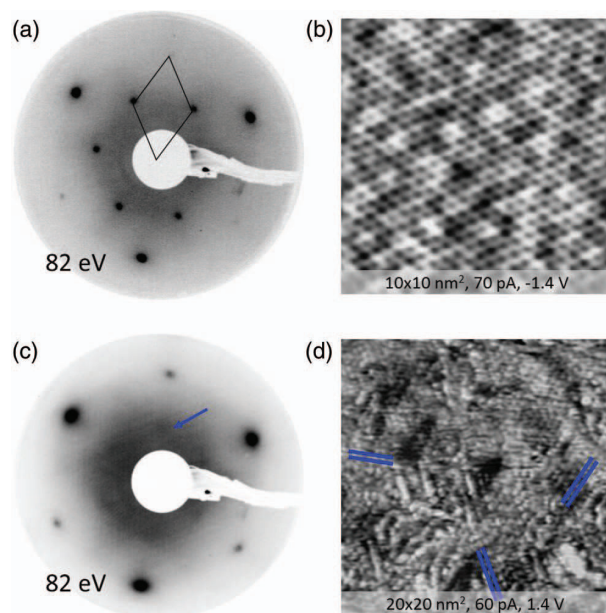


FIG. 5. (a) LEED pattern of the 1 MLE In film on Pd(111) after annealing at 690 K and (b) corresponding STM image ($10 \times 10 \text{ nm}^2$, $V = -1.4 \text{ V}$, $I = 0.07 \text{ nA}$). (c) LEED pattern of the 2 MLE In film on Pd(111) after annealing at 690 K and (d) corresponding STM image ($20 \times 20 \text{ nm}^2$, $V = +1.4 \text{ V}$, $I = 0.06 \text{ nA}$). Atomic rows can be distinguished according to three different orientations as indicated by straight lines in (d). The arrow in (c) points towards one of the diffuse spots arising from the surface alloy.

shown in Fig. 5(c) is obtained where the (1×1) diffraction spots coexist with faint diffuse spots of the InPd surface alloy. An STM image of the corresponding film is shown in Fig. 5(d). The surface alloy is not well ordered but nevertheless domains can be seen presenting atomic rows. The chemical composition of the surface alloy is estimated at $\text{In}_{47}\text{Pd}_{53}$ following the peak fitting procedure described above. Further annealing of the 2 MLE film above 690 K leads to an even sharper (1×1) LEED pattern and a progressive loss of the In content in the near-surface region.

B. High coverage regime ($\theta \geq 4 \text{ MLE}$)

After deposition of 4 MLE of In on Pd(111) at room temperature, the LEED pattern shown in Fig. 6(a) is observed. It is actually similar to the one obtained after 2 MLE deposition at room temperature except that the diffraction spots are now better resolved. The quality of the LEED pattern can be further improved by annealing the film up to 500 K as shown in Fig. 6(b). At this stage, the LEED pattern can be described as consisting of three rotational domains of a rectangular structure. The three domains and their relationship with the Pd(111) substrate are depicted in the LEED pattern in Fig. 6(b). The domains are rotated by 60° from each other. By calibrating the reciprocal space using the LEED pattern of the clean Pd(111) surface recorded under the same experimental conditions, it is deduced that the rectangular surface unit cells have dimensions $a = 3.28 \pm 0.1 \text{ \AA}$ and $b = 4.64 \pm 0.1 \text{ \AA}$. These values are close to those of the rectangular unit cell of InPd(110) ($a = 3.25 \text{ \AA}$ and $b = 4.6 \text{ \AA}$) and are thus consistent

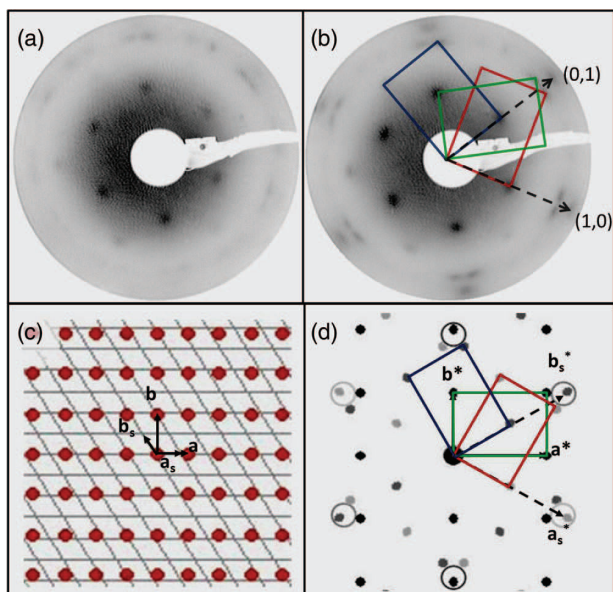


FIG. 6. LEED patterns of (a) the 4 MLE In thin film deposited on Pd(111) at room temperature and (b) after annealing at 500 K. The two patterns were recorded at an incident beam energy of 50 eV. The three rotational domains of the InPd(110) rectangular mesh are superimposed. The dashed arrows correspond to the Pd(111) lattice vectors. The first order substrate spots are in coincidence with the (0, 2) and (0, -2) spots of the InPd(110) domains. (c) Real space model of a single InPd(110) domain with lattice vectors (a, b) on a Pd(111) substrate with lattice vector (a_s, b_s). (d) Reciprocal space for three rotational domains of InPd(110) on Pd(111) substrate. Large circles indicate coincidence reciprocal lattice spots between the surface alloy and the substrate.

with the formation of three rotational domains of InPd(110) surface alloy on Pd(111). The orientation of the InPd(110) domains with respect to the Pd(111) substrate is determined by the coincidence of the (0,2) and (0,-2) reciprocal lattice spots of the InPd overlayer with the (0,1) and (0,-1) or (-1,0) and (1,0) or (-1,1) and (1,-1) substrate spots, respectively, hence the three rotational domains observed. A schematic of the model is shown in Figs. 6(c) and 6(d), in both real and reciprocal space. Considering the bulk parameters of Pd and InPd compounds, this locking into registry would imply a small lattice expansion of the surface alloy by 3.6%.

At low electron beam energy, additional triplet of spots appear for the same growth conditions; i.e., In deposition of 4 MLE at room temperature. They are slightly better defined after annealing up to 500 K (Fig. 7(a)) but disappear after annealing at 550 K (Fig. 7(b)). These triplets of spots do not originate from the InPd(110) domains themselves but correspond to a structure possessing a larger unit cell. The reciprocal lattice vectors (a_R^*, b_R^*) of this larger structure are shown in the LEED pattern in Fig. 7(a) together with the lattice vector (a^*, b^*) of a single InPd(110) domain. The larger structure corresponds to an oblique surface unit cell having parameters $a_R = b_R = 7.7 \pm 0.1 \text{ \AA}$ and $\gamma = 71^\circ \pm 2^\circ$ or equivalently to a centred rectangular net with dimensions $a_R = 9.2 \pm 0.5 \text{ \AA}$ and $b_R = 13 \pm 1 \text{ \AA}$. There are two possibilities to interpret this structure. From a purely geometrical point of view, it can be interpreted as a $c(4 \times 2)$ surface reconstruction of InPd(110) domains on the Pd(111) substrate as sketched in the model

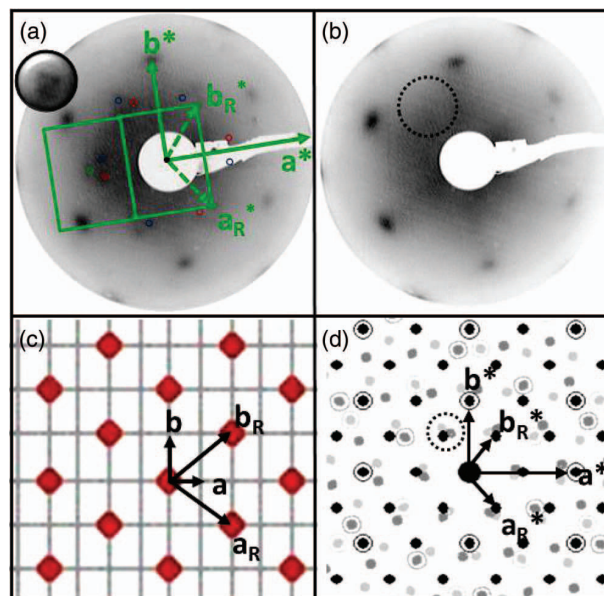


FIG. 7. (a) and (b) LEED patterns recorded at 21 eV beam energy for a 4 MLE In thin film on Pd(111) after annealing at 500 K and 550 K, respectively. The additional triplets of spots observed at 500 K disappear after annealing at 550 K. The reciprocal lattice vectors (a^*, b^*) of a single InPd(110) domain are outlined in (a) as well as those (a_R^*, b_R^*) of the larger structure. The equivalent centered rectangular net is also outlined for a single domain. The first nodes of the two other domains are outlined by empty circles in blue and red, respectively. The circular inset is a magnified view of one triplet of spots. The dotted circle in (b) indicates the position of the missing triplet after annealing at 550 K. (c) Real space model of the “ $c(4 \times 2)$ reconstruction” with lattice vector (a_R, b_R) on a single domain of InPd(110). As explained in the text, the “ $c(4 \times 2)$ ” phase can alternatively be interpreted as In₇Pd₃-(110) domains. (d) Reciprocal space model for three rotational domains of $c(4 \times 2)$ -InPd(110) domains. The dotted circle indicates the triplet of spots observed in LEED patterns.

shown in Figs. 7(c) and 7(d) in both real and reciprocal space. However, the physical origin of such reconstruction is unclear. Considering the fact that its characteristic diffraction spots disappear upon further annealing at 550 K and that the In concentration in the near-surface region tends to decrease upon annealing as verified by XPS, we can suppose that this structural change is linked to a change in the chemistry of the diffracting overlayer. The In-Pd phase diagram contains several intermetallic compounds. On the In-rich side, one finds the In₇Pd₃ compound whose structure is closely related to the γ -brass structure type.³² It has $Im\bar{3}m$ space group and a lattice parameter $a = 9.436 \text{ \AA}$. The surface unit cell in its (110) plane would thus have dimensions $a = 9.436 \text{ \AA}$ and $b = 13.344 \text{ \AA}$, i.e., close to the values (a_R, b_R) measured experimentally. Therefore this additional structure could alternatively be interpreted as three rotational domains of In₇Pd₃-(110) instead of $c(4 \times 2)$ -InPd(110) domains.

Atomically resolved STM images of the different structures are shown in Figure 8. The three rotational domains can be clearly observed in Fig. 8(a). The dimensions of the surface unit cell (Fig. 8(b)) are in agreement with the LEED measurements. Such structure is observed either directly after room temperature deposition of $\theta \geq 4$ MLE or after annealing up to 500 K to improve the structural quality. In these images,

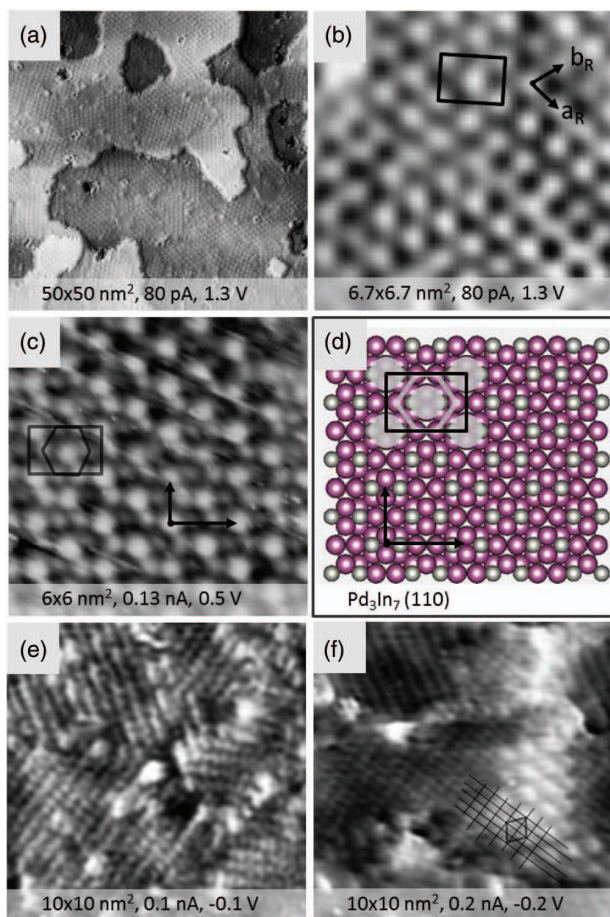
084702-6 McGuirk *et al.*J. Chem. Phys. **141**, 084702 (2014)

FIG. 8. (a) STM image of the 4 MLE In thin film on Pd(111) after annealing at 500 K showing multiple domains of the “ $c(4 \times 2)$ ” structure and (b) its atomic structure. The lattice vectors (a_R, b_R) are superimposed on the image, as well as the centered rectangular unit cell. (c) High-resolution STM image of the same structure obtained after room temperature deposition of 16 MLE In on Pd(111) showing additional contrast within the rectangular unit cell forming an elongated hexagon around each bright dot. (d) Structure model of the $\text{In}_7\text{Pd}_3(110)$ surface. (e) STM image of a 4 MLE In thin film on Pd(111) after annealing at 550 K showing multiple domains of InPd(110). (f) STM image of the same film as in (e) showing the coexistence of $\text{In}_7\text{Pd}_3(110)$ and InPd(110) phases and their orientation relationship.

one can only distinguished bright features at the nodes and at the center of the rectangular unit cell. Therefore it is not possible from such images to discriminate between the two structure models proposed earlier based on LEED patterns, *i.e.*, rotational domains of either $\text{In}_7\text{Pd}_3(110)$ or $c(4 \times 2)$ -InPd(110). However, in rare cases, a better resolution could be achieved by STM as shown in Fig. 8(c) for a 16 MLE thin film after room temperature deposition. In addition to the bright dots at the nodes and centers of the rectangular mesh, one can distinguish 6 additional features surrounding each bright dot forming an elongated hexagon. The structure model of the (110) surface of the In_7Pd_3 intermetallic compound is shown in Fig. 8(d) assuming a bulk termination at dense puckered layer. At the nodes and center of the rectangular mesh, one finds a group of 4 atoms (2 Pd and 2 In atoms forming a cross) slightly protruding above the mean position of the plane. Each of these motifs is surrounded by 6 addi-

tional In atoms located at about 0.6 \AA below. It is reasonable to assume that the groups of 4 protruding atoms are imaged as a bright dots by STM and that the 6 surrounding In atoms appear dimmer because they lie below the mean position of the surface plane. This model presents a good agreement with the experimental observations, supporting the formation of $\text{In}_7\text{Pd}_3(110)$ domains rather than a $c(4 \times 2)$ reconstruction of InPd(110) domains. The film structure changes upon annealing at 550 K as can be seen in the STM image shown in Fig. 8(e). Now the film structure consists of three rotational domains of the InPd(110) phase in agreement with the LEED results. The dimensions of the surface unit cell measured by STM ($a = 3.25 \pm 0.1 \text{ \AA}$ and $b = 4.6 \pm 0.1 \text{ \AA}$) are consistent with expected values. It is to be noted that the two structures, $\text{In}_7\text{Pd}_3(110)$ domains and InPd(110) domains, are found to coexist at the surface, the former one being the dominant structure after room temperature deposition and annealing up to 500 K while the latter become the predominant structure after annealing to 550 K. The orientation relationship between the two structures is illustrated in the STM image shown Fig. 8(f), in which a $\text{In}_7\text{Pd}_3(110)$ domain appears adjacent to a InPd(110) domain.

To summarize this section on In thin films ($\theta \geq 4$ MLE) on Pd(111), surface alloying is observed already after room temperature deposition leading to the formation of three rotational domains of a In_7Pd_3 compound with (110) orientation. This In-rich compound may grow directly on top of the Pd(111) substrate or may develop on top of InPd(110) domains formed as an interfacial layer in the early stage of the growth. Such near-surface layer is found to be stable up to annealing at 500 K but transforms into pure InPd(110) domains upon further annealing to 550 K. This sequence of surface phases has been observed for various coverages, including 4, 8, 16, and 35 MLE, the transition temperature always being in the range of 500 to 600 K. When the films are further annealed above 690 K, a LEED pattern similar to a Pd (1×1) pattern is recovered, consistent with what has been already observed for the 2 MLE thin film. Thus the InPd surface alloy is not stable in this temperature range and further In diffusion into the bulk or In desorption must take place. Figure 9 summarizes in a schematic way the different phases formed as a function of coverage and temperature.

Up to now, we have assumed the formation of In-Pd surface alloys based on structural information obtained by LEED and STM. The concentration in the near-surface region has been measured by XPS for the different coverages, before and after annealing in a temperature window of 500 to 600 K. The XPS core-level lines are shown in Figs. 10 and 11 for the different conditions. The composition of the near-surface alloy can be estimated assuming that the surface alloy is chemically homogeneous along the surface normal, a criterion which is most likely not satisfied. We nevertheless use this approximation in order to derive the basic trends in the chemical composition in the near-surface region. Before annealing, the surface alloy composition is In-rich and slowly evolves from $\text{In}_{64}\text{Pd}_{36}$ at 4 MLE to $\text{In}_{79}\text{Pd}_{21}$ at 35 MLE. After annealing, the In concentration in the surface alloy decreases to about 55%, *i.e.*, within the InPd compositional range, for all coverages above $\theta \geq 4$ MLE. A Pd bulk component in the Pd 3d

> 690 K	(1x1)					
690 K	($\sqrt{3} \times \sqrt{3}$)R30°	(1x1)				
550-600 K	undefined	3xInPd-(110)				
500 K		3xIn ₃ Pd ₇ -(110)				
300 K	3xInPd(110)					
T / θ	1 MLE	2 MLE	4 MLE	8 MLE	16 MLE	35 MLE

FIG. 9. Schematic summary of the different phases formed as a function of coverage and temperature.

line can still be observed directly after dosing up to 8 MLE, consistent with the probing depth by XPS. However, after annealing the 8 MLE, the Pd bulk component is not detected, which means that the thickness of the surface alloy has increased. The expected surface alloy thickness for a 1:1 stoichiometry at 8 MLE corresponds to 16 atomic planes equivalent to a thickness of 3.7 nm, i.e., larger than the XPS probing depth. Therefore annealing to 500–600 K is a necessary step to complete the alloy formation. Note that the chemical composition of the near-surface region measured after annealing the films at 500 K or 600 K is almost similar within the accuracy of the measurements, although this temperature window corresponds to the transition from the In-rich surface structure (In₇Pd₃) to the 1:1 InPd compound as determined by LEED

and STM. However, for a given coverage, angle-dependent XPS measurements show a small increase of the In content for more surface sensitive conditions (20° take-off angle instead of 45°). These observations are consistent with a gradient of In concentration after room temperature deposition in this coverage regime, decreasing from surface to bulk and being more marked with increasing initial coverage. Probably the InPd compound is first formed at the interface region during growth and then the In₇Pd₃ phase is formed on top because the intermixing is not fast enough under these experimental conditions. Upon mild annealing, further diffusion takes place deeper in the bulk allowing the formation of a thicker InPd interface layer. In the temperature range 500–600 K, the In₇Pd₃ surface alloy should disappear to leave

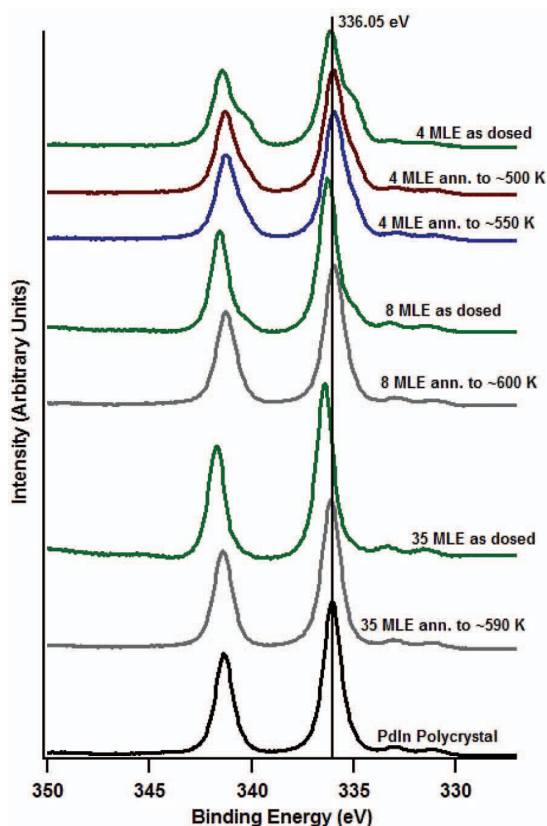


FIG. 10. XPS Pd 3d core-level lines for different film thicknesses, before and after annealing and for the reference InPd polycrystalline sample.

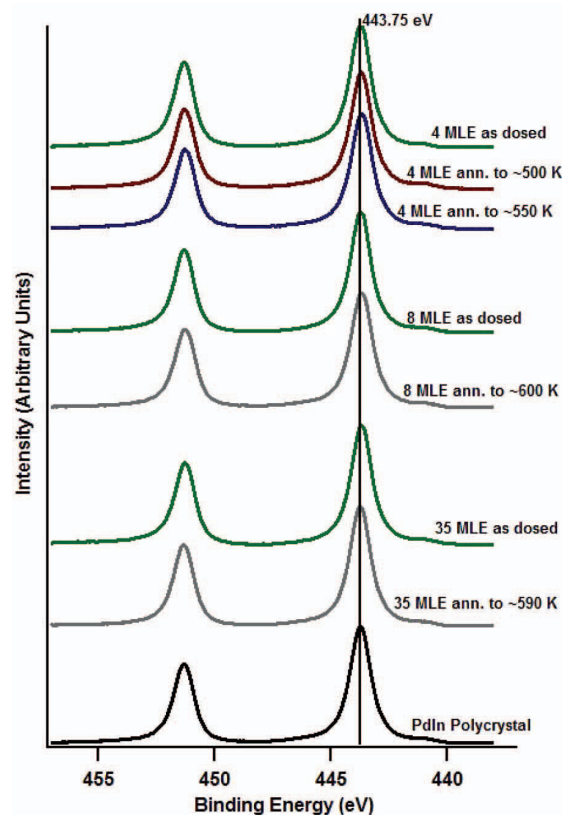


FIG. 11. XPS In 3d core-level lines for different film thicknesses, before and after annealing and for the reference InPd polycrystalline sample.

084702-8 McGuirk *et al.*J. Chem. Phys. **141**, 084702 (2014)

TABLE I. Main characteristics of the XPS core-level spectra measured on the reference InPd polycrystalline sample.

	In 3d _{3/2}	In 3d _{5/2}	Pd 3d _{3/2}	Pd 3d _{5/2}
Position (eV)	451.30	443.77	341.35	336.05
FWHM (eV)	0.97	1.01	1.01	1.00

a single phase InPd surface alloy. This scenario is consistent with all presented observations. Note that due to the fact that such surface phase transformations are linked to diffusion and intermixing, the exact conditions under which a phase appears should not only depend on initial coverage and annealing temperature but also on the time elapsed between the deposition and the experimental observation.

As observed in Figs. 10 and 11, there is a systematic shift of the Pd 3d lines towards lower binding energy upon annealing the films while the In 3d line appears mostly at the same binding energy, independently of the conditions shown. We mention however the In 3d_{3/2} core-level line shifts to 443.5 eV for higher annealing temperature (690 K, not shown in Fig. 11), associated with a decrease of the In content. The final line shape and binding energies of Pd 3d and In 3d core-levels of the surface alloys after 500–600 K annealing are in good agreement with those measured for the polycrystalline reference samples (± 0.05 eV). The main characteristics of the lines are provided in Table I. The XPS valence band spectra recorded for the same conditions are shown in Fig. 12. The

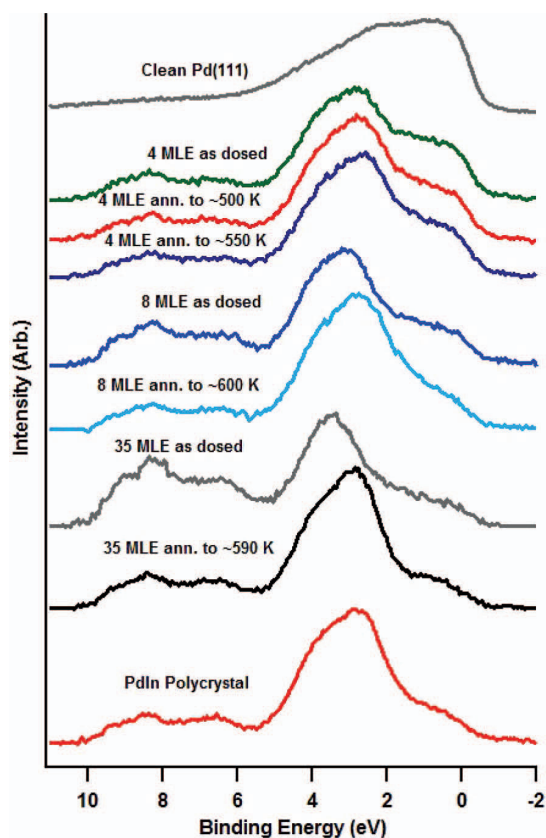


FIG. 12. XPS valence band data showed filling of Pd 4d bands to a Cu-like state upon dosing and annealing In/Pd(111) films.

broad main peak at approximately 2 to 4 eV below E_F arises from the Pd d band of the surface alloy and is being increasingly shifted to higher binding energies with increasing coverage after room temperature deposition. The spectral weight between 2 eV and E_F can be due to some Pd d states contribution of the InPd compound which has some sizable DOS in this energy range (see Ref. 25) as well as some additional contribution from d states of bulk Pd at low enough coverages. Upon annealing, the position of the main Pd d band shifts back to that measured in the reference polycrystalline sample. Simultaneously, the relative spectral weight within 2 eV below E_F decreases, consistent with an increase in the surface alloy thickness and thus a reduced Pd bulk contribution. The valence band spectra of the annealed films and of the polycrystal agree well and are resembling a “Cu-like” DOS expected for catalytic properties. However, the calculated DOS of the InPd compound shows significant difference with that of bulk Cu in the energy range of 1.5 eV to E_F , because of significant d states contribution in the intermetallic phase. This is similar to the cases of ZnPd and GaPd compounds.^{33,34}

IV. DISCUSSION AND CONCLUSIONS

The experimental results indicate that surface alloying takes place at room temperature upon In dosing on the Pd(111) surface. This agrees with the theoretical prediction of a negative mixing enthalpy for the $\text{In}_x\text{Pd}_{1-x}$ solid solution in the dilute In limit reported in Ref. 25. In the low coverage regime ($\theta \leq 2$ MLE), the LEED patterns are consistent with the formation of three rotational domains of InPd(110) on top of the Pd(111) substrate. However, the structural quality of the surface alloy is rather low at this stage as evidenced by the diffuse diffraction spots. In addition, both the core-levels and valence band XPS spectra show that the surface alloy does not fully exhibit the electronic structure characteristic of the stoichiometric phase under these conditions. Annealing the 1 MLE thin film up to 690 K yields a well ordered ($\sqrt{3} \times \sqrt{3}$) R30° superstructure with hexagonal unit cell dimension of 4.75 Å and an estimated surface alloy composition of $\text{In}_{41}\text{Pd}_{59}$. This observation is consistent with previous reports on a related system, Sn on Pd(111), for which a similar ($\sqrt{3} \times \sqrt{3}$) R30° phase was identified after annealing and ascribed to the formation of a Pd₂Sn monolayer surface alloy with fcc structure.^{31,35,36} Calculations of segregation energies indicate that an In-doped layer buried in a Pd(111) substrate is preferentially located at the surface, therefore we expect this surface alloy to be confined in the outermost plane at this stage.²⁵ When the film is further annealed above 690 K, the In content in the near-surface region decreases and a (1 × 1) pattern is recovered in our case.

The ($\sqrt{3} \times \sqrt{3}$) R30° superstructure is not observed for thicker films. Successive annealing of the 2 MLE thin film leads to the progressive disappearance of the InPd diffraction spots till a sharp (1 × 1) pattern is recovered above 690 K.

In the high coverage regime (from 4 to 35 MLE), LEED, STM, and XPS results indicate the formation of three rotational domains of a In_xPd_3 compound with (110) orientation. This In-rich phase grows either directly on top of the Pd(111) substrate or on top of InPd(110) domains formed as an

interfacial layer in the early stage of the growth. The near-surface layer is found to be stable upon annealing up to about 500 K and transforms into pure InPd(110) domains in a temperature range comprised between 500 and 600 K depending on the initial coverage. At this stage, the surface alloy exhibits core-level chemical shifts and VB spectra identical to those of the stoichiometric InPd intermetallic compound. In particular, a “Cu-like” DOS is observed. Annealing at higher temperatures leads to a decrease of the In concentration in the near-surface region suggesting that the surface alloy is not stable in this temperature range. A (1×1) LEED pattern is recovered at 690 K, together with a Pd-like DOS.

Our results are consistent with the conclusions of a previous XPS study on In-doped Pd foil performed by Rameshan *et al.*²⁴ In this work, a 4 MLE In thin film was deposited on a polycrystalline Pd substrate and the chemical composition of the NSIP as well as chemical shifts and VB were monitored as a function of the annealing temperature using synchrotron radiation based XPS. A high degree of alloying was also reported at room temperature. Upon successive annealing, the Pd 3d peaks gradually shifted towards lower binding energies associated with a decrease of the In content in the near-surface region and correlated with a transition from a “Cu-like” DOS to a more “Pd-like” (i.e., a shift of the d band center towards E_F). By varying the photon source energy (and hence the probing depth), a concentration gradient was highlighted from an In-rich next to the surface to a more In-depleted alloy in deeper layers. The concentration gradient was found to be more pronounced after low temperature annealing, from $\text{In}_{63}\text{Pd}_{37}$ at 0.4 nm inelastic mean-free path (IMFP) to $\text{In}_{51}\text{Pd}_{49}$ at 1 nm at 363 K annealing. These concentration values support our hypothesis that a In_7Pd_3 phase is formed on top of a 1:1 InPd interface layer. Annealing to 453 K yielded to a 1:1 In/Pd ratio in the near-surface region exhibiting a “Cu-like” DOS and In depth distribution similar to the MSR-selective multilayer ZnPd counterpart.¹⁶ The 4 MLE In thin film annealed at 453 K was therefore used as a model surface to study the catalytic properties of the InPd system. In these experiments, the temperature was measured with a thermocouple directly attached to the sample, thus providing more reliable temperature values than those reported in the present work. Using the gradual shift of the Pd 3d peaks upon annealing as an internal temperature calibration, we determined that the 453 K-annealed state in Ref. 24 corresponds to our 500 to 550 K annealed state. In Rameshan *et al.*,²⁴ the structure of the 1:1 InPd NSIP was considered as that of a substitutional alloy with progressive replacement of Pd atoms by In within the Pd-*fcc* lattice with no relationship with bulk intermetallic phases of the In-Pd system. Our STM and LEED results show that the structure of the surface alloys formed on the Pd(111) substrate under similar conditions actually corresponds to intermetallic phases rather than substitutional alloys, either cubic CsCl-type InPd or *bcc*- In_7Pd_3 depending on the conditions. This conclusion is also consistent with a previous analysis by x-ray diffraction of In/Pd multilayer stackings on SiO_2 demonstrating the formation of these two compounds induced by room temperature interdiffusion.³⁷ The near-surface intermetallic phases are not stable upon annealing at higher temperatures. The

In content decreases to reach a In/Pd ratio of about 20:80 and a (1×1) LEED pattern is recovered. This conclusion is again consistent with earlier reports indicating a similar In/Pd ratio throughout the near-surface region after annealing the 4 MLE thin film at 673 K.²⁴ Therefore the InPd surface alloys must be considered as metastable phases. This conclusion is consistent with the results of a theoretical study of InPd surface alloys using first-principles calculations demonstrating that In-doped Pd layers on Pd(111) are energetically more stable for In concentrations lower than 50 at.%.²⁵

The formation of metastable phases with a global 1:1 composition is common to the related Zn/Pd(111)^{10,16,18,27,38} and Ga/Pd(111)¹⁹ systems. However, the composition changes are more gradual in the cases of Ga/Pd(111) and In/Pd(111) compared to Zn/Pd(111) for which a more pronounced plateau in the surface composition was observed between 400 and 550 K. For Zn/Pd(111), the 1:1 plateau correlates with the formation of an ordered (2×2) surface structure corresponding to 3 rotational domains of ZnPd(111)- (2×1) ^{27,39} whereas for Ga/Pd(111) the surface alloy is disordered in the same temperature range.¹⁹ The onset temperatures for alloy formation were found to be different for Ga and Zn on Pd(111) (200 K for the former versus 300 K for the latter). This was interpreted as a consequence of the larger thermodynamic driving force for Ga-Pd compound formation compared to Zn-Pd based on the calculated cohesive energies. The onset alloying temperature was not determined in the present study but is lower or equal to 300 K. This is consistent with the cohesive energy calculated for the InPd compound (-3.57 eV/atom)²⁵ which is intermediate between that of PdGa (-3.9 eV/atom)^{19,40} and ZnPd (-3.0 eV/atom).⁴¹ Concerning the orientation of the surface alloys, we found that the cubic 1:1 InPd NSIP adopts a (110) orientation with respect to the Pd(111) substrate whereas the 1:1 tetragonal ZnPd NSIP adopts a (111) orientation. In both cases, it corresponds to stoichiometric layers consisting of alternating atomic rows of Pd and In (or Zn) metals. Only one type of atomic rows is observed in corresponding STM images. For Zn/Pd(111), this feature can be ascribed to an outward shift of the Zn atoms and an inward shift of the Pd atoms (into the bulk) with respect to the bulk-terminated geometry as demonstrated by DFT calculations.^{39,41} This is consistent with the lower elemental surface energy of Zn compared to Pd. A similar effect is expected to occur on the InPd surface alloy, as the elemental surface energy of In is also much lower than that of Pd. Such type of surface relaxation can have a significant effect on the surface reactivity and is investigated theoretically in the part II of this article (Ref. 25).

ACKNOWLEDGMENTS

This work was supported by the ANR CAPRICE 2011-INTB 1001-01, the European C-MAC consortium and COST Action CM0904 “Intermetallic compounds as catalyst for steam reforming of methanol (IMC-SRM).”

¹D. R. Palo, R. A. Dagle, and J. D. Holladay, *Chem. Rev.* **107**, 3992 (2007).

²N. Iwasa, S. Masuda, N. Ogawa, and N. Takezawa, *Appl. Catal. A* **125**, 145 (1995).

084702-10 McGuirk *et al.*J. Chem. Phys. **141**, 084702 (2014)

- ³N. Iwasa and N. Takezawa, *Top. Catal.* **22**, 215 (2003).
- ⁴H. Gabasch, A. Knop-Gericke, R. Schlögl, S. Penner, B. Jenewein, K. Hayek, and B. Klötzer, *J. Phys. Chem. B* **110**, 11391 (2006).
- ⁵S. Liu, K. Takahashi, and M. Ayabe, *Catal. Today* **87**, 247 (2003).
- ⁶S. Liu, K. Takahashi, K. Uematsu, and M. Ayabe, *Appl. Catal. A* **277**, 265 (2004).
- ⁷D. L. Trimm and Z. I. Önsan, *Catal. Rev.* **43**, 31 (2001).
- ⁸N. Takezawa and N. Iwasa, *Catal. Today* **36**, 45 (1997).
- ⁹H. Lorenz, S. Turner, O. I. Lebedev, G. V. Tendeloo, B. Klötzer, C. Rameshan, K. Pfaller, and S. Penner, *Appl. Catal. A* **374**, 180 (2010).
- ¹⁰A. Bayer, K. Flechtner, R. Denecke, H. Steinruck, K. Neyman, and N. Rosch, *Surf. Sci.* **600**, 78 (2006).
- ¹¹K. Nozawa, N. Endo, S. Kameoka, A. P. Tsai, and Y. Ishii, *J. Phys. Soc. Jpn.* **80**, 064801 (2011).
- ¹²M. Friedrich, D. Teschner, A. Knop-Gericke, and M. Armbrüster, *J. Catal.* **285**, 41 (2012).
- ¹³M. Friedrich, S. Penner, M. Heggen, and M. Armbrüster, *Angew. Chem. Int. Ed.* **52**, 4389 (2013).
- ¹⁴M. Armbrüster, M. Behrens, K. Fttinger, M. Friedrich, É. Gaudry, S. K. Matam, and H. R. Sharma, *Catal. Rev. Sci. Eng.* **55**, 289 (2013).
- ¹⁵S. Penner, B. Jenewein, H. Gabasch, B. Klötzer, D. Wang, A. Knop-Gericke, R. Schlögl, and K. Hayek, *J. Catal.* **241**, 14 (2006).
- ¹⁶C. Rameshan, C. Weilach, W. Stadlmayr, S. Penner, H. Lorenz, M. Havecker, R. Blume, T. Rocha, D. Teschner, A. Knop-Gericke, R. Schlögl, D. Zemlyanov, N. Memmel, G. Rupprechter, and B. Klötzer, *J. Catal.* **276**, 101 (2010).
- ¹⁷C. Rameshan, W. Stadlmayr, C. Weilach, S. Penner, H. Lorenz, M. Hävecker, R. Blume, T. Rocha, D. Teschner, A. Knop-Gericke, R. Schlögl, N. Memmel, D. Zemlyanov, G. Rupprechter, and B. Klötzer, *Angew. Chem. Int. Ed.* **49**, 3224 (2010).
- ¹⁸W. Stadlmayr, C. Rameshan, C. Weilach, H. Lorenz, M. Haevecker, R. Blume, T. Rocha, D. Teschner, A. Knop-Gericke, D. Zemlyanov, S. Penner, R. Schlögl, G. Rupprechter, B. Klötzer, and N. Memmel, *J. Phys. Chem. C* **114**, 10850 (2010).
- ¹⁹W. Stadlmayr, V. Huber, S. Penner, B. Klötzer, and N. Memmel, *J. Phys. Chem. C* **117**, 19558 (2013).
- ²⁰N. Iwasa, T. Mayanagi, N. Ogawa, K. Sakata, and N. Takezawa, *Catal. Lett.* **54**, 119 (1998).
- ²¹R. Fink, B. U. Runge, K. Jacobs, G. Krausch, B. Luckscheiter, R. Platzer, U. Wöhrmann, and G. Schatz, *Hyperfine Interact.* **78**, 309 (1993).
- ²²R. Fink, T. Koch, G. Krausch, J. Marien, A. Plewnia, B.-U. Runge, G. Schatz, A. Siber, and P. Ziemann, *Phys. Rev. B* **47**, 10048 (1993).
- ²³R. Fink, B. U. Runge, K. Jacobs, G. Krausch, J. Lohmüller, B. Luckscheiter, U. Wöhrmann, and G. Schatz, *J. Phys. Condens. Matter* **5**, 3837 (1993).
- ²⁴C. Rameshan, H. Lorenz, L. Mayr, S. Penner, D. Zemlyanov, R. Arrigo, M. Haevecker, R. Blume, A. Knop-Gericke, R. Schlögl, and B. Klötzer, *J. Catal.* **295**, 186 (2012).
- ²⁵É. Gaudry, G. M. McGuirk, J. Ledieu, and V. Fournée, *J. Chem. Phys.* **141**, 084703 (2014).
- ²⁶H. Okamoto, *J. Phase Equilib.* **24**, 481 (2003).
- ²⁷G. Weirum, M. Kratzer, H. P. Koch, A. Tamtoegl, J. Killmann, I. Bako, A. Winkler, S. Surnev, F. P. Netzer, and R. Schennach, *J. Phys. Chem. C* **113**, 9788 (2009).
- ²⁸G. D. Mahan, *Phys. Rev.* **163**, 612 (1967).
- ²⁹G. K. Wertheim and P. H. Citrin, *Photoemission in Solids I* (Springer-Verlag, 1978).
- ³⁰F. U. Hillebrecht, J. C. Fuggle, P. A. Bennett, and Z. Zonierek, *Phys. Rev. B* **27**, 2179 (1983).
- ³¹A. Pancotti, A. de Siervo, M. Carazzolle, R. Landers, and G. Kleiman, *J. Electron Spectrosc. Relat. Phenom.* **156-158**, 307 (2007).
- ³²H. Flandorfer, *J. Alloys Compd.* **336**, 176 (2002).
- ³³S. A. Villaseca, D. Kandaskolov, É. Gaudry, and M. Armbrüster, *Z. Anorg. Allg. Chem.* **640**, 753 (2014).
- ³⁴K. Kovnir, M. Armbrüster, D. Teschner, T. Venkov, F. Jentoft, A. Knop-Gericke, Y. Grin, and R. Schlögl, *Sci. Technol. Adv. Mater.* **8**, 420 (2007).
- ³⁵A. F. Lee, C. J. Baddeley, M. S. Tikhov, and R. M. Lambert, *Surf. Sci.* **373**, 195 (1997).
- ³⁶M. Carazzolle, G. Kleiman, R. Landers, A. Pancotti, A. de Siervo, and E. Soares, *J. Mol. Catal. A: Chem.* **281**, 9 (2008).
- ³⁷A. Wronkowska, A. Wronkowski, A. Bukaluk, M. Trzeciński, and K. Okulewicz, *Appl. Surf. Sci.* **253**, 3367 (2007).
- ³⁸W. Stadlmayr, S. Penner, B. Klötzer, and N. Memmel, *Surf. Sci.* **603**, 251 (2009).
- ³⁹H. Koch, I. Bako, and R. Schennach, *Surf. Sci.* **604**, 596 (2010).
- ⁴⁰J. Prinz, R. Gaspari, C. A. Pignedoli, J. Vogt, P. Gille, M. Armbrüster, H. Brune, O. Gröning, and R. Widmer, *Angew. Chem., Int. Ed.* **51**, 9339 (2012).
- ⁴¹Z.-X. Chen, K. Neyman, A. Gordienko, and N. Rösch, *Phys. Rev. B* **68**, 075417 (2003).

3.3 Part II: Theoretical study of surface energies, alloying and segregation effects (Article)



Surface structures of In-Pd intermetallic compounds. II. A theoretical study

É. Gaudry, G. M. McGuirk, J. Ledieu, and V. Fournée

Institut Jean Lamour, Université de Lorraine CNRS UMR 7198, Parc de Saurupt, 54011 Nancy Cedex, France

(Received 2 May 2014; accepted 24 July 2014; published online 25 August 2014)

The (110) surface of the InPd intermetallic compound and the In-Pd surface alloy properties are investigated in the framework of the density functional theory, within the projector augmented plane-wave method. Surface segregation is calculated to be energetically unfavorable at stoichiometric InPd(110) surfaces, while indium antisites are shown to segregate to the surface in off-stoichiometric InPd(110) systems. Concerning surface alloys obtained by burying In-doped Pd layers in Pd(111), we demonstrated that the most stable ones are those presenting atomic indium concentrations below 50 at. % (11 at. %, 25 at. %, 33 at. %). According to our calculations, the In-doped Pd layers with concentration above or equal to 50% lead to In-doped Pd multilayers, each presenting an atomic indium concentration below 50 at. %. Alloying and segregation effects in InPd intermetallic compound and In-Pd surface alloys clearly agree with the larger bonding strength of In-Pd (-0.44 eV) compared to In-In (-0.29 eV) and Pd-Pd (-0.31 eV). © 2014 AIP Publishing LLC. [<http://dx.doi.org/10.1063/1.4892409>]

I. INTRODUCTION

In a context where fossil fuels are becoming increasingly costly, the development of new clean sources of energy is awaited. A few years ago, Olah suggested to use methanol to store energy and to produce convenient hydrocarbon-based fuels and products.^{1,2} Among other advantages, methanol possesses high potential as hydrogen carrier³⁻⁵ and methanol steam reforming (MSR) is a promising reaction to release hydrogen. Indeed, it represents the chemical reaction with the highest hydrogen concentration in the gas products ($\text{CH}_3\text{OH} + \text{H}_2\text{O} \rightarrow 3\text{H}_2 + \text{CO}_2$). Selectivity in this reaction is crucial: the complete methanol decomposition ($\text{CH}_3\text{OH} \rightarrow 2\text{H}_2 + \text{CO}$) produces CO, which is poisonous, at concentrations above 20 ppm, to the Pt-electrode in the proton exchange membrane fuel cells.^{6,7} Hence, the choice of the catalyst is of great importance to reach a high conversion rate and selectivity, while still preserving a long-term stability. Copper-based catalysts are the most commonly used materials. However, these types of catalysts are pyrophoric and deactivated by thermal sintering. Pd and Pt catalysts, usually supported on oxide supports like ZnO or In_2O_3 , also present high performances towards MSR. The intermetallic compounds (ZnPd, ZnPt, or InPd) formed during the reaction by partial reduction of the supporting oxide, are frequently observed, and are supposed to play a role in the reactivity.⁸⁻¹³ In particular, their electronic structures exhibit a valence electron density of state similar to pure Cu.^{13,14}

The rational design and optimization of active and selective MSR catalysts require the understanding of the reaction mechanism at an atomic scale on model systems. The knowledge of the surface structure is a prerequisite for such studies. Experimentally, surface investigations under ultra-high vacuum are usually realized using single crystals. When sizable single crystals are not available, it is also possible to use surface alloys for surface science studies, by evaporating metals in vacuum onto metal surfaces. In the latter case, intermix-

ing at the atomic scale may occur during deposition, or can be induced by successive thermal treatments.¹⁵ In the case of Zn-Pd surface alloys, the deposition of Zn on a Pd(111) surface leads experimentally to various structures, depending on the Zn coverage.^{16,17} A $p(2 \times 1)$ surface structure has been identified for a Zn coverage between 0.8 ML and 1.5 ML, by an approach combining both experimental and theoretical results.¹⁷ Calculations based on Monte Carlo simulations highlight the dependence of the surface structure on the Zn coverage. For one or more layer of Zn deposited on Pd(111), a multilayer 1:1 Zn-Pd surface alloy is formed, while surface alloy islands dominated by Pd are shown to be formed at submonolayer Zn coverage.¹⁸ The resulting structure of surface alloys highly depends on preparation conditions. Indeed, in such systems, the balance between the alloying effect and the surface segregation dictates the surface structure. Theoretical calculations are essential to analyze in details the experimental observations and to understand the segregation trends in a system.¹⁹⁻²¹ Multiscale segregation simulations can also provide a prediction of the temperature-dependent alloy composition at the surface.²²

The present paper aims to bring a deeper understanding of the experimental results obtained for the In/Pd(111) system reported in Ref. 23. It is also the basis for a theoretical analysis of the InPd(110) surface and of indium segregation in Pd(111). The paper is organized as follows. We first provide computational details in Sec. II. The results are presented in Sec. III for bulk systems (Pd, In, InPd, and In_7Pd_3), for the InPd(110) surface and for In-Pd surface alloys. The results are discussed in terms of bonding strengths and in the light of an experimental study of In/Pd(111)²³ (Sec. IV) before we conclude.

II. METHOD

Calculations are performed using the Vienna *ab initio* Simulation Package (VASP) based on the Density

084703-2 Gaudry *et al.*J. Chem. Phys. **141**, 084703 (2014)

Functional Theory (DFT).^{24,25} The interaction between the valence electrons and the ionic core is described using the projector-augmented wave (PAW) method.^{26,27} The electronic exchange and correlation contribution is described using the generalized gradient approximation GGA-PBE.^{28,29} Geometries are optimized by the calculation of the Hellmann-Feynman forces acting on atoms and their minimization via a conjugate gradient algorithm (forces on moving atoms are less than 0.02 eV/Å). The parameters linked to the numerical implementation of the DFT, i.e., the plane-wave cutoff E_{cut} and the density of k -points sampling the Brillouin zone, were converged by means of a series of test calculations to ensure the same energy precision in all calculations (less than 1 meV), leading to the following values: E_{cut} (450 eV) and $\sigma = 0.2$ eV. The k -points grid was set to $23 \times 23 \times 23$ for bulk InPd (2 at./cell), as well as for bulk Pd and bulk In. For other geometries, the k -points grid was set to reach the same precision. Surfaces are modeled by slabs separated by a 15 Å void thickness.

The surface energy of the InPd(110) surface is calculated in Sec. III B 1. A common method for calculating surface energies γ for simple metal surfaces is based on the difference between the total energy $E_{surf}(Nlayers)$ of a symmetric N -layer thick slab (1 atom per layer) and the one of the corresponding bulk (E_{bulk} , expressed in eV/at.)

$$\gamma = \frac{E_{surf}(Nlayers) - NE_{bulk}}{2A}, \quad (1)$$

where A is the surface area of the unit cell. The factor $\frac{1}{2}$ accounts for the two surfaces of the slab model. This equation is still valid for a stoichiometric surface, where the slab model is built by a stacking of planes with a chemical composition identical to the bulk composition. Usually, the computation of the total energy of a series of slabs of different thickness is used to extract the surface energy from Eq. (1), to prevent surface energies divergence as a function of the slab thickness.^{30,31} More recently, Da Silva *et al.*³² have shown that the surface energy, computed from Eq. (1) with slab and total energies obtained from separate DFT calculations, converges as a function of the number of layers in the slab, providing that both calculations are carried out with the same high accuracy.

III. RESULTS

A. Bulk structures and cohesive energies

The bulk cell parameters and cohesive energies of Pd, In, InPd, and In₇Pd₃ are summarized in Table I. Our PAW calculations are in overall agreement with experimental data. Our calculated equilibrium lattice parameters of *bcc* indium and *fcc* palladium are 1%-2% larger than those deduced from experiments, while the one calculated within the local density approximation scheme are found to be 1%-2% smaller.³³ This is in agreement with the usual LDA over-binding and GGA over-corrections. Concerning bulk Pd, our PAW-PBE calculations are also in agreement with previously published all electron calculations,³² justifying the use of time-saving pseudopotentials rather than all electron potentials.

TABLE I. Bulk lattice parameters and cohesive energies E_c of Pd, In, InPd, and In₇Pd₃.

	Latt. param. (Å)		E_c (eV/at.)	
	Exp.	Calc.	Exp.	Calc.
Pd	3.884 ³⁴	3.94 3.85 (LDA) ^{32,33} 3.95 (PBE) ^{32,36}	-3.94 ³⁵	-3.77 -5.04 (LDA) ³² -3.68 (PBE) ³⁶ -3.65 (PBE) ³²
In	$a = 3.256$ ³⁷ $c = 4.940$ ³⁷	$a = 3.31$ $c = 5.03$ $a = 3.18$ (LDA) ³³ $c = 4.89$ (LDA) ³³	-2.52 ³⁵	-2.35
InPd	3.25 ³⁸	3.30	...	-3.57
In ₇ Pd ₃	9.4359 ³⁷	9.59	...	-3.18

In this paper, the surface energy of InPd(110) is evaluated, along with segregation energies for the In/Pd(111) system. This requires the determination, as a first step, of the In_xPd_{1-x} mixing enthalpy and the dilute impurity enthalpy. The calculation of these quantities are detailed in the following.

The mixing enthalpy per atom, ΔH_m , for the In_xPd_{1-x} solid solution is defined by

$$\Delta H_m = E_c(\text{In}_x\text{Pd}_{1-x}) - (1-x)E_c(\text{Pd}) - xE_c(\text{In}), \quad (2)$$

where $E_c(\text{In}_x\text{Pd}_{1-x})$ is the cohesive energy per atom of the solid solution, $E_c(\text{Pd})$ and $E_c(\text{In})$ are the cohesive energies per atom of the pure Pd and In phases. For the stoichiometric InPd and In₇Pd₃ compounds ($x = 0.5$ and $x = 0.7$, respectively), the mixing enthalpy is also known as the formation enthalpy ΔH_f . We found $\Delta H_f(\text{InPd}) = -0.51$ eV/at. and $\Delta H_f(\text{In}_7\text{Pd}_3) = -0.40$ eV/at., to be compared to the experimental values $\Delta H_f(\text{InPd}) = -0.65$ eV/at.³⁹ and $\Delta H_f(\text{In}_7\text{Pd}_3) = -0.45$ eV/at.⁴⁰ measured at $\simeq 300$ K. The mixing enthalpy ΔH_m was also calculated in the dilute In limit, by considering a $3 \times 3 \times 3$ *fcc*-Pd supercell, containing $N = 108$ atoms, where one Pd atom was substituted by one In atom

$$N\Delta H_m(x = \frac{1}{N}) = E[(N-1)\text{Pd}, \text{In}] - \frac{N-1}{N}E[N\text{Pd}] - \frac{1}{N}E[N\text{In}]. \quad (3)$$

We find $\Delta H_m(0.92\%) = -18$ meV/at. Negative mixing enthalpies at $T = 0$ K, as presently obtained in the dilute limit, means that the alloy will form a solid solution in the absence of any competing ordered phase. We also checked the stability of the In_xPd_{1-x} alloy, with $x = 0.92\%$, against a demixion in pure Pd and the ordered InPd₂ phase by evaluating the energy difference $E[(N-1)\text{Pd}, \text{In}] - E[\text{InPd}_2] - (N-3)E[\text{Pd}]$ (-3 meV/at.). The stability against the demixion in pure Pd and InPd₃ has not been evaluated, since this compound contains some disorder.⁴¹

The mixing enthalpy can then be expressed as a function of the dilute impurity enthalpy per In atom ΔH_{imp}

$$\Delta H_m(x) = x\Delta H_{imp}, \quad (4)$$

084703-3 Gaudry *et al.*J. Chem. Phys. **141**, 084703 (2014)

where the dilute impurity enthalpy per In atom is defined by

$$\begin{aligned}\Delta H_{imp} &= \lim_{x \rightarrow 0} \left(\frac{1}{x} \Delta H_m(x) \right) \\ &= \mu_{In}(x \rightarrow 0) - \mu_{In}(x \rightarrow 1) \\ &= \mu_{In}(x \rightarrow 0) - E_c(In).\end{aligned}\quad (5)$$

In the previous equation, $\mu_{In}(x)$ is the chemical potential or partial enthalpy per atom of In in the In-Pd alloy at concentration x . We found $\Delta H_{imp} = -1.91$ eV/at. and $\mu_{In}(x \rightarrow 0) = -4.26$ eV.

B. InPd(110) surface

1. Surface energy

The surface energy of the non-relaxed (110) surface has been evaluated by a linear regression on the total energy of different slabs built with an increased number of planes. For a symmetric slab built with n atomic layers, the non-relaxed surface energy $\gamma_{(110)}^{non-relax}$ is given by

$$E_n^{tot} = 2\gamma_{(110)}^{non-relax} A_{(110)} + 2nE_c^{InPd}, \quad (6)$$

where E_n^{tot} is the total energy of the slab, $A_{(110)}$ is the area of the surface unit cell (15.40 \AA^2), and E_c^{InPd} is the cohesive energy of InPd. The surface energy of the unrelaxed system has been derived from fitting E_n^{tot} in various ranges, $n = 8 - 12$, $n = 9 - 12$, $n = 10 - 12$, leading to $\gamma_{(110)}^{non-relax} = 0.82 \text{ J/m}^2$ within $\simeq 10 \text{ mJ/m}^2$. The fitting procedure also leads to $E_c^{InPd} = -3.57 \text{ eV/at.}$, whatever is the range chosen for n , in good agreement with the value deduced from a direct calculation (Table I, $E_c^{InPd} = -3.57 \text{ eV/at.}$).

The same procedure can be applied with an asymmetric slab (5 fixed planes and $n - 5$ planes allowed to relax). A similar equation as above was used to determine the surface energy

$$E_n^{tot} = \gamma_{(110)}^{non-relax} A_{(110)} + \gamma_{(110)}^{relax} A_{(110)} + 2nE_c^{InPd}, \quad (7)$$

where $\gamma_{(110)}^{relax}$ is the relaxed surface energy. The fitting procedure ($n = 8 - 12$) gives $\gamma_{(110)}^{relax} = 0.72 \text{ J/m}^2$ and we check that the value found for E_c^{InPd} (-3.57 eV) is again in good agreement with the previous values. The relaxation energy of the surface is then evaluated to be equal to 0.10 J/m^2 (more than 10%), which is quite high compared to simple metals. In this latter case, the variation of the surface energy due to relaxation is typically of the order of 2%-5%.⁴²⁻⁴⁴ Here, the relaxation energy of the InPd(110) surface is related to atomic relaxations (see Sec. III B 2).

2. Atomic relaxations

The relative interlayer relaxations $\Delta_{\ell, \ell-1}$, defined by

$$\Delta_{\ell, \ell-1} = \frac{(d_{\ell, \ell-1} - d_{bulk})}{d_{bulk}}, \quad (8)$$

where $d_{\ell, \ell-1}$ is the interlayer spacing between layers ℓ and $\ell - 1$ are small: $\Delta_{S, S-1} = 0.02$ at the surface and decreases rapidly for subsurface layers. The corrugation χ^ℓ of

the atomic plane ℓ , defined by

$$\chi^\ell = z^\ell(\text{In}) - z^\ell(\text{Pd}) \quad (9)$$

is non-negligible for the first two layers: $\chi^S = 0.26 \text{ \AA}$, $\chi^{S-1} = 0.12 \text{ \AA}$, while $\chi^\ell < 0.02 \text{ \AA}$ for $\ell = S - 3, S - 4$, etc. The Pd atom moves slightly inward, with respect to its position in the unrelaxed slab while the In atom moves slightly outward. This result can be rationalized by the smaller surface energy of In compared to Pd: $\gamma_{Pd(111)}^{fcc} = 2.05 \text{ J/m}^2$ and $\gamma_{In(001)}^{bcc} = 0.675 \text{ J/m}^2$.⁴⁵ This behavior is very similar to what occurs on the stoichiometric ZnPd surface.¹⁴

3. Electronic structure

We discuss here the electronic structure of the InPd(110) surface. Indeed, the valence d states of this surface are of particular importance for the surface reactivity, which is the ultimate target of the present investigation of alloy catalyst.

The electronic structure of bulk InPd is represented in Fig. 1 (bottom), highlighting the similarity in the valence electron DOS for InPd and pure Cu, except near the Fermi energy ($[E_F - 1.5 \text{ V}; E_F]$). The electronic structure of the InPd(110) surface is also represented in Fig. 1. The surface

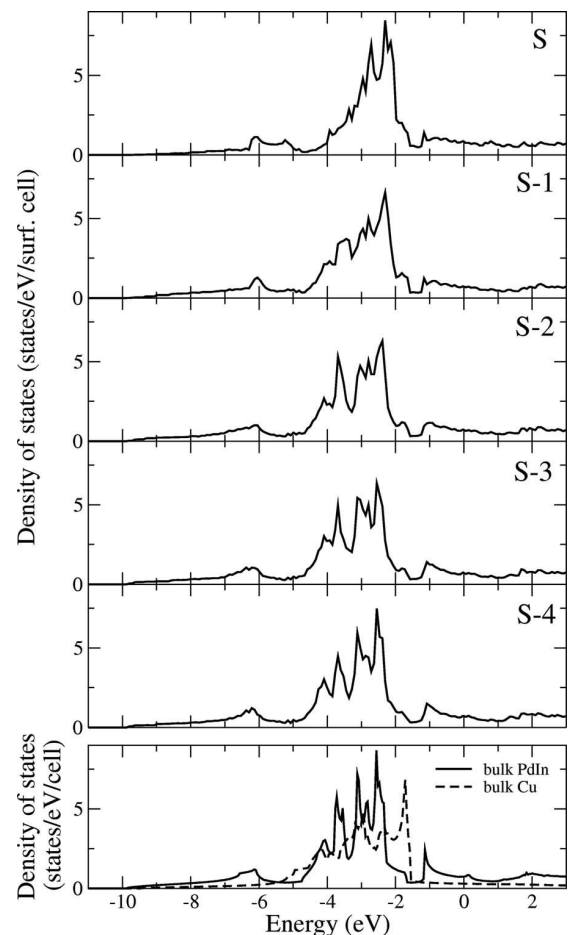


FIG. 1. Electronic structure of the InPd(110) surface, showing the contributions of the different atomic layers. The electronic structure of bulk Cu and InPd are given for comparison.

084703-4 Gaudry *et al.*J. Chem. Phys. **141**, 084703 (2014)

contribution of the d -band is narrower and shifted ($\simeq 0.45$ eV) towards the Fermi energy compared to the bulk one. The same occurs in the subsurface layer, to a lesser extent. Within the Friedel's model, where the density of states of the d -band is modeled by a rectangular shape, these results can be rationalized as follows. Since the width of the band depends on the hybridization of neighboring atomic orbitals (the higher the coordination, the more overlap and the broader the band is), and since the whole material has a single Fermi energy, the reduced coordination of the surface atoms leads to a narrowing and a shift of the valence d -band (the shift aims to avoid an unrealistic lack or excess on electronic charge on the surface atoms).⁴⁶

4. Indium surface segregation in InPd

In Secs. III B 1–III B 3, we considered a perfect bulk terminated InPd(110). In simple alloys, it is well known that surface segregation often occurs. Here, we give first results concerning segregation at InPd(110) surface.

Indium segregation at the InPd(110) surface is evaluated by comparing the relative formation energies for a bilayer of pure In or In-doped Pd deposited on the InPd(110). The relative formation energy $\Delta E_f(c_S, c_{S-1})$ of a surface bilayer with In concentration (c_S, c_{S-1}) in the surface and subsurface layers, respectively, is defined by

$$\Delta E_f(c_S, c_{S-1}) = E_{slab}(c_S, c_{S-1}) - E_{slab}(50\%, 50\%), \quad (10)$$

where $E_{slab}(c_S, c_{S-1})$ is the total energy of a slab with a surface bilayer of composition (c_S, c_{S-1}). We found $\Delta E_f(100\%, 0\%) = 0.78$ eV and $\Delta E_f(75\%, 25\%) = 0.37$ eV. The positive value for ΔE_f indicates that indium segregation is not energetically favorable, due to the quite large energy required to break In-Pd bonds.

In the previous paragraph, we considered a perfect InPd intermetallic compound. According to the phase diagram, the existence of cubic InPd ranges from 45 at. % Pd to 61.5 at. % Pd. The constitutional point defects are identified to be Pd vacancies (In-rich alloys) and Pd antisites (Pd-rich alloys) by first principles calculations.³³ The presence of such defects can modify strongly the In segregation pattern.^{47–49} To investigate the influence of the composition on surface segregation, we have compared the total energies of slabs containing one point defect either in surface or in “bulklike” layer (position $S - 4$). The surface cell dimensions are $4.67 \times 6.60 \text{ \AA}^2$ (1×2) and the shortest distance between two points defects due to periodic conditions is 4.67 \AA . This distance might be a little too short to avoid any interactions between defects. However, these possible interactions exist both for defects in the surface and “bulklike” atomic layers. We then expect that these interactions are negligible when calculating relative energies. Results gathered in Table II highlight a large negative value for In antisites, and positive values for other defects. According to these results, In antisites are expected to segregate to the InPd(110) surface, while other defects are supposed to stay in the bulk. In the case of Pd antisites, this can be understood with the relatively high surface energy of Pd(111) ($\gamma_{Pd(111)}^{fcc} = 2.05 \text{ J/m}^2$).⁴⁵ Concerning vacancies, the calculated stabilization energies are small ($\delta E \simeq 0.1$ eV). The present

TABLE II. Energy difference $\Delta E = E_{surf}(x) - E_{bulklike}(x)$ between the surface and bulklike defects in off-stoichiometric InPd intermetallic compounds.

	Pd-rich		In-rich	
	Pd antisite	In vacancy	Pd vacancy	In antisite
Comp. (Pd at. %)	52.1	51.1	48.9	47.9
ΔE (eV)	0.74	0.09	0.14	-1.35

calculations cannot exclude in this case a contribution from interaction between vacancies.

C. Indium surface segregation in Pd(111)

The segregation of indium at the (111) surface of Pd was studied systematically by burying a layer with different indium concentrations into a Pd(111) crystal. The considered asymmetric slabs consist of 13 layers: 12 pure Pd layers (6 fixed at the bottom and 6 allowed to relax) and one layer containing In, allowed to relax. The Pd(111) slab is thick enough to bury the In-doped Pd layer in the first five surface planes. The layer by layer surface segregation study evaluates the total energy of a slab, built by substituting an increasing number of Pd atoms in a given Pd layer ℓ . The In concentration in layer ℓ has been varied from the almost dilute limit (1/9) up to a complete In monolayer. The segregation energy per In atom, with In layer concentration c in surface layer ℓ , is defined as the energy gained, by indium atom when a concentration c of In atoms are transferred from a bulk layer to that of the surface layer⁴⁴

$$E_{seg}(c, \ell) = \frac{E_{slab}(c, \ell, x) - \lim_{\ell' \rightarrow \infty} E_{slab}(c, \ell', x)}{c}, \quad (11)$$

where $E_{slab}(c, \ell, x)$ is the energy of a semi-infinite $\text{Pd}_{1-x}\text{In}_x$ alloy with an indium concentration c in layer ℓ . When ℓ tends to infinity, $E_{seg}(c, \ell)$ tends to zero.

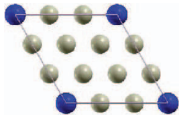
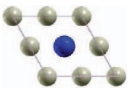
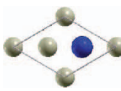
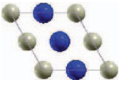
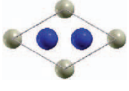
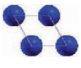
In this paper, we considered only ordered phases, for which the mixing entropy is small.⁵⁰ We should emphasize here that the number of configurations investigated is obviously limited by the size of the unit cell, so that only highly ordered structures can be simulated. Other structures besides those explicitly considered here could have lower energies, and disordered structures could play a role as well. These problems are typically dealt with, in alloy simulations, using a cluster expansion approach.⁵¹ This latter approach is beyond the scope of the present paper.

1. Single indium-doped layer buried in Pd(111)

In this section, we study the stability of a single In-doped Pd layer buried in Pd(111) with concentrations from 11% to 100% at. In. The considered systems correspond to different ordered alloys with a In-doped layer structure shown in Table III. For the three lower In concentrations (11%, 25%, 33%, first row of Table III), the In atoms of the In-doped Pd plane are surrounded only by Pd atoms, the distance between two nearest neighbors In atoms being equal to 3, 2, and $\sqrt{3}$

084703-5 Gaudry *et al.*J. Chem. Phys. **141**, 084703 (2014)

TABLE III. Structure of the planes containing In buried in Pd(111). Blue spheres (resp. gray spheres) represent In atoms (resp. Pd atoms). c is the concentration of the In-doped Pd plane. The nearest neighbors (NN) of In and Pd atoms, in the considered In-doped Pd plane, are detailed for each system, along with the ratio d_{ij}/d , where d_{ij} is the nearest neighbor distances In–In, In–Pd, and Pd–Pd and d is the calculated nearest neighbor distance in bulk Pd (2.79 Å).

			
c	11%	25%	33%
surf. cell	3×3	2×2	$\sqrt{3} \times \sqrt{3}$
In NN	6 Pd	6 Pd	6 Pd
Pd NN	5.25 Pd + 0.75 In	4 Pd + 2 In	3 Pd + 3 In
$d_{\text{In-In}}/d$	3	2	$\sqrt{3}$
$d_{\text{Pd-In}}/d$	1	1	1
$d_{\text{Pd-Pd}}/d$	1	1	1
			
c	50%	67%	100%
surf. cell	2×2	$\sqrt{3} \times \sqrt{3}$	1×1
In NN	4 Pd + 2 In	3 Pd + 3 In	6 In
Pd NN	2 Pd + 4 In	6 In	...
$d_{\text{In-In}}/d$	1	1	1
$d_{\text{Pd-In}}/d$	1	1	...
$d_{\text{Pd-Pd}}/d$	1	$\sqrt{3}$...

times the nearest neighbor distance in Pd ($d = 2.79$ Å). For higher In concentrations, interatomic In–In distances equal to d occurs. In the case of In-doped Pd layer with In concentration equal to 67%, Pd atoms are surrounded by 6 In atoms. Interestingly, in the case of In-doped Pd layer with In concentration equal to 50%, In atoms are located in the center of a rectangle, in a similar way compared to the (110) surface. However, the dimensions of these two rectangles are not exactly the same: $\sqrt{3}d \times d$ (4.83×2.79 Å²) for the In-doped Pd layer with In concentration equal to 50% and $\sqrt{2}a \times a$ (4.67×3.30 Å²), where a is the cell parameter of bulk InPd, for the InPd(110) surface.

The evolution of the segregation energy with the position ℓ clearly shows that the surface S layer, and to a lesser extent the subsurface $S - 1$ layer, is a highly favorable position with negative segregation energy. The segregation energies for positions $S - 2$ and $S - 3$ is almost zero, and can then be assimilated to the bulk one ($S - 4$) within the uncertainty of the calculation. The surface segregation energy is lower for the In-rich layers, i.e., 67% and 100% and higher for the In-poor layers, i.e., 11%, 25%, and 33% (Table IV). The 50% concentration represents an intermediate case.

TABLE IV. Surface segregation energies.

c	11%	25%	33%	50%	67%	100%
$E_{\text{seg}}(c, S)$ (eV)	−0.30	−0.28	−0.28	−0.23	−0.18	−0.16

The introduction of indium in the Pd(111) substrate leads to atomic relaxations. It is worth noticing that while the layer relaxation is very weak in the dilute In limit (less than 1%), it can reach relatively high values for systems with a plane containing 100% In atomic concentration. In this latter case, if the indium plane is located at the surface, the relative interlayer relaxation $\Delta_{S, S-1}$ is 3.7%. Again, when In is located at the surface, it lies slightly above the mean position of the plane ($\simeq 0.1$ Å in the dilute limit).

In the dilute limit, the surface segregation energy is usually decomposed into three independent contributions. The main contribution comes from the differences in surface energies, giving the nature of the segregating species in 95% of bimetallic systems.²¹ This contribution favors the segregation at the surface of the element with the lowest surface energy, which, in our case, is indium. The elastic energy contribution, proportional to the difference in elastic strain energy between the layer and the bulk, is due to the solute-solvent atomic size mismatch. In the dilute limit, within the elasticity theory, it always favors the segregation of the solute atoms at the surface, hence the surface segregation of indium in our case.^{21,44} The ordering contribution depends on the alloy composition.²¹ For a system presenting a tendency to bulk ordering, which is the case of InPd, the alloying term favors segregation of the majority element (Pd in this case). Given our results, this latter contribution is certainly small here.

2. Indium-doped Pd(111) multilayers

The previous stabilization energies are lower for the most highly In-doped Pd layers. Then, the question arises about the possibility for the In-doped Pd layer to transform into In-doped Pd multilayers. In the following, we evaluate this possibility as a function of both the concentration of the In-doped Pd layer and the thickness of the multilayers.

The influence of the concentration of the In-doped Pd plane on the previous process is evaluated by comparing the total energy of a surface or subsurface In-doped Pd single layer with the total energy of a surface In-doped Pd bilayer (each layer with the concentration $c/2$). It appears that the formation of a bilayer is favorable for all considered concentrations (100%, 67%, 50%), and even more favorable for a pure indium surface layer on Pd(111) (see Table V).

The next step aims to evaluate the thickness of the multilayer formed during the previous process. We calculated then the energy differences between the total energy of a n -layer thick In-doped Pd(111) system and a pure indium surface

TABLE V. Influence of surface or subsurface indium concentration (c) on the formation of a In-doped Pd surface bilayer. The table contains the energy differences (eV/In at.) between the total energy of a single layer and a bilayer: $E_{2\text{layers}}(c/2) - E_{1\text{layer}}(c, \ell)$. For a pure indium layer, the energy difference corresponds to a mean value.

Position of the single layer	Indium concentration (%)		
	50	67	100
S	−0.34	−0.65	−1.02
S−1	−0.43	−0.70	−1.11

084703-6 Gaudry *et al.*J. Chem. Phys. **141**, 084703 (2014)

TABLE VI. Influence of the thickness of the multilayer formed from the splitting of a pure indium surface layer on Pd(111). The table contains the energy differences (eV/In at.) between the total energy of a n -layer thick In-doped Pd(111) system and a pure indium surface layer on Pd(111).

Nb. of planes	1	2	3	4
ΔE (eV/In. at.)	0.00	-1.00	-1.49	-1.51

layer on Pd(111). The number of configurations of a n -layer thick In-doped Pd slab increases rapidly with n . In the case of bilayers, we considered the two possible configurations, leading to the conclusion that the energy difference between two configurations is smaller than 50 meV, i.e., well below the previous energy difference ($\simeq -1$ eV). In the following, only one configuration is considered for a given n ($n \in \{1; 4\}$). From Table VI, it appears that the transformation of a pure surface In layer into n -layer thick In-doped Pd layers is favorable, whatever is $n \in \{1; 4\}$. The transformation is especially favorable energetically when the In concentration in the multilayer reaches a value below 50% (25% or 33%). For these two concentrations (c equal to 25% or 33%), the corresponding formation energy of a single layer

$$E_f = E_{slab}(c) - E_{slab}(0) + E_c(Pd) - \mu_{In}(x \rightarrow 0), \quad (12)$$

where $E_{slab}(c)$ is the energy of the Pd(111) slab containing one In-doped surface layer (c In at. conc.) is negative, which is not the case for In-doped layers at higher concentrations.

3. Electronic structures

Finally, we discuss the electronic structure of few surface alloys. Surface DOS are calculated for the first two surface atomic layers of the relaxed slabs (Fig. 2). The surface electronic structure of pure indium monolayer film on Pd(111) is very similar to the one of pure Pd, with a large band ($\simeq 5$ eV),

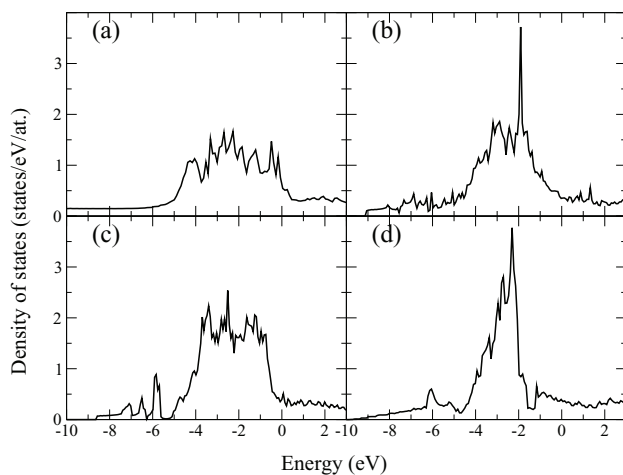


FIG. 2. Contribution of the surface bilayer (S and S-1) to the density of states of surface alloys on Pd(111) (a)–(c) and InPd(110) (d). (a) The surface layer is a pure indium layer while the subsurface layers are pure Pd layers. (b) The surface and subsurface are In-doped Pd layers, each with 50% In at. composition. This 2-layer thick film is deposited on Pd(111). (c) The surface, subsurface, and subsurface are In-doped Pd layers, each with 33% In at. composition. This 3-layer thick film is deposited on Pd(111).

due to a strong contribution of Pd d -states (Fig. 2(a)). A shift of this band towards lower energies (higher binding energies), along with a decrease of the band width, is noticeable for the other two surface alloys (33% and 50% In at. concentration per In-doped Pd layer, Figs. 2(b) and 2(c)), which tends to give a shape for these DOS similar to the one of InPd(110). However, even the 1:1 In-Pd surface alloy DOS (Fig. 2(b)) is quite different from the InPd(110) alloy (Fig. 2(d)). These results are very similar with the ones obtained from an experimental approach (Fig. 4 of Ref. 23).

Comparing in more details the InPd(110) surface DOS with the one of the 1:1 In-Pd bilayer film on Pd(111) (Figs. 2(b) and 2(d)) leads to the conclusion that the main band of the surface alloy is shifted towards the Fermi energy and broaden compared to InPd(110). As mentioned before, the environments of surface Pd and In atoms in Pd(110) and in the 1:1 bilayer film on Pd(111) are similar: each In atom lies in a rectangle made of Pd atoms. However, the dimensions do not match exactly, leading to larger atomic relaxations in the 1:1 alloy film on Pd(111) compared to InPd(110). Since the d -band width is inversely proportional to the third to fifth power of the distance between atoms,^{52,53} the band width of InPd(110) is expected to be smaller than the one of the surface alloy: nearest neighbor In-Pd distances are equal to 2.79 Å in the surface alloy, while they are 2.86 Å in InPd(110).

IV. DISCUSSION

A. Surface alloying and segregation

Results from first-principles calculations indicate that surface alloying takes place upon In dosing on the Pd(111) surface. This behavior is due to the quite large exothermic alloy formation energy. At an atomic scale, it means that the energy gain by forming Pd-In bonds is sufficient to overcome the indium surface segregation.

The In-In, Pd-Pd, and Pd-In bonding energies can be evaluated from a simple model based on the nearest-neighbor approximation and calculated cohesive energy (Sec. III A). There are 8 nearest neighbors around each indium atom in the bulk, the In-In bonding energy is then calculated to be $E_{In-In} = -0.29$ eV. A similar reasoning leads to $E_{Pd-Pd} = -0.31$ eV, in good agreement with Ref. 54 (12 nearest neighbors around each palladium atom in the bulk) and $E_{Pd-In} = -0.44$ eV (the coordination number of each In atom in InPd is 8). The energy change due to the formation of one Pd-In bond from Pd-Pd and In-In bond is $E_{Pd-In} - \frac{1}{2}(E_{In-In} + E_{Pd-Pd})$ (-0.14 eV). Surface alloying can then be attributed to the exothermic formation energy of Pd-In bonds, since forming Pd-In bonds is energetically more favorable than forming Pd-Pd and/or In-In bonds. The alloying effect has been shown to be more favorable for In-doped Pd layers with low In concentration (11 at. %, 25 at. %, and 33 at. %). In this case, the number of Pd-In bonds is maximized within one In-doped Pd layer, each In atom being surrounded by 6 Pd atoms. In addition, the d -bands calculated for these surface alloys (Figs. 2(b) and 2(c)) are shifted towards lower energy (higher binding energy) compared to the surface alloy built from one pure In layer on Pd(111) (Fig. 2(a)), supporting the idea that stronger Pd-In

bonds result in a stabilization of the surface alloy. The shift is even larger for InPd(110) (Fig. 2(d)), for which the Pd–In bond is stronger.

The exothermic formation energy of Pd–In bonds is also related to the absence of surface segregation calculated in perfect InPd(110) (Sec. III B 4). Here, the suppressed surface segregation is due to the large energy required to break Pd–In bonds compared to Pd–Pd and In–In bonds. This behavior is very similar to the absence of segregation calculated for perfect 1:1 Zn–Pd alloy,⁵⁴ also due to the exothermic Pd–Zn bond formation energy (−0.13 eV). It is worth noticing that this absence of surface segregation holds only for perfect 1:1 samples: off-stoichiometric defects like In antisites are shown to segregate to the surface (Sec. III B 4). In the same way, in Zn–Pd films with 1:3 and 3:1 composition, an enrichment of the dominant component has been predicted from *ab initio* calculations.⁵⁴ This result can be related to the lower number of Pd–In or Pd–Zn bonds in such off-stoichiometric samples compared to a stoichiometric InPd intermetallic compound.

The previous results concerning segregation have been calculated for a clean surface, i.e., without taking into account the possible role of adsorbates. However, it is well known that segregation strongly depends on the surface environment. In particular, the presence of oxygen may invert the segregation profile. While in the absence of oxygen, the element with the lowest surface energy is usually exposed, the element with the highest affinity with oxygen generally segregates to the surface. This has been demonstrated for the Ag₃Pd alloy⁵⁵ and for the Ag–Cu⁵⁶ and Pt–Ru systems.⁵⁷ In the case of InPd, the element with the lowest surface energy (indium) is probably also the element with the highest affinity to oxygen ($\Delta G_f(\text{In}_2\text{O}_3) = -926.4$ kJ/mol and $\Delta G_f(\text{PdO}) = -115.6$ kJ/mol). Here, possible modifications of the InPd segregation profile upon adsorption is left to future work.

B. Comparison with experimental observations

The present study aims to bring a deeper understanding of the experimental results reported in Ref. 23.

Experimentally, a well-ordered phase of $(\sqrt{3} \times \sqrt{3})R30^\circ$ is observed for low indium coverage (≈ 1 MLE, i.e., 1 monolayer equivalent) after annealing, with an indium surface atomic concentration equal roughly to 30–40 at. %. This is in good agreement with the theoretical study, that shows the higher stability of a three-layer thick film (In at. % = 33%) on Pd(111) compared to a pure In monolayer on Pd(111), the stabilization energy being roughly equal to 1.5 eV/In atom.

At higher In coverage (4–35 MLE) on Pd(111), surface alloying is observed after room temperature deposition. Annealing the sample leads to the formation of two different structures depending on the annealing temperature T_a : a In₇Pd₃ surface alloy with (110) orientation ($T_a \leq 500$ K) and a InPd surface alloy with (110) orientation ($T_a = 550$ – 600 K). From the experimental study, the In-rich phase grows either directly on top of the Pd(111) substrate or on top of InPd(110) domains formed as an interfacial layer in the early stage of the growth. The present theoretical study shows that the energetically favorable surface alloys contain less than 50% In

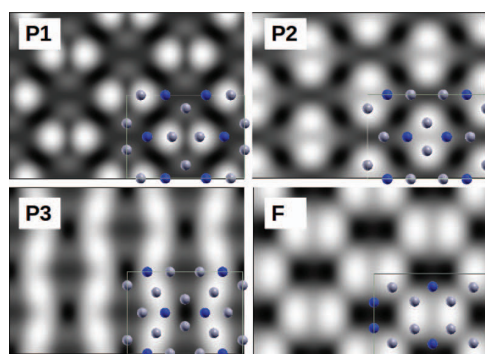


FIG. 3. Simulated STM images ($V_{bias} = +0.5$ eV, $27.1 \times 19.8 \text{ \AA}^2$) of possible surface terminations of the In₇Pd₃(100) surface. Blue spheres (resp. gray spheres) represent Pd atoms (resp. In atoms).

at. concentration. This conclusion is in agreement with the experimental observations, indicating that the InPd(110) and In₇Pd₃(110) surface alloys are metastable, as annealing to temperatures higher than 600 K leads to surface alloys with an indium concentration roughly equal to 20%.

The orientation of the 1:1 In–Pd surface alloy obtained experimentally has been determined from the observation of scanning tunnelling microscopy (STM) images. Alternating bright and dark rows on STM images are attributed to alternating atomic rows of Pd and In in the stoichiometric (110) atomic layers of InPd, assuming an outward shift of In atoms and an inward shift of Pd atoms, similar to what was calculated on the stoichiometric ZnPd surface.⁵⁸ The present theoretical study confirms the expected surface buckling, with an inward shift of surface Pd atoms ($\Delta z^s(\text{Pd}) = -0.10 \text{ \AA}$) and an outward shift of surface In atoms ($\Delta z^s(\text{In}) = 0.15 \text{ \AA}$).

The structure model of the In₇Pd₃(110) surface alloy assumes a bulk termination at a dense puckered layer.²³ Possible surface terminations of In₇Pd₃(110), including both puckered (P1, P2, P3) and flat (F) topmost layers, have been modelled. The corresponding STM images have been simulated within the Tersoff-Hamann approximation. Results are presented in Fig. 3. The best agreement between the simulated and the experimental image (Fig. 8(c) in Ref. 23) is obtained for the P1 termination. However, differences in the relative brightness of features are noticeable between the simulated and experimental images. Indeed, the simulation assumes a bulk termination at a dense puckered layer of In₇Pd₃(110), without taking into account the role of the substrate. A more detailed study would be required here to fully interpret the experimental observations, which is beyond the scope of this paper.

Finally, calculated density of states show that the *d*-band of In–Pd surface alloys are shifted away from the Fermi energy compared to a pure In layer on Pd(111), highlighting the alloying effect. The corresponding electronic structure is still not identical to the one of a perfect InPd(110) surface. Here, the Pd(111) surface lattice parameters have been kept fixed during atomic relaxation, leading to Pd–In bonds in the surface alloy shorter (2.79 \AA) than in the stoichiometric InPd (2.86 \AA). That could affect the shape and the position of the *d*-band. However, it still suggests that a sufficient thickness is required to recover the “Cu-like” electronic structure of

084703-8 Gaudry *et al.*J. Chem. Phys. **141**, 084703 (2014)

stoichiometric InPd. This conclusion is in line with what was calculated for the Zn/Pd(111) system:⁵⁸ the electronic structure of the Zn layers deposited on a Pd(111) substrate was found to approach the bulk Zn state only after a 4-layer thick film of Zn.

V. CONCLUSION

In this paper, we presented a detailed density functional theory study of the surface structure and the alloying and segregation effects of both the InPd intermetallic compound and In-Pd surface alloys obtained by burying a In-doped Pd layer in Pd(111).

Calculations show that segregation is energetically unfavorable at the perfect InPd(110) surface, while In anti-sites tend to segregate to the surface in off-stoichiometric InPd(110) systems.

Surface alloys are studied by burying an In-doped Pd layer of various compositions in Pd(111). We demonstrated that the most favorable atomic In concentrations of the In-doped Pd layer are below 50 at. % (11 at. %, 25 at. %, 33 at. %). Then, the 1:1 In-Pd surface alloy on Pd(111), obtained experimentally in Ref. 23, is not expected to be stable at the thermodynamic equilibrium. According to our calculations, the In-doped Pd layers with concentration above or equal to 50 at. % tend to transform to In-doped Pd multilayers, each presenting an atomic In concentration below 50 at. %.

Finally, the electronic structure of both InPd(110) and In/Pd(111) are investigated, suggesting that a relatively thick surface alloy is required to recover the “Cu-like” electronic structure, which is a necessary condition for the catalytic properties of InPd towards the methanol steam reforming. From the experimental and theoretical point of view, these two companion papers lay the foundations for further studies of surface reactivity.

ACKNOWLEDGMENTS

This work was supported by the ANR CAPRICE 2011-INTB-1001-01, the European C-MAC consortium, and COST Action CM0904 “Intermetallic compounds as catalyst for steam reforming of methanol (IMC-SRM).” This work was granted access to the HPC resources of the French institute IDRIS (Institut du Développement et des Ressources en Informatique Scientifique) under allocation 2013-99642 made by GENCI (Grand Equipement National de Calcul Scientifique).

- ¹G. A. Olah, “Beyond oil and gas: The methanol economy,” *Angew. Chem., Int. Ed.* **44**, 2636–2639 (2005).
- ²G. A. Olah, A. Goepfert, and G. K. Surya-Prakash, *Beyond Oil and Gas: The Methanol Economy* (Wiley-VCH, Berlin, 2009).
- ³B. Lindström and L. J. Pettersson, “Hydrogen generation by steam reforming of methanol over copper-based catalysts for fuel cell applications,” *Int. J. Hydrogen Energy* **26**, 923 (2001).
- ⁴R. M. Navarro, M. A. Pena, and J. L. G. Fierro, “Hydrogen production reactions from carbon feedstocks: Fossil fuels and biomass,” *Chem. Rev.* **107**, 3952 (2007).
- ⁵D. R. Palo, R. A. Dagle, and J. D. Holladay, “Methanol steam reforming for hydrogen production,” *Chem. Rev.* **107**, 3992 (2007).
- ⁶K. Narusawa, M. Hayashida, Y. Kamiya, H. Roppongi, D. Kurashima, and K. Wakabayashi, “Deterioration in fuel cell performance resulting from hy-

drogen fuel containing impurities: Poisoning effects by CO, CH₄, HCHO and HCOOH,” *JSAE Rev.* **24**, 41 (2003).

- ⁷X. Cheng, Z. Shi, N. Glass, L. Zhang, J. Zhang, D. Song, Z.-S. Liu, H. Wang, and J. Shen, “A review of PEM hydrogen fuel cell contamination: Impacts, mechanisms, and mitigation,” *J. Power Sources* **165**, 739 (2007).
- ⁸N. Iwasa, S. Masuda, N. Ogawa, and N. Takezawa, “Steam reforming of methanol over Pd/ZnO: Effect of the formation of PdZn alloys upon the reaction,” *Appl. Catal. A* **125**, 145 (1995).
- ⁹N. Iwasa, T. Mayanagi, N. Ogawa, K. Sakata, and N. Takezawa, “New catalytic functions of PdZn, PdGa, PdIn, PtZn, PtGa and PtIn alloys in the conversions of methanol,” *Catal. Lett.* **54**, 119–123 (1998).
- ¹⁰N. Iwasa and N. Takezawa, “New supported Pd and Pt alloy catalysts for steam reforming and dehydrogenation of methanol,” *Top. Catal.* **22**, 215 (2003).
- ¹¹Y. Men, G. Kolb, R. Zapf, M. O’Connell, and A. Ziogas, “Methanol steam reforming over bimetallic Pd-In/Al₂O₃ catalysts in a microstructured reactor,” *Appl. Catal. A* **380**, 15–20 (2010).
- ¹²N. Iwasa, T. Mayanagi, S. Masuda, and N. Takezawa, “Steam reforming of methanol over Pd-Zn catalysts,” *React. Kinet. Catal. Lett.* **69**, 355 (2000).
- ¹³C. Rameshan, H. Lorenz, L. Mayr, S. Penner, D. Zemlyanov, R. Arrigo, M. Haevecker, R. Blume, A. Knop-Gericke, R. Schlögl, and B. Klötzer, “CO₂-selective methanol steam reforming on In-doped Pd studied by *in situ* x-ray photoelectron spectroscopy,” *J. Catal.* **295**, 186–194 (2012).
- ¹⁴Z.-X. Chen, K. M. Neyman, A. B. Gordienko, and N. Rösch, “Surface structure and stability of PdZn and PtZn alloys: Density-functional slab model studies,” *Phys. Rev. B* **68**, 075417 (2003).
- ¹⁵U. Bardi, “The atomic structure of surface alloys and alloys surfaces,” *Rep. Prog. Phys.* **57**, 939–987 (1994).
- ¹⁶A. Bayer, K. Flechtner, R. Denecke, H. P. Steinruck, K. M. Neyman, and N. Rösch, “Electronic properties of thin Zn layers on Pd(111) during growth and alloying,” *Surf. Sci.* **600**, 78–94 (2006).
- ¹⁷G. Weirum, M. Kratzer, H. P. Koch, A. Tamtögl, J. Killmann, I. Bako, A. Winkler, S. Surnev, and R. Schennach, “Growth and desorption kinetics of ultrathin Zn layers on Pd(111),” *J. Phys. Chem. C* **113**, 9788–9796 (2009).
- ¹⁸X. He, Y. Huang, and Z.-X. Chen, “Zinc coverage dependent structure of PdZn surface alloy,” *Phys. Chem. Chem. Phys.* **13**, 107–109 (2011).
- ¹⁹A. Benali, “Étude *ab initio* d’alliages AlCu: phénomènes de ségrégation et modification de la réactivité de surface vis-à-vis de l’oxygène,” Ph.D. thesis, École doctorale Science de la Matière, Toulouse, 2010.
- ²⁰D. Rouxel and B. Weber, “Surface des solides-physisorption-chimisorption-ségrégation,” available online at <http://www.techniques-ingenieur.fr/base-documentaire/sciences-fondamentales-th8/etats-de-la-matiere-42109210/surface-des-solides-af3680/>.
- ²¹G. Tréglia, B. Legrand, F. Ducastelle, A. Saul, C. Gallis, I. Meunier, C. Mottet, and A. Senhaji, “Alloy surfaces: Segregation, reconstruction and phase transitions,” *Comput. Mater. Sci.* **15**, 196–235 (1999).
- ²²H. Kwak, Y. K. Shin, A. C. T. van Duin, and A. V. Vasenkov, “*Ab initio* based multiscale modeling of alloy surface segregation,” *J. Phys.: Condens. Matter* **24**, 485006 (2012).
- ²³G. McGuirk, J. Ledieu, É. Gaudry, M.-C. de Weerd, and V. Fournée, “Surface structures of Pd-In intermetallic compounds. I. Experimental study of structure and alloying of In thin films on Pd(111),” *J. Chem. Phys.* **141**, 084702 (2014).
- ²⁴G. Kresse and J. Furthmüller, “Efficient iterative schemes for *ab initio* total-energy calculations using a plane-wave basis set,” *Phys. Rev. B* **54**, 11169–11186 (1996).
- ²⁵G. Kresse and J. Furthmüller, “Efficiency of *ab-initio* total energy calculations for metals and semiconductors using a plane wave basis set,” *Comput. Mater. Sci.* **6**, 15–50 (1996).
- ²⁶P. E. Blöchl, “Projector augmented-wave method,” *Phys. Rev. B* **50**, 17953 (1994).
- ²⁷G. Kresse and D. Joubert, “From ultrasoft pseudopotentials to the projector augmented-wave method,” *Phys. Rev. B* **59**, 1758 (1999).
- ²⁸J. P. Perdew, K. Burke, and M. Ernzerhof, “Generalized gradient approximation made simple,” *Phys. Rev. Lett.* **77**, 3865 (1996).
- ²⁹J. P. Perdew, K. Burke, and M. Ernzerhof, “Erratum: Generalized gradient approximation made simple,” *Phys. Rev. Lett.* **78**, 1396 (1997).
- ³⁰J. C. Boettger, “Nonconvergence of surface energies obtained from thin-film calculations,” *Phys. Rev. B* **49**, 16798–16800 (1994).
- ³¹J. C. Boettger, J. R. Smith, U. Birkenheuer, N. Rösch, S. B. Trickey, R. Sabin, and S. P. Apell, “Extracting convergent surface formation energies from slab calculations,” *J. Phys.: Condens. Matter* **10**, 893 (1998).

084703-9 Gaudry *et al.*J. Chem. Phys. **141**, 084703 (2014)

- ³²J. L. F. Da Silva, C. Stampfl, and M. Scheffler, "Converged properties of clean metal surfaces by all-electron first principles calculations," *Surf. Sci.* **600**, 703–715 (2006).
- ³³C. Jiang, L.-Q. Chen, and Z.-K. Liu, "First-principles study of constitutional and thermal point defects in b2 PdIn," *Intermetallics* **14**, 248–254 (2006).
- ³⁴D. S. dos Santos, S. Miraglia, and D. Fruchart, "A high pressure investigation of Pd and the Pd-H system," *J. Alloys Comp.* **291**, L1–L5 (1999).
- ³⁵C. Kittel, *Introduction to Solid State Physics*, 7th ed. (John Wiley and Sons, USA, 1996).
- ³⁶Y. Zhang, "First-principles statistical mechanics approach to step decoration at solid surfaces," Ph.D. thesis, Freie Universität Berlin, 2008.
- ³⁷H. Flandorfer, "Phase relationships in the in-rich part of the In-Pd system," *J. Alloys Comp.* **336**, 176–180 (2002).
- ³⁸M. Giovannini, A. Saccone, S. Delfino, and P. Rogl, "A comparative investigation of isothermal sections of Rare Earth-Pd-In systems," *Intermetallics* **11**, 1237–1243 (2003).
- ³⁹S. V. Meschel and O. J. Kleppa, "Standard enthalpies of formation of some transition metal indium compounds by high temperature direct synthesis calorimetry," *J. Alloys Comp.* **333**, 91–98 (2002).
- ⁴⁰S. Amore, S. Delsante, N. Parodi, and G. Borzone, "Thermochemistry of Pd-In, Pd-Sn and Pd-Zn alloy systems," *Thermochim. Acta* **481**, 1–6 (2009).
- ⁴¹H. Kohlmann and C. Ritter, "Refinement of the crystal structures of palladium-rich In-Pd compounds by x-ray and neutron powder diffraction," *Z. Naturforsch. B* **62**, 929–934 (2007).
- ⁴²M. Mansfield and R. J. Needs, "Surface energy and stress of lead (111) and (110) surfaces," *Phys. Rev. B* **43**, 8829–8833 (1991).
- ⁴³P. J. Feibelman, "First-principles calculation of the geometric and electronic structure of the Be(0001) surface," *Phys. Rev. B* **46**, 2532–2539 (1992).
- ⁴⁴A. Benali, C. Lacaze-Dufaure, and J. Morillo, "Density functional study of copper segregation in aluminum," *Surf. Sci.* **605**, 341–350 (2011).
- ⁴⁵F. R. De Boer, R. Boom, W. C. M. Mattens, A. R. Miedema, and A. K. Niessen, *Cohesion in Metals* (Elsevier, Amsterdam, 1988).
- ⁴⁶A. Michaelidis and M. Scheffler, "Introduction to the theory of metal surfaces," *Surface and Interface Science. Volume 1: Concepts and Methods*, edited by K. Wandelt (Wiley, 2012).
- ⁴⁷L. Hammer, V. Blum, Ch. Schmidt, O. Wieckhorst, W. Meier, S. Müller, and K. Heinz, "Role of Co antisite segregation in the CoAl(111) surface," *Phys. Rev. B* **71**, 075413 (2005).
- ⁴⁸V. Blum, L. Hammer, Ch. Schmidt, O. Wieckhorst, S. Müller, and K. Heinz, "Segregation in strongly ordering compounds: A key role of constitutional defects," *Phys. Rev. Lett.* **89**, 266102 (2002).
- ⁴⁹A. V. Ruban, "Surface composition of ordered alloys: An off-stoichiometric effect," *Phys. Rev. B* **65**, 174201 (2002).
- ⁵⁰A. Christensen, A. V. Ruban, P. Stoltze, K. W. Jacobsen, H. L. Skriver, J. K. Norskov, and F. Besenbacher, "Phase diagrams for surface alloys," *Phys. Rev. B* **56**, 5822–5834 (1997).
- ⁵¹K. Yuge, A. Seko, A. Kuwabara, F. Oba, and I. Tanaka, "Ordering and segregation of a Cu₇₅Pt₂₅(111) surface: A first-principles cluster expansion study," *Phys. Rev. B* **76**, 045407 (2007).
- ⁵²O. K. Andersen, W. Klose, and H. Nohl, "Electronic structure of chevrephase high-critical-field superconductors," *Phys. Rev. B* **17**, 1209–1237 (1978).
- ⁵³*Theory of Alloy Phase Formation*, in *Proceedings of the TMS-AIME Alloy Phases Committee and the Chemistry and Physics of Metals Committee at the 108th AIME Annual Meeting, New Orleans, USA, 19–20 February 1980*, edited by L. H. Bennett (Metallurgical Society of AIME, Warrendale, PA, 1980).
- ⁵⁴Z.-X. Chen, K. M. Neyman, and N. Rösch, "Theoretical study of segregation of Zn and Pd in Pd-In alloys," *Surf. Sci.* **548**, 291–300 (2004).
- ⁵⁵J. R. Kitchin, K. Reuter, and M. Scheffler, "Alloy surface segregation in reactive environments: First-principles atomistic thermodynamics study of Ag₃Pd(111) in oxygen atmospheres," *Phys. Rev. B* **77**, 075437 (2008).
- ⁵⁶S. Piccinin, C. Stampfl, and M. Scheffler, "Ag-Cu alloy surfaces in an oxidizing environment: A first-principles study," *Surf. Sci.* **603**, 1467–1475 (2009).
- ⁵⁷B. C. Han, A. Van der Ven, G. Ceder, and B. J. Hwang, "Surface segregation and ordering of alloy surfaces in the presence of adsorbates," *Phys. Rev. B* **72**, 205409 (2005).
- ⁵⁸H. P. Koch, I. Bako, G. Weirum, M. Kratzer, and R. Schennach, "A theoretical study of Zn adsorption and desorption on a Pd(111) substrate," *Surf. Sci.* **604**, 926–931 (2010).

Chapter 4

Bulk InPd IMC surfaces

4.1 Introduction

Studies of polycrystalline and single crystal InPd help us understand the bulk - surface interactions. Because catalytic properties at the surface are clearly influenced by sub-surface behavior (e.g. through surface segregation for example), this understanding is essential. Multifaceted polycrystalline metallic foils are often used as a more practical and realistic representation of compounds found in real catalysts [128, 129, 131, 146]. However, surface reactions are usually discussed based on the global composition and little is known regarding the influence of grain boundaries and orientations.

Furthermore, to understand the reaction mechanism for IMCs in MSR, basic knowledge of intrinsic surface and bulk properties is required [50]. A first step towards gaining this insight comes from the successful growth of bulk InPd. For our work, polycrystalline and single crystalline InPd were grown using induction melting and the Czochralski method respectively. This was followed by surface science investigations under UHV conditions.

4.2 Growth of bulk InPd

4.2.1 InPd single crystals

The growth of InPd single crystals was performed at the Ludwig-Maximilians-Universität in München in the group of Professor P. Gille. First, a homogeneous In-Pd solution was formed by dissolving 35.5 to 37.5 at. % Pd in indium. The first crystal was grown from an InPd seed formed by spontaneous nucleation on a wedge-shaped tantalum tip.

The starting growth solution was indium rich ($\text{In}_{64.5}\text{Pd}_{35.5}$) and the crystal grew preferentially along the [110] axis by slowly pulling the tip ($200 \mu\text{m/h}$ down to $50 \mu\text{m/h}$). This strategy was conjured as a consequence of In having a high vapor pressure and a continually decreasing In-Pd liquidus temperature dependent on the amount of material crystallized. The first crystal showed multiple inclusions (In_7Pd_3 and In_3Pd_2) towards the lower regions of the crystal, so the starting In composition was refined [50].

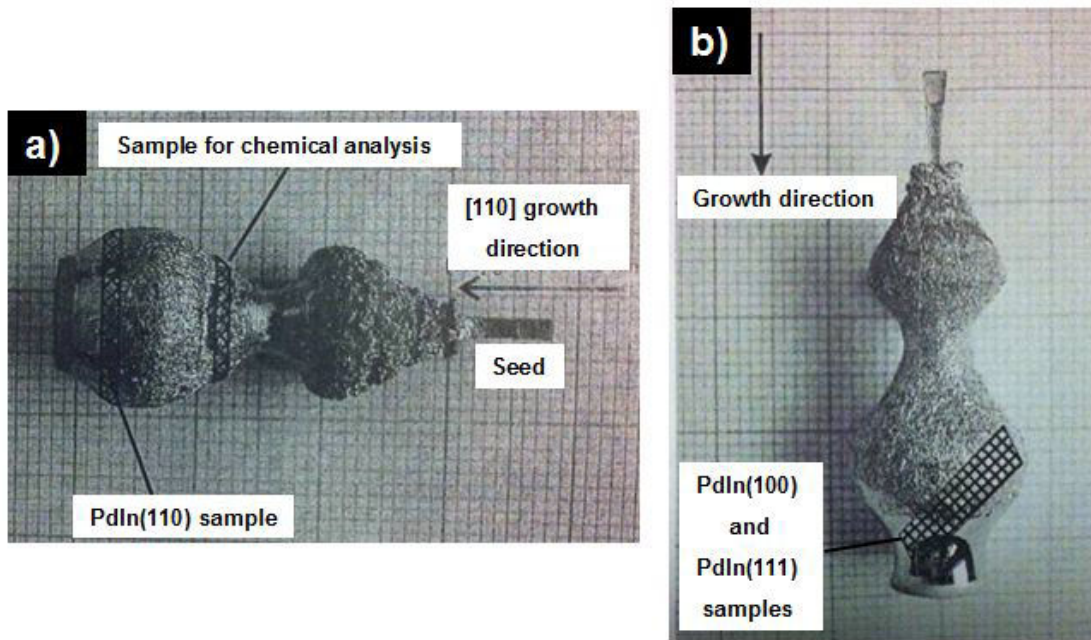


FIGURE 4.1: Images (a) and (b) are the single crystals grown at the Ludwig-Maximilians-Universität in München. The regions where single crystal samples were taken are labeled appropriately (a) - InPd(110) and (b) - InPd(100) and InPd(111). A chemical analysis taken from a different portion of crystal (a) showed 52.1:47.9 In:Pd. Towards the bottom of the samples, EPMA axial measurements indicated our samples were slightly more Indium rich ($\lesssim 54$ at. % In) [50, 64].

Three samples having either (100), (110) or (111) orientation, were extracted from two separate ingots for surface investigations. The two ingots were grown with a starting composition of $\text{In}_{62.5}\text{Pd}_{37.5}$ and determined inclusion-free by optical microscopy and EPMA (electron probe microanalysis) measurements. Pulling rates for crystal (a) (crystal (b)) were $200 \mu\text{m/h}$ down to $50 \mu\text{m/h}$ ($100 \mu\text{m/h}$ down to $50 \mu\text{m/h}$). The respective single crystals are shown in Fig. 4.1 (a) and (b). The marked areas of (a) and (b) show portions cut for our samples as described in the caption. The lower part of the crystals were determined to be In-rich and the measured bulk composition of our samples was between 52 and 54 at. % In [50, 64]. Orientations of the three samples were verified with backscattered X-ray Laue diffraction. The surfaces were polished down to $0.25 \mu\text{m}$ sized diamond grains followed by a final step using Syton OP-S. The samples were mounted on Ta plates. The first plate housed InPd(110) (Fig. 4.2 (a)) having dimensions of $8.5 \times$

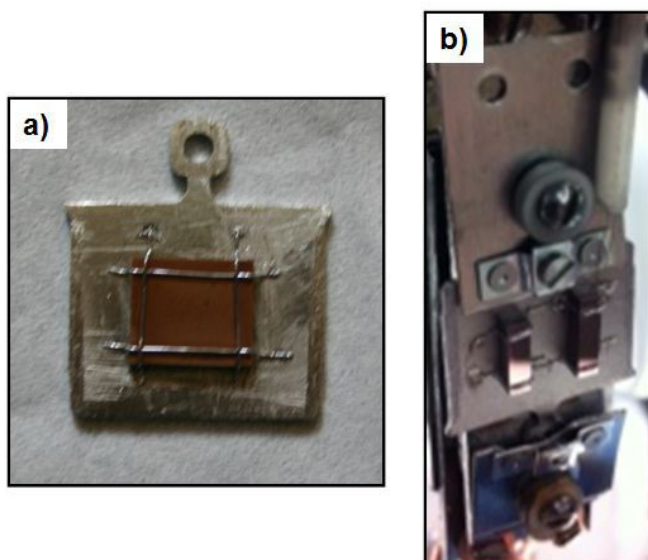


FIGURE 4.2: The images above show a) InPd(110) and b) InPd(100) and InPd(111) samples mounted on a Ta back plate. For LEED I(E), the InPd(100) and InPd(111) samples (b) were additionally mounted to a Mo sample holder. This sample holder was attached to a manipulator having an extra degree of freedom so that normal incident LEED I(E) data could be acquired.

7.5 x 2 mm ($l \times w \times h$, h = sample thickness). On the second plate, smaller InPd(100) (7.9 x 2.1 x 2.0 mm) and InPd(111) (6.9 x 2.0 x 2.0 mm) samples were mounted side by side as shown in Fig. 4.2 (b).

4.2.2 Polycrystalline InPd

The polycrystalline sample was grown in-house. The ingot was prepared in an induction furnace as described in Chapter 3 (p. 43). The sample showed good crystallinity with a lattice constant of 3.23 Å and bulk composition of In₄₇Pd₅₃. The surface portrayed little porosity and huge grains with an average diameter of roughly 0.70 mm. This is shown by the optical micrograph in Fig. 4.3 (left).

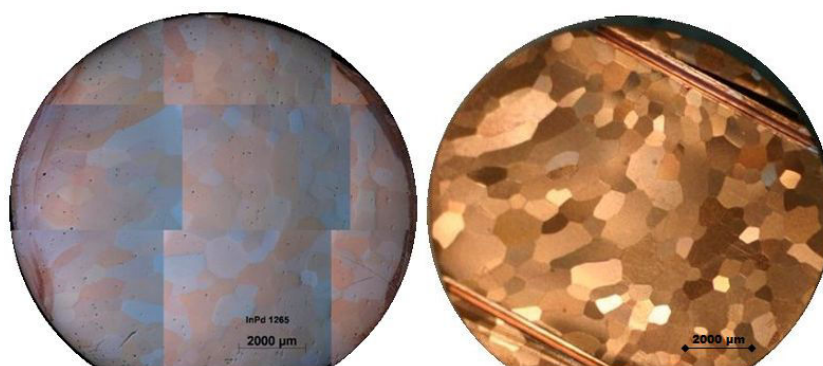


FIGURE 4.3: Optical micrography using polarized light (left) and normal photographed images (right) were taken of the InPd polycrystalline surface.

<i>Alloy surface phases</i>	a (Å)	b (Å)	dz (Å)
InPd(110)-(1x1)	3.249	4.595	2.297
InPd(110)-(2x1)	6.498	4.595	2.297
InPd(110)-c(4x2)	12.996*	9.190*	2.297
InPd(111)-(1x1)	4.595	4.595	0.938
InPd(111)-($\sqrt{3} \times \sqrt{3}$)R30°	7.959	7.959	0.938
<i>InPd(100)-(1x1)</i>	<i>3.249</i>	<i>3.249</i>	<i>1.625</i>
InPd(100)-p(4x4)	12.996	12.996	12.996
InPd(100)-c($3\sqrt{2} \times \sqrt{2}$)R45°	13.784 [‡]	4.595 [‡]	1.625

TABLE 4.1: The theoretical unit cell dimensions of 2D surface meshes of all InPd(110), InPd(111), and InPd(100) surface reconstructions shown in Fig. 4.4 are displayed above. *Bulk-truncated InPd(100) is the only phase listed above not observed.* The primitive unit cell dimension of ‘c’ (centered) lattices are: $a=b=7.959$ Å, $\psi=70.5^\circ$ *; and $a=b=7.265$ Å, $\psi=36.9^\circ$ [‡]. The angle ψ between a and b is 90° for InPd(110)/InPd(100), and 120° for the hexagonal InPd(111) reconstructions.

4.3 Single crystal InPd surfaces

4.3.1 Overview

In an effort to prepare InPd surfaces within the stoichiometric composition window for surface characterization, we needed a basic grasp on the delicate balance between ion energy/exposure time for sputtering and temperature/time for annealing. We found depletion of In after sputtering at all ion energies tested (1.0 keV, 1.5 keV, and 2.0 keV). Annealing the samples past room temperature gradually re-segregated In at the surface to a point slightly beyond InPd composition ($\gtrsim 55\%$ at. In).

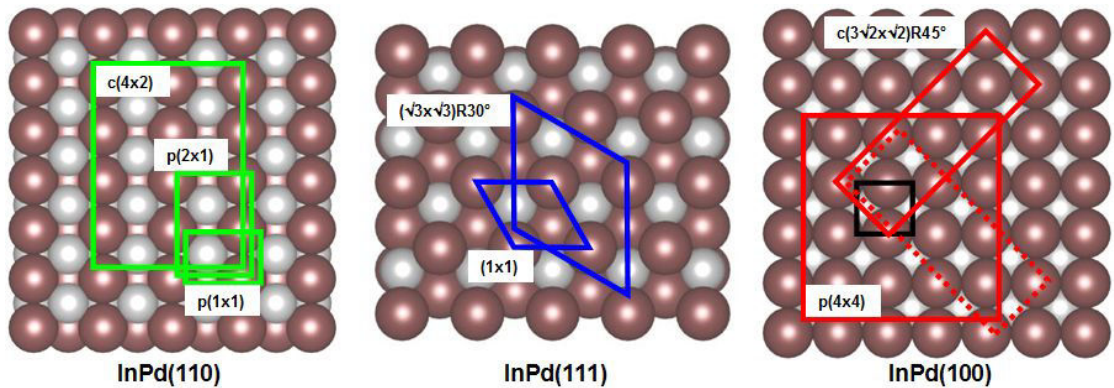


FIGURE 4.4: The three crystal surfaces examined under UHV conditions are shown above (theoretical). The unit cells of all surface reconstructions observed during surface preparation are drawn and labeled accordingly. A InPd(100)-(1x1) is shown for reference (not observed), represented by the small black square. The corresponding unit cell dimensions and interlayer spacings are found in Table 4.1

This compositional change in the near surface region with sputtering and annealing temperature, resulted in seven different superstructures as observed by LEED. The theoretical unit cells of the superstructures, over bulk truncated models of the three surfaces, are shown in Fig. 4.4. The corresponding unit cell dimensions, shown in Table 4.1, are referenced in the following presentation of XPS, STM, and LEED results for InPd(100), InPd(110), and InPd(111) single crystals.

4.3.2 InPd(100)

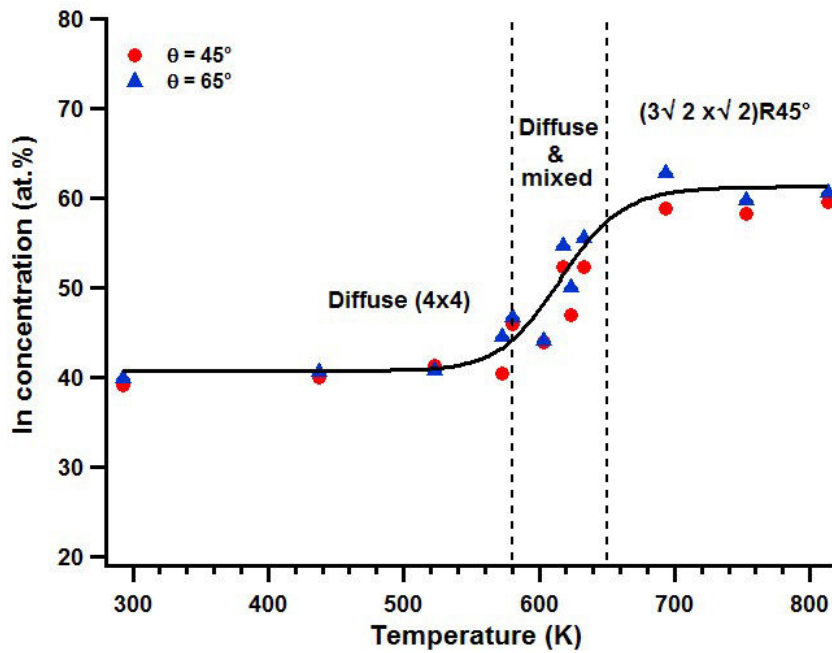


FIGURE 4.5: Concentration measurements after Ar+ sputtering (2 keV for 30 minutes) and annealing the InPd(100) surface are deduced from XPS data for two different take-off angles (θ is the angle between the surface normal and analyzer). The solid line in this figure is a guide for the eye only.

The mean surface composition, for two different take-off angles, was measured by XPS after sputtering and after annealing to various temperatures (this also being the case for InPd(110) and InPd(111) in the next two subsections). The results are shown in Fig. 4.5. The depletion of In after Ar+ sputtering InPd(100) allowed for the formations of two metastable superstructures within the stoichiometric window (38.5 % to 55 % at. In). After sputtering and annealing over 500 K, the Pd-rich InPd surface appeared as a quasi-ordered (4x4) superstructure. Further annealing to temperatures between ~ 580 and 650 K, both $c(3\sqrt{2} \times \sqrt{2})R45^\circ$ and (4x4) phases appeared alone or coexisted with each other. During this transitional state, LEED patterns were diffuse and STM images showed quasi-ordered structures. These observations accompanied the transition from Pd-rich to In-rich InPd, so we could not correlate one particular superstructure to 1:1

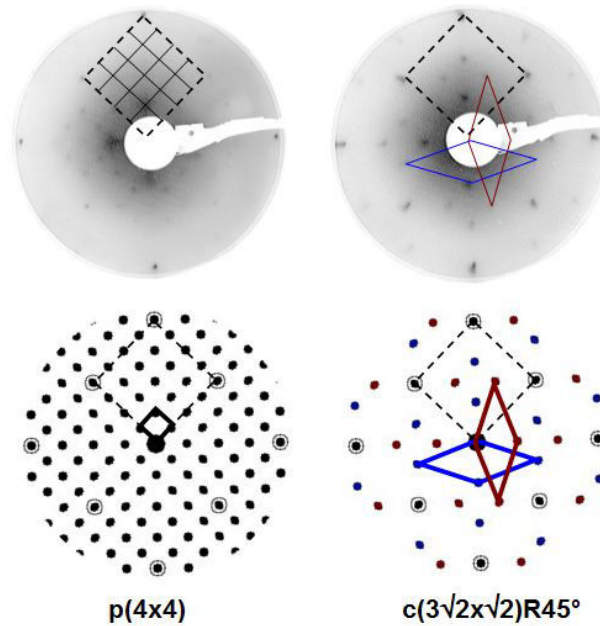


FIGURE 4.6: For InPd(100), the above $p(4 \times 4)$ (left) and $c(3\sqrt{2} \times \sqrt{2})R45^\circ$ (right) LEED images (48 eV) were obtained before and after the transition depicted in Fig. 4.5. The thickest lines, shown in the simulated LEED patterns, represent primitive reciprocal space unit cells for $p(4 \times 4)$ (black) and $c(3\sqrt{2} \times \sqrt{2})R45^\circ$ domains (dark red/blue). The InPd(100)-(1x1) reciprocal space unit cell corresponds to the dashed line.

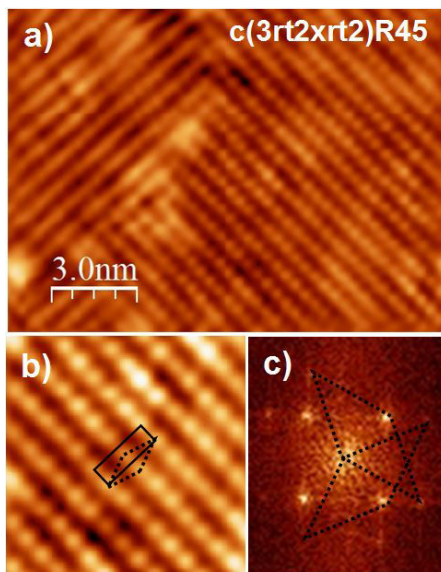


FIGURE 4.7: STM images of the InPd(100)- $c(3\sqrt{2} \times \sqrt{2})R45^\circ$ superstructure are shown above. The FFT-filtered top image (a) (15 nm x 11 nm, +1.4 V, 0.25 nA) shows two domains of atomically resolved InPd(100)- $c(3\sqrt{2} \times \sqrt{2})R45^\circ$. At the bottom (b), both rectangular (solid line) and primitive (dashed line) unit cells are superimposed over a zoomed-in portion of (a) (5 nm x 5 nm). The calculated FFT (c), taken over the original image (a), shows the primitive reciprocal space unit cells from both domains. Note that the images are rotated by 45° with respect to all other InPd(100) STM images.

In:Pd. When annealing to temperatures corresponding to the upper plateau of Fig. 4.5, a sharp $c(3\sqrt{2} \times \sqrt{2})R45^\circ$ superstructure was first observed by LEED.

The LEED pattern observed at high annealing temperatures (Fig. 4.6 - right side) indicated that two domains of $c(3\sqrt{2} \times \sqrt{2})R45^\circ$ structures dominated the surface. The domains were rotated by 90° with respect to each other. This accounted for the four, rather than two, interior beams within the (1x1) reciprocal space unit cell. Calculated

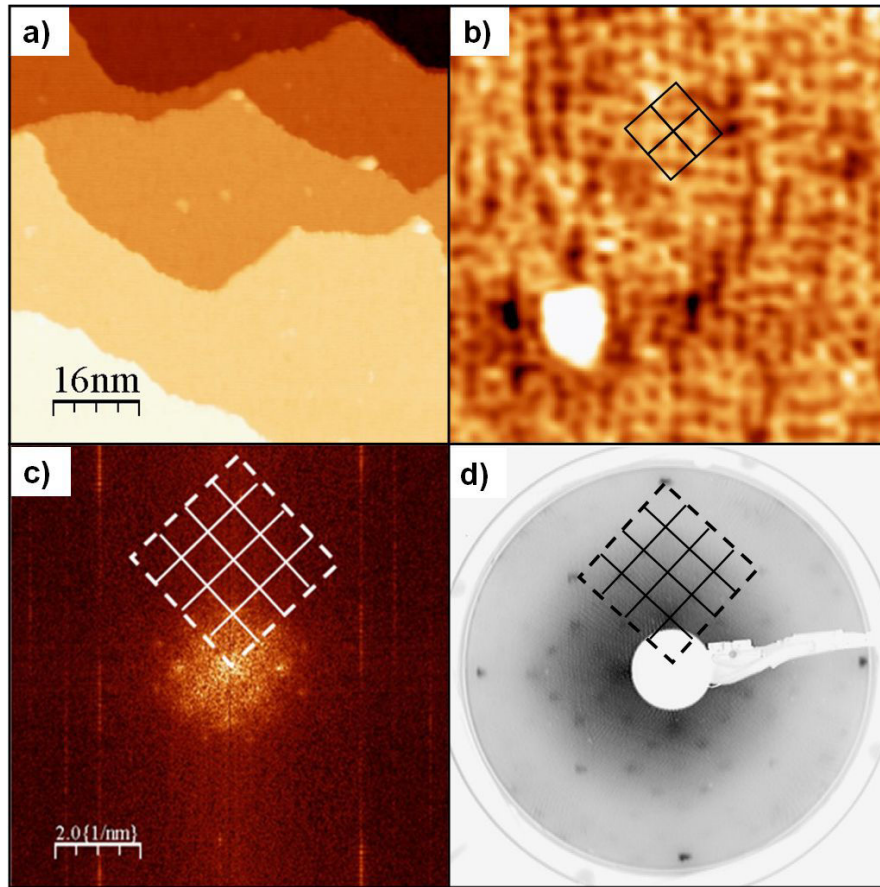


FIGURE 4.8: STM images and corresponding LEED pattern of the InPd(100)-p(4x4) structure are shown above. The quasi-ordered square structures (b - 15 nm x 15 nm/+1.8 V; 0.09 nA) form on top of the terraces (a - 80 nm x 80 nm/+1.8 V; 0.09 nA). The calculated FFT (c) taken over a larger, well-resolved image (not shown - 50 nm x 50 nm/-0.7 V; 0.07 nA) corresponds to a p(4x4). This is in agreement with the LEED pattern (50 eV) presented in (d).

FFTs of the corresponding STM images reproduce the main features present in the LEED pattern (bottom of Fig. 4.7 compared to right side of Fig. 4.6). The rectangular unit cell dimensions were $a=13.5 \pm 0.5 \text{ \AA}$ and $b=4.6 \pm 0.5 \text{ \AA}$, as measured by STM. Also measured were step heights of $3.30 \pm 0.10 \text{ \AA} \simeq 2 \times d_{100}$, therefore suggesting either In or Pd-terminated InPd(100) (not shown). However, other terraces were separated by large steps of several \AA . This was likely from step bunching or the onset of faceting.

The terrace step heights of (4x4) structures had an average value of $3.20 \pm 0.10 \text{ \AA}$ (Fig. 4.8 (a)). The p(4x4) superstructure appeared in calculated FFTs of atomically resolved STM images over $\sim 50 \times 50 \text{ nm}^2$, and in corresponding LEED patterns (shown in Fig. 4.8 (c) and (d)). The random disorder of the prominent pseudo-square structures seen in real-space images was manifested in the diffuse spots of the calculated FFTs over large images. The calculated FFT showed a p(4x4) superstructure with spots having non-homogeneous sharpness and intensity. The average STM measurements from the

FFT (Fig. 4.8 c) and 2D autocorrelation real space images (not shown) were $a=b=12.5 \pm 0.50 \text{ \AA}$ for the p(4x4) unit cell ($8.80 \pm 0.50 \text{ \AA}$ for the pseudo-square structures).

4.3.3 InPd(110)

The InPd(110) surface, similar to the InPd(100) surface, exhibited a Pd-rich to In-rich transformation upon annealing an In-depleted sputtered surface. This was observed in three separate sets of experiments. The first two sets of experiments involved annealing to high temperatures that induced surface faceting. Consequently, the sample was repolished in-between each set of experiments. The following presentation of our results will begin with the low-temperature data set (third set of experiments), which provides the best comparison between InPd(100) and InPd(111).

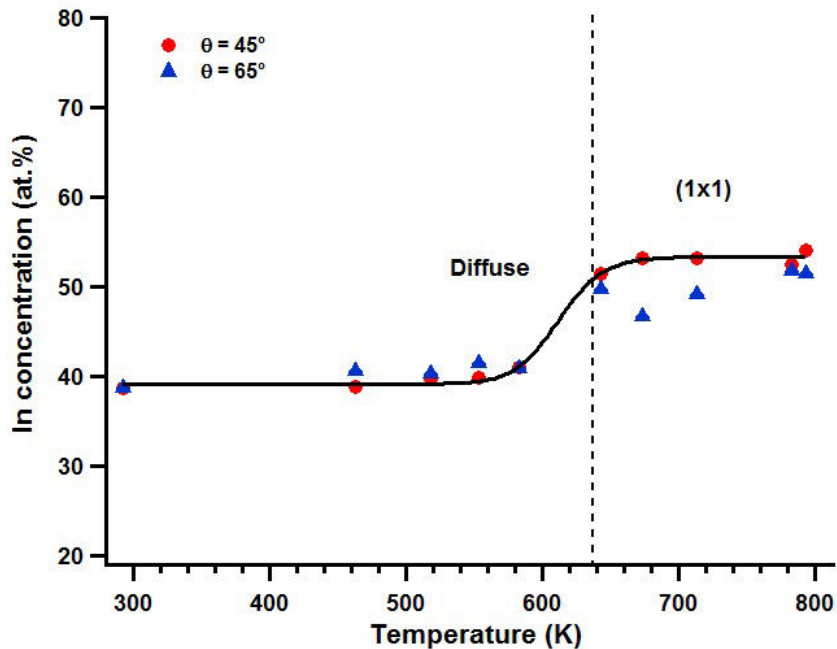


FIGURE 4.9: Concentration measurements after Ar+ sputtering (2 keV for 30 minutes) and annealing the InPd(110) surface are deduced from XPS data for two different take-off angles (θ is the angle between the surface normal and analyzer). The solid line in this figure is a guide for the eye only.

The XPS data, taken from the third set of experiments, showed a transition from a Pd-rich to a near stoichiometric surface (Fig. 4.9). In comparison, InPd(100) and InPd(111) transitioned to InPd near the In-rich limit (with roughly 5 % more In than for InPd(110)) after annealing to similar temperatures. For InPd(110), a good quality (1x1) LEED pattern was observed near the transition point. This LEED pattern (Fig. 4.10 (a)) was consistent with the atomically resolved rows shown in (Fig. 4.10 (b)). The row spacing was measured at $4.40 \pm 0.50 \text{ \AA}$; this being consistent with the expected

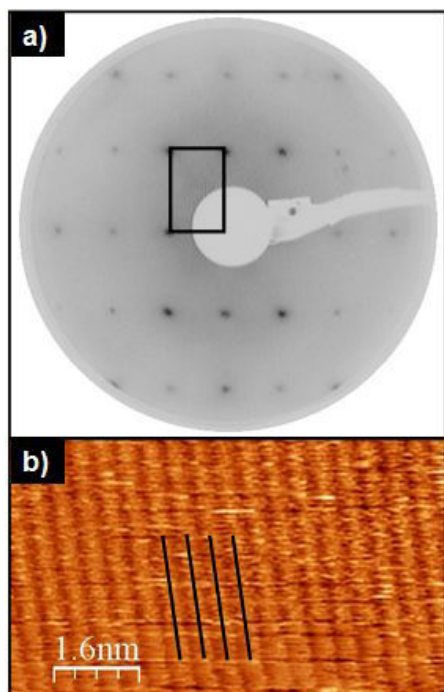


FIGURE 4.10: This LEED pattern (a) and STM image (b) were acquired immediately following the transition to near stoichiometric InPd(110) (after annealing to 640 K as seen in Fig. 4.9). The LEED pattern, taken at 140 eV, is clearly InPd(110)-(1x1). The corresponding STM (8 nm x 4.7 nm/-1.5 V; 0.08 nA) shows atomically resolved rows of either In or Pd atoms (one element slightly protrudes from the surface plane).

b vector (4.60 Å) of the rectangular unit cell (Fig. 4.4 and Table 4.1). The atomic structure along the rows could not be resolved. The terrace step heights equal to 2.30 ± 0.50 Å (not shown) also agreed with the theoretical interlayer spacing (2.30 Å) of bulk truncated InPd(110).

The other two experimental sets revealed two In-rich surface reconstructions and faceting resulting from high-temperature annealing. For the first set of experiments, the sample was initially degassed to 980 K. This immediately led to a change in the visual appearance of the surface. About half of the surface became dull in luster. Next, a sputter - anneal (760 K) cycle followed by another (annealing to 620 K) were performed. After respective sputter - anneal cycles, (2x1) and (1x1) LEED patterns were observed (4.11 (a) and (b)). Only the (2x1) exhibited streaking, but both patterns showed extra beams characteristic of faceting (In LEED, (h,k) beams from a flat surface converge towards the center (0,0) beam with increasing e-beam energy, whereas beams from facets often diverge). The LEED evidence of faceting was confirmed after the sample was removed from the chamber and scanning electron microscopy (SEM) was performed. The facets were on the order of a few microns (4.11 (c)). Facets had either square/rectangular or truncated hexagonal shapes, suggesting (100) or (111) orientations respectively. Furthermore, composition measurements from XPS data, taken before the sample was removed from UHV conditions, suggested the surface had a composition near the In-rich limit (55 % In). After this first set of experiments, the sample was re-polished and put back into the UHV chamber.

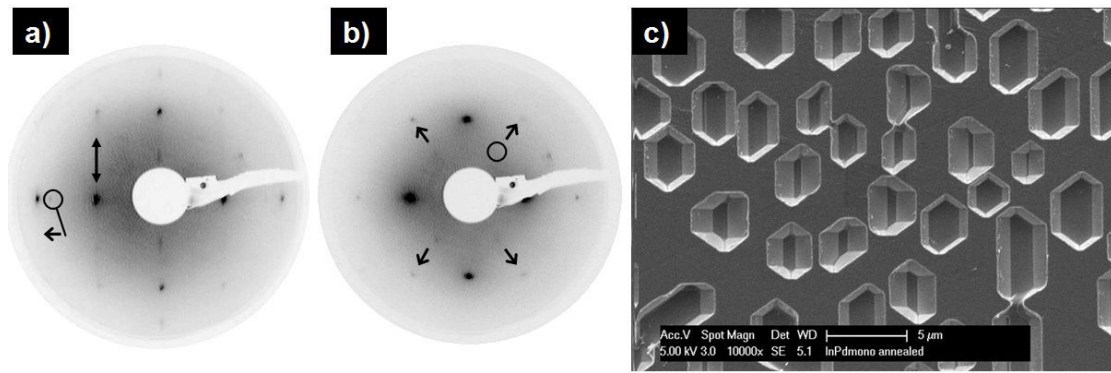


FIGURE 4.11: The diffuse LEED images from the first set of experiments on InPd(110) show additional (h,k) beams from a faceted surface seen in scanning electron microscopy (c). These beams are barely visible in both (2×1) (a) and (1×1) LEED patterns taken at 70 and 80 eV respectively. They are located at the bottom of the arrow or enclosed in circles. The arrows show the directions of the beams with increasing beam energy. The double arrow represents streaking observed for the (2×1) (a) reconstruction.

In the second series of experiments, the sample was initially degassed at 470 K followed by several sputter - anneal cycles. The annealing temperature progressively increased by about 50 K over the course of one or two cycles. A diffuse (1×1) LEED pattern was first observed (not shown), which improved in quality until a $c(4 \times 2)$ was observed near 675 K (Fig. 4.12 (a)). Annealing to 735 K showed a weak (2×1) LEED pattern. A (2×1) without and then with facets was observed after annealing to successively higher temperatures. Consequently, once faceting occurred, an InPd(110)- $c(4 \times 2)$ pattern could not be reproduced by the same sputtering and annealing conditions. Instead, only (2×1) LEED patterns resulted, both with and without facets (Fig. 4.12 (b) is from a non-faceted observation after annealing to about 700 K).

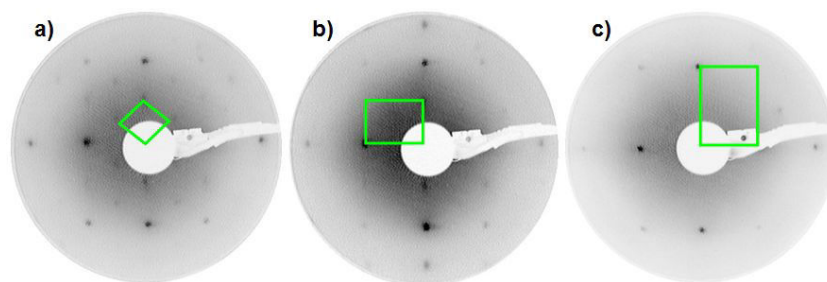


FIGURE 4.12: The above $c(4 \times 2)$ (a), (2×1) (b), and (1×1) (c) LEED patterns are the three reconstructions of the InPd(110) surface. The primitive reciprocal space unit cells for each image, taken at the same beam energy of 63 eV, are shown.

The STM image in Fig. 4.13 (a), acquired under the above conditions, indicated that wedding cake/column-like formations were present when a $p(2 \times 1)$ LEED pattern was observed. Similar images (not shown) were also observed in conjunction with a $c(4 \times 2)$ LEED pattern. Both $p(2 \times 1)$ and $c(4 \times 2)$ reconstructions observed by LEED could not

be atomically resolved by STM, however they likely existed on these small terraces. The flat terraces and corresponding histogram showing the evenly spaced terraces (Fig. 4.13 (a) and (b)), were from another observation of InPd(110)-(1x1). The details of this structure will be addressed in the next paragraph.

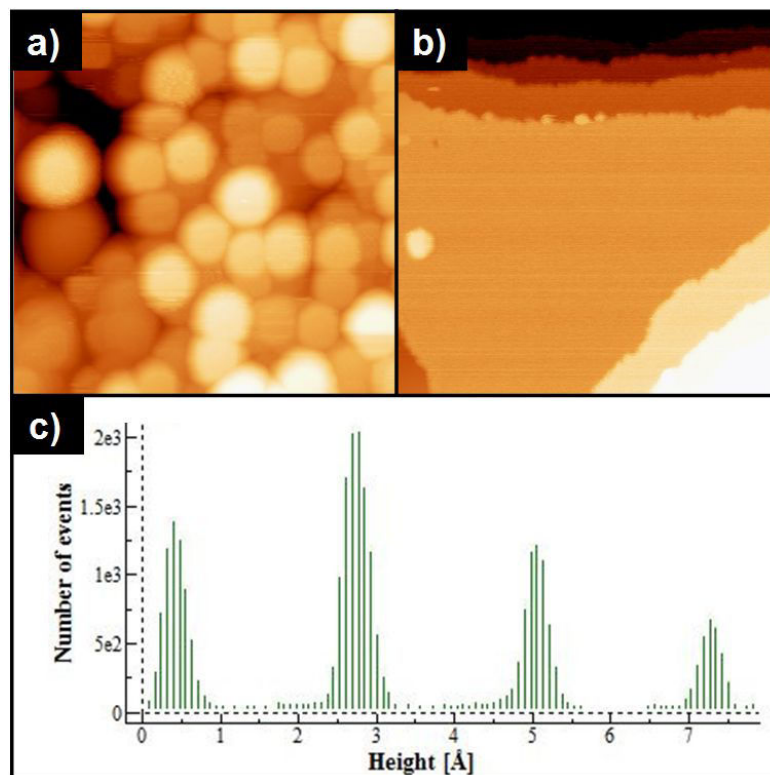


FIGURE 4.13: These STM images, show both small rounded terraces (a) and large flat terraces (b) formed on InPd(110). The formations of (a) occurred in conjunction with the (2x1) LEED pattern in Fig. 4.12 (b), whereas InPd(110)-(1x1) formed on the flat terraces of (b) (corresponding LEED image: Fig. 4.12 (c)). A histogram (c) taken over four terraces was used to approximate step height measurements for InPd(110)-(1x1). The STM image size/tunneling conditions for (a) and (b), are (50 nm x 50 nm)/(+1.4 V; 0.07 nA) and (40 nm x 40 nm)/(-0.5 V; 0.09 nA) respectively.

After annealing to 970 K, the appearance of the surface changed as observed in the first set of experiments. The LEED pattern was a diffuse p(2x1). Upon reaching higher annealing temperatures, LEED patterns showed (1x1) patterns both with and without facets. For the non-faceted case (Figs. 4.12 (c) and 4.13 (b-c) obtained after annealing to 1170 K), STM images of smooth terraces allowed for accurate step-height measurements ($2.29 \pm 0.05 \text{ \AA}$) corresponding to the interplanar distance d_{110} . The structures on terraces were resolved in one direction only allowing for measurements of atomic rows with an average row spacing of $4.60 \pm 0.10 \text{ \AA}$. These measurements are in agreement with theoretical bulk truncated parameters as shown in Fig. 4.4 (left image, (1x1)) and Table 4.1. Moreover, they agree with the low-temperature InPd(110)-(1x1) previously discussed and shown in Fig. 4.10. This structure was also consistent with XPS surface

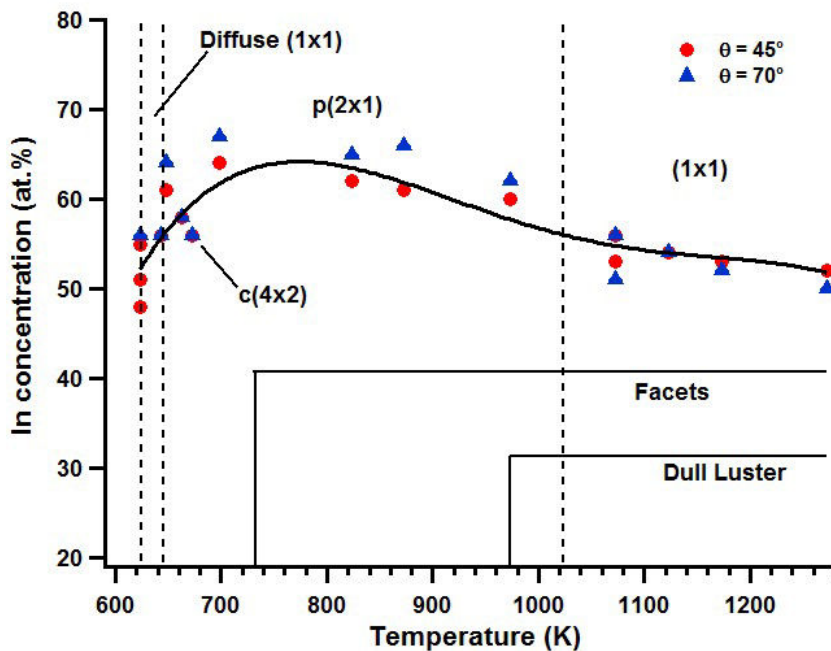


FIGURE 4.14: Surface compositions and LEED observations from the second set of InPd(110) experiments are displayed above. Each measurement/observation was performed after sputtering and annealing the surface. The windows labeled ‘Facets’ and ‘Dull Luster’ represent the respective annealing temperature range where initial faceting and surface appearance change can be expected. However once observed, it seems faceting can occur at all temperatures. The ‘Dull Luster’ is irreversible until the sample is re-polished.

composition measurements (1173 K point of Fig.4.14) showing $\text{In}_{52.0 \pm 5.0} \text{Pd}_{48.0 \pm 5.0}$ in the top layer and $\text{In}_{53.0 \pm 5.0} \text{Pd}_{47.0 \pm 5.0}$ in the top two layers. These estimated information depths in composition assume that measurements were taken using 99 % of the In $3d_{5/2}$ and Pd $3d_{5/2}$ signal intensity; this method is described elsewhere [32, 123]. Most importantly, we find homogeneity between the surface and subsurface layer within error of the expected 1:1 In:Pd for bulk truncated InPd. Therefore, XPS, STM, and LEED unambiguously pointed towards bulk-truncated InPd(110).

The formation of bulk-truncated InPd(110) is highly desirable for studying chemical reactions pertaining to MSR catalysis. This is because each In(Pd) atom is surrounded by a (Pd)In atom in the only low-coordinated 1:1 In:Pd plane, i.e. a very simple surface where useful information on electronic and geometrical effects could be gained. The first two sets of experiments we performed, before reaching a reproducible recipe to form InPd(110)-(1x1), highlight the potential complexities associated with preparing surfaces of IMCs and alloy surfaces in general.

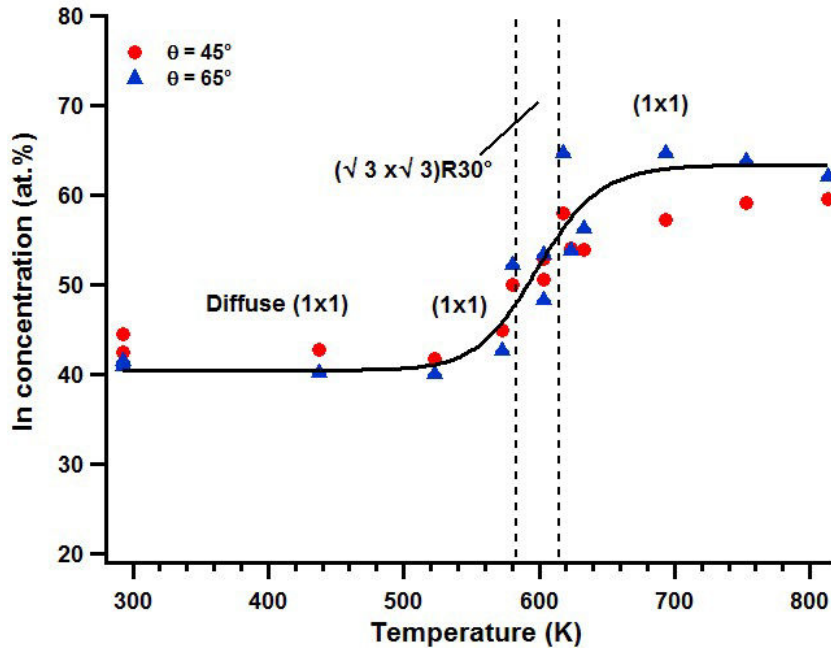


FIGURE 4.15: Concentration measurements after Ar+ sputtering (2 keV for 30 minutes) and annealing the InPd(111) surface are deduced from XPS data for two different take-off angles (θ is the angle between the surface normal and analyzer). The solid line in this figure is a guide for the eye only.

4.3.4 InPd(111)

The InPd(111) surface was examined with both XPS, LEED, and STM and by LEED I(E), as mentioned in Chapter 2. XPS data shows a similar trend to those of InPd(100) InPd(110). A (1x1) structure was predominantly observed with LEED. It appeared with both Pd-rich and In-rich compositions (Fig. 4.15). During the transition, a $(\sqrt{3} \times \sqrt{3})R30^\circ$ superstructure was observed (LEED and STM) for a stoichiometric (within error) InPd surface. However, it existed as the primary structure within a very narrow composition window. Note that the boundary-lines of Fig. 4.15 correspond to observations of weak $(\sqrt{3} \times \sqrt{3})R30^\circ$ LEED patterns.

LEED (Fig. 4.16 (a)) and STM (Fig. 4.17 (a)) measurements confirmed the presence of $(\sqrt{3} \times \sqrt{3})R30^\circ$ domains across the surface. STM measurements yielded a $(\sqrt{3} \times \sqrt{3})R30^\circ$ unit cell with lattice constant $a=7.90 \pm 0.10 \text{ \AA}$, in agreement with expected theoretical values (Fig. 4.4 and Table 4.1). The contrast showed negligible dependence on the tip bias, which was varied in 0.2 V increments from -1.4 to +1.4 V. Therefore, we cannot rule-out a true topographical effect. Note that the atomic radii difference of In and Pd is only 0.15 \AA [147], which is smaller than the surface roughness. Although the local chemical ordering may have been influenced by the abundance of surface and subsurface defects, there seemed to be no long-range chemical ordering.

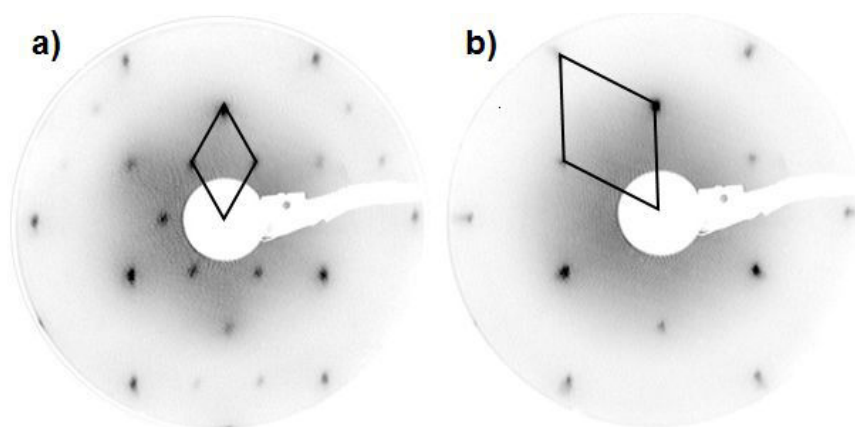


FIGURE 4.16: These LEED images, both taken at 50 eV, show the two superstructures for InPd(111). The unit cells of the $(\sqrt{3} \times \sqrt{3})R30^\circ$ (a) and (1×1) (b) LEED patterns are marked accordingly.

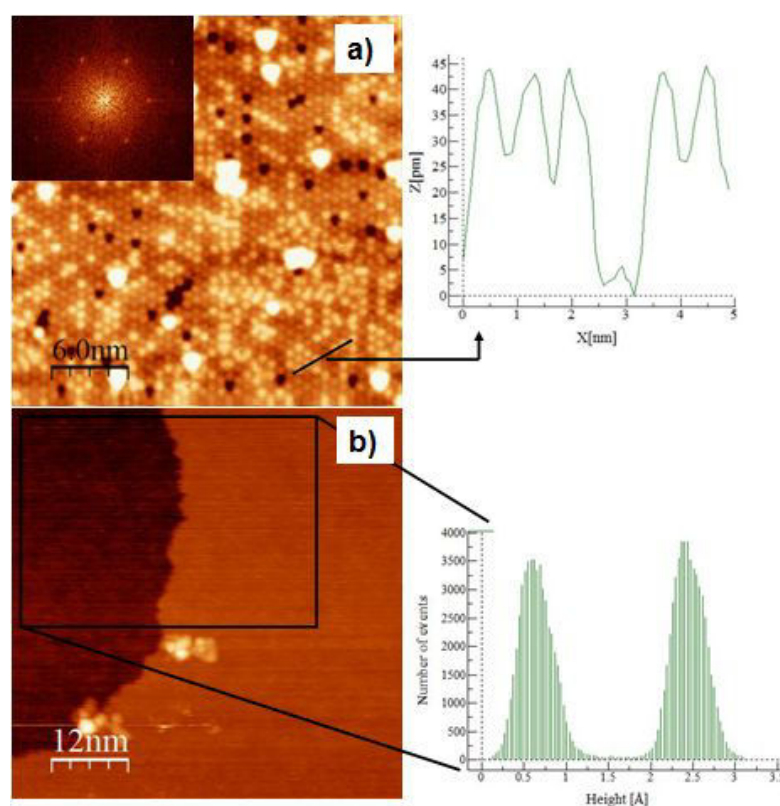


FIGURE 4.17: The above STM images correspond to InPd(111)- $(\sqrt{3} \times \sqrt{3})R30^\circ$ (a) and InPd(111)- (1×1) phases (b). The $(\sqrt{3} \times \sqrt{3})R30^\circ$ phase includes a 1D plot to show the difference between the two main types of contrast. An FFT of the 30 nm x 30 nm image (+1.8 V; 0.09 nA) confirms the hexagonal superstructure defined as a $(\sqrt{3} \times \sqrt{3})R30^\circ$ surface reconstruction. Image (b) (62 nm x 62 nm/+0.5 V; 0.07 nA) shows the step edge between two large terraces.

Moreover, the step heights were $1.85 \pm 0.05 \text{ \AA}$. This suggested underlying InPd(111) had a preferred In or Pd termination ($2 \times d_{(111)} = 1.876 \text{ \AA}$), but atomically resolved STM

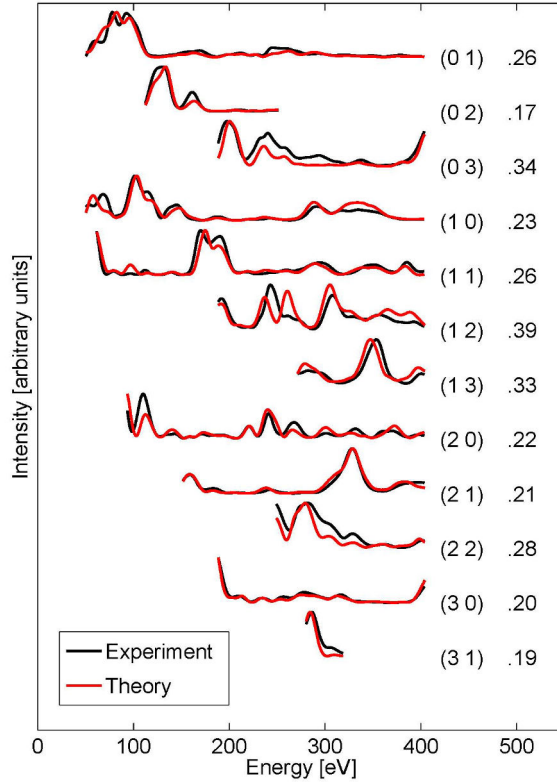


FIGURE 4.18: The experimental vs. theoretical $I(E)$ curves for 12 separate beams of the Pd-rich InPd(111)-(1x1) structure are shown. The theoretical data are from the best-fitted model of Fig. 4.19 and Table 4.2. Individual R factors for each (h,k) beam are indicated next to respective plots. A total R factor of .26 was calculated from the entire data set (total range of 2700 eV).

images pointed towards a chemically mixed-plane surface. A nearly identical step-height ($1.84 \pm 0.05 \text{ \AA}$) was measured for In-rich InPd(111)-(1x1), as shown in Fig. 4.17 (b). This image, and the corresponding LEED (Fig. 4.16 (b)) were taken after annealing to 773 K. The corresponding composition showed a slight enrichment of In ($\lesssim 5 \%$) in the top few layers, but within error of In-rich InPd(111). For InPd(111) ($\sqrt{3} \times \sqrt{3}$)R30°, the composition was near 1:1 In:Pd and uniform between top layers (1-3) and sublayers (3-5).

The composition measured for Pd-rich InPd(111)-(1x1) (Fig. 4.15) generally showed a slightly higher percentage of Pd in top layers, in agreement with the LEED $I(E)$ structure analysis, which will be described hereafter. Theoretical and experimental $I(E)$ data were acquired using the SATLEED code [58] and the EasyLEED program [98] respectively. The agreement between the experiment and calculations was evaluated using the Pendry R-factor, and the statistical errors were calculated using the Pendry RR-function [121]. The total energy range for the dataset was 2700 eV and included 12 beams. Fig. 4.18 shows the $I(E)$ experimental vs. theoretical data comparison for the best structure, which will be described next.

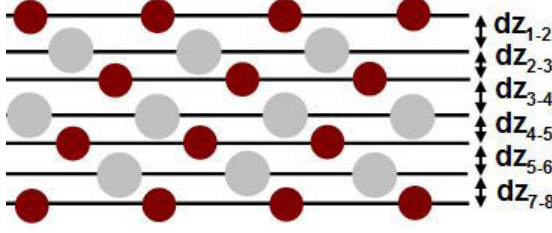


FIGURE 4.19: The above profile of the Pd-rich InPd(111)-(1x1) surface, viewed along the $[\bar{1} 0 1]$ axis, illustrates interlayer spacings in accordance with values of Table 4.2. The expansions/contractions of planes are slightly exaggerated for clarity.

Interlayer spacing (dz_{a-b}) [\AA]

dz_{1-2}	$= 1.01 \pm 0.02$
dz_{2-3}	$= 0.82 \pm 0.02$
dz_{3-4}	$= 1.07 \pm 0.02$
dz_{4-5}	$= 0.89 \pm 0.02$
dz_{5-6}	$= 0.95 \pm 0.02$
dz_{6-7}	$= 0.92 \pm 0.03$
dz_{7-8}	$= 0.93 \pm 0.03$
dz_{8-9}	$= 0.96 \pm 0.03$
dz_{9-10}	$= 0.88 \pm 0.04$
dz_{10-bk}	$= 0.97 \pm 0.05$

TABLE 4.2: The above values are the relaxed interlayer spacings for the best fit geometry of InPd(111)-(1x1) LEED I(E) analysis; they correspond to an overall R factor of 0.26.

We found the best overall Pendry R-factor was 0.26 for simple ordered InPd, with Pd on the top layer. The optimized structure (model in Fig. 4.19) showed a substantial outward expansion of the top and third layer. The second and fourth layer contracted into the bulk (bulk interplanar distance: 0.9379 \AA). These parameters, along with all interplanar spacings for the top 10 layers, are shown in Table 4.2.

Other models were also tested. This included disordered alloys with In:Pd 50:50 mixture in both top and top two layers. These were tested over both In-terminated and Pd-terminated bulk InPd(111) for a total of 4 combinations. Initial agreement for all scenarios (≥ 0.60) was worse than for our model. So we can rule-out a 50:50 mixed terminated surface as was determined by LEED I(E) analysis on NiAl(111) [108], another CsCl-type compound. Furthermore, seven other ordered structures (corresponding to pure In or Pd terminations) were tested. Terminations of the top four layers differed as such: In-Pd-In-Pd, Pd-In-In-Pd, In-Pd-Pd-In, In-Pd-In-In, Pd-In-Pd-Pd, Pd-Pd-In-Pd, In-In-Pd-In. The fifth layer had the opposite termination as the fourth layer and lower planes alternated as expected for bulk InPd(111).

4.4 The polycrystalline surface

The polycrystalline sample was examined both ‘in-house’ (STM, XPS) and at beamline I06 (LEEM, μ XPS, and micro-spot LEED) of the Diamond Light Source (UK). The sample was prepared by Ar+ sputtering - annealing cycles. The final annealing temperature for the STM results, presented at the end of this section, was $\sim 1125 \text{ K}$. For all other results, the annealing temperatures were between 875 and 935 K.

The majority of results were obtained at beamline I06 and will be presented first. We will start with the LEEM results. This will be followed by LEED observations of the few individual grains studied. Next, surface compositions derived from μ XPS data of five individual grains will be presented. Then, we will give a description of the electronic structure of these five grains. Finally, STM and electron back-scattering diffraction (EBSD) data will be shown and compared to the results obtained at the synchrotron.

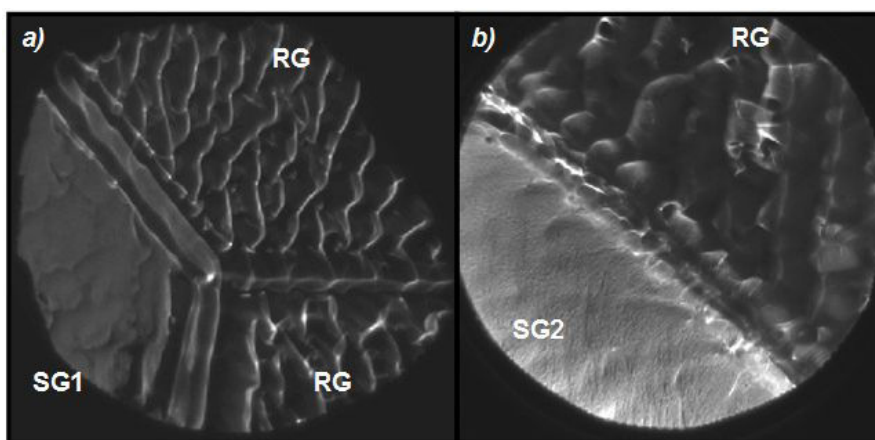


FIGURE 4.20: These LEEM images (a - 80 μm field of view (FOV) and b - 30 μm FOV) show InPd polycrystalline grain boundaries that are surrounded by features ~ 4 to 14 μm (a-SG1) and ~ 3 μm wide (b-SG2). Note that the ‘rough grains’ surrounding both ‘smooth grains’ are similar to, but not the same as RG1 and RG2.

In a general sense, we found two microscopically distinguishable grain surfaces formed in the region of the sample examined, namely, smooth grains (SGs) and rough grains (RGs). The first set of LEEM images, shown in Fig. 4.20, showed two distinct smooth grains (SG1 and SG2) surrounded by RGs. These RGs were different than those examined by μ XPS data (discussed later). Although we have categorized SG1 and SG2 as SGs, a closer look at the LEEM images in Fig. 4.20 showed the smooth grains were not perfectly flat. We found rather large smooth regions between ~ 5 to 15 μm on SG1 (Fig. 4.21). These features, probably from topographical defects, disrupted the overall flatness of SG1 and made it difficult to align the optical axis to the surface normal during experiments.

Similar features were not as apparent on SG2. This accounted for, in part, a more diffuse LEED pattern for SG1 (Fig. 4.22 (a)) than for SG2 (Fig. 4.22 (b)). Furthermore, the LEED pattern showed no obvious changes to SG2 after dosing the clean surface with 20 L of H_2 (Fig. 4.23). Comparisons of LEED patterns (at the same energy - not shown) showed no differences, in relative intensity between (h, k) spots of the ‘clean’ and ‘ H_2 - dosed’ surfaces.

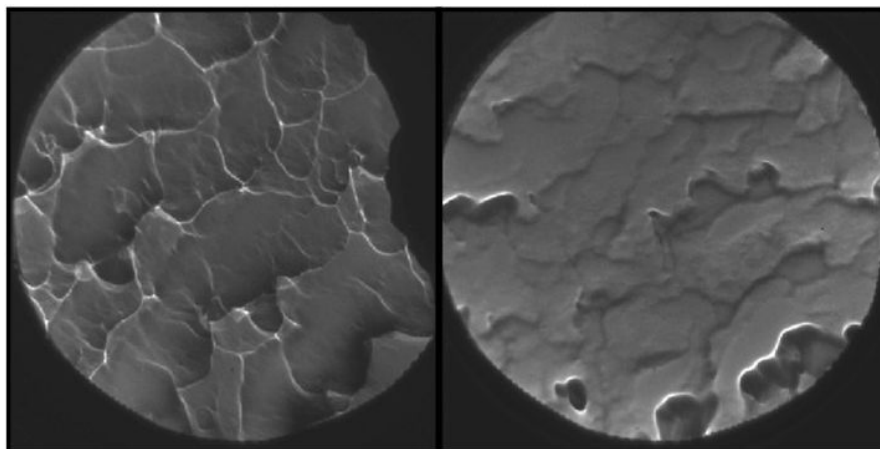


FIGURE 4.21: Contrast from flat features on SG1 (InPd polycrystal) are shown in two different imaging modes. Both images were taken at a 50 μm FOV.

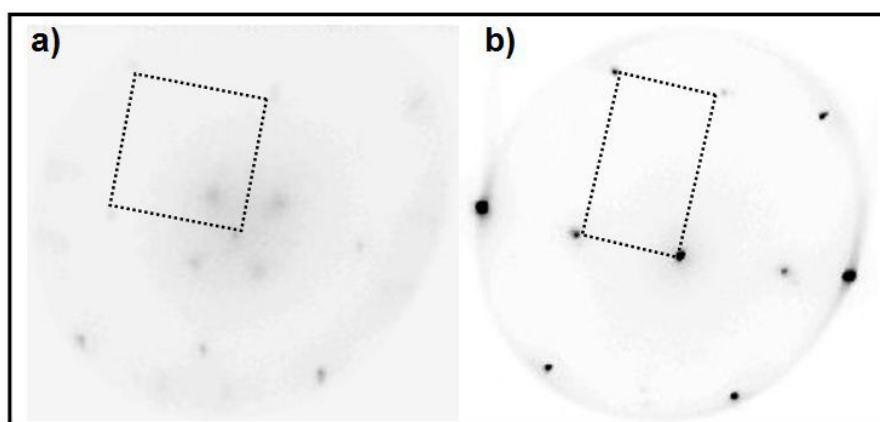


FIGURE 4.22: a) The 29 eV micro-spot LEED Image of SG1 (InPd polycrystal) shows a square unit cell having interior beams from an unknown surface reconstruction. b) This image of SG2, taken at 30 eV, shows a well-ordered InPd phase.

The LEED patterns of Fig. 4.22 showed two distinct LEED patterns resulting from surface reconstructions of differing InPd orientations. The (h,k) beams within the unit cell of SG1 pointed towards a large surface structure, whereas the sharp LEED pattern from SG2 was of a low-indexed surface. In comparison to our findings on InPd(100) and InPd(110), we found LEED patterns of SG1 and SG2 were consistent with $p(4\times 4)$ and (1×1) structures observed from the respective single crystals (further discussed at the end of this section). We also found the SG2 LEED pattern remained after 30L exposure of O_2 to the clean surface at room temperature (LEED image not shown).

In agreement with LEED, there was no O 1s peak visible in corresponding μXPS data on the same grain. However, greater In concentration (O_2 -dosed SG2: $\text{In}_{59}\text{Pd}_{41}$ vs. non- O_2 -dosed SG2: $\text{In}_{40}\text{Pd}_{60}$) was noted in the area sampled. This suggests In segregation is induced by O_2 exposure. Note that all references to SG2 refer to non- O_2 -dosed SG2

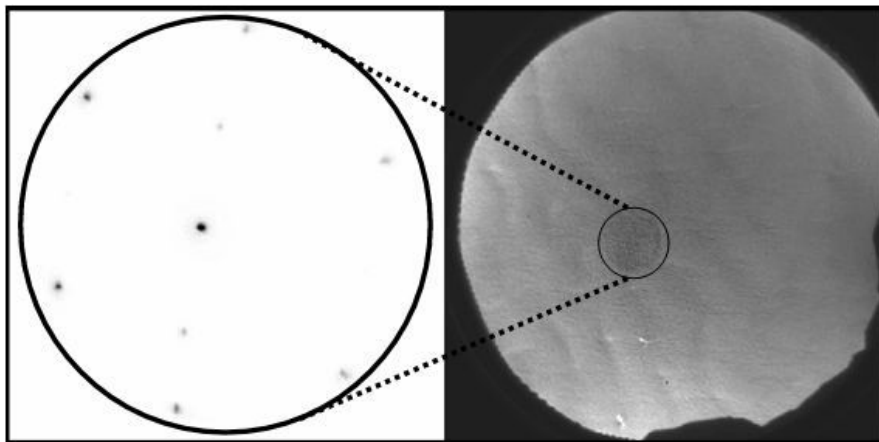


FIGURE 4.23: The LEED (left: 38 eV) and LEEM image (right: 50 μm FOV) of SG2 (InPd polycrystal) were acquired after 20L exposure to H_2 . The electron beam caused damage to the surface in LEED mode; this shows the micro-spot sampling area ($\sim 6 \mu\text{m}$ diameter).

unless otherwise stated. This region of O_2 -dosed SG2 was close to the grain boundary of SG3. For SG3, μXPS data indicated In-rich InPd towards the boundary ($\text{In}_{59}\text{Pd}_{37}\text{O}_4$) with a small but measurable amount of O_2 (so there was an excess of In on both sides of this smooth to smooth grain boundary). Possibly, oxygen trapped at grain boundaries induces In enrichment.

The VB data of SG3 showed a negligible change in comparison to the Pd - rich, InPd SG2 (Fig. 4.24). However, the rough grains RG1 ($\text{In}_{57}\text{Pd}_{43}$) and RG2 ($\text{In}_{53}\text{Pd}_{47}$) both showed an increase in DOS at ~ 2 eV in the top-most layers (top RG spectra of respective Fig. 4.25 and Fig. 4.24). The IMFP for top spectra of Fig. 4.25 corresponded to a depth of ~ 2 to 8 ML for the lowest coordinated facets of InPd. The IMFPs for In $3d_{5/2}$ and Pd $3d_{5/2}$, used in surface composition measurements, were calculated at 4.68 \AA and 4.85 \AA respectively (about half the value as IMPFs for top spectra of Fig. 4.25). The most notable observation were differences between VB data of SG1 and SG2 (bottom of Fig. 4.24). We would expect the grain with higher In composition (SG1: $\text{In}_{56}\text{Pd}_{44}$) to exhibit a narrower DOS further away from E_F , but we observe just the opposite. However, the VB spectra of both SG1 and SG2 have a localized peak maximum around 2 eV. So there is only an apparent difference in relative intensities and we cannot rule-out an effect from the experiment.

A separate set of concentration measurements were performed on data taken with traditional XPS. The intensities were measured from a Mg K_α source (1253.6 eV) with an analyzer aperture setting for a lateral sampling area of ~ 1.6 mm. We found a global composition of $\text{In}_{53}\text{Pd}_{47}$, which was the same as the average value of our clean surface SG and RG measurements.

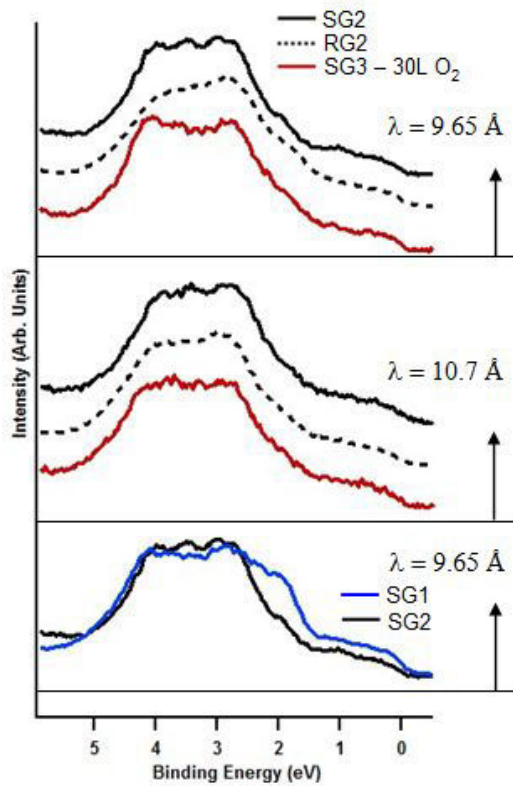
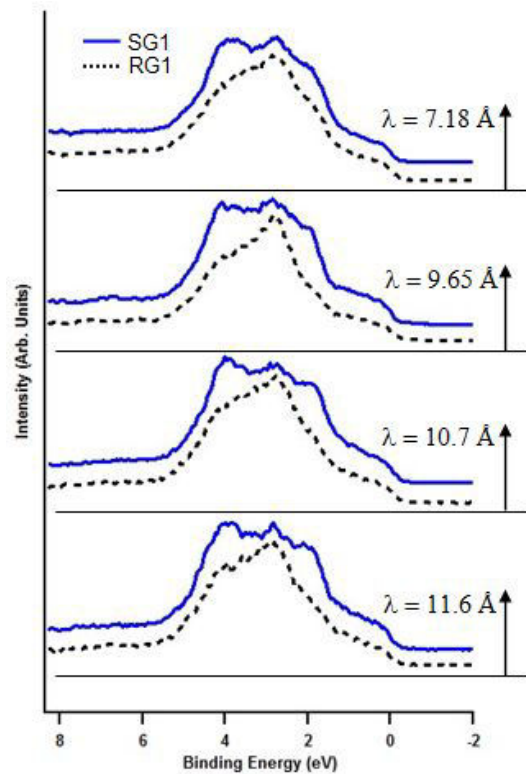


FIGURE 4.24: The spectra show VB data of SG2 and RG2 (InPd polycrystal). The calculated IMFPs were based on stop voltages of 445.5 eV (top) and 545.1 eV (middle). Another smooth grain (SG3) shows similar features to SG2 despite a small but measurable amount of surface oxygen. At the bottom of the figure, overlapped intensities shows substantial difference in the DOS between SG1 and SG2.

FIGURE 4.25: The VB data from SG1 and RG1 (InPd polycrystal) are displayed such that the top spectra is more surface sensitive whereas the bottom spectra is more bulk-like. The IMFPs displayed next to the graph were approximated using the kinetic energy within the dispersion plane corresponding to the stop voltages, from top to bottom: 245.5 eV, 445.5 eV, 543.5 eV, and 643.5 eV.



Moreover, we observed formations of flat terraces and heavy step bunching with STM. This depended on the grain examined. We can indirectly correlate these observations to ‘smooth’ and ‘rough’ grains. In particular, we observed structures on large terraces having a pseudo-square centered structure as shown in Fig. 4.26. The corresponding calculated FFT eluded to an agreement (of first order beams) to the LEED image shown in Fig. 4.22 (a). However, the elusive structures could not be measured to the precision necessary to be conclusive.

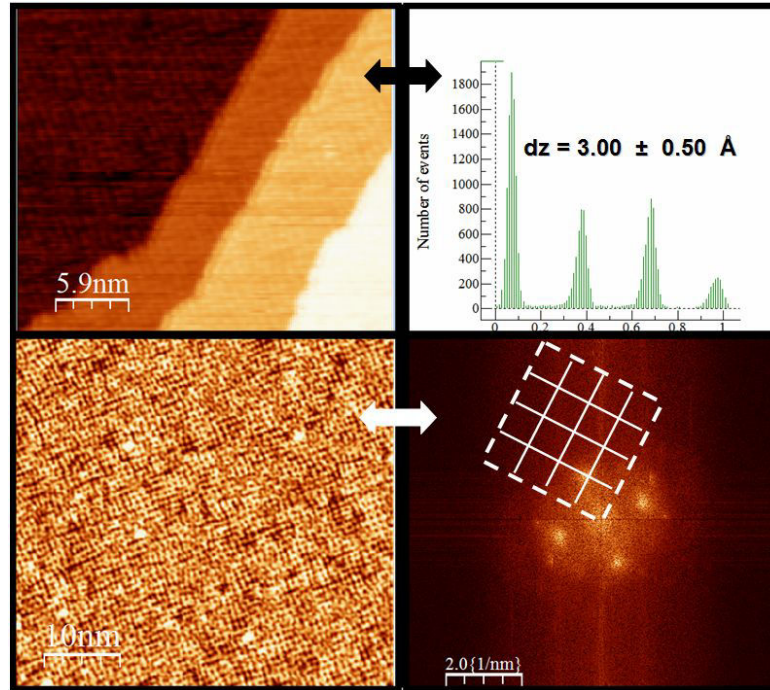


FIGURE 4.26: The STM images above show formations of quasi-ordered rectangular centered structures on terraces of the polycrystalline sample. The upper-left image (100 nm^2 ; $V=+1.1 \text{ V}$; $I=0.08 \text{ nA}$) and lower-left image (50 nm^2 ; $V=+1.1 \text{ V}$; $I=0.08 \text{ nA}$) show respective terraces and atomically resolved quasi-ordered structures. Measurements of the average terrace height and FFT of the primitive unit cell are indicated appropriately.

A comparison between the LEED of SG1 (Fig. 4.22 (a)), the aforementioned STM data (Fig. 4.26), and InPd(100)-(4x4) (Fig. 4.8) reveal striking similarities. Measurements of the small quasi-square structures/terrace heights (STM) were similar to those of InPd(100)-(4x4). Although the FFT did not show a long-range p(4x4) pattern, it can be attributed to poorer quality images. Moreover, when comparing LEED patterns (obtainable for SG1 and InPd(100)-(4x4)), SG1 had first-ordered (h,k) beams as those of InPd(100)-(4x4). Therefore, we attribute one type of the ‘smooth’ grain structure to InPd(100)-(4x4). This was likely the structure of SG1.

The other smooth grain, SG2, showed a sharp LEED pattern and a unit cell of a low-coordinated structure with an $a^*:b^*$ ratio of InPd(110)-(1x1). However, the same ratio

exists for InPd(110)-(2x1). Hence, we compared relative intensities of (1x1) beams between both data sets taken over the same energy range. This was accomplished by noting which supposed (1,0) or (0,1) beam intensity was brighter at each selected energy. We found SG2 was indeed InPd(110)-(1x1).

Although we found structural similarities between the InPd(100)/InPd(110) single crystals and SG1/SG2, it is important to point-out differences in annealing temperatures. For LEEM, micro-spot LEED, and μ -XPS data on SG1 and SG2, the polycrystalline sample was annealed to 875 K. The polycrystalline sample was annealed to 1125 K for the STM data obtained on the single grain containing the InPd(100)-p(4x4) superstructure (4.26). However, this superstructure was observed between 550 and 650 K on the single crystal, i.e. near the stoichiometric composition. The single crystal was not tested beyond ~ 825 K (to avoid potential faceting), but it is likely that In-rich $c(3\sqrt{2} \times \sqrt{2})R45^\circ$ superstructures would decompose after surface In-depletion upon reaching higher annealing temperatures. This was observed for InPd(110), where (1x1) structures were observed at a similar low-temperature transition region and after annealing past ~ 1020 K.

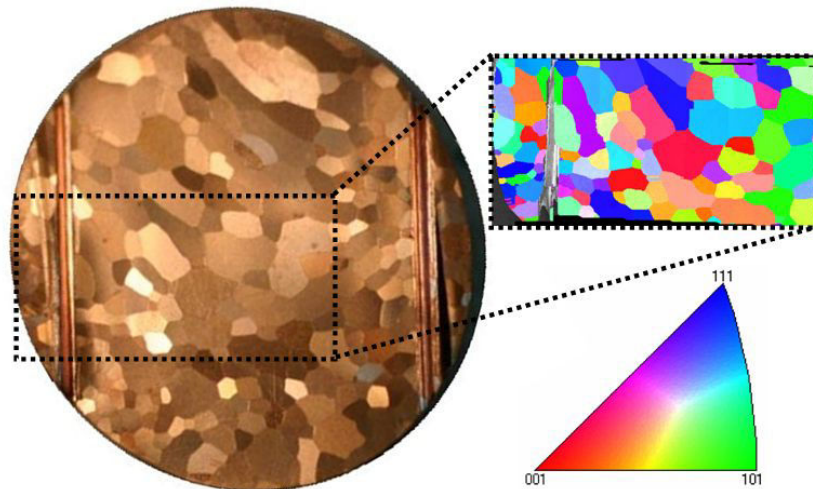
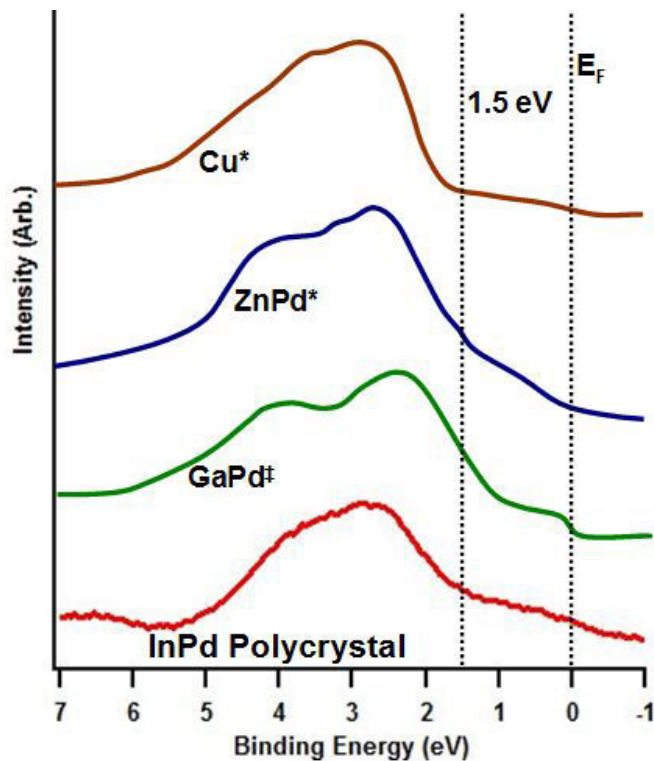


FIGURE 4.27: The following EBSD data of the polycrystalline sample shows a variety of grain orientations (color coded). The EBSD data is acquired from probing depth on the order of $1 \mu\text{m}$. The grain orientations are deduced from an average surface normal (of the area sampled, shown by the dotted rectangle).

Furthermore, electron backscattering diffraction (EBSD) indicated the presence of several InPd(110) and InPd(100) grains. More specifically, towards the center of the sample, the data indicated both these grains existed next to others of various orientations; this being the general area where micro-spot LEED, μ XPS, and STM experiments were performed. Unfortunately, it was not possible to correctly map the grains under LEEM, due to their large size and the limited x-y range of the instrument from the center of

FIGURE 4.28: The XPS VB data of Cu, ZnPd and GaPd are retraces from the work by Tsai *et al.* [118]* and Kovnir *et al.* [79].[‡] These data, and our VB data from the InPd polycrystal, exhibit a ‘Cu-like’ DOS.



the sample. However, knowing orientations of all center-located grains, coupled with our other findings discussed above, we can presume SG1 was InPd(100)-(4x4), SG2 was InPd(110)-(1x1), and the ‘rough grains’ were likely of higher indexed crystallites.

4.5 Discussion and Conclusion

When considering the multiple grains of various orientations, as clearly depicted by EBSD data (Fig. 4.27), ‘global’ information for electronic structures can be most adequately compared to other experimental work on Zn-Pd and Ga-Pd systems. Our VB data show InPd to have a d-band center and width very similar to Cu, GaPd, and ZnPd (shown in Fig. 4.28). However, all three IMCs have more occupied DOS within 1.5 eV from the Fermi edge than Cu. Note that the GaPd spectra was taken at a synchrotron using a much lower photon energy.

The VB data from our polycrystal sample also compared well to ZnPd for its given surface composition (In₅₃Pd₄₇). Although not shown, the width and d-band center is nearly identical to Zn_{53.2}Pd_{46.8}, as opposed to the wider and shifted (towards E_F) VB observed for Pd-rich ZnPd (Not shown) [43].

As pure IMCs, both InPd and ZnPd exhibit much higher selectivity towards MSR than GaPd, yet all three have similar VB spectra. However, following reductive treatment, Pd-Ga/Ga₂O₃ is known to transform from CO-selective methanol dehydrogenation to

CO₂ MSR because of IMC formations [69]. This exemplifies the importance of the oxide support and preparation method in real powder catalysts.

Our work however, is focused on the IMC InPd. In addition to the ‘global’ VB data we obtained for polycrystalline InPd, we also characterized a few individual grains by LEEM, micro-spot LEED, and μ XPS. We found the sample exhibited an inhomogeneous composition as a consequence of In-rich grain boundaries. The microscopic appearance of individual grains had either ‘smooth’ or ‘rough’ textures. The inhomogeneities near well-ordered ‘smooth’ grain boundaries were evidenced by μ XPS. Namely, an increase from about 40 to 59 at. % In towards the boundary of an InPd(110) grain was measured. The corresponding micro-spot LEED showed a diffuse (1x1) pattern near the boundary, but a very sharp (1x1) where the composition was measured at 40 at. % In. These findings can be compared to a previous study that investigated the properties of point defects in sputtered Pd_{1-x}In_x films [174, 175]. The authors found that texture in In-rich InPd films, depended on In/Pd concentrations and the presence of In-rich grain boundaries. Our non-textured polycrystal also showed an enrichment of In near grain boundaries. Furthermore, an increase of Pd vacancies near grain boundaries may have caused our (1x1) LEED pattern to appear diffuse. It was noted by Wu *et al.* that an InPd unit cell with one In atom and one Pd vacancy [174] was found at In-rich grain boundaries. However, we cannot conclude that the same structure formed towards the In-rich grain boundary of InPd(110). This is because DFT calculations, performed in our group, indicate favorable surface segregation for In antisites for In-rich InPd(110).

For the single crystals, we found In was preferentially sputtered during preparation. Upon annealing the sputtered surfaces, seven different metastable structures were observed during the re-segregation of In towards top layers (Fig. 4.4 and Table 4.1). Our major findings included faceting of the InPd(110) surface, the InPd(111)-($\sqrt{3} \times \sqrt{3}$)R30° superstructure, and the surface structure of InPd(111)-(1x1) from LEED I(E) analysis. The faceting of InPd(110) has been recently studied by P. Gille’s research group in München [64]. It seems that changes to the bulk volume from In-loss while annealing may induce faceting, i.e. the lattice constant increases when Pd vacancies of In-rich InPd dissipate. Note that we cannot exclude faceting of InPd(100) and InPd(111) at high enough annealing temperatures. For the ($\sqrt{3} \times \sqrt{3}$)R30° superstructure on InPd(111), STM showed negligible contrast variation ranging from a -1.4 to 1.4 V tip bias. So the mixed-plane surface could be from both chemical and topographical inhomogeneities. The same crystal also exhibited (1x1) structures for both Pd-rich InPd and In-rich InPd. LEED I(E) data showed good agreement (overall R-factor of 0.26) for Pd-rich (1x1). The model had a Pd-terminated top layer, as expected from XPS surface composition measurements. Moreover, we attempted to determine an In-rich InPd(111)-(1x1) structure, but the R-factor of the best model was too poor to draw any conclusions.

Nevertheless, it is worth mentioning that In-terminated models showed worse agreement than those of Pd-terminations for In-rich InPd. Although there was Auger electron spectroscopy (AES) data taken for this experiment, which indicated In-rich InPd(111), there was a significant discrepancy in the annealing temperatures used for LEED I(E)/AES experiments versus those corresponding to the accurate composition measurements of XPS data. We estimated temperature readings for LEED I(E)/AES experiments to be roughly 50 K higher than those of XPS, STM, and LEED experiments. Additionally, our DFT calculations suggested In-terminated InPd(111) had a lower surface energy (0.67 J/m^2) than Pd-terminated InPd(111) (1.14 J/m^2) in the In-rich limit. If our In-rich observation was a Pd-terminated structure, it would seem that thermodynamic equilibrium between the bulk and altered surface layers was likely not established during our low-temperature preparation method.

Chapter 5

Conclusion

A series of In-Pd intermetallic compounds have been investigated in order to obtain some basic knowledge on electronic and geometric/crystallographic surface structures at the atomic scale, using model systems. These results are important not only as such but will also be helpful to better understand the catalytic properties of these intermetallic compounds for the MSR reaction. The surfaces have been characterized by photoemission spectroscopy, low-energy electron diffraction and scanning tunneling microscopy. Additional dynamical LEED-I(V) was also performed as well as micro-LEED and PEEM. These experimental results were complemented by DFT calculations performed in our research group to assist the interpretation of the results.

A first set of experiments was first performed on surface alloys (or near surface intermetallic phases) obtained by depositing In thin films on a Pd(111) substrate in ultrahigh vacuum with subsequent annealing. Various phases could be identified, depending on the initial thickness of the deposited In film and the annealing temperature. This allowed us to propose a schematic ‘phase diagram’ and provide an atomic scale description of each phase and the associated valence band structure as derived by photoemission spectroscopy. Indium is found to readily intermix with the Pd substrate at room temperature. At large enough coverages, the InPd cubic phase is formed with (110) orientation and three rotational domains coexisting on the Pd(111) substrate. The near surface intermetallic compound has an electronic structure characteristic of the bulk phase and can thus be considered as a model system for further surface reactivity study. For the largest coverages investigated, we also found that an In-rich phase can also be formed on top of the near stoichiometric InPd phase. This phase could be identified as an In_7Pd_3 compound, another cubic phase characterized by a relatively large unit cell. It is found unstable and transforms at moderate annealing temperature into the InPd phase. The InPd near surface intermetallic phase is itself unstable and disappears upon annealing

the system above 600 K as a result of either In diffusion into the bulk or In returning to the gas phase. This conclusion is consistent with the results of our theoretical study of InPd surface alloys using first-principles calculations demonstrating that In-doped Pd layers on Pd(111) are energetically more stable for In concentrations lower than 50 at. %. The formation of metastable phases with a global 1:1 composition are common to the related Zn/Pd(111) and Ga/Pd(111) systems. However, the composition changes are more gradual in the cases of Ga/Pd(111) and In/Pd(111) compared to Zn/Pd(111) for which a more pronounced plateau in the surface composition was observed between 400 and 550 K. The onset temperatures for alloy formation for the In on Pd(111) system was not determined in the present study but is lower or equal to 300 K. This is consistent with the cohesive energy calculated for the InPd compound (-3.57 eV/atom) which is intermediate between that of PdGa (-3.9 eV/atom) and ZnPd (-3.0 eV/atom). Concerning the orientation of the surface alloys, we found that the cubic 1:1 InPd near surface intermetallic phase adopts a (110) orientation with respect to the Pd(111) substrate whereas the 1:1 tetragonal ZnPd adopts a (111) orientation. In both cases, it corresponds to stoichiometric layers consisting of alternating atomic rows of Pd and In (or Zn) metals. Only one type of atomic rows is observed in corresponding STM images. For Zn/Pd(111), this feature can be ascribed to an outward shift of the Zn atoms and an inward shift of the Pd atoms (into the bulk) with respect to the bulk-terminated. This is consistent with the lower elemental surface energy of Zn compared to Pd. A similar effect was found to occur on the InPd surface alloy, as the elemental surface energy of In is also much lower than that of Pd. Such type of surface relaxation can have a significant effect on the surface reactivity.

In a second set of experiments, we could investigate the atomic structure of low index surfaces of the InPd CsCl cubic phase thanks to the availability of single crystals prepared by the group of Prof. Gille at the Ludwig Maximilians University in Munich. The three investigated surfaces ((100), (110) and (111)) showed a transition from an In-depleted near surface composition induced by preferential sputtering to an In-rich near surface composition upon annealing, the transition occurring in a temperature range between 580 to 650 K. The In concentration in the In-rich limit of the transition was higher for the (100) and (111) surface (~ 62 at. %) than for the (110) surface (~ 52 at. %). This may be not surprising as the (110) surface is stoichiometric while the (100) and the (111) surfaces are not. This concentration difference in the In-rich limit might be a consequence of surface plane selection at pure In bulk planes in the case of (100) and (111) surfaces while this is not possible for (110) surface. The surface energies of the three low-index surface have been evaluated by DFT and it was found that the In-terminated surface is indeed preferred in the In-rich limit of the chemical potential, thus in agreement with the experiments. These changes in the near surface chemical composition were accompanied

by various structural phase transitions and a large variety of surface reconstructions could be identified and characterized. Altogether, our results do not point towards a massive In surface segregation in these systems and therefore single crystal surfaces should be considered as better model systems as near surface intermetallic phases for further surface reactivity studies, as they appear to have a better thermal stability. However, we found that surface faceting starts to occur probably above 800 K. This temperature range should be considered as a limit above which the surface might be modified. We also found that grains from a polycrystalline sample observed individually reproduced the behavior expected from single crystal studies, thus providing a ‘trustful average’ of all low index orientations although far less convenient for comprehensive surface studies.

The end goal of this work would be to better understand the MSR reaction mechanism, so that catalysts can be engineered for optimal performance. This begins with understanding the surface where the reactions take place, as described in this manuscript. This will be the starting point for future studies involving molecular adsorption.

By exposing our well-characterized IMC surfaces to methanol and water under UHV, we could gain valuable knowledge regarding adsorption and dissociation behavior of the two primary MSR reactants. Furthermore, exposure to intermediates such as formaldehyde would provide insight on secondary reactions. The findings from these studies however, could be difficult to interpret without a prior understanding of O₂ and H₂ surface interactions. We have already begun exploring O₂ adsorption on our crystal surfaces. Our initial results show O₂ exposure at moderate temperature induces In oxide formation with long range crystalline order, the structure of which is still to be understood.

Appendix A

Pendry R-Factor

Excerpt from Master's Thesis [99]:

The Pendry r-factor reflects similarity between theoretical and experimental curves. It accounts for the derivative of intensity (I) by introducing a logarithmic derivative function, $L(E)$, expressed as follows:

$$L(E) = \frac{dI/dE}{I} \quad (\text{A.1})$$

By including the imaginary part of an interaction potential (V_{0i}), which is related to attenuation of scattered electrons that affect $I(E)$ peak widths, the following term can be defined:

$$Y(E) = \frac{L^{-1}}{L^{-2} + V_{0i}^2} \quad (\text{A.2})$$

And the Pendry r-factor is defined as follows:

$$R = \frac{\int (Y_t - Y_e)^2 dE}{\int (Y_t + Y_e) dE} \quad (\text{A.3})$$

Y_e and Y_t are from experimental and theoretical data respectively. This expression, being normalized to 1 for two completely uncorrelated curves, vanishes when $Y_t \rightarrow Y_e$ [88, 121].

Y_t can be fine-tuned by adjusting several SATLEED parameters until the smallest r-factor for a given model is obtained. Generally, the smallest r-factor is considered to show best agreement, but the range of data should also be considered [99].

Appendix B

LEED

Excerpt from Master's Thesis [99]:

LEED can be considered the most comprehensive and versatile surface crystallography technique to date [54]. Since the 1960s, it has been widely used as a surface characterization tool [54, 86]. The basic principles of LEED come from conservation of energy and momentum.

A coherent beam of electrons with a wavelength of $(150/E)^{1/2}$ Å (the energy of the incoming electrons is expressed in eV), ideally incident to a crystal surface, scatter off underlying crystal planes. The electron energy is a controllable parameter during experiments, and therefore the wavelength. This is due to the de Broglie wave relationship:

$$\lambda_e = \frac{h}{m_e v} = \sqrt{\frac{150eV}{E_{k_0}}} \text{Å} \quad (\text{B.1})$$

Waves of electrons are scattered off only a few surface planes because of a small inelastic mean free path typically around an angstrom. In comparison to X-Ray diffraction, which has a photon path typically a few microns and periodicity lateral and perpendicular to the surface represented in the Laue equation,

$$\Delta\mathbf{k}(m_1\mathbf{a}_1 + m_2\mathbf{a}_2 + m_3\mathbf{a}_3) = 2\pi n \quad (\text{B.2})$$

the shorter penetration depth of electrons (from LEED) only clearly shows periodicity parallel to the surface plane so the Laue equation for LEED becomes:

$$\Delta\mathbf{k}(m_1\mathbf{a}_1 + m_2\mathbf{a}_2 + m_3\mathbf{a}_3) = 2\pi n \rightarrow \Delta\mathbf{k}_{\parallel} = \mathbf{g}_{\mathbf{h},\mathbf{k}} \quad (\text{B.3})$$

Where $\Delta\mathbf{k} = \mathbf{k} - \mathbf{k}_0$, \mathbf{k}_0 is the incoming wave vector and \mathbf{k} is the elastically scattered wave vector; $\Delta\mathbf{k}_{\parallel}$ is the component of $\Delta\mathbf{k}$ parallel to the surface, h and k are integers and $\mathbf{g}_{h,k}$ are reciprocal lattice vectors [54, 86]. A more quantitative treatment and further background of the above equation can be found in ref. [169]. When including scattering from individual atoms, phase differences in path lengths and multiple scatterings, the lattice sum can be defined as follows:

$$A_{\Delta k} = \sum_n \sum_m \exp(i\Delta\mathbf{k} \cdot \mathbf{A}) F_{\Delta k} \quad (\text{B.4})$$

Where $\mathbf{A} = n\mathbf{a} + m\mathbf{b}$, a real surface vector and the geometrical structure factor, $F_{\Delta k}$ is defined as:

$$F_{\Delta k} = \sum_j f_j \exp(i\Delta\mathbf{k} \cdot \mathbf{r}_j) \quad (\text{B.5})$$

This is an important result because, because the amplitude of $A_{\Delta k}$ vanishes except when $\Delta\mathbf{k}_{\parallel} = \mathbf{g}_{h,k}$ so multiple scattering effects of $F_{\Delta k}$ can be separated out [169].

When the LEED beam is at normal incidence and $\Delta\mathbf{k}_{\parallel} \rightarrow \mathbf{k}_{\parallel}$, perpendicular k-components (\mathbf{k}_z) can be examined by considering conservation of energy and momentum of an elastically scattered incoming wave as follows:

$$k_z(h, k) = \sqrt{\frac{2m_e E_{k_0}}{\hbar^2} - |\mathbf{k}_{\parallel}(h, k)|^2} \quad (\text{B.6})$$

Because $|\mathbf{k}_0|^2 = 2mE/\hbar^2$, for fixed values of $|\mathbf{k}_{\parallel}|$, only k_z values change as a function of beam energy [54]. By considering both this and the scattering amplitude of $A_{\Delta k}$, z-component information buried in intensity patterns of LEED (h, k) beams can be found by varying incident beam energies (I(E) or I(V) data). These intensities usually have peak values similar to Bragg peaks at specific energies in X-Ray diffraction. But, instead of sharp peaks corresponding to periodic z components, LEED I(E) intensity peaks are broadened due to multiple scatterings. Also, the beam only probes top surface layers so Bragg peaks are much less pronounced. On the contrary though, surface features are more pronounced in LEED I(E) data. For a full discussion on I(E) peak data pertaining to specific surface features, please see discussion in ref. [54, 169].

Dynamical Theory is the basis for LEED quantitative calculations of this thesis and described in refs. [54, 86, 88, 169]. This theory is an extension from what was just discussed, but accounts for large electron cross sections of ion cores so that multiple scatterings become important [30, 73].

Bibliography

- [1] ARMBRÜSTER, M., SCHLÖGL, R., AND GRIN, Y. Intermetallic compounds in heterogeneous catalysis—a quickly developing field. *Science and Technology of Advanced Materials* 15, 3 (2014), 034803.
- [2] ARMBRÜSTER, M., BEHRENS, M., FOETTINGER, K., FRIEDRICH, M., GAUDRY, E., MATAM, S. K., AND SHARMA, H. R. The intermetallic compound ZnPd and its role in methanol steam reforming. *Catalysis Reviews - Science and Engineering* 55, 3 (2013), 289–367.
- [3] ATREI, A., BARDI, U., TORRINI, M., ZANAZZI, E., ROVIDA, G., KASAMURA, H., AND KUDO, M. Structure of a non-bulk termination of the clean Pt₃Sn(111) surface: a study by low-energy electron diffraction and x-ray photoelectron diffraction. *Journal of Physics: Condensed Matter* 5, 14 (1993), L207.
- [4] ATREI, A., PEDOCCHI, L., BARDI, U., ROVIDA, G., TORRINI, M., ZANAZZI, E., HOVE, M. V., AND ROSS, P. LEED structural analysis of the (001) surface of the ordered fcc Pt₃Ti alloy. *Surface Science* 261, 1–3 (1992), 64 – 68.
- [5] ATTARD, G., AND BARNES, C. *Surfaces*. Oxford Chemistry Primers. Oxford University Press, Incorporated, 1998.
- [6] BARDI, U. The atomic structure of alloy surfaces and surface alloys. *Reports on Progress in Physics* 57, 10 (1994), 939.
- [7] BARDI, U., ATREI, A., CORTIGIANI, B., ROVIDA, G., AND TORRINI, M. X-ray photoelectron diffraction study of an oxidized Pt/Co(001) alloy surface: evidence for atomic scale rippling of the CoO overlayer. *Surface Science* 282, 3 (1993), L365 – L369.
- [8] BAUER, E. Low-energy-electron microscopy. *Reports on Progress in Physics* 57, 9 (1994), 895–938.
- [9] BAUER, E. LEEM basics. *Surface Review and Letters* 5, 6 (1998), 1275–1286.

- [10] BAYER, A., FLECHTNER, K., DENECKE, R., STEINRUCK, H., NEYMAN, K., AND ROSCH, N. Electronic properties of thin Zn layers on Pd(111) during growth and alloying. *Surface Science* 600, 1 (2006), 78–94.
- [11] BECCAT, P., GAUTHIER, Y., BAUDOING-SAVOIS, R., AND BERTOLNI, J. Monotonous concentration profile and reconstruction at Pt₈₀Fe₂₀(111): LEED study of a catalyst. *Surface Science* 238, 1–3 (1990), 105 – 118.
- [12] BIELZ, T., LORENZ, H., AMANN, P., KLÖTZER, B., AND PENNER, S. Water-gas shift and formaldehyde reforming activity determined by defect chemistry of polycrystalline In₂O₃. *The Journal of Physical Chemistry C* 115, 14 (2011), 6622–6628.
- [13] BLIGAARD, T., AND NØRSKOV, J. K. Ligand effects in heterogeneous catalysis and electrochemistry. *Electrochimica Acta* 52, 18 (2007), 5512 – 5516.
- [14] BORODZIŃSKI, A., AND BOND, G. C. Selective hydrogenation of ethyne in ethene-rich streams on palladium catalysts. part 1. effect of changes to the catalyst during reaction. *Catalysis Reviews* 48, 2 (2006), 91–144.
- [15] BORODZIŃSKI, A., AND BOND, G. C. Selective hydrogenation of ethyne in ethene-rich streams on palladium catalysts, part 2: Steady-state kinetics and effects of palladium particle size, carbon monoxide, and promoters. *Catalysis Reviews* 50, 3 (2008), 379–469.
- [16] BRADLEY, A. J., AND TAYLOR, A. *X-Ray Analysis of the Nickel-Aluminum System*. Proc. Roy. Soc. (London), 1937.
- [17] BRUNDLE, C., AND BAKER, A. E. *Electron Spectroscopy: Theory, Techniques and Applications*. No. 2 in *Electron Spectroscopy: Theory, Techniques and Applications*. Academic Press, 1978.
- [18] BRYANT, A. W., AND PRATT, J. N. Some calorimetric studies of palladium - indium alloys. *Proc. Colloque Int. du C.N.R.S. No. 201, Thermochimie 6th Edition* (1972), 241–247.
- [19] CARAZZOLLE, M., KLEIMAN, G., LANDERS, R., PANCOTTI, A., DE SIERVO, A., AND SOARES, E. Electronic structure and atomic positions of metallic surface alloys. *Journal of Molecular Catalysis A: Chemical* 281, 1–2 (2008), 9 – 13.
- [20] CASA SOFTWARE LTD. *Quantification using Asymmetric Line-Shapes*, 2005. http://www.casaxps.com/help_manual/manual_updates/calib_asymmetric_peaks.pdf.

- [21] CASA SOFTWARE LTD. *Peak Fitting in XPS*, 2006. http://www.casaxps.com/help_manual/manual_updates/peak_fitting_in_xps.pdf.
- [22] CASA SOFTWARE LTD. *CasaXPS Manual 2.3.15: Spectroscopy*, 1.3 ed., 2009. <http://www.casaxps.com/ebooks/OrangeBookRev1.3ebook.pdf>.
- [23] CASAXPS. *Line Shapes*. Casa Software Ltd., accessed May 12, 2014. http://www.casaxps.com/help_manual/line_shapes.htm.
- [24] CHEN, W., PAUL, J. A. K., BARBIERI, A., HOVE, M. A. V., CAMERON, S., AND DWYER, D. J. Structure determination of Pt₃Ti(111) by automated tensor LEED. *Journal of Physics: Condensed Matter* 5, 27 (1993), 4585.
- [25] CHEN, Z.-X., NEYMAN, K., GORDIENKO, A., AND RÖSCH, N. Surface structure and stability of PdZn and PtZn alloys: Density functional slab model studies. *Phys. Rev. B* 68, 2 (2003), 75417.
- [26] CHEN, Z.-X., NEYMAN, K. M., AND RÖSCH, N. Theoretical study of segregation of Zn and Pd in Pd–Zn alloys. *Surface Science* 548, 1–3 (2004), 291 – 300.
- [27] CHRISTENSEN, A., RUBAN, A. V., STOLTZE, P., JACOBSEN, K. W., SKRIVER, H. L., NØRSKOV, J. K., AND BESENBACHER, F. Phase diagrams for surface alloys. *Phys. Rev. B* 56 (1997), 5822–5834.
- [28] DHESI, S. S., CAVILL, S. A., POTENZA, A., MARCHETTO, H., MOTT, R. A., STEADMAN, P., PEACH, A., SHEPHERD, E. L., REN, X., WAGNER, U. H., AND REININGER, R. The nanoscience beamline (i06) at diamond light source. R. Garrett, I. Gentle, K. Nugent, and S. Wilkins, Eds., vol. 1234 of *AIP Conference Proceedings*, pp. 311–314. SRI 2009: 10th International Conference on Synchrotron Radiation Instrumentation, Australian Synchrotron, Melbourne, Australia, Sep 27-Oct 02, 2009.
- [29] DIAMOND LIGHT SOURCE LTD. Beamlines/surfaces and interfaces/i06: Nanoscience web area. <http://www.diamond.ac.uk/beamlines/surfaces-and-interfaces/i06.htm>, accessed March 30, 2014.
- [30] DIEHL, R. Adsorption studies using low energy electron diffraction. In *The Time Domain in Surface and Structural Dynamics*, G. Long and F. Grandjean, Eds., vol. 228 of *NATO ASI Series*. Springer Netherlands, 1988, pp. 439–465.
- [31] DONIACH, S., AND SUNJIC, M. Many-electron singularity in x-ray photoemission and x-ray line spectra from metals. *Journal of Physics C: Solid State Physics* 3, 2 (1970), 285.

- [32] DUGUET, T., GAUDRY, E., DENIOZOU, T., LEDIEU, J., DE WEERD, M. C., BELMONTE, T., DUBOIS, J. M., AND FOURNÉE, V. Complex metallic surface phases in the Al/Cu(111) system: An experimental and computational study. *Phys. Rev. B* 80 (2009), 205412.
- [33] EL-BORAGY, M., AND SCHUBERT, K. *Z. Metallkd* 62 (1971), 667.
- [34] ELLIOTT, R. P. *Constitution of Binary Alloys (1st Supplement)*. McGraw-Hill, 1965.
- [35] ELMITEC. LEEM and PEEM web area. <http://www.elmitec-gmbh.com/index.php>, accessed March 30, 2014.
- [36] FAIRLEY, N. *CasaXPS Manual: 2.3.15 Introduction to XPS and AES*, 1.2 ed. Casa Software Ltd., 2009. <http://www.casaxps.com/ebooks/XPS%20AES%20Book%20new%20margins%20rev%201.2%20for%20web.pdf>.
- [37] FINK, R., KOCH, T., KRAUSCH, G., MARIEN, J., PLEWNIA, A., RUNGE, B.-U., SCHATZ, G., SIBER, A., AND ZIEMANN, P. Formation of an ultrathin amorphous layer at In/Pd interfaces observed by local and nonlocal techniques. *Phys. Rev. B* 47 (1993), 10048–10051.
- [38] FINK, R., RUNGE, B. U., JACOBS, K., KRAUSCH, G., LUCKSCHEITER, B., PLATZER, R., WÖHRMANN, U., AND SCHATZ, G. Compound formation at Pd(100)/In interfaces. *Hyperfine Interactions* 78 (1993), 309–314.
- [39] FLANDORFER, H. Phase relationships in the In-rich part of the In-Pd system. *Journal of Alloys and Compounds* 336 (2002), 176–180.
- [40] FORT, D., SMALLMAN, R. E., AND HARRIS, I. R. A study of the β' -PdIn phase. *Journal of the Less-Common Metals* 31 (1973), 263–279.
- [41] FOURNÉE, V., PINHERO, P., ANDEREGG, J., LOGRASSO, T., ROSS, A., CANFIELD, P., FISHER, I., AND THIEL, P. Electronic structure of quasicrystalline surfaces: Effects of surface preparation and bulk structure. *Physical Review B* 62, 21 (2000), 14049–14060.
- [42] FRANCHY, R., AND SCHMITZ, G. Stabilization of the PdIn(111) surface via oxygen adsorption – studied by high-resolution electron energy loss spectroscopy and scanning tunneling microscopy. *EPL (Europhysics Letters)* 51, 5 (2000), 534.
- [43] FRIEDRICH, M., TESCHNER, D., KNOP-GERICKE, A., AND ARMBRÜSTER, M. Influence of bulk composition of the intermetallic compound ZnPd on surface composition and methanol steam reforming properties. *Journal of Catalysis* 285, 1 (2012), 41 – 47.

- [44] FU, H., AND HUANG, T. Comparison study of Pd/In/Pd, Pd-In/Pd, and Pd-In ohmic contacts to N-GaAs. *Solid-State Electronics* 38, 1 (1995), 89–94.
- [45] FUGGLE, J., AND ZOLNIEREK, Z. The relationship between empty d-state density and xps satellite intensities in nickel alloys. *Solid State Communications* 38, 9 (1981), 799 – 802.
- [46] GABASCH, H., KNOP-GERICKE, A., SCHLÖGL, R., PENNER, S., JENEWEIN, B., HAYEK, K., AND KLÖTZER, B. Zn adsorption on Pd(111) ZnO and PdZn alloy formation. *The Journal of Physical Chemistry B* 110, 23 (2006), 11391–11398.
- [47] GAEBLER, W., JACOBI, K., AND RANKE, W. The structure and electronic properties of thin palladium films on zinc oxide studied by AES and UPS. *Surface Science* 75, 2 (1978), 355 – 367.
- [48] GALEOTTI, M., ATREI, A., BARDI, U., ROVIDA, G., AND TORRINI, M. Surface alloying at the Sn—Pt(111) interface: a study by x-ray photoelectron diffraction. *Surface Science* 313, 3 (1994), 349 – 354.
- [49] GIOVANNINI, M., SACCONI, A., DELFINO, S., AND ROGL, P. A comparative investigation of isothermal sections of rare earth-Pd-In systems. *Intermetallics* 11, 11-12 (2003), 1237–1243.
- [50] HAHNE, M., AND GILLE, P. Single crystal growth of the intermetallic compound InPd. *Journal of Crystal Growth* 401 (2013), 622–626.
- [51] HAMMER, B., AND NØRSKOV, J. Theoretical surface science and catalysis—calculations and concepts. In *Impact of Surface Science on Catalysis*, H. K. Bruce C. Gates, Ed., vol. 45 of *Advances in Catalysis*. Academic Press, 2000, pp. 71 – 129.
- [52] HANSEN, M., AND ANDERKO, K. *Constitution of binary alloys*. No. 1 in Metallurgy and metallurgical engineering series. McGraw-Hill, 1965.
- [53] HARRIS, I., NORMAN, M., AND BRYANT, A. A study of some palladium-indium, platinum-indium and platinum-tin alloys. *Journal of the Less Common Metals* 16, 4 (1968), 427 – 440.
- [54] HELD, G. Low-energy electron diffraction crystallography of surfaces and interfaces. *Bunsen-Magazin* 12, 12 (2010), 124–131.
- [55] HELLNER, E., AND LAVES, F. Kristallchemie des In und Ga in legierungen mit einigen übergangselementen (NI, PD, PT, CU, AG und AU). *Zeitschrift Fur Naturforschung Section A: A Journal of Physical Sciences* 2, 3 (1947), 177–183.

- [56] HILLEBRECHT, F. U., FUGGLE, J. C., BENNETT, P. A., AND ZOŁNIEREK, Z. Electronic structure of Ni and Pd alloys. ii. x-ray photoelectron core-level spectra. *Physical Review B* 27 (1983), 2179–2193.
- [57] HORN, K., THEIS, W., PAGGEL, J. J., BARMAN, S. R., ROTENBERG, E., EBERT, P., AND URBAN, K. Core and valence level photoemission and photoabsorption study of icosahedral Al–Pd–Mn quasicrystals. *Journal of Physics: Condensed Matter* 18, 2 (2006), 435.
- [58] HOVE, M. V., MORITZ, W., OVER, H., ROUS, P., WANDER, A., BARBIERI, A., MATERER, N., STARKE, U., AND SOMORJAI, G. Automated determination of complex surface structures by LEED. *Surface Science Reports* 19, 3–6 (1993), 191 – 229.
- [59] HUANG, M., AND CHANG, Y. A. Disorder–order phase transformation in sputter deposited Pd₃In thin films. *Journal of Alloys and Compounds* 455, 1–2 (2008), 174 – 177.
- [60] HUANG, M., XIE, F., YAN, X., AND CHANG, Y. Vacancy concentrations in the B2 intermetallic phase PdIn at 900 degrees C. *Intermetallics* 9, 6 (2001), 457–460.
- [61] HÜFNER, S. *Photoelectron Spectroscopy: Principles and Applications*. Advanced Texts in Physics. Springer, 2003.
- [62] HUNGER, E., HAAS, H., AND GRAWE, H. Adsorption sites of ¹¹¹In and ^{111m}Cd on Pd(111) surfaces characterized by the electric field gradient. *Hyperfine Interactions* 60, 1-4 (1990), 999–1002.
- [63] INDEPENDENT COORDINATION WITH I06 STAFF, March, 2014.
- [64] INDEPENDENT COORDINATION WITH MICHAEL HAHNE, May, 2014.
- [65] IWASA, N., KUDO, S., TAKAHASHI, H., MASUDA, S., AND TAKEZAWA, N. Highly selective supported Pd catalysts for steam reforming of methanol. *Catalysis Letters* 19, 2-3 (1993), 211–216.
- [66] IWASA, N., MASUDA, S., OGAWA, N., AND TAKEZAWA, N. Steam reforming of methanol over Pd/ZnO: Effect of the formation of PdZn alloys upon the reaction. *Applied Catalysis A: General* 125, 1 (1995), 145 – 157.
- [67] IWASA, N., MAYANAGI, T., MASUDA, S., AND TAKEZAWA, N. Steam reforming of methanol over Pd-Zn catalysts. *Reaction Kinetics and Catalysis Letters* 69 (2000), 355–360.

- [68] IWASA, N., NOMURA, W., MAYANAGI, T., ICHIRO FUJITA, S., ARAI, M., AND TAKEZAWA, N. Hydrogen production by steam reforming of methanol. *Journal of Chemical Engineering of Japan* 37, 2 (2004), 286–293.
- [69] IWASA, N., AND TAKEZAWA, N. New supported Pd and Pt alloy catalysts for steam reforming and dehydrogenation of methanol. *Topics in Catalysis* 22 (2003), 215–224.
- [70] JABLONSKI, A., AND POWELL, C. The electron attenuation length revisited. *Surface Science Reports* 47, 2-3 (2002), 35–91.
- [71] JERORO, E., LEBARBIER, V., DATYE, A., WANG, Y., AND VOHS, J. Interaction of CO with surface PdZn alloys. *Surface Science* 601, 23 (2007), 5546 – 5554.
- [72] JIANG, C., AND LIU, Z.-K. Thermodynamic modeling of the indium-palladium system. *Metallurgical and Materials Transactions A* 33 (2002), 3597–3603.
- [73] KING, D., AND WOODRUFF, D. *The Chemical Physics of Solid Surfaces and Heterogeneous Catalysis*. Elsevier, 1981.
- [74] KNIGHT, J. R., AND RHYS, D. W. The systems palladium - indium and palladium - tin. *Journal of the Less-Common Metals* 1 (1959), 292–303.
- [75] KOCH, H., BAKO, I., WEIRUM, G., KRATZER, M., AND SCHENNACH, R. A theoretical study of Zn adsorption and desorption on a Pd(111) substrate. *Surface Science* 604, 11–12 (2010), 926 – 931.
- [76] KOHLMANN, H., AND RITTER, C. Refinement of the crystal structures of palladium-rich In-Pd compounds by x-ray and neutron powder diffraction. *ChemInform* 38, 37 (2007), 929–934.
- [77] KOHLMANN, H., AND RITTER, C. Reaction pathways in the formation of intermetallic InPd₃ polymorphs. *Zeitschrift für anorganische und allgemeine Chemie* 635, 11 (2009), 1573–1579.
- [78] KOVNIR, K., ARMBRÜSTER, M., TESCHNER, D., VENKOV, T., JENTOFT, F., KNOP-GERICKE, A., GRIN, Y., AND SCHLÖGL, R. A new approach to well-defined, stable and site-isolated catalysts. *Science and Technology of Advanced Materials* 8, 5 (2007), 420 – 427.
- [79] KOVNIR, K., ARMBRÜSTER, M., TESCHNER, D., VENKOV, T., SZENTMIKLÓSI, L., JENTOFT, F., KNOP-GERICKE, A., GRIN, Y., AND SCHLÖGL, R. In situ surface characterization of the intermetallic compound PdGa – a highly selective hydrogenation catalyst. *Surface Science* 603, 10–12 (2009), 1784 – 1792.

- [80] KRAUSE, M. O., AND FERREIRA, J. G. K x-ray emission spectra of Mg and Al. *Journal of Physics B: Atomic and Molecular Physics* 8, 12 (1975), 2007.
- [81] KRAWCZYK, M., JABLONSKI, A., ZOMMER, L., TÓTH, J., VARGA, D., KÖVÉR, L., GERGELY, G., MENYHARD, M., SULYOK, A., BENDEK, Z., GRUZZA, B., AND ROBERT, C. Determination of inelastic mean free paths for AuPd alloys by elastic peak electron spectroscopy (EPES). *Surface and Interface Analysis* 33, 1 (2002), 23–28.
- [82] KRAWCZYK, M., ZOMMER, L., JABLONSKI, A., ROBERT, C., PAVLUCH, J., BIDEUX, L., AND GRUZZA, B. Electron inelastic mean free paths (IMFPs) in binary Au-Cu alloys determined by elastic peak electron spectroscopy. *Surface and Interface Analysis* 31, 5 (2001), 415–420.
- [83] KRAWCZYK, M., ZOMMER, L., LESIAK, B., AND JABLONSKI, A. Surface composition of the CoPd alloys studied by electron spectroscopies. *Surface and Interface Analysis* 25, 5 (1997), 356–365.
- [84] KRAWCZYK, M., ZOMMER, L., SOB CZAK, J., AND JABLONSKI, A. Determination of the electron inelastic mean free path in some binary alloys for application in quantitative surface analysis. *Applied Surface Science* 235, 1-2 (2004), 15–20.
- [85] KRAWCZYK, M., ZOMMER, L., SOB CZAK, J., JABLONSKI, A., PETIT, M., ROBERT-GOUMET, C., AND GRUZZA, B. IMFP measurements near Au-Ni alloy surfaces by EPES: indirect evidence of submonolayer Au surface enrichment. *Surface Science* 566, 2 (2004), 856–861.
- [86] LEATHERMAN, G. *Low-Energy Electron Diffraction Study of Alkali Metals Adsorbed on Silver (111), and Their Coadsorption with Rare Gases*. PhD thesis, Department of Physics, The Pennsylvania State University, University Park, PA, U.S., 1996.
- [87] LEDIEU, J., GAUDRY, E., AND FOURNÉE, V. Surfaces of Al-based complex metallic alloys: atomic structure, thin film growth and reactivity. *Science and Technology of Advanced Materials* 15, 3 (2014), 034802.
- [88] LI, H.-I. *Structural Analysis and Interactions of C60 on Ag(111) and Pb(111)*. PhD thesis, Department of Physics, The Pennsylvania State University, University Park, PA, U.S., 2010.
- [89] LIU, S., TAKAHASHI, K., AND AYABE, M. Hydrogen production by oxidative methanol reforming on Pd/ZnO catalyst: effects of Pd loading. *Catalysis Today* 87, 1–4 (2003), 247 – 253.

- [90] LIU, S., TAKAHASHI, K., UEMATSU, K., AND AYABE, M. Hydrogen production by oxidative methanol reforming on Pd/ZnO catalyst: effects of the addition of a third metal component. *Applied Catalysis A: General* 277, 1–2 (2004), 265 – 270.
- [91] LOCATELLI, A., AND BAUER, E. Recent advances in chemical and magnetic imaging of surfaces and interfaces by XPEEM. *Journal of Physics-Condensed Matter* 20, 9 (2008).
- [92] LORENZ, H., JOCHUM, W., KLÖTZER, B., STÖGER-POLLACH, M., SCHWARZ, S., PFALLER, K., AND PENNER, S. Novel methanol steam reforming activity and selectivity of pure In_2O_3 . *Applied Catalysis A: General* 347, 1 (2008), 34 – 42.
- [93] LORENZ, H., TURNER, S., LEBEDEV, O. I., TENDELOO, G. V., KLÖTZER, B., RAMESHAN, C., PFALLER, K., AND PENNER, S. Pd– In_2O_3 interaction due to reduction in hydrogen: Consequences for methanol steam reforming. *Applied Catalysis A: General* 374, 1–2 (2010), 180 – 188.
- [94] LOS ALAMOS NATIONAL LABORATORY. Chemistry division/periodic table of elements: Period table of elements: Lanl web area. <http://periodic.lanl.gov/index.shtml>, accessed May 1, 2014.
- [95] LOVVIK, O. Surface segregation in palladium based alloys from density-functional calculations. *Surface Science* 583, 1 (2005), 100 – 106.
- [96] MACLAREN, D. A., JOHNSTON, J., DUNCAN, D. A., MARCHETTO, H., DHESI, S. S., GADEGAARDE, N., AND KADODWALA, M. Asymmetric photoelectron transmission through chirally-sculpted, polycrystalline gold. *Physical Chemistry Chemical Physics* 11, 38 (2009), 8413–8416.
- [97] MATOLÍN, V., JOHÁNEK, V., STARÁ, I., TSUD, N., AND VELTRUSKÁ, K. Study of bimetallic interactions between transition- and s,p- metals: Pd/ AlO_x and Pd/ SnO_x catalysts and sensors. *Anal. Sci.* 17 (Suppl.) 68 (2001), i151.
- [98] MAYER, A., SALOPAASI, H., PUSSI, K., AND DIEHL, R. D. A novel method for the extraction of intensity–energy spectra from low-energy electron diffraction patterns. *Computer Physics Communications* 183, 7 (2012), 1443 – 1447.
- [99] MCGUIRK, G. M. Au(111) surface restructuring from sulfur adsorbates. Master’s thesis, Department of Physics, The Pennsylvania State University, University Park, PA, U.S., December 2011.
- [100] MEN, Y., KOLB, G., ZAPF, R., O’CONNELL, M., AND ZIOGAS, A. Methanol steam reforming over bimetallic Pd–In/ Al_2O_3 catalysts in a microstructured reactor. *Applied Catalysis A: General* 380, 1–2 (2010), 15 – 20.

- [101] MIEDEMA, A., AND DORLEIJN, J. Quantitative predictions of the heat of adsorption of metals on metallic substrates. *Surface Science* 95 (1980), 447 – 464.
- [102] MOHNEY, S. E., AND CHANG, Y. A. Solid phase equilibria in the In-P-Pd system. *Mat. Sci. Eng. B18* (1993), 94–99.
- [103] MORI, G., LAZZARINO, M., ERCOLANI, D., BIASIOL, G., LOCATELLI, A., SORBA, L., AND HEUN, S. X-ray induced variation of the chemistry of gas/alas oxide nanostructures. *Nuclear Instruments & Methods in Physics Research Section B: Beam Interactions with Materials and Atoms* 246, 1 (2006), 39–44.
- [104] MROZEK, P., JABLONSKI, A., AND SULYOK, A. The inelastic mean free path of electrons in the ordered Al₄₈Ni₅₂ alloy. *Surface and Interface Analysis* 11, 10 (1988), 499–501.
- [105] MULLINS, D., AND OVERBURY, S. The structure and composition of the NiAl(110) and NiAl(100) surfaces. *Surface Science* 199, 1–2 (1988), 141 – 153.
- [106] MUNROE, P., BAKER, I., AND NAGPAL, P. Room-temperature deformation of PdIn. *Journal of Materials Science* 26, 16 (1991), 4303–4306.
- [107] NOMEROVANNAYA, L. V., KIRILLOVA, M. M., AND SHAIKIN, A. B. Interband absorption in the coloured intermetallic compounds PdIn. *physica status solidi (b)* 102, 2 (1980), 715–720.
- [108] NOONAN, J. R., AND DAVIS, H. L. Mixture of ordered domains in the NiAl(111) surface. *Phys. Rev. Lett.* 59 (1987), 1714–1717.
- [109] NOZAWA, K., ENDO, N., KAMEOKA, S., PANG TSAI, A., AND ISHII, Y. Catalytic properties dominated by electronic structures in PdZn, NiZn, and PtZn intermetallic compounds. *Journal of the Physical Society of Japan* 80, 6 (2011), 064801.
- [110] NØRSKOV, J. K., ABILD-PEDERSEN, F., STUDDT, F., AND BLIGAARD, T. Density functional theory in surface chemistry and catalysis. *Proceedings of the National Academy of Sciences* 108, 3 (2011), 937–943.
- [111] OCI VACUUM MICROENGINEERING. *Back-Display LEED-Auger Optics and Power Supply*. Ontario, 1999.
- [112] OKAMOTO, H. In-Pd (Indium-Palladium). *Journal of Phase Equilibria* 24, 5 (2003), 481.
- [113] OMICRON NANOTECHNOLOGY GMBH. *SpectraLEED Optics and Electron Source: User's Guide*, 4.3 ed., October 2003.

- [114] OMICRON NANOTECHNOLOGY GMBH. *DAR 400 X-ray Source and NG DAR 400 Power Supply*, 2.3 ed., October 2004.
- [115] OMICRON NANOTECHNOLOGY GMBH. *MATRIX Application Manual*, 3.0 ed., October 2010.
- [116] OVERBURY, S. H., AND KU, Y.-S. Formation of stable, two-dimensional alloy-surface phases: Sn on Cu(111), Ni(111), and Pt(111). *Phys. Rev. B* *46* (1992), 7868–7872.
- [117] PANCOTTI, A., DE SIERVO, A., CARAZZOLLE, M., LANDERS, R., AND KLEIMAN, G. The effect of alloying on shake-up satellites: The case of Pd in SbPd₂ and InPd₂ surface alloys. *Journal of Electron Spectroscopy and Related Phenomena* *156–158*, 0 (2007), 307 – 309.
- [118] PANG TSAI, A., KAMEOKA, S., AND ISHII, Y. PdZn=Cu: Can an intermetallic compound replace an element? *Journal of the Physical Society of Japan* *73*, 12 (2004), 3270–3273.
- [119] PARRINO, J., AND OF LOUISVILLE, U. *Chemiresistive Hydrogen Sensors Using Gold Palladium and Silver Palladium Hexanethiolate Coated Alloy Monolayer-protected Clusters*. University of Louisville, 2008.
- [120] PAUL, J., CAMERON, S., DWYER, D., AND HOFFMANN, F. The interaction of CO and O₂ with the (111) surface of Pt₃Ti. *Surface Science* *177*, 1 (1986), 121 – 138.
- [121] PENDRY, J. B. Reliability factors for LEED calculations. *Journal of Physics C: Solid State Physics* *13*, 5 (1980), 937.
- [122] PEPPLLEY, B., AMPHLETT, J., KEARNS, L., AND MANN, R. Methanol-steam reforming on Cu/ZnO/Al₂O₃ catalysts. part 2. a comprehensive kinetic model. *Applied Catalysis A-General* *179*, 1-2 (1999), 31–49.
- [123] POWELL, C., AND JABLONSKI, A. Surface sensitivity of x-ray photoelectron spectroscopy. *Nuclear Instruments and Methods in Physics Research Section A: Accelerators, Spectrometers, Detectors and Associated Equipment* *601*, 1–2 (2009), 54 – 65. Special issue in honour of Prof. Kai Siegbahn.
- [124] PRINZ, J., GASPARI, R., PIGNEDOLI, C. A., VOGT, J., GILLE, P., ARMBRÜSTER, M., BRUNE, H., GRÖNING, O., PASSERONE, D., AND WIDMER, R. Isolated Pd sites on the intermetallic PdGa(111) and PdGa($\bar{1}\bar{1}\bar{1}$) model catalyst surfaces. *Angewandte Chemie* *124*, 37 (2012), 9473–9477.

- [125] PRINZ, J., GASPARI, R., STÖCKL, Q. S., GILLE, P., ARMBRÜSTER, M., BRUNE, H., GRÖNING, O., PIGNEDOLI, C. A., PASSERONE, D., AND WIDMER, R. Ensemble effect evidenced by CO adsorption on the 3-fold PdGa surfaces. *The Journal of Physical Chemistry C* 118, 23 (2014), 12260–12265.
- [126] PRINZ, J., PIGNEDOLI, C. A., STÖCKL, Q. S., ARMBRÜSTER, M., BRUNE, H., GRÖNING, O., WIDMER, R., AND PASSERONE, D. Adsorption of small hydrocarbons on the three-fold PdGa surfaces: The road to selective hydrogenation. *Journal of the American Chemical Society* 136, 33 (2014), 11792–11798.
- [127] PUTZ, H., AND BRANDENBURG, K. Pearson’s crystal data: Crystal structure database for inorganic compounds (cd-rom software version 1.4), 2010.
- [128] RAMESHAN, C., LORENZ, H., MAYR, L., PENNER, S., ZEMLYANOV, D., ARRIGO, R., HAEVECKER, M., BLUME, R., KNOP-GERICKE, A., SCHLÖGL, R., AND KLÖTZER, B. CO₂-selective methanol steam reforming on In-doped Pd studied by in situ x-ray photoelectron spectroscopy. *Journal of Catalysis* 295 (2012), 186 – 194.
- [129] RAMESHAN, C., STADLMAYR, W., PENNER, S., LORENZ, H., MAYR, L., HÄVECKER, M., BLUME, R., ROCHA, T., TESCHNER, D., KNOP-GERICKE, A., SCHLÖGL, R., ZEMLYANOV, D., MEMMEL, N., AND KLÖTZER, B. In situ XPS study of methanol reforming on PdGa near-surface intermetallic phases. *Journal of Catalysis* 290 (2012), 126 – 137.
- [130] RAMESHAN, C., STADLMAYR, W., WEILACH, C., PENNER, S., LORENZ, H., HÄVECKER, M., BLUME, R., ROCHA, T., TESCHNER, D., KNOP-GERICKE, A., SCHLÖGL, R., MEMMEL, N., ZEMLYANOV, D., RUPPRECHTER, G., AND KLÖTZER, B. Subsurface-controlled CO₂ selectivity of PdZn near-surface alloys in H₂ generation by methanol steam reforming. *Angewandte Chemie International Edition* 49, 18 (2010).
- [131] RAMESHAN, C., WEILACH, C., STADLMAYR, W., PENNER, S., LORENZ, H., HÄVECKER, M., BLUME, R., ROCHA, T., TESCHNER, D., KNOP-GERICKE, A., SCHLÖGL, R., ZEMLYANOV, D., MEMMEL, N., RUPPRECHTER, G., AND KLÖTZER, B. Steam reforming of methanol on PdZn near-surface alloys on Pd(111) and Pd foil studied by in-situ XPS, LEIS and PM-IRAS. *Journal of Catalysis* 276, 1 (2010), 101–113.
- [132] RIDLEY, N. Densities of some indium solid solutions. *Journal of the Less Common Metals* 8, 5 (1965), 354 –357.

- [133] ROSENTHAL, D., WIDMER, R., WAGNER, R., GILLE, P., ARMBRÜSTER, M., GRIN, Y., SCHLÖGL, R., AND GRÖNING, O. Surface investigation of intermetallic PdGa($\bar{1}\bar{1}\bar{1}$). *Langmuir* 28, 17 (2012), 6848–6856.
- [134] SA, S., SILVA, H., BRANDAO, L., SOUSA, J. M., AND MENDES, A. Catalysts for methanol steam reforming—a review. *Applied Catalysis B-Environmental* 99, 1-2 (2010), 43–57.
- [135] SACHTLER, W. M. H. Chemisorption complexes on alloy surfaces. *Catalysis Reviews* 14, 1 (1976), 193–210.
- [136] SANDERSON, R. *Chemical Bonds and Bond Energy*. No. 2. Academic Press, New York, 1976.
- [137] SCHMID, E. E., AND CARLE, V. Title unknown. *Prakt. Metallogr.* 25 (1988), 340–348.
- [138] SCHUBERT, K., LUKAS, H. L., MEISSNER, H. G., AND BAHN, S. Title unknown. *Z. Metallkd* 50 (1959), 534–540.
- [139] SCOFIELD, J. Hartree-slater subshell photoionization cross-sections at 1254 and 1487 eV. *Journal of Electron Spectroscopy and Related Phenomena* 8, 2 (1976), 129 – 137.
- [140] SCOFIELD, J., AND LAWRENCE LIVERMORE LABORATORY. *Theoretical Photoionization Cross Sections from 1 to 1500 KeV*. UCRL, 1973.
- [141] SEAH, M., GILMORE, I., AND SPENCER, S. Signal linearity in XPS counting systems. *Journal of Electron Spectroscopy and Related Phenomena* 104, 1-3 (1999), 73–89.
- [142] SEAH, M. P. An accurate and simple universal curve for the energy-dependent electron inelastic mean free path. *Surface and Interface Analysis* 44, 4 (2012), 497–503.
- [143] SEAH, M. P. Simple universal curve for the energy-dependent electron attenuation length for all materials. *Surface and Interface Analysis* 44, 10 (2012), 1353–1359.
- [144] SEAH, M. P., AND DENCH, W. A. Quantitative electron spectroscopy of surfaces: A standard data base for electron inelastic mean free paths in solids. *Surface and Interface Analysis* 1, 1 (1979), 2–11.
- [145] SHIRLEY, D. A. High-resolution x-ray photoemission spectrum of the valence bands of gold. *Phys. Rev. B* 5 (1972), 4709–4714.

- [146] SKALA, T., VELTRUSKA, K., MOROSEAC, M., MATOLINOVA, I., KOROTCHENKOV, G., AND MATOLIN, V. Study of Pd-In interaction during Pd deposition on pyrolytically prepared In_2O_3 . *Applied Surface Science* 205, 1-4 (2003), 196–205.
- [147] SLATER, J. C. Atomic radii in crystals. *The Journal of Chemical Physics* 41, 10 (1964).
- [148] SPENCER, M. Surface segregation in some non-ideal platinum alloys: I. platinum-titanium alloys. *Surface Science* 145, 1 (1984), 145 – 152.
- [149] STADLMAYR, W., HUBER, V., PENNER, S., KLÖTZER, B., AND MEMMEL, N. Alloying and structure of ultrathin gallium films on the (111) and (110) surfaces of palladium. *The Journal of Physical Chemistry C* 117, 38 (2013), 19558–19567.
- [150] STADLMAYR, W., KLÖTZER, B., PENNER, S., AND MEMMEL, N. Growth and alloying of ultra-thin Zn layers on Pd(110). *The Journal of Physical Chemistry C* 116, 5 (2012), 3635–3644.
- [151] STADLMAYR, W., RAMESHAN, C., WEILACH, C., LORENZ, H., HAEVECKER, M., BLUME, R., ROCHA, T., TESCHNER, D., KNOP-GERICKE, A., ZEMLYANOV, D., PENNER, S., SCHLOEGL, R., RUPPRECHTER, G., KLOETZER, B., AND MEMMEL, N. Temperature-induced modifications of PdZn layers on Pd(111). *Journal of Physical Chemistry C* 114, 24 (2010), 10850–10856.
- [152] TAKAHASHI, K., TAKEZAWA, N., AND KOBAYASHI, H. The mechanism of steam reforming of methanol over a copper-silica catalyst. *Applied Catalysis* 2, 6 (1982), 363 – 366.
- [153] TAKEZAWA, N., AND IWASA, N. Steam reforming and dehydrogenation of methanol: Difference in the catalytic functions of copper and group viii metals. *Catalysis Today* 36, 1 (1997), 45 – 56.
- [154] TANUMA, S. Calculations of electron inelastic free paths in Au-Cu and Au-Ag alloys. *Bunseki Kagaku* 40, 11 (1991), 667–672.
- [155] TANUMA, S., POWELL, C., AND PENN, D. Material dependence of electron inelastic mean free paths at low energies. *Journal of Vacuum Science & Technology A-Vacuum Surfaces and Films* 8, 3, 2 (1990), 2213–2216.
- [156] TANUMA, S., POWELL, C., AND PENN, D. Calculations of electron inelastic mean free paths .2. data for 27 elements over the 50-2000-eV range. *Surface and Interface Analysis* 17, 13 (1991), 911–926.

- [157] TANUMA, S., POWELL, C., AND PENN, D. Calculations of electron inelastic mean free paths .3. data for 15 inorganic-compounds over the 50-2000-eV range. *Surface and Interface Analysis* 17, 13 (1991), 927–939.
- [158] TANUMA, S., POWELL, C. J., AND PENN, D. R. Calculations of electron inelastic mean free paths for 31 materials. *Surface and Interface Analysis* 11, 11 (1988), 577–589.
- [159] TANUMA, S., POWELL, C. J., AND PENN, D. R. Calculations of electron inelastic mean free paths. ix. data for 41 elemental solids over the 50 eV to 30 keV range. *Surface and Interface Analysis* 43, 3 (2011), 689–713.
- [160] TERSOFF, J., AND HAMANN, D. R. Theory and application for the scanning tunneling microscope. *Phys. Rev. Lett.* 50 (1983), 1998–2001.
- [161] TERSOFF, J., AND HAMANN, D. R. Theory of the scanning tunneling microscope. *Phys. Rev. B* 31 (1985), 805–813.
- [162] WAGNER, C.D. AND RIGGS, W.M. AND DAVIS, L.E. AND MOULDER, J.F. AND MUILENBERG, G.E. (EDITOR). *Handbook of X-Ray Photoelectron Spectroscopy*. Perkin-Elmer Corporation, Physical Electronics Division, 6509 Flying Cloud Drive, Eden Prairie, Minnesota 55344, 1979.
- [163] WEIGAND, P., HOFER, W., AND VARGA, P. Investigation of Pt₂₅Ni₇₅(111): preferential sputtering and surface segregation. *Surface Science* 287–288, Part 1 (1993), 350 – 354.
- [164] WEIRUM, G., KRATZER, M., KOCH, H. P., TAMTOEGL, A., KILLMANN, J., BAKO, I., WINKLER, A., SURNEV, S., NETZER, F. P., AND SCHENNACH, R. Growth and desorption kinetics of ultrathin Zn layers on Pd(111). *Journal of Physical Chemistry C* 113, 22 (2009), 9788–9796.
- [165] WENCKA, M., HAHNE, M., KOCJAN, A., VRTNIK, S., KOŽELJ, P., KORŽE, D., JAGLIČIĆ, Z., SORIĆ, M., POPČEVIĆ, P., IVKOV, J., SMONTARA, A., GILLE, P., JURGA, S., TOMEŠ, P., PASCHEN, S., ORMECI, A., ARMBRÜSTER, M., GRIN, Y., AND DOLINŠEK, J. Physical properties of the InPd intermetallic catalyst. *Intermetallics* 55 (2014), 56 – 65.
- [166] WHITE, C. E. T., AND OKAMOTO, H. E. *Phase Diagrams of Indium Alloys and Their Engineering Applications*. ASM International, Materials Park, OH, 1992.
- [167] WIESENDANGER, R. *Scanning Probe Microscopy and Spectroscopy: Methods and Applications*.

- [168] WOODRUFF, D. *Surface Alloys and Alloy Surfaces*. The Chemical Physics of Solid Surfaces. Elsevier Science, 2002.
- [169] WOODRUFF, D., AND DELCHAR, T. *Modern techniques of surface science*. Cambridge solid state science series. Cambridge University Press, 1986.
- [170] WOODRUFF, D., AND DELCHAR, T. *Modern Techniques of Surface Science (2nd ed.)*. Cambridge Solid State Science Series. Cambridge University Press, 1994.
- [171] WOODRUFF, D., AND ROBINSON, J. Some structural issues in surface alloys and alloy surfaces: rumpling, stacking faults and disorder. *Applied Surface Science* 219 (2003), 1 – 10.
- [172] WRONKOWSKA, A., WRONKOWSKI, A., BUKALUK, A., TRZCIŃSKI, M., AND OKULEWICZ, K. Characterization of In/Pd and Pd/In/Pd thin films by ellipsometric, XRD and AES methods. *Applied Surface Science* 253, 7 (2007), 3367 – 3371.
- [173] WRONKOWSKA, A. A., ARWIN, H., BUKALUK, A., SKOWROISKI, L., TRZCINSKI, M., OKULEWICZ, K., AND WRONKOWSKI, A. IR-VIS-UV ellipsometry, XRD and AES investigation of In/Cu and In/Pd thin films. *physica status solidi (c)* 5, 5 (2008), 1141–1144.
- [174] WU, W., SCHMID, P., LEVY, F., AND BUSSY, F. Point defects and texture of Pd_{1-x}In_x sputtered intermetallic thin films. *Intermetallics* 4, 8 (1996), 617–623.
- [175] WU, W., SCHMID, P., POSTERNAK, M., AND LÉVY, F. Role of point defects on the optical properties of Pd-based Hume-Rothery alloys. *Thin Solid Films* 275, 1–2 (1996), 254 – 257.
- [176] YE, J., LIU, C., AND GE, Q. A DFT study of methanol dehydrogenation on the PdIn(110) surface. *Phys. Chem. Chem. Phys.* 14 (2012), 16660–16667.
- [177] YUEN, C. D., UNAL, B., JING, D., AND THIEL, P. A. Weak bonding of Zn in an Al-based approximant based on surface measurements. *Philosophical Magazine* 91, 19-21 (2011), 2879–2888.

Publications

G. M. MCGUIRK, J. LEDIEU, É. GAUDRY, M. C. DE WEERD, V. FOURNÉE. Surface structures of In-Pd intermetallic compounds. Part I: Experimental study of In thin films on Pd(111) and alloy formation. *J. Chem. Phys* *141*, (2014), 084702.

É. GAUDRY, G. M. MCGUIRK, J. LEDIEU, V. FOURNÉE. Surface structures of In-Pd intermetallic compounds. Part II – A theoretical study. *J. Chem. Phys.* *141*, (2014), 084703.

HEEKEUN SHIN, A. SCHWARZE, R. D. DIEHL, K. PUSSI, A. COLOMBIER, E. GAUDRY, J. LEDIEU, G. M. MCGUIRK, L. N. SERKOVIC LOLI, V. FOURNÉE, L. L. WANG, G. SCHULL, R. BERNDT. The structure and dynamics of C60 molecules on Au(111). *Physical Review B* *89*, (2014), 245428.

G. M. MCGUIRK, H. SHIN, M. CARAGIU, S. ASH, P. K. BANDYOPADHYAY, R. H. PRINCE, R. D. DIEHL. Au(111) surface structures induced by adsorption: LEED I(E) analysis of (1 x 1) and (5 x 5) Au(111)-S phases. *Surface Science* *610*, (2013), 42-47.

Structure de surface d'alliages et de composés intermétalliques In-Pd

Ce travail de thèse s'inscrit dans un programme de recherche européen qui vise à développer de façon rationnelle de nouveaux catalyseurs possédant une activité et une sélectivité élevées pour le vaporeformage du méthanol. L'impact socio-économique de cette réaction est considéré comme très important puisque le méthanol est un vecteur important d'hydrogène pour la production d'énergie dans les piles à combustible via la réaction $\text{CH}_3\text{OH} + \text{H}_2\text{O} \rightarrow \text{CO}_2 + 3\text{H}_2$. Depuis quelques années, la communauté scientifique s'intéresse à une nouvelle génération de catalyseurs de type Pd/ZnO, Pd/Ga₂O₃ ou encore Pd/In₂O₃. L'origine des propriétés catalytiques est généralement attribuée à la formation de composés intermétalliques de type M-Pd (M=Zn, Ga ou In) au cours de la réaction après réduction de l'oxyde. Il est donc essentiel de déterminer les structures électroniques et géométriques/cristallographiques des surfaces de ces intermétalliques à l'échelle atomique, sur des systèmes modèles, pour pouvoir ensuite appréhender leur réactivité chimique. C'est l'objectif principal de la thèse. Le manuscrit comporte cinq parties. Un premier chapitre présente une introduction générale sur l'intérêt des intermétalliques en catalyse hétérogène avec un accent particulier sur le vaporeformage du méthanol. On trouvera également quelques généralités sur les alliages de surface ainsi qu'une revue bibliographique présentant l'état de l'art des connaissances sur les systèmes M-Pd (M=Zn, Ga et In). Les différentes phases connues du diagramme In-Pd sont décrites dans ce chapitre également. Le deuxième chapitre concerne les méthodes expérimentales. Les structures de surfaces ont été étudiées en utilisant essentiellement des méthodes expérimentales de science des surfaces comme la spectroscopie de photoémission X et UV (XPS, UPS), la microscopie à effet tunnel (STM) et la diffraction d'électrons lents (LEED) sous ultravide (UHV). Tous les résultats sont rassemblés dans les chapitres III et IV. Ils constituent une description assez exhaustive de la variété des phases de surface rencontrées dans ce système In-Pd. Une première étude portant sur la formation et la structure d'alliages de surface dans le système In/Pd (111) est présentée dans le chapitre III. Une seconde étude portant sur les différentes surfaces de monocristaux InPd ainsi que sur un échantillon polycristallin InPd est présentée dans le chapitre IV. Finalement, les conclusions et perspectives de ce travail sont exposées dans le chapitre V.

Mots clés: Alliages intermétalliques, structure atomique, structure électronique, surfaces, alliages de surface, STM, LEED, XPS, UPS, InPd, catalyse

Surface structures of In-Pd alloys and intermetallic compounds

This study is part of an European research program that aims to the rational development of new catalytic materials with high activity and selectivity towards the steam reforming of methanol. The socio-economic impact of this reaction is considered very important because methanol is a major vector for the production of hydrogen energy in fuel cells via the reaction $\text{CH}_3\text{OH} + \text{H}_2\text{O} \rightarrow \text{CO}_2 + 3\text{H}_2$. In recent years, the scientific community has become interested in a new generation of catalysts including Pd/ZnO, Pd/Ga₂O₃ or Pd/In₂O₃. The origin of their catalytic properties is generally attributed to the formation of intermetallic compounds of type M-Pd (M = Zn, Ga or In) during the reaction after reduction of the oxide. It is therefore essential to determine the electronic and geometric/crystallographic structures of these intermetallic surfaces at the atomic scale, using model systems, which is a first step towards the understanding of their chemical reactivity. This is the main objective of the thesis. The manuscript consists of five parts. The first chapter presents a general introduction on the interest in intermetallics for heterogeneous catalysis with a particular emphasis on steam reforming of methanol. Some generalities can also be found on surface alloys and a literature review on the state of the art on M-Pd systems (M = Zn, Ga and In). The different phases of the known diagram In-Pd are also described in this chapter. The second chapter deals with experimental methods. The surface structures were studied primarily using experimental surface science methods like photoemission spectroscopy (XPS, UPS), scanning tunneling microscopy (STM) and low energy electron diffraction (LEED) under ultrahigh vacuum (UHV). All results are summarized in Chapters III and IV. They present a fairly comprehensive description of the variety of surface phases encountered in this In-Pd system. A first study of the formation and structure of surface alloys in the In/Pd (111) system is presented in Chapter III. A second study on the different low-index surfaces of InPd single crystals as well as a polycrystalline InPd sample is presented in Chapter IV. Finally, conclusions and perspectives are discussed in Chapter V.

Keywords: Intermetallic compounds, atomic structure, electronic structure, surfaces, surface alloys, STM, LEED, XPS, UPS, InPd, catalysis